Laminar-to-turbulent transition in airfoil boundary layer flows at oscillating inflow conditions

A thesis accepted by the Faculty of
Aerospace Engineering and Geodesy of the University of Stuttgart
in partial fulfillment of the requirements for the degree of
Doctor of Engineering Sciences (Dr.-Ing.)

by

Duncan M. Ohno
born in Stuttgart

main-referee: apl. Prof. Dr.-Ing. Ulrich Rist
co-referee: Prof. Dr.-Ing. Cameron Tropea
chair: Prof. Dr.-Ing. Jens von Wolfersdorf

Date of defence: August 24, 2023

Institute of Aerodynamics and Gas Dynamics
University of Stuttgart
2023

Vorwort

Die Arbeit entstand während meiner Tätigkeit als wissenschaftlicher Mitarbeiter am Institut für Aerodynamik und Gasdynamik der Universität Stuttgart.

Zunächst danke ich Prof. Jens von Wolfersdorf für die Übernahme des Prüfungsvorsitzes. Prof. Cameron Tropea danke ich für die Übernahme des Mitberichts und für die gute Zusammenarbeit im Rahmen des LTT Projekts.

Besonderer Dank gilt meinem Doktorvater und Hauptberichter Prof. Ulrich Rist. Er hat mir viel Freiraum gegeben und stand mir bei allen Fragestellungen stets fachlich zur Seite. Dank des Vertrauens konnte ich in den letzten Jahren einige meiner Ideen und Ansätze erfolgreich umsetzen. Auch möchte ich ihm für seine menschliche und positive Art danken. Diese hat nicht nur mir persönlich geholfen, sondern auch wesentlich zum freundschaftlichen Klima in der Arbeitsgruppe beigetragen.

Bei Prof. Ewald Krämer bedanke ich mich für das mir entgegengebrachte Vertrauen als Doktorand am IAG und für die Unterstützung der Forschungsvorhaben. Außerdem danke ich Dr. Markus Kloker für die fachlichen Gespräche sowie für das Vertrauen, welches er mir zuvor in meiner Studienzeit entgegengebracht hat.

Für die Leitung der parallel laufenden Untersuchungen im Laminarwindkanal sowie die wissenschaftlichen Betreuung der Projekte bedanke ich mich bei Dr. Werner Würz. Die anspruchsvollen experimentellen Untersuchungen wurden von meinen Projektpartnern Jonas Romblad und Michael Greiner durchgeführt, bei welchen ich mich für die gelungene Zusammenarbeit bedanken will.

Meinen ehemaligen Kolleginnen und Kollegen am IAG danke ich für das freundschaftliche Miteinander und die produktive fachliche Zusammenarbeit. Die große Hilfsbereitschaft innerhalb sowie außerhalb der Arbeitsgruppe hat zum Gelingen meiner Arbeit beigetragen.

Mein größtes Privileg – und teilweise auch meine größte persönliche Leistung – ist mein starkes privates Umfeld. Ohne diesen verlässlichen Rückhalt wäre die Arbeit nicht möglich gewesen. Vielen Dank euch allen!

Stuttgart, im August 2023

Duncan Ohno

Contents

Abstract

Laminar-to-turbulent transition in boundary-layer flows on natural laminar flow (NLF) airfoils under oscillating inflow conditions is numerically investigated. In the cases studied, large-scale fluctuations in the form of periodic vertical gusts with the reduced frequency κ and amplitude v'_{gust} generate an oscillating pressure gradient which results in a complex transient behavior of the boundary layer. Under these conditions, two scenarios are investigated: an attached flow with natural Tollmien–Schlichting (TS) wave transition and a boundary-layer flow featuring a laminar separation bubble (LSB). The study aims to provide an in-depth understanding of the transient mechanisms as well as the basis for new transition prediction methods at unsteady conditions.

Direct numerical simulations (DNS) are performed where the gust disturbance is imposed on the fully-resolved transitional boundary layers via unsteady boundary conditions. In this novel (hybrid) approach, transient base flows are generated in advance with unsteady Reynolds-averaged Navier–Stokes (URANS) simulations of entire unsteady airfoil flows in conjunction with the so-called disturbance velocity approach (DVA) to introduce sinusoidal gusts. The spatio-temporal evolution of the modal disturbances is analyzed using the continuous wavelet transform (CWT), which is then compared with linear stability theory (LST) by employing a trajectory-following method developed for transient flows. The numerical methods are validated with experimental results.

In the *attached-flow scenario* with a chord-based Reynolds number $Re = 3.4 \cdot 10^6$, the unsteady boundary layer on the pressure side of an airfoil with an (oscillating but continuous) adverse pressure gradient is investigated for gusts with $0 \leq \kappa \leq 8$ and $0.01 \leq v'_{gust}/u_\infty \leq 0.06$. The physical effects involved are identified and the observations from previous experimental studies are classified. First, the unsteady response of the pressure gradient to the gust and the resulting behavior of the lagging velocity profiles of the viscous boundary layer from URANS are characterized. Due to the corresponding delay of the amplification rates as well as the slow phase velocities of the TS-waves, a strongly time-dependent behavior of the transition location appears according to the LST. In agreement with the experimental investigations, a temporal hysteresis of the transition front is revealed, moving faster in the upstream direction and slower in the downstream direction. This behavior is most pronounced when the gust period roughly corresponds to the lifetime of the TS-waves. A new non-dimensional number to quantify the degree of unsteadiness is proposed, which proves to characterize the transition-front velocities according to linear theory for all investigated cases.

Transient non-linear effects are studied with DNS, where fundamental resonance is chosen as the secondary mechanism for breakdown to turbulence. The so-called convective-transition mode with a subsequent calmed region is found for cases with a high degree of unsteadiness. This phenomenon refers to a periodic termination of the natural transition and is well known in the literature. This study is the first to provide a physical explanation for this mechanism, identifying a delay of the transient mean flow distortion as the primary cause. This delay causes an attenuation of the amplification rates (transient branch II) which can initialize the self-perpetuating convective-transition mode. A tipping-point for the emergence of this phenomenon depending on gust amplitude and frequency can be clearly identified and physically justified by employing the new non-dimensional quantity. Further considerations of non-linear effects are suggested with an analogy to the Doppler effect regarding the arrival of wave crests at the transition front.

In the *separated-flow scenario* with a chord-based Reynolds number $Re = 8.8{\cdot}10^5$, the unsteady boundary layer on the suction side of an airfoil is examined for gusts with $0 \leq \kappa \leq 8$ at $v'_{gust}/u_\infty = 0.04$. The behavior of the LSB with respect to the separation point, the shear-layer transition, and the turbulent reattachment is investigated using DNS with the initiated oblique-resonance scenario as well as DNS without additionally introduced perturbations. Several transient effects of the separated flow are identified. As in the attached-flow scenario, the spatio-temporal amplitude evolution of the convective modes follows linear theory. This determines the motion of the transition location—which oscillates less drastically due to the higher amplification rates in the separated shear-layer—and consequently also the motion of the subsequent turbulent reattachment. The separation point responds much faster to the oscillating pressure gradient than the transition and reattachment, which lag behind due to the low phase velocity of the modes. As the frequency increases, this leads to a "breathing" LSB, which grows or shrinks simultaneously in both the upstream and downstream directions. In addition to the presence of the convective instability, an increase in the influence of the absolute instability inherent to the LSB is observed toward higher gust frequencies. At the highest frequency studied, a clear lock-in or resonance of the laminar separation bubble to the gust is identified.

Zusammenfassung

Die laminar-turbulente Transition in Grenzschichtströmungen von Laminarprofilen unter oszillierenden Anströmbedingungen wird numerisch untersucht. In den behandelten Fällen erzeugen großskalige Störungen in Form periodischer vertikaler Böen mit reduzierter Frequenz κ sowie Amplitude v'_{gust} einen oszillierenden Druckgradienten, was zu einem komplexen transienten Verhalten der Grenzschicht führt. Unter diesen Bedingungen werden zwei Szenarien untersucht: eine anliegende Strömung mit natürlicher Transition durch Tollmien–Schlichting (TS) Wellen und eine Grenzschichtströmung mit einer laminaren Ablöseblase (LSB). Die Studie zielt darauf ab, ein tieferes Verständnis der transienten Mechanismen sowie die Grundlage für neue Methoden zur Transitionsvorhersage unter instationären Bedingungen zu schaffen.

Es werden direkte numerische Simulationen (DNS) durchgeführt, bei denen der Böeneinfluss über instationäre Randbedingungen den vollständig aufgelösten transitionellen Grenzschichten aufgeprägt wird. In diesem neuartigen (hybriden) Ansatz werden transiente Grundströmungen vorab mit Reynolds-gemittelte Navier–Stokes (URANS) Simulationen der gesamten instationären Umströmung von Flügelprofilen erzeugt, wobei mit dem so genannten Störgeschwindigkeitsansatz (DVA) sinusförmige Böen eingeführt werden. Die räumlich-zeitliche Entwicklung der modalen Störungen wird mit Hilfe der kontinuierlichen Wavelet-Transformation (CWT) analysiert, welche dann Dank einer eigens entwickelten Methode zur Trajektorienverfolgung mit den Ergebnissen der linearen Stabilitätstheorie (LST) verglichen werden kann. Die numerischen Methoden sind mit experimentellen Ergebnissen validiert.

Im Fall der *anliegenden Strömung* mit einer Reynoldszahl $Re = 3.4 \cdot 10^6$ (bezogen auf die Sehnenlänge) wird die instationäre Grenzschicht auf der Druckseite eines Profils mit einem (oszillierenden aber durchgängig) positiven Druckgradienten bei Böen mit $0 \leq \kappa \leq 8$ und $0.01 \leq v'_{gust}/u_\infty \leq 0.06$ untersucht. Dabei werden die involvierten physikalischen Effekte identifiziert sowie die Beobachtungen von vorherigen experimentellen Untersuchungen eingeordnet. Zunächst wird die instationäre Reaktion des Druckgradienten auf die Böe und das resultierende nacheilende Verhalten der Geschwindigkeitsprofile der viskosen Grenzschicht mit URANS Ergebnisse charakterisiert. Aufgrund der entsprechenden Verzögerung der Anfachungsraten sowie der langsamen Phasengeschwindigkeiten der TS-Wellen ergibt sich nach der LST ein stark zeitabhängiges Verhalten der Transitionslage. In Übereinstimmung mit den experimentellen Untersuchungen zeigt sich eine zeitliche Hysterese der Transitionsfront, welche sich schneller stromauf und langsamer stromab bewegt. Dieses Verhalten ist am stärksten ausgeprägt, wenn die Böenperiode etwa der Lebensdauer der TS-Wellen entspricht. Es wird eine neue dimensionslose Zahl zur Quantifizierung der

Instationarität vorgeschlagen, welche die Geschwindigkeiten der Transitionsfronten nach der linearen Theorie für alle untersuchten Fälle charakterisieren kann.

Transiente nicht-lineare Effekte werden mit DNS untersucht, wobei die fundamentale Resonanz als sekundärer Mechanismus für den Übergang zur Turbulenz gewählt wird. Der so genannte konvektive Transitionsmodus mit einer beruhigten Region wird bei den Fällen mit hoher Instationarität beobachtet. Bei diesem Phänomen, welches aus der Literatur bekannt ist, wird die natürliche Transition periodisch unterbrochen. Diese Studie liefert eine erstmalige physikalische Erklärung für diesen Mechanismus wobei die Verzögerung der transienten mittleren Grundströmungsverzerrung als primäre Ursache identifiziert wird. Diese Verzögerung führt zu einer Verminderung der Anfachungsraten (transienter branch II), die den sich selbst erhaltenden konvektiven Transitionsmodus einleiten kann. Ein Kipppunkt für das Auftreten dieses Phänomens in Abhängigkeit der Böenamplitude sowie Frequenz kann eindeutig identifiziert und mit Hilfe der neuen dimensionslosen Kennzahl physikalisch begründet werden. Weitere Überlegungen zu nicht-linearen Effekten werden mit einer Analogie zum Doppler-Effekt hinsichtlich der Ankunft von Wellenbergen an der Transitionssfront angestellt.

Im Fall der *abgelösten Strömung* mit einer Reynoldszahl $Re = 8.8 \cdot 10^5$ (bezogen auf die Sehnenlänge) wird die instationäre Grenzschicht auf der Saugseite eines Profils bei Böen mit $0 \leq \kappa \leq 8$ und $v'_{gust}/u_\infty = 0.04$ untersucht. Das Verhalten der LSB in Bezug auf den Ablösungspunkt, der Transition in der Scherschicht sowie der turbulenten Wiederanlagerung wird durch DNS mit eingeleiteter Resonanz durch schräglaufende Moden sowie durch DNS ohne zusätzlich eingeführte Störungen untersucht. Es werden mehrere transiente Effekte der abgelösten Strömung identifiziert. Wie beim Fall mit der anliegenden Strömung entspricht die räumlich-zeitliche Amplitudenentwicklung der konvektiven Moden der linearen Theorie. Dies bestimmt die Bewegung der Transitionslage welche aufgrund der hohen Anfachungsraten in der abgelösten Scherschicht weniger stark oszilliert sowie entsprechend auch die Bewegung der darauf folgenden turbulenten Wiederanlegung. Der Ablösungspunkt reagiert wesentlich schneller auf den oszillierenden Druckgradienten im Vergleich zur Transition und Wiederanlagerung, die wegen der niedrigen Phasengeschwindigkeit der Moden hinterherhinken. Mit zunehmender Frequenz führt dies zu einer "atmenden" LSB, die gleichzeitig in stromauf als auch in stromab Richtung wächst bzw. schrumpft. Neben dem Vorhandensein der konvektiven Instabilität wird eine Zunahme des Einflusses der absoluten Instabilität, die der LSB inherent ist, bei höheren Böenfrequenzen beobachtet. Bei der höchsten untersuchten Frequenz ist ein deutliches Einklinken bzw. eine Resonanz der laminaren Ablöseblase auf die Böe festzustellen.

Notation

Latin letters

A	disturbance amplitude
AoA	angle of attack or inflow angle
AoA_-, AoA_+	minimum and maximum angle of attack or inflow angle
a	speed of sound
C	Theodorsen function
C_3	M-TERA intermittency method parameter
c	phase velocity
$c_1 \dots c_5$	characteristic variables
c_f	skin-friction coefficient
c_l	lift coefficient
c_p	pressure coefficient
c_p, c_v	heat capacity at constant pressure and volume, respectively
D	polynomial ramp function
D_{tr}	transitional density
d	dilation of wavelet
E	total energy
$\boldsymbol{F}$, $\boldsymbol{G}$, $\boldsymbol{H}$	flux vectors of Navier–Stokes equations
f	frequency
f_c	center frequency of wavelet
f_b	time-decay parameter of wavelet
f_s	sampling frequency
G	spatial distribution of sponge/forcing terms strength
g, g_m, g_d	function for spatial modulation; monopole; dipole
h	temporal harmonic
$H_0^{(2)}$, $H_1^{(2)}$	Hankel functions of second kind
H_{12}	shape factor
$i = \sqrt{-1}$	imaginary unit
J_0, J_1	Bessel functions of the first kind
K	turbulent kinetic energy
k	spanwise harmonic
L	length
L_c	chord length
L^k	Lagrange polynomial of order k

Ma	Mach number
$\mathcal{N}$	compressible Navier–Stokes operator
N	envelope of all n-factors
$N(d)$	normalization of wavelet
n	n-factor
Pr	Prandtl number
p	pressure
$\boldsymbol{Q}$	state vector of conservative variables
Q	Q-criterion for vortex visualization
$\boldsymbol{q}$	state vector of primitive pariables
q_x, q_y, q_z	heat-flux density in x, y and z direction, respectively
Re	Reynolds number
Re_{NS}	non-steady Reynolds number
Re_x	streamwise Reynolds number
S	Sears function
St	Strouhal number
T	temperature
T	gust period
t	time
$\boldsymbol{u} = (u, v, w)^T$	chordwise, vertical (w.r.t. chord) and spanwise velocity comp.
$\boldsymbol{u}_g = (u_g, v_g, w)^T$	streamwise, vertical and spanwise velocity components
$\boldsymbol{u}_s = (u_s, v_s, w)^T$	tangential, wall-normal and spanwise velocity components
$\hat{W}$	complex wavelet coefficient
$\boldsymbol{x} = (x, y, z)^T$	chordwise, vertical (w.r.t. chord) and spanwise coordinates
$\boldsymbol{x}_g = (x_g, y_g, z)^T$	streamwise, vertical and spanwise coordinates (geodesic system)
$\boldsymbol{x}_s = (x_s, y_s, z)^T$	arc length and coordinates in wall-normal and spanwise direction

Greek letters

$\alpha = \alpha_r + i\alpha_i$	streamwise wavenumber
β	spanwise wavenumber
γ	ratio of specific heats
γ_z	spatial intermittency in spanwise direction
γ_{tr}	fraction of convective-mode phase
Δx, Δy, Δz	step sizes of the computational grid
Δt	time step
δ_1	displacement thickness
δ_2	momentum thickness
η	dimensionless self-similar wall-normal coordinate
θ	phase, temporal shift
ϑ	thermal conductivity

κ	reduced frequency of oscillation/gust
κ^{tr}	dimensionless number for unsteady, transitional flow
λ	wavelength
λ_{δ_2}	Pohlhausen pressure-gradient parameter
μ	dynamic viscosity
μ_t	eddy viscosity
ν	kinematic viscosity
ξ	angle of wave propagation
ρ	density
$\boldsymbol{\tau}$	strain-rate tensor
$\boldsymbol{\tau}_t$	turbulent shear-stress tensor
ϕ	primitive variable, boundary-layer property
φ	phase
χ	gird stretching factor
Ψ	complex wavelet function
ω	angular frequency
ω_z	spanwise vorticity

Subscripts

0	fundamental or initial quantity
∞	free-stream quantity
bI	branch I/point of neutral stability
bf	base-flow quantity
cr	quantity of calmed region
crit	critical quantity
cwt	quantity of continuous wavelet transform
d	quantity of downstream motion
DVA	disturbance velocity approach
DS	quantity of actuation with disturbance strip
front	quantity of transition front
g	quantity in geodesic coordinate system
gust	quantity of gust disturbance
in	quantity of inflow boundary condition
LSB	quantity of the laminar separation bubble
le	quantity of leading-edge motion
max	maximum value
min	minimum value
mode	quantity of linear mode
NSE	Navier–Stokes equations
out	quantity of outflow boundary condition

pressure	quantity on the pressure side of airfoil
qs	quantity w.r.t. to quasi-steady consideration
ref	reference quantity
rms	root mean square
s	quantity in streamline-oriented/wall-normal coordinate system
sears	quantity w.r.t. Sears function
sec	quantity of secondary mode
sep	quantity of separation point
sim	quantity based on fundamental period of simulation
sp	quantity of sponge/forcing terms
suction	quantity on the suction side of airfoil
t	quantity of turbulent spot/strip
tbf	transient base flow
te	quantity of trailing-edge motion
top	quantity of free-stream boundary condition
tr	quantity of laminar-to-turbulent transition
TS	quantity of Tollmien–Schlichting mode
u	quantity of upstream motion
w	quantity at the wall

Superscripts

$'$	disturbance quantity (zero-to-peak value)
$\dagger$	complex conjugate
$*$	normalization of coordinate to interval; scaled value
$+$	wall units
T	vector transpose

Symbols

Δ	difference operator (peak-to-peak value)
Δ^r	difference to reference case
Δ^l	difference to transient laminar flow
$\bar{}$	time-averaged quantity
$\tilde{}$	dimensional quantity
$\dot{}$	temporal derivative
$\lvert\ \rvert$	absolute value (modulus)
$\hat{}$	complex amplitude function
$\langle\ \rangle_\omega$	moving average based on period w.r.t. to frequency ω

Abbreviations

1D, 2D, 3D	one-, two- and three-dimensional
APG	adverse pressure gradient
COI	cone of influence
CWT	continuous wavelet transform
DNS	direct numerical simulation
DLR	Deutsches Zentrum für Luft- und Raumfahrt (German Aerospace Center)
DS	disturbance strip
FFT	fast Fourier transform
FPG	favorable pressure gradient
IAG	Institute of Aerodynamics and Gas Dynamics
LAINA	Untersuchung laminarer Ablöseblasen unter instationären Anströmbedingungen zur Verbesserung von Profilentwurfsverfahren (Investigation of laminar separation bubbles under unsteady inflow conditions for the improvement of airfoil design methods)
LSB	laminar separation bubble
LST	linear stability theory
LTT	Laminar-turbulente Transition unter instationären Anströmbedingungen (Laminar-to-turbulent transition under unsteady inflow conditions)
MFD	mean flow distortion
NS3D	in-house Fortran code for direct numerical simulation
NSE	Navier–Stokes equations
Q-S	quasi-steady
RANS	Reynolds-averaged Navier–Stokes equations
RMS	root mean square
TS	Tollmien–Schlichting
URANS	unsteady Reynolds-averaged Navier–Stokes equations
ZPG	zero pressure gradient

1 Introduction

Despite the questioning of habits in the face of the challenges that lie ahead for humanity, air travel appears to be an indispensable part of the modern globalized world. One approach for the reduction of greenhouse gas emissions is to develop efficient aircraft designs that aim to minimize the viscous friction drag. Natural laminar flow (NLF) airfoils, well-established in gliders, have the potential to play an important role in eco-efficient concepts for future aircraft. These airfoils feature an extended laminar flow resulting from geometry that places the point of maximum thickness relatively far downstream. This significantly decreases the friction drag due to the shorter stretch of the turbulent boundary layer. Examples for NLF airfoils used for smaller business aircraft include the Piaggio P.180 Avanti, see de'Pompeis *et al.* (1991), or the recently developed Otto Celera 500L, see McKenzie (2022). As part of the Clean Sky Program, the application on large commercial aircraft has also recently been investigated with flight tests of the "BLADE" demonstrator. The experimental aircraft used in this project is based on an A340 with the outer wing sections replaced by NLF panels of lower sweep, see Williams (2017). Another example for large aircraft is the work on the NLF variant of NASA's Common Research Model, see e.g. Helm *et al.* (2023).

Most of the mechanisms of the natural transition from laminar to turbulent flow as present in airfoil boundary-layer flows, are already well understood for steady-state conditions. These fundamentals have been instrumental in developing transition prediction methods, which are still essential for designing airfoils. However, atmospheric turbulence causing unsteady inflow to the airfoil may occur under realistic flight conditions. In the case of large-scale fluctuations, the pressure gradient is particularly affected, and its variation can have a significant influence on the properties of the boundary-layer flow including the transition. A general formulation of a transition prediction method for unsteady flows is not available at this time. Therefore, it is of great interest to fundamentally understand and characterize the behavior and mechanisms of the transition under unsteady flow conditions. Laminar separation bubbles—which cause a drag penalty and are highly susceptible to external disturbances—are also of interest in this context.

For fundamental research on transient flow, the use of a periodic definition for large-scale gusts is an obvious choice to start with. Therefore, a study of the natural transition in an oscillating boundary layer can also contribute to the understanding of effects in other flow scenarios, especially in the presence of rotating elements in engineering applications. These include wind turbines (where NLF airfoils are also used), turbine blades, or aircraft surfaces affected by the wake of propellers.

First, this chapter provides a brief historical overview of research on transition and separation as it relates to the investigations of the present thesis. This is followed by a review of previous (state-of-the-art) studies on transition and separation under unsteady inflow conditions. At last, the objectives of this work are briefly outlined.

1.1 Boundary-layer transition and separation

The phenomenon of laminar-to-turbulent transition was first described for a pipe flow by Reynolds (1883). Following the boundary-layer theory of Prandtl (1904) and the assumption of very small perturbations, Orr (1907) and Sommerfeld (1908) independently developed an equation that provided the first insights into the transition process in flows on airplane wings. The so-called Orr–Sommerfeld equation is derived from the linearized Navier–Stokes equations and can be used to analyze the properties of the primary instability in boundary-layer flows. Tollmien (1929) was the first to solve the equation, after Heisenberg (1924), among others, had worked on the subject. Shortly after, Schlichting (1933) successfully applied the equation for a flow over a flat plate. The eigenfunctions found for the exponentially growing perturbations with the linear stability theory (LST) were appropriately named "Tollmien–Schlichting" (TS) waves. The experimental verification of the theory was carried out by Schubauer & Skramstad (1947) during the Second World War and was published afterwards due to censorship. Since then, the LST has been the foundation of transition research. Subsequent theoretical studies, see e.g. Gaster (1965), have led to a deeper understanding of the spatio-temporal evolution of the modes. The first direct numerical simulations (DNS) of TS-waves in a flow over a flat plate were carried out by Fasel (1976).

Based on linear stability analysis, van Ingen (1956) and Smith & Gamberoni (1956) independently developed the e^n-method, which is still state of the art for transition prediction. In this semi-empirical method, n-factors representing the modal amplitudes are determined by the downstream integration of the amplification rates from the LST. Consequently, the transition location can be determined with an empirical threshold value n_{crit} based on flow properties such as varying turbulence intensity, see Mack (1977), or surface roughness, see Crouch & Ng (2000).

The three-dimensional breakdown to turbulence is preceded by a (weakly) nonlinear stage in which secondary mechanisms are active. One scenario is the so-called fundamental resonance which results to aligned Λ-vortices and was first described by Klebanoff *et al.* (1962). The traits shown in that study would later be known as the K-type regime which is driven by a primary 2D mode and a pair of oblique secondary modes at the same frequency. The subharmonic resonance (H-type) with the oblique modes at half the frequency and resulting staggered Λ-vortices was intensively studied by Herbert (1983). A mathematical description of the secondary

stability analysis is given by Herbert (1988) using Floquet theory. Oblique resonance (O-type) with two waves running in opposite spanwise direction was first investigated by Thumm (1991) and Schmid & Henningson (1992). A detailed summary of different resonance scenarios is given in Kachanov (1994). DNS of those breakdown scenarios have been performed e.g. by Rist & Fasel (1995) or Sayadi *et al.* (2013).

Under certain conditions (e.g. high adverse pressure gradient), laminar separation of the boundary-layer flow may occur, usually followed by a rapid laminar-to-turbulent transition due to the shear-layer instability. The turbulent fluctuations cause the flow to reattach, which closes the so-called laminar separation bubble (LSB). The topology of an LSB including the separation point, a dead-air region, the transition, the reverse-flow vortex, and the turbulent reattachment has been studied e.g. by Tani (1964) and Gaster (1967) and will be discussed later in this thesis in chapter 4. In general, the transition process in a separated shear-layer can also be dominated by an absolute or global instability rather than by convective modes, see Huerre & Monkewitz (1985, 1990) for theoretical background. This was investigated e.g. by Rist *et al.* (1996) and Alam & Sandham (2000) using DNS.

1.2 Impact of oscillating inflow conditions

Under realistic flight conditions, the boundary layer of an airfoil is subjected to perturbations over a wide range of length scales. With respect to transition and separation, two scales of perturbation from atmospheric turbulence are particularly relevant: Small-scale disturbances, which mostly provide the initial amplitudes of modal disturbances in the boundary layer, and large-scale disturbances, which can be considered as gusts or unsteady inflow-angle variations. Considering the model for isotropic free-stream turbulence of Pope (2000) based on the Kolmogorov (1941) hypothesis, the former case can be placed within the dissipation range and the latter case at the edge of the eddy-containing range, see Reeh (2014). The present work focuses on the impact of large-scale disturbances, which mainly affect the boundary-layer flow due to the resulting unsteady pressure gradient.

First investigations on transition in oscillating boundary-layer flows were made by Miller & Fejer (1964) for flow over a flat plate. In these measurements, turbulent bursts or strips were identified which formed periodically at the frequency of the oscillating free stream. These experimental investigations were followed up by Obremski & Fejer (1967), where the unsteady behavior of the transition was studied for several cases including favorable and adverse pressure gradients. In this detailed study, the evolution of the turbulent spots that appear in some of the oscillating cases was characterized by two phases: A “creative phase”, in which a natural transition occurs due to a preceding high-amplitude “wave packet”, and a “convective phase”, in which the turbulent flow migrates downstream with constant leading-

and trailing-edge velocities. Furthermore, a non-steady Reynolds number was proposed, which seemed to be able to describe the unsteady transition behavior to some extent, see also White (2006). Later, using stability analysis with a quasi-steady approach for periodic flows, Obremski & Morkovin (1969) confirmed that the creative phase found in the measurements of Obremski & Fejer (1967) can be attributed to a natural transition with TS-waves. A critical review of these pioneering studies with some identified shortcomings has been given by Loehrke *et al.* (1975).

The "convective-transition mode" was also observed by Studer *et al.* (2006) in the boundary layer of a NACA0015 airfoil subjected to inflow-angle variations. However, this study did not show temporarily spatially closed turbulent spots, but a continuous laminar-turbulent interface with an upstream moving creative phase followed by a downstream moving convective phase. Direct comparison with the amplitudes from the continuous wavelet transform (CWT) confirmed the quasi-steady stability behavior of the amplified modes of the creative phase. Romblad *et al.* (2020) performed further wind-tunnel measurements with a NLF airfoil utilizing a gust generator to simulate realistic large-scale disturbances. Despite the absence of a convective-transition mode in these investigations, the transition front moved significantly faster in upstream direction than in downstream direction during the oscillation. This temporal "asymmetric" or "skewed" behavior became more pronounced at higher gust frequencies. Applying a quasi-steady approach with an unsteady extension of the e^n-method, Ohno *et al.* (2022) attributed the unsteady transition movement observed in Romblad *et al.* (2020) entirely to effects covered by linear theory.

Other examples of the application of LST at unsteady conditions are Radespiel *et al.* (2007) for URANS simulations of laminar separation bubbles or Reeh (2014) with a formulation of an unsteady boundary layer on an NLF airfoil. A more sophisticated approach using complex-ray theory for linear stability analysis has been shown by Citro & Luchini (2013, 2015). Studies employing DNS of natural transition under unsteady conditions that preceded this work are not known.

The potential importance of the so-called calmed region which occurs with the convective-transition phase was emphasized by Obremski & Fejer (1967). Previously, Schubauer & Klebanoff (1955) observed this quiescent region of non-turbulent flow in the wake of a turbulent spot during downstream convection. This transient zone can be interpreted as a phase where the characteristics of the flow recovers from the turbulent state back to the laminar state. Since the velocity profiles are accordingly very full, this region exhibits a significantly increased stability to external disturbances. For this reason, Obremski & Fejer (1967) suggested that the calmed region might be involved in the termination of the creative-transition phase. The calmed region was also observed in later studies on turbulent spots, including Wygnanski *et al.* (1976) for a Blasius flow, Zilberman *et al.* (1977) for a transitional flow, or Katz *et al.* (1990) for a flow with a favorable pressure gradient.

The (periodic) occurrence of the calmed region during wake-induced transition also gained interest in the fundamental research motivated by turbomachinery, see e.g. Pfeil *et al.* (1983), Walker (1989) or Mayle & Dullenkopf (1991). Authors such as Walker (1993) and Orth (1993) assumed that the calmed region is inaccessible to TS-waves because the trailing-edge velocity of the region is considerably faster then the phase speed of the modes. However, the investigations of Seifert & Wygnanski (1995) on a turbulent spot under an adverse pressure gradient showed a stronger and "decelerated" calmed region which can be penetrated by TS-waves. This was also pointed out by Gostelow *et al.* (1997), who provided a detailed analysis of the calmed region. Previously, Gostelow *et al.* (1996) characterized turbulent spots for different self-similar pressure gradients with respect to the leading-edge and trailing-edge velocities. A theoretical mathematical model of the calmed region was derived by Brown & Smith (2005). In addition, there are various studies on turbulent spots with DNS, see e.g. Jocksch & Kleiser (2008).

In general, the transitional flows in turbomachinery are characterized by lower Reynolds numbers and higher turbulence intensities compared to the boundary layers on the NLF airfoils of aircraft in free flight. However, phenomena such as TS-wave transition, laminar separation, and the calmed region can also occur here, see the detailed overview of different scenarios on turbine blades by Halstead *et al.* (1997). An empirical unsteady transition prediction method based on the measurements of Walker *et al.* (1999) is given by Solomon *et al.* (1999). Hughes & Walker (2001) used the CWT to analyze the TS-wave transition in a compressor flow.

In recent years, several numerical and experimental investigations of laminar separation bubbles at relatively low Reynolds numbers for pitching or plunging airfoils have been carried out, for example by Lee & Gerontakos (2004), Radespiel *et al.* (2007), Nati *et al.* (2015) or Guerra *et al.* (2021). The first DNS of a laminar separation bubble in the presence of an external oscillating flow was performed by Wissink & Rodi (2003) on a flat plate. In that study, the variation of the inflow velocity combined with a certain shape of the upper (slip) boundary condition generates a pressure gradient in the streamwise direction, oscillating in time. The formation of a new separation bubble in each period was observed, in that setup, which is characterized by a low Reynolds number and a relatively high oscillation amplitude. Recently, Yarusevych & Kotsonis (2017) studied the transient response of a laminar separation bubble to a harmonic, time-modulated excitation.

1.3 Objectives and thesis outline

The objective of the present work is to improve the understanding of laminar-to-turbulent transition under unsteady conditions with an oscillating inflow. Understanding the basic physical effects should aid in the design of transition models, e.g.

for URANS simulations. The findings and resulting models can serve in the design of future eco-efficient aviation concepts featuring reduced pollutant emissions. For the numerical investigations, the (U)RANS code *TAU* and the in-house DNS code *NS3D* for compressible flows were used. The periodic gusts were generated with URANS simulations employing the disturbance velocity approach (DVA). A transient extension of the linear stability analysis also proved to be an important part of the theoretical considerations. Chapter 2 provides a detailed introduction to the numerical methods. The studies include two cases of unswept 2D boundary-layer flows with different geometries of NLF airfoils. Both airfoil flows are subjected to periodic vertical gusts using the same numerical formulation which corresponds to realistic flight conditions.

In the first case, the unsteady laminar-to-turbulent transition due to convective TS-waves in an attached flow is investigated. The purpose of this research is to better understand and classify the observations of previous work by Obremski & Fejer (1967), Studer *et al.* (2006) and Romblad *et al.* (2020). Special attention is given to the distinction between linear and non-linear effects, which will help to understand the mechanism of the so-called convective-transition mode. The work was carried out within the project "Laminar-turbulente Transition unter instationären Anströmbedingungen zur Verbesserung von Profilentwurfsverfahren" (LTT), which was accompanied by experimental studies, see Romblad *et al.* (2020); Romblad (2023); Guissart *et al.* (2021). This attached-flow scenario is discussed in chapter 3 and will be referred to as "LTT case" in the following.

In the second case, the influence of periodic gusts on a laminar separation bubble is investigated. The study aims to characterize the unsteady behavior of the separation point, the laminar-to-turbulent transition of the shear-layer, and the turbulent reattachment. In addition, the influence of an absolute instability as well as possible lock-in effects of the bubble on the gust are investigated. Experimental studies accompanied the project titled "Untersuchung laminarer Ablöseblasen unter instationären Anströmbedingungen zur Verbesserung von Profilentwurfsverfahren" (LAINA), see Greiner & Würz (2021); Greiner (2024). This separated-flow scenario is presented in chapter 4 and will be referred to as "LAINA case" in the following.

Parts of the introduction to numerical methods in chapter 2 and most of the results and discussion of the LAINA case in chapter 4 are also published in Ohno *et al.* (2023*a*). The relevant figures were adapted for this thesis and the original text was prepared exclusively by the author of this work. The results of the LTT case in chapter 3 have not been published elsewhere at the time of publication of this thesis. However, a preliminary study on unsteady stability analysis (in which URANS with DVA have not yet been used) has been published in Ohno *et al.* (2022).

2 Numerical methods

The simulation results of fully resolved transitional boundary layers presented in this work are obtained with the compressible, high-order, in-house DNS code *NS3D*. Fundamentals of the code can be found in Babucke (2009) and Keller (2016). The preceding computation of the entire unsteady airfoil flow is performed with the unsteady Reynolds-Averaged Navier–Stokes (URANS) solver *TAU*, which was developed by the German Aerospace Center (DLR), see Schwamborn *et al.* (2006). In these simulations, large-scale periodic gusts are introduced into the simulation domain using the so-called disturbance velocity approach (DVA), see Heinrich & Reimer (2013). A novel (hybrid) approach is used in this work where the oscillating URANS flow fields are employed as transient base flows in DNS via unsteady boundary conditions.

The governing equations and general notations are introduced in the following section, whereas definitions including coordinate systems relevant for the unsteady airfoil flow are provided in section 2.2. Fundamentals of the conducted (U)RANS simulations are given in section 2.3, while the unsteady extension of linear stability analysis for periodic flows is discussed in section 2.5. A review of the DNS with emphasis on the modification of boundary conditions and forcing zones for transient flows is presented in section 2.6. Finally, the continuous wavelet transform (CWT) for spectral analysis for transient DNS results is presented in section 2.7.

2.1 Governing equations

The three-dimensional, time-dependent, compressible Navier–Stokes equations (NSE) describe the viscous fluid flow in a continuum. In general, this term refers to the set of partial differential equations consisting of the continuity equation, the momentum equation and the energy equation. However, in a stricter sense, the NSE only refers to the momentum conservation. In the DNS code *NS3D*, this unaltered system of equations is solved. The (U)RANS solver *TAU*, however, solves the NSE in Reynolds averaged form with additional turbulence models. Furthermore, the underlying equations of the linear stability analysis are derived from the linearization of the NSE.

Throughout this work, non-dimensional quantities are generally used. However, some dimensional values are given which are denoted by $\tilde{\bullet}$. The vector $\boldsymbol{u} = (u, v, w)^T$ represents the velocities in the chordwise, vertical (with respect to chord) and spanwise directions x, y, z, respectively. Additional primitive variables of the compressible flow are density ρ, temperature T and pressure p. Velocity and length scales

are normalized by the free-stream velocity $\tilde{u}_\infty$ and the reference length $\tilde{L}_{ref}$, respectively. Consequently, the non-dimensional time is defined $t = \tilde{t}(\tilde{u}_\infty/\tilde{L}_{ref})$. Density and temperature are normalized by their respective free-stream values $\tilde{\rho}_\infty$ and $\tilde{T}_\infty$, whereas the pressure is normalized with the double dynamic pressure $\tilde{\rho}_\infty \tilde{u}_\infty^2$.

The NSE in non-dimensional conservative formulation are

$$\frac{\partial \rho}{\partial t} + \nabla \cdot (\rho \boldsymbol{u}) = 0\,, \tag{2.1a}$$

$$\frac{\partial (\rho \boldsymbol{u})}{\partial t} + \nabla \cdot (\rho \boldsymbol{u}\boldsymbol{u}) = -\nabla p + \frac{1}{Re}\nabla \cdot \boldsymbol{\tau}\,, \tag{2.1b}$$

$$\begin{aligned} \frac{\partial E}{\partial t} + \nabla \cdot (E\boldsymbol{u}) = {} & \frac{1}{(\gamma-1)RePrMa^2}\nabla \cdot (\vartheta \nabla T) \\ & - \nabla \cdot (p\boldsymbol{u}) + \frac{1}{Re}\nabla \cdot (\boldsymbol{\tau}\boldsymbol{u})\,, \end{aligned} \tag{2.1c}$$

with the Cartesian coordinates $\boldsymbol{x} = (x, y, z)$, the total energy E, thermal conductivity ϑ and the ratio of specific heats $\gamma = c_p/c_v = 1.4$. Including Stokes' hypothesis for the relation of bulk viscosity and dynamic viscosity μ, the viscous-stress tensor for a Newtonian fluid is given by

$$\boldsymbol{\tau} = \mu \left(\nabla \boldsymbol{u} + (\nabla \boldsymbol{u})^T - \frac{2}{3}(\nabla \cdot \boldsymbol{u})\boldsymbol{I} \right)\,, \tag{2.2}$$

with $\boldsymbol{I}$ as the identity matrix. The temperature dependence of the dynamic viscosity $\mu(T)$ is modeled by Sutherland's law. Note: The dynamic viscosity is related with the kinematic viscosity by $\nu = \mu/\rho$. Closure of the system is achieved with the equation of state in non-dimensional form

$$p = \frac{\rho T}{\gamma Ma^2}\,. \tag{2.3}$$

With the assumption of a calorically perfect gas, the temperature can be calculated with

$$T = \gamma(\gamma-1)Ma^2 \left(\frac{E}{\rho} - \frac{1}{2}(\boldsymbol{u} \cdot \boldsymbol{u}) \right)\,. \tag{2.4}$$

The equations (2.1) are formulated with the dimensionless quantities

$$Re = \frac{\tilde{u}_\infty \tilde{L}_{ref}}{\tilde{\nu}_\infty}\,, \quad Pr = \frac{\tilde{c}_p \tilde{\mu}_\infty}{\tilde{\vartheta}_\infty}\,, \quad Ma = \frac{\tilde{u}_\infty}{\tilde{a}_\infty}\,, \tag{2.5}$$

where $\tilde{a}_\infty$ denotes the speed of sound in free stream. The Reynolds number Re describes the ratio of inertial forces to viscous forces, the Prandtl number Pr the ratio of momentum to thermal diffusivity and the Mach number Ma the impact of compressibility. $Pr = 0.72$ is selected in both flow scenarios simulated in this work.

2.2 Definitions for unsteady airfoil flow

To numerically investigate the oscillating airfoil boundary layer including periodic gusts, different coordinate systems have to be defined, cf. figure 2.1. In the illustration, the airfoil with its coordinate systems is mirrored vertically, since the boundary layer under investigation is located on the pressure side. For both (U)RANS and DNS simulations, the Cartesian coordinates $\boldsymbol{x} = (x, y, z)^T$ are generally used, with the origin placed at the leading edge and x representing the chordwise direction. However, to describe gusts in the URANS simulations with the DVA, a geodesic coordinate system $\boldsymbol{x_g} = (x_g, y_g, z)^T$ based on free-flow direction is introduced, thus taking into account the angle of attack AoA_{ref}. Furthermore, a wall-normal coordinate system $\boldsymbol{x}_s = (x_s, y_s, z)^T$ is defined, combining arc length and the wall-normal and spanwise directions, respectively. This coordinate system with its velocity vector $\boldsymbol{u}_s$—see tangential velocity u_s and wall-normal velocity v_s in figure 2.1—is used to analyze the simulation results in terms of boundary-layer properties and to perform linear stability calculations. In this work, however, the results are always plotted versus x. It should be noted, that the base flows and gust disturbances in the investigated flow scenarios are purely two-dimensional, hence $w_\infty = w'_{gust} = 0$.

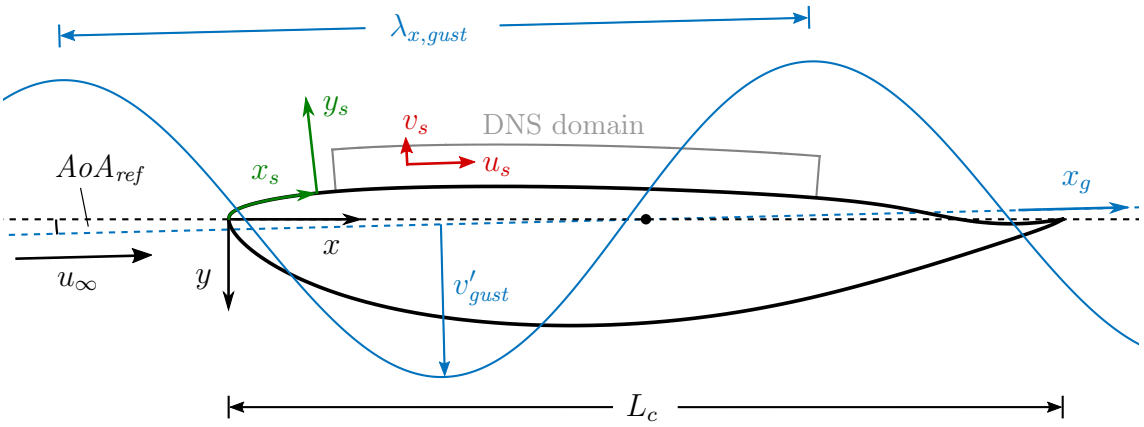

Figure 2.1: Schematic illustration of an airfoil (LTT case, mirrored vertically) with a gust moving with u_∞ in x_g direction. The chord-oriented coordinates are denoted with $\boldsymbol{x}$, the coordinates of the wall-normal system are denoted with $\boldsymbol{x}_s$ where u_s and v_s represent the tangential and wall-normal velocities, respectively.

Following the notation introduced in the previous section, normalized angular frequencies, wavenumbers and wavelengths can be calculated with $\omega = \tilde{\omega}(\tilde{L}_{ref}/\tilde{u}_\infty)$, $\alpha = \tilde{\alpha}\tilde{L}_{ref}$ and $\lambda = \tilde{\lambda}/\tilde{L}_{ref}$, respectively. The respective chord lengths in the two flow scenarios are chosen as the reference length $\tilde{L}_{ref} = \tilde{L}_c$ in this work. Therefore, the dimensionless coordinate x equals the standard normalization $\tilde{x}/\tilde{L}_c$ for airfoil

investigations. The reduced frequency

$$\kappa = \frac{\pi \tilde{f}_{gust} \tilde{L}_c}{\tilde{u}_\infty} = \frac{\omega_{gust}}{2}\,, \tag{2.6}$$

based on the semi-chord length with the dimensional frequency $\tilde{f}_{gust}$ is commonly used to characterize unsteady airfoil behavior, see Leishman (2006). Here, the dimensionless quantity is applied to specify the investigated unsteady cases containing gusts. Other authors, e.g. Studer *et al.* (2006), use the Strouhal number $St = \kappa/\pi$ for gust characterization. To relate the gust oscillation to the frequencies of all other disturbances occurring in the flow, ω_{gust} is defined in equation (2.6). In figure 2.1 a downstream traveling gust with u_∞ in x_g direction is depicted. With the Taylor's hypothesis of frozen turbulence, the streamwise wavelength of the gust

$$\lambda_{x,gust} = \frac{\pi}{\kappa} = \frac{2\pi}{\omega_{gust}}\,, \tag{2.7}$$

can be obtained. Using the DVA in the URANS simulations, continuous sinusoidal gusts are defined, which are convecting with free-stream velocity u_∞ in x_g direction. The gust is described spatially and temporally ($\kappa > 0$) by a vertical velocity disturbance

$$v'_g(x_g, t) = v'_{gust} \cdot \sin\left(\frac{2\pi x_g}{\lambda_{x,gust}} - \omega_{gust} t\right) \tag{2.8}$$

in the geodesic system with the gust amplitude v'_{gust}. Therefore, the gust corresponds to a traveling wave and its influence on the lift can be estimated by the formulation of Sears (1941). Standing-wave gusts—in some sense corresponding to the formulation of Theodorsen (1935) for pitching airfoils, see Turhan *et al.* (2022)—are not considered in this work.

For fundamental characterization of the flow scenario, the theoretical case $\kappa \to 0$ with an "infinitely large" gust $\lambda_{x,gust} \to \infty$ or $\lambda_{x,gust} \gg L_c$, can be investigated. This is realized by analyzing the steady-state flow at different inflow angles, which correspond to the phases of the gusts with respect to the gust amplitude v'_{gust}. The zero-to-peak fluctuation of the inflow angle induced by the gust is

$$AoA' = \arctan\left(\frac{v'_{gust}}{u_\infty}\right). \tag{2.9}$$

The resulting angle of attack for a steady-state phase-sweep with $\varphi \in [0, 1)$ can be calculated with

$$AoA(\varphi) = AoA_{ref} + AoA' \sin(2\pi\varphi)\,, \tag{2.10}$$

where AoA_{ref} represents the reference angle of attack of the respective scenario. Here, this is referred to as the quasi-steady consideration (Q-S) and the cases with

minimum and maximum inflow angle AoA according to equation (2.10) are denoted AoA_- and AoA_+, respectively. In the case $\kappa \to 0$, the formulations of Sears (1941) and Theodorsen (1935) for the estimation of the lift coincide, see Leishman (2006).

2.3 (Unsteady) RANS simulation

On currently available HPC systems, DNS of the entire flow field around an airfoil at very high Reynolds numbers are still very expensive. Therefore, only the relevant areas of boundary-layer flow past the leading edge of the airfoil are computed with highly-resolved DNS in the scenarios investigated here. In order to generate the correct physical representation of flow properties at the boundaries of the DNS domain, two-dimensional (U)RANS simulations of the entire flow field are performed beforehand. Steady or unsteady flow solutions from RANS or URANS, respectively, are interpolated to the grid of the subsequent DNS, serving as an initial solution and as (unsteady) boundary conditions. In figure 2.2(b), the full extent of the DNS domain (LTT case) on top of the (U)RANS flow field can be seen on the pressure side of the airfoil. Furthermore, this hybrid approach allows to focus on the flow physics of interest while disregarding secondary effects such as leading-edge receptivity or trailing-edge noise.

The fundamental equations for the computation of the airfoil flow are based on Reynolds averaging of the unsteady NSE, which are introduced in section 2.1. Thereby, all flow quantities are decomposed to a mean part ($\overline{\bullet}$) and fluctuating ($\bullet'$) part, e.g.

$$u(t) = \overline{u} + u'(t) \tag{2.11}$$

for the streamwise velocity component. The resulting time-averaged system of equations contains a non-linear term known as the Reynolds stresses. With the Boussinesq hypothesis, the term can be related to the mean flow by introducing the concept of eddy viscosity. For compressible flows, the modeled tensor of turbulent shear/Reynolds stresses reads

$$\overline{\boldsymbol{\tau}_t} = \mu_t \left(\nabla \boldsymbol{u} + (\nabla \boldsymbol{u})^T - \frac{2}{3}(\nabla \cdot \boldsymbol{u})\boldsymbol{I} \right) - \frac{2}{3}\overline{\rho} K \boldsymbol{I} \tag{2.12}$$

with the eddy viscosity μ_t and the turbulent kinetic energy K. In the system of differential equations, this term can now be combined with the tensor of molecular stresses from equation (2.2), yielding

$$\overline{\boldsymbol{\tau}} = \overline{\boldsymbol{\tau}_{mol}} + \overline{\boldsymbol{\tau}_t} = (\mu + \mu_t) \left(\nabla \boldsymbol{u} + (\nabla \boldsymbol{u})^T - \frac{2}{3}(\nabla \cdot \boldsymbol{u})\boldsymbol{I} \right) - \frac{1}{3}\overline{\rho} K \boldsymbol{I}\,. \tag{2.13}$$

For closure of the problem, several turbulence models considering K and μ_t are

available, usually adding further transport equations to the system of Reynolds-averaged NSE.

NLF airfoils usually feature extended laminar boundary layers downstream of the leading edge where no turbulent fluctuations are present. Turbulence models can naturally only consider turbulent regions of the boundary layer and are not able to predict the laminar-to-turbulent transition. However, stretches of laminar flow can be included in (U)RANS simulations by suppressing the production of eddy viscosity upstream of the transition location. The length of laminar boundary layers can be determined either by a transition model or by prescribing a fixed transition location. In this work, the latter method is chosen, where the transition position is mainly determined based on prior linear stability calculations. This is illustrated in figure 2.2(b), where the transition location x_{tr} is predefined in the (U)RANS simulations. Turbulent boundary layers are thicker, feature higher values of skin friction and their velocity profiles are less prone to separation in regions with adverse pressure gradients. Consequently, the turbulent regions in the rear section have an effect on the macroscopic airfoil flow which includes the overall circulation. Although the region of laminar flow is primarily relevant for the subsequent DNS and linear stability analysis, the turbulent boundary layers therefore have to be included for correct physical representation of the flow.

2.3.1 Finite volume solver and numerical grid

The DLR code *TAU* solves the above described compressible Reynolds-averaged Navier–Stokes equations with a finite volume method. Computations of complex flows can be performed on hybrid and unstructured grids, whereby several different turbulence models are available. An overview including a summary of recent applications of the solver is given in Schwamborn *et al.* (2006).

In this work, the turbulence model of Spalart & Allmaras (1991) is exclusively applied, in which the eddy-viscosity factor is solved by an additional transport equation. This turbulence model is well established for aerospace applications and is considered very robust for wall-bounded flows with adverse pressure gradients (APG). Moreover, it was used exclusively in the previous studies on the disturbance velocity approach (see next section) and exhibited good performance. For the time stepping, the implicit backward Euler method is selected with the lower-upper symmetric Gauss-Seidel (LU-SGS) algorithm for the inner iterations. Furthermore, multigrid methods for better convergence are applied and a preconditioner is used in order to allow low Mach number simulations. While the transient cases with DVA gusts are necessarily simulated with URANS, the steady-state cases can be simulated with simple RANS. However, unlike the attached-flow scenario (LTT case), URANS also had to be utilized for the steady-state flow of the laminar separation scenario (LAINA case) due to its inherent flow instability. A residual of 10^{-8} is chosen as the

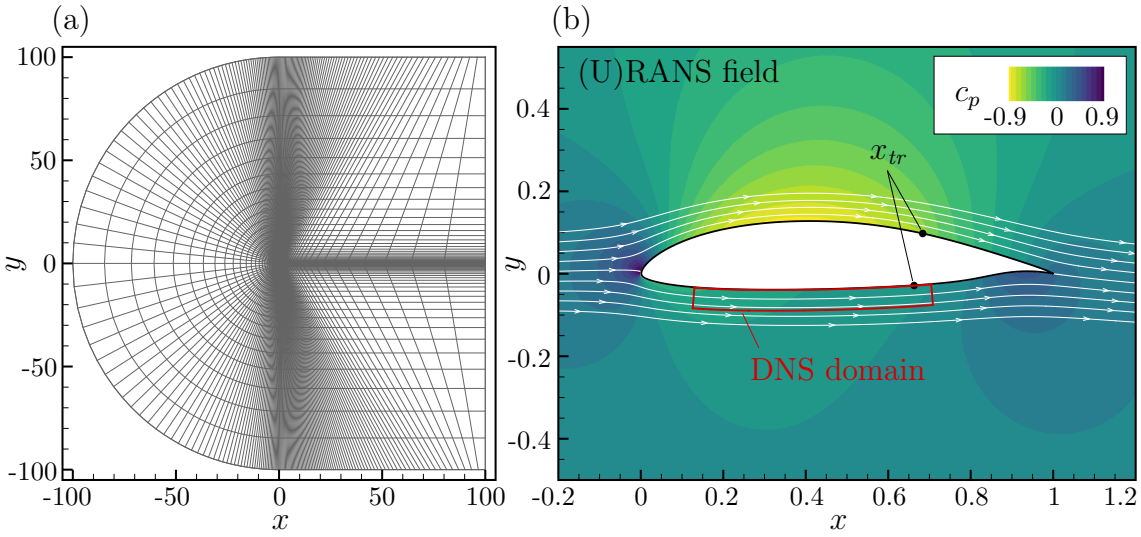

Figure 2.2: Configuration of (U)RANS simulations. (a) Structured far-field C-grid of airfoil, resolution reduced by factor ≈ 5 for clarity. (b) Close-up of the 2D airfoil flow (LTT case) with streamlines and pressure distribution $c_p = (p - p_\infty)/(0.5\rho_\infty u_\infty^2)$.

criterion for final convergence in the RANS simulations. In both scenarios, no-slip, adiabatic boundary conditions are prescribed on the airfoil surface. The free-flow properties as well as the corresponding dimensionless quantities are given in the respective sections of both flow scenarios.

To ensure consistency between the (U)RANS grids and the grids of the subsequent DNS and LST, a curve fit of the airfoil surface with NURBS (Non-uniform rational basis spline) of the order of 10 is employed. This method produces a unique analytical expression for the slightly smoothed contour of the airfoil. Numerical problems such as inconsistencies on the wall during interpolation or undesired fluctuations in the DNS can thus be avoided. Based on the work of Kurz (2016), MATLAB® is used to generate the required NURBS. Furthermore, this tool is used in post-processing to convert the arc length x_s to the chord-based position x, and vice versa.

For the (U)RANS simulations of both flow scenarios, a structured C-mesh around the airfoil with 7.0×10^5 grid points (resulting to 3.5×10^5 gird cells) is generated with the meshing software Gridgen®. According to the base flows of the investigated scenarios with the assumption of an infinite span, the (U)RANS simulations are performed purely two-dimensional. Hence, only one cell in spanwise direction is necessary. The grid for the RANS simulations, including the entire far-field, is depicted in figure 2.2(a) with a reduced resolution. On both sides of the airfoil, 400 surface points are placed with a hyperbolic tangent distribution between the leading edge and the trailing edge. The wall-normal distribution is chosen to resolve the boundary layer with at least 30 grid points and to ensure $\Delta y_s^+|_w < 1$ for the grid cells on the wall in the turbulent region. The boundaries of the far-field are chosen

to provide a distance of at least $L_c \times 100$ from the airfoil. In the steady-state RANS simulations, the angle of attack AoA is determined via the velocities at the far-field boundary conditions. However, in the case of URANS simulations employing DVA, the Chimera method is necessary to consider different (static) AoA via rotation due to numerical reasons, see Müller *et al.* (2021*b*).

2.3.2 Disturbance velocity approach

URANS simulations with gusts ($\kappa > 0$) are performed using the so-called disturbance velocity approach (DVA) by Heinrich & Reimer (2013). Instead of fully resolving gusts, this simplified approach adds the velocity vector of the gust disturbance $-\boldsymbol{u}'_g$ to the flux balance via superposition. Consequently, the velocity vectors in all equations of the system are manipulated with

$$\boldsymbol{u}_{g,DVA} = \boldsymbol{u}_g - \boldsymbol{u}'_g \,, \tag{2.14}$$

for each physical time step. The spatial and temporal description of the gust disturbance

$$\boldsymbol{u}'_g(x_g, t) = (0, v'_g, 0)^T \,, \tag{2.15}$$

consists solely of a vertical velocity component representing the sinusoidal gust, see equation (2.8). Consequently, the periodic gust affects the entire URANS airfoil flow including its circulation. This disturbance leads to a change of all other primitive variables of the flow, with the tangential velocity component u_s in the boundary layer and the streamwise pressure gradient $\mathrm{d}p/\mathrm{d}x$ being most relevant for the subsequent DNS and the flow physics studied here. However, this method only covers the influence of the gust on the airfoil, but neglects the change in velocity and shape of the gust induced by the airfoil. Nevertheless, Müller *et al.* (2020, 2021*a*,*b*) showed that the method provides satisfactory results at wavelengths larger than the chord length. In the present work, using wavelengths smaller than the chord length can still be considered valid, since the region of interest is the resulting oscillating boundary layer and less the accuracy of global aerodynamic coefficients.

At least 150 physical time steps per propagation of one gust wavelength past the airfoil with 250 inner iterations are applied. The subsequent unsteady LST as well as the DNS with unsteady boundary conditions is implemented such that an equidistant temporal resolution of the flow field over one or multiple gust periods is assumed, see figure 2.5. Therefore, the physical time step Δt of the URANS simulation is chosen to be a common factor of the gust period. Thus, a clean period can be recorded and temporal interpolation can be avoided. In most cases, the flow field is extracted over one period in time, once no significant changes in the periodicity of the aerodynamic coefficients are observed. However, in some cases at very high gust amplitudes, temporary flow separation on the opposing side of

interest of the airfoil can occur and introduce frequencies which are not multiples of the fundamental gust frequency. In these cases, multiple gust periods are recorded in order to avoid temporal discontinuities in the unsteady boundary condition of the subsequent DNS.

2.4 (Transient) base flows

Structured curvilinear grids are created for the DNS and LST, which are oriented along the airfoil surface at a constant domain height. As an example, the domain margins for the DNS on the airfoil pressure side is illustrated in figure 2.2(b) for the LTT case. The wall-normal extrusion in y_s direction of the body-fitted coordinate system is determined by a mathematical series enforcing a constant stretching factor χ_y for a desired number of grid points with the initial step size Δy_w at the wall for a given overall height of the domain. Here, by manual iteration, it is ensured that $\chi_y < 1.025$ applies for the corresponding grid configuration. In streamwise direction, an equidistant step size with respect to the arc length x_s is defined, with the exception of the outflow in the DNS grid, where stretching is applied, see section 2.6.2. The NURB-spline described above can provide both a normal vector and an integrated arc length along the curvature with high accuracy for wall-normal extrusion and discretization in the flow direction, respectively. No smoothing or grid relaxation is applied, making the almost perfectly streamline-oriented grid suitable for post-processing without further interpolation. The exact properties of the grids are explained in the respective sections of the simulated scenarios.

Finally, the converged RANS solutions of the steady-state flows as well as the individual instantaneous URANS flow fields—representing the cases with periodic gusts—are interpolated to the two-dimensional grids for the subsequent LST and DNS. This is performed with the means of a sixth order Lagrangian interpolation scheme outlined by Sherer & Scott (2005). In this work, the procedure implemented in MATLAB® by Kurz (2016) is applied. It should be noted that the interpolation of URANS results with gusts is performed purely spatially, with each snapshot treated individually. Since the *TAU* code operates with dimensional quantities, the normalization introduced in section 2.1 must be applied for further processing in DNS and LST. Moreover, for URANS simulations with DVA, the time-dependent sinusoidal gust must be added to the resulting unsteady flow field, since it is subtracted again in the standard output of *TAU*. Thereby, the transformation from the geodesic coordinate system to the airfoil coordinate system has to be considered.

In the following, the generated time-dependent URANS flow fields on the curvilinear grids are referred to as *transient base flows* for the LST and DNS. This designation refers to the unsteady behavior of disturbances in the flow which can be described by linear theory. In some sense—when considering linear modes ϕ'_{mode}—,

a triple decomposition of the primitive variables

$$\phi = \underbrace{\overline{\phi}_{ref} + \phi'_{\Delta gust}}_{\phi_{tbf}} + \phi'_{mode} \,, \tag{2.16}$$

can be introduced where $\overline{\phi}_{ref}$ denotes the steady-state base flow without gusts and $\phi'_{\Delta gust}$ the periodic deviation of the flow field induced by the gusts. $\phi'_{\Delta gust}$ is not to be confused with v'_{gust} from equation (2.8), which represents the gust disturbance absent/well ahead of the airfoil. In this work, the resulting component of the gust perturbation lies in the order of magnitude of $\phi'_{\Delta gust} = \mathcal{O}(10^{-2})$ to $\mathcal{O}(10^{-1})$, while the linear behavior of the modes ranges from $\phi'_{mode} = \mathcal{O}(10^{-6})$ to $\mathcal{O}(10^{-2})$. Furthermore, the gust frequency is one to two orders of magnitude smaller than that of the amplified modes. Consequently, the transient base flow $\phi_{tbf}(t)$ which determines the unsteady behavior of the linear modes is composed with the first two components in equation (2.16). The results of this work in chapters 3 & 4 verify the validity of this *separation-of-scales* approach since it is shown that the unsteady linear amplification of modes can be described with a quasi-steady approach using steady-state LST on $\phi_{tbf}(t)$.

It should be mentioned, that in the LAINA case of chapter 4, the transient base flow of the URANS simulation can only be used for the DNS, since the length of the separation bubble is underestimated. Therefore, the resulting unsteady (spanwise averaged) flow field of the DNS with a prolonged separated region is used later as a transient base for the unsteady LST.

2.5 (Unsteady) linear stability analysis

The behavior of flow instabilities such as Tollmien–Schlichting (TS) waves can be characterized in terms of frequency range and growth rate using LST. In this work, the stability properties of given base flows are computed using an in-house LST code, see Schmidt & Rist (2014), which employs a compressible formulation given by Mack (1984). The laminar flow region of both the URANS solutions as well as the spanwise averaged DNS flow can be used as a base flow for linear stability analysis. In this section, the basics of classical LST are briefly discussed, and an unsteady extension of the e^n-method for time-dependent transition prediction is presented.

2.5.1 Linear-stability-theory fundamentals

Based on the assumption of very small perturbations, the flow field expressed in primitive variables $\boldsymbol{q} = (\rho, u, v, w, T)^T$ is decomposed into a steady base flow and a disturbance flow, i.e. $\boldsymbol{q} = \overline{\boldsymbol{q}} + \boldsymbol{q}'$. By applying this approach to the NSE intro-

duced in section (2.1) and neglecting the resulting non-linear terms, the so-called linearized Navier–Stokes equations can be derived. The equations are further simplified with the parallel-flow assumption, thus leading to the classical local stability analysis. For the cases investigated here, this also entails neglecting the surface curvature. Since the base flow is two-dimensional and therefore uniform in spanwise direction, only 1D-eigenfunctions in the wall-normal direction y_s need to be solved. The disturbances are described as Fourier modes in x_s and z directions employing the traveling-wave ansatz

$$\boldsymbol{q'}(x_s, y_s, z, t) = \hat{\boldsymbol{q}}(y_s)\, e^{i(\alpha x_s + \beta z - \omega t)}\,, \tag{2.17}$$

with the eigenfunction $\hat{\boldsymbol{q}} \in \mathbb{C}$, the streamwise wavenumber $\alpha \in \mathbb{C}$ and $\omega, \beta \in \mathbb{R}$ as the angular frequency and spanwise wavenumber, respectively. In this work, the so-called spatial theory with the complex wavenumber $\alpha = \alpha_r + i\alpha_i$ is considered, in which it is assumed that the disturbances grow spatially with the amplification rate α_i (amplification for $\alpha_i < 0$) as they travel downstream. In this case, ω and β can be considered as variables of the stability problem while α corresponds to the complex eigenvalue of a respective amplified mode with the complex eigenfunction $\hat{\boldsymbol{q}}$. The quadratic eigenvalue problem is computed with a matrix solver while employing a Chebyshev collocation method, see Schmidt & Rist (2014).

2.5.2 e^n-method for steady conditions

The most commonly known prediction method for natural transition is the so-called e^n-method, which was independently developed by van Ingen (1956, 2008) and Smith & Gamberoni (1956). This approach, which is derived only for steady-state problems, is based on the stability behavior of the amplified modes (e.g. TS-waves) calculated with LST with the steady base flow $\overline{\boldsymbol{q}}$. The fundamental idea of this method is that the amplitude A of a mode equals e^n times its initial amplitude A_0 in downstream direction. The exponent, also widely known as the n-factor, however, depends on the streamwise location x_s and can be calculated based on a preceding linear stability calculation for a mode with a constant frequency ω. This is done by the integration of α_i

$$n(x_s) = -\int_{x_{s,0}}^{x_s} \alpha_i(x_s)\, \mathrm{d}x_s = \ln\left(\frac{A(x_s)}{A_0}\right)\,, \tag{2.18}$$

starting from the location $x_{s,0}$ where the corresponding initial amplitude A_0 is assumed. Usually, the point of first neutral stability $x_{s,bI}$ with $\alpha_i = 0$ is selected for $x_{s,0}$, since it represents the streamwise location where a mode enters the amplified region. This point is also commonly referred to as branch I and its location also depends on the frequency ω. For flows in natural conditions without additional

actuation, this location is assumed to be most critical for incoming disturbances—such as free-stream turbulence—that may enter the boundary layer via receptivity and ultimately lead to transition. In this work, however, disturbances can also be introduced to the boundary layer with a disturbance strip in the already amplified region. Since the amplitude A_0 of the introduced modes is chosen to exceed the amplitudes of natural perturbations which started further upstream, the position of the disturbance strip $x_{s,DS}$ can be selected as the initial point $x_{s,0}$ for integration of the n-factor. An observed amplitude A, e.g. in the DNS, can therefore be compared with the resulting n-factor, which allows to evaluate the extent of linear effects in the modal downstream development.

As described above, the frequency-specific n-factor represents the amplification of a single mode. In natural flows as e.g. also in the wind tunnel, however, a broad spectrum covering all frequencies of the amplified range is usually present. Therefore, the envelope $N(x_s)$ of all n-factors for all relevant frequencies ω is considered for transition prediction. With this analytical foundation, a critical N-factor can be identified as a threshold value for a measured transition position x_{tr} of a given flow, making the e^n-method a semi-empirical approach. Values for N_{crit} in quiet wind tunnels or free flight are usually found between 9 and 12. There are several variable N-factor methods for the prediction of x_{tr} via a threshold value, which take into account the flow conditions including the free-stream turbulence level, see Mack (1977), or receptivity due to surface roughness, see Crouch & Ng (2000). In case of only one introduced frequency with a disturbance strip, a threshold value n_{crit}—mostly depending on the initial actuation amplitude A_0—can just as well be determined.

2.5.3 Modification for unsteady conditions

For unsteady flows as in this work, the linear stability analysis including the e^n-method needs to be modified. For that reason, the amplification rates—which are solved with the classical LST based on the velocity profiles of the above-mentioned transient base flows u_{tbf}, see equation (2.16),—are integrated along the spatio-temporal trajectories. Thus, time-dependent n-factors can be obtained for the periodically oscillating boundary-layer flow. This general concept has already been applied in different variations by Obremski & Morkovin (1969), Studer *et al.* (2006) and Reeh (2014) for interpretation of experimental results. In the present work, however, a general formulation of the e^n-method modified for unsteady flows is provided. The corresponding results of the wind-tunnel measurements and the DNS demonstrate the validity of the approach presented here, see chapter 3.

In figure 2.3, the trajectory-following method is illustrated in the x_s/t plane for two oscillation periods T with the trajectories (dotted) of two exemplary modes with the frequency ω_1 and $\omega_2 > \omega_1$, respectively. Since the analysis for unsteady

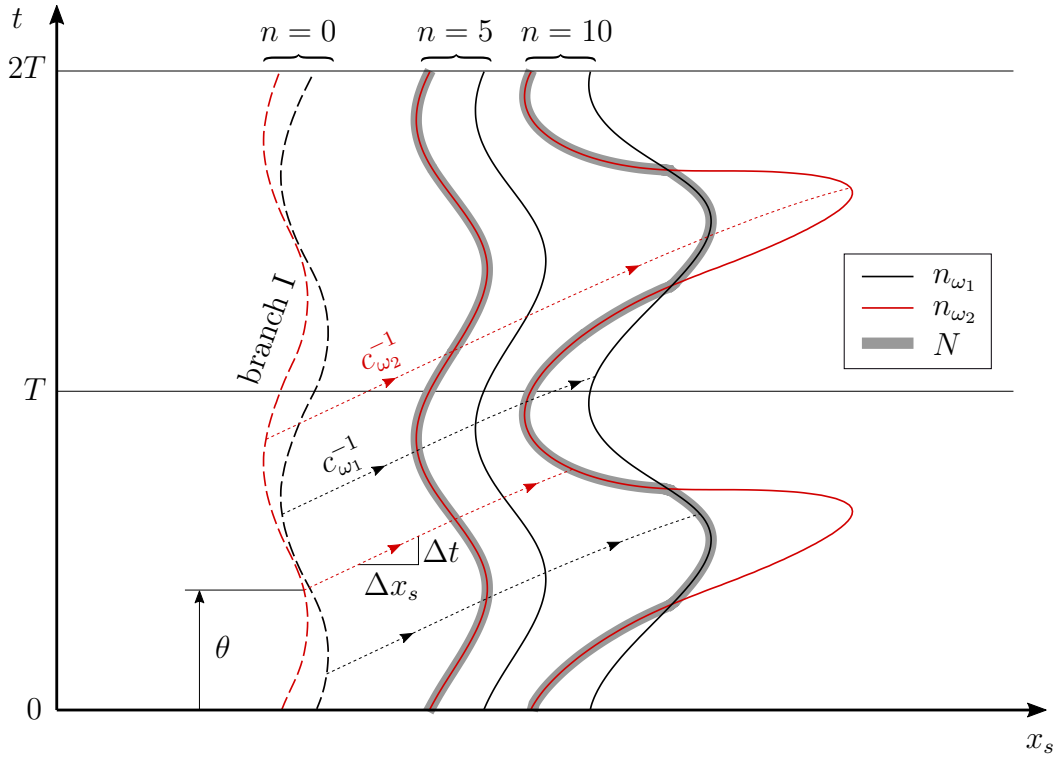

Figure 2.3: Schematic depiction of the spatio-temporal trajectory-following method for the unsteady linear stability analysis with the n-factors of two amplified modes ($\omega_1 < \omega_2$). N represents the resulting time-dependent envelope.

transition prediction should be kept as close as possible to the assumptions of the classical steady-state method, the starting point of integration with $n = 0$ is set to be at branch I. This implies that branch I—which now oscillates upstream and downstream over time—is still assumed to be the most critical point for incoming disturbances. As in the steady-state conditions, the position of the branch I also depends on the frequency ω of the amplified mode, cf. black and red dashed lines in figure 2.3. The phase θ represents the time relative to the oscillation period T at which the wave is numerically "spawned" at $x_{s,bI}$.

Here, each steady-state linear stability analysis is performed based on the transient base flow $\boldsymbol{q}_{tbf}(t) = \overline{\boldsymbol{q}}_{ref} + \boldsymbol{q}'_{\Delta gust}(t)$ introduced in section 2.4, for the respective time t. The complex eigenvalue α of the spatial approach yields the streamwise wavenumber α_r and the spatial amplification rate α_i. Both parts are crucial for the presented method, whereas the first is used to calculate the local phase speed of a mode $c_{mode} = \omega/\alpha_r$. The local gradient of the trajectories in the x_s/t plane therefore corresponds to the reciprocal of the local phase velocity of the corresponding wave c_{mode}, see labeling of the dotted lines in figure 2.3. In order to numerically follow the modes with the equidistant time discretization Δt of the transient base flows,

their change in position in the space-time diagram is determined with

$$\Delta x_s = c_{mode} \cdot \Delta t = \frac{\omega}{\alpha_r} \cdot \Delta t \ . \tag{2.19}$$

The phase speed of a downstream traveling mode might increase strongly depending on the solution of the LST, therefore locally changing the inclination of a trajectory. Thus, a position x_s for a time t can be perpetually calculated, at which the local linear stability analysis of the instantaneous velocity field is performed. The amplification rates for all modes are integrated along the resulting trajectories with

$$n_\theta(x_s) = -\int_{x_{s,0}}^{x_s} \alpha_i(x_s, \theta + t)\ \mathrm{d}x_s \,, \tag{2.20}$$

where the frequency- and phase-dependent position of branch I is chosen as the respective starting point $x_{s,0} = x_{s,bI}(\theta, \omega)$. In this work, the periodically treated problem with $0 \leq \theta/T < 1$ is computed by integrating 100 trajectories spawned at individual phases θ. Beforehand, the generated transient base flows explained in section 2.4 are therefore temporally interpolated to 100 snapshots with Δt for one period T using Lagrangian polynomials, see appendix B. The resulting values of n_θ for a respective modal frequency ω are scattered in space and time along the trajectories. Using Kriging interpolation on a 2D mesh in spatial and temporal directions, a time-dependent $n(x_s, t)$ can be computed, yielding continuous isolines for the n-factors, as illustrated in figure 2.3.

In contrast to the steady-state flow, every mode experiences an individual history of amplification while traveling downstream in the oscillating flow. This leads to a characteristic (unsteady) motion of the n-factors in the x_s/t plane, see $n = 5$ and 10 for both modes with the frequencies ω_1 and ω_2 in figure 2.3. Analogous to the classical steady-state method, an envelope $N(x_s, t)$ can also be built here, which in addition to the spatial dependency also features a periodic time-dependency. This is shown schematically for the two example frequencies in figure 2.3, see gray thick line representing the resulting unsteady N-factor. Depending on the case, integration along the trajectories is done for 50 to 100 different frequencies ω, which lie in the relevant range of amplified modes. Unsteady transition prediction can now be carried out with the above-mentioned threshold value for N, which may be acquired from a corresponding steady-state case of the flow. This method has already been employed as a simplified version in a previous study, see Ohno *et al.* (2022) and Khaled (2019), where the transient base flows are built with steady flow fields at different AoA instead of time-resolved flow fields containing physical gusts.

The procedure described above is very well suited for the unsteady prediction of the natural transition under realistic conditions as present in the wind tunnel. However, in the DNS performed for this work, only discrete modes are introduced

to the boundary layer via a disturbance strip (see section 2.6.4) in the already amplified region. In this case, the n-factor for the fundamental (primary) mode with the frequency ω_{DS} is integrated starting from the location of the disturbance strip $x_{s,0} = x_{s,DS}$.

It should be pointed out that the classical framework of local stability theory as explained in section 2.5.1 is used here, hence making this a quasi-steady approach where $\partial \boldsymbol{u}/\partial t$-terms are neglected. The assumption of the validity of this separation-of-scales approach for the presented cases is based on the fact that the frequencies of the fundamental oscillation (gusts) are one to two orders of magnitude lower than those of the amplified modes. Furthermore, when considering the trajectory of the followed mode, the changes of the velocity profiles in the spatial direction for Δx_s are significantly stronger than their variation in time for $\Delta t = \Delta x_s / c_{mode}$. Effectively, this approach extends the parallel-flow assumption of the local stability analysis—which usually applies only to the spatial direction x_s—to the spatial direction x_s *and* the temporal direction t. However, for unsteady flows with oscillation frequencies near the modal frequency, the method may be extended with Floquet analysis, analogous to secondary stability theory (Herbert (1988)), cf. Luo & Wu (2010).

A potential time-variation of the receptivity leading to a variation of the initial amplitudes A_0 at branch I (or at the disturbance strip in the DNS) due to oscillation of the boundary-layer thickness is neglected here. Moreover, the local linear theory does not necessarily predict the amplitudes of convective disturbances correctly, especially for the case of strongly non-parallel or unsteady flows. However, the n-factors can be compared with the amplitudes of the actual perturbations in the simulations, which allows an evaluation of the validity of the presented transient analysis and reveals the contribution of linear effects.

2.6 Direct numerical simulations

DNS of the fully-resolved boundary-layer flows are carried out with the steady and unsteady base flows obtained beforehand with URANS simulations, see section 2.3. For the simulations, the compressible NSE (2.1) are rearranged to a formulation involving flux vectors, see equation (A.1), with the solution vector $\boldsymbol{Q} = (\rho, \rho u, \rho v, \rho w, E)^T$ consisting of conservative variables. The resulting system of equations as implemented in *NS3D*, which includes flux vectors, stresses, heat fluxes and total energy, can be found in appendix A. With the differential equation

$$\left.\frac{\partial \boldsymbol{Q}}{\partial t}\right|_{NSE} = \mathcal{N}(\boldsymbol{Q}) \tag{2.21}$$

where $\mathcal{N}$ represents the compressible Navier–Stokes operator, see equation (A.1), the vector $\boldsymbol{Q}$ is solved numerically. Despite the recasting of the equations, the

fundamentals in section 2.1 concerning notation and the description of gas properties are still valid here. This section briefly describes the numerical scheme of the DNS code, the implemented (unsteady) boundary conditions as well as the modal actuation with a disturbance strip.

2.6.1 Spatial discretization and time integration

A revised version of the in-house DNS code *NS3D* developed by Babucke (2009) is used. For the spatial discretization, explicit 8^{th}-order finite differences are chosen for all three directions here, which are well suited for subsonic flows, see Keller (2016); Wenzel (2019). To allow curvilinear meshes including grid stretching as used in this work, a grid transformation is implemented, see Babucke (2009); Keller (2016). For time integration, the classical explicit 4^{th}-order, four-step Runge-Kutta method is applied. Furthermore, to numerically stabilize the computations, alternating forward- and backward-biased finite differences for the convective first derivatives are employed, see Kloker (1997); Babucke (2009) for details.

For additional stabilization of the numerical scheme, a spatial 10^{th}-order implicit filter implemented by Selent & Rist (2010) is invoked at every completed time step for all three directions. For details, see Colonius *et al.* (1993); Visbal & Gaitonde (2002). The effectiveness of the filter is even increased when employing grid stretching towards the domain boundaries, which may prevent reflections, see next section.

The basics for generating the (two-dimensional) DNS grids have already been explained in section 2.4, whereby the specific properties of the grids are given in the two chapters of the respective flow scenarios. The 2D grids of the base flows are extruded uniformly in spanwise direction z up to a domain extent equal to the fundamental wavelength of the introduced spanwise traveling modes $\lambda_{z,0}$, see section 2.6.4 for more details. In order to sufficiently resolve the turbulent parts of the boundary layer, the number of grid points in all spatial directions is generally chosen based on the resulting values of the inner units Δx_s^+, $\Delta y_s^+|_w$, and Δz^+.

2.6.2 Boundary conditions and sponge zones

In all simulations, adiabatic no-slip boundary conditions are chosen for the wall, which is consistent with the base flows of the preceding (U)RANS computations. In spanwise direction z, cyclic boundary conditions are used.

For the simulation of subsonic flows in a compressible framework as in this work, the use of characteristic boundary conditions are advantageous in order to prevent acoustic reflections, see Poinsot & Lele (1992). A formulation of characteristic boundary conditions by Giles (1990) is therefore employed at the inflow, outflow, and free stream, see blue lines at the edges of the DNS domain (LTT case) in figure 2.4. These boundary conditions are effective in normal direction as well as in time

to allow harmonic perturbations to leave the domain while still maintaining the base flow. In the proximity of the boundary, the disturbance flow field

$$\phi' = \phi - \phi_{ref} \tag{2.22}$$

is transformed to characteristic variables based on a one-dimensional decomposition of the Euler equations into upstream and downstream traveling waves. For an inflow boundary on the left side of the domain, the characteristic variables can be calculated with

$$\begin{pmatrix} c_1 \\ c_2 \\ c_3 \\ c_4 \\ c_5 \end{pmatrix} = \begin{pmatrix} -a_{ref}^2 & 0 & 0 & 0 & 1 \\ 0 & 0 & \rho_{ref} a_{ref} & 0 & 0 \\ 0 & 0 & 0 & \rho_{ref} a_{ref} & 0 \\ 0 & \rho_{ref} a_{ref} & 0 & 0 & 1 \\ 0 & -\rho_{ref} a_{ref} & 0 & 0 & 1 \end{pmatrix} \cdot \begin{pmatrix} \rho' \\ u' \\ v' \\ w' \\ p' \end{pmatrix} \tag{2.23}$$

where a represents the local speed of sound. In case of steady-state boundary conditions, all variables with the subscript *ref* are set to base-flow values $\phi_{ref} = \phi_{bf}$. The characteristic variables represent entropy perturbations (c_1), vorticity perturbations in the spanwise and streamwise directions (c_2, c_3), as well as downstream and upstream traveling sound waves (c_4, c_5). The boundary condition sets the incoming disturbances ($c_1 \dots c_4$) to zero and extrapolates the characteristic variable c_5 of the upstream traveling acoustic wave with a 2$^{\text{nd}}$-order stencil, see Babucke (2009). In a final step, the primitive variables are computed by an inversion of equation (2.23) and added to the current flow field. Analogously, this boundary condition is also applied at the free stream and the outflow. Due to the curvature of the airfoil surface oriented grids, a transformation of the velocities at the edges must be performed. However, it should be noted that this method only works for waves moving perpendicular to the domain boundaries and oblique waves may be reflected, see Kurz (2016).

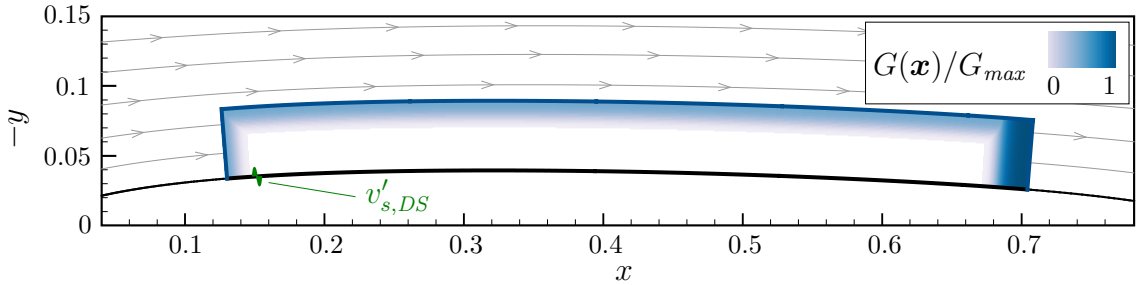

Figure 2.4: DNS domain on airfoil with streamlines of the outer (U)RANS base flow (LTT case). The blue shading illustrates the spatial distribution of the sponge gain (uniform in spanwise direction), whereas the white area means that no forcing terms are active. The disturbance strip is indicated with the actuation function $v'_{s,DS}$.

An additional measure to improve numerical stability and reduce reflections is

to apply sponge zones in front of the boundary conditions, realized through forcing terms, see Kurz & Kloker (2014); Kurz (2016); Dörr (2018). Using equation

$$\frac{\partial \boldsymbol{Q}}{\partial t} = \left.\frac{\partial \boldsymbol{Q}}{\partial t}\right|_{NSE} - G(\boldsymbol{x}) \cdot (\boldsymbol{Q} - \boldsymbol{Q}_{ref}) \,, \tag{2.24}$$

the time derivative of the conservative numerical fluxes $\boldsymbol{Q}$ of the unsteady solution is forced to the reference state (i.e. the base flow from (U)RANS), with a gain field $G(\boldsymbol{x})$. Typically, this field specifies the magnitude and spatial distribution of the gain G from a maximum value at (or close to) the boundaries to the null parameter $G = 0$ in the inner computational domain which can be used for analysis. As a fading function in wall-normal and streamwise direction, the 5^{th}-order polynomial

$$D(x^*) = 6x^{*5} - 15x^{*4} + 10x^{*3} \,, \quad x^* \in [0, 1] \,, \tag{2.25}$$

is chosen. Therefore, the normalized coordinate x^* is projected on the fading area in the corresponding direction where $G(x^*) \sim D(x^*)$ holds. The two-dimensional distribution of $G(\boldsymbol{x})$—which in principle determines the strength of the forcing terms—is shown exemplarily in figure 2.4 for the LTT case. For simulations as conducted for this work, it is essential to use such damping zones, especially at the free stream and the outflow to avoid distortions due to the above-mentioned oblique portions at the boundary conditions. In a simulation at steady-state conditions, the conservative reference field $\boldsymbol{Q}_{ref}$ is calculated with all primitive variables ϕ_{bf} of the steady base flow.

In a sense, grid stretching towards the domain boundary while using the spatial filter explained in section 2.6.1 acts as an additional component of the boundary condition, see Wenzel (2019). Due to the standard refinement in wall-normal direction, this applies in any case to the upper free-stream boundary. To suppress numerical perturbations, an additional grid stretching is applied at the outflow, starting shortly after the beginning of the sponge zone. The stretching factor in streamwise direction is consequently ramped-up with equation (2.25) over a few grid points starting from the equidistant portion with $\chi_x = 1$ to the final value $\chi_x \leq 1.015$.

In previous work with *NS3D*, where the boundary conditions also originate from RANS simulations, 2D simulations were carried out with the DNS code beforehand in order to obtain converged base flows, see Kurz (2016). Less prescriptive boundary conditions (e.g. $\partial^2/\partial x^2 = 0$ with $p = const.$) were used at the outlet and an inner spatial section of the converged base flow was used for the further 3D simulations. This approach—which is in general applied to account for the minor deviations between the RANS and steady DNS flow—is *not* used in this work, since convergence is not feasible in the unsteady simulations with transient base flows. For consistency, this also applies for the steady-state cases. Therefore, the interpolated solutions from the (U)RANS flow fields always represent the respective (transient) base flows here,

which e.g. also includes the calculation of the mean flow distortion.

2.6.3 Modification for unsteady conditions

In order to carry out transient simulations with gusts, the boundary conditions including the forcing zones need to be modulated in time. In setups with a domain extent as in figure 2.4, the physics of the unsteady flow is mostly determined by the fluctuating velocity profile at the inflow and the oscillating pressure gradient at the free stream. However, since a complex airfoil flow including curvature is simulated here, all primitive variables oscillating in time are consistently prescribed with the means of the boundary conditions introduced in section 2.6.2.

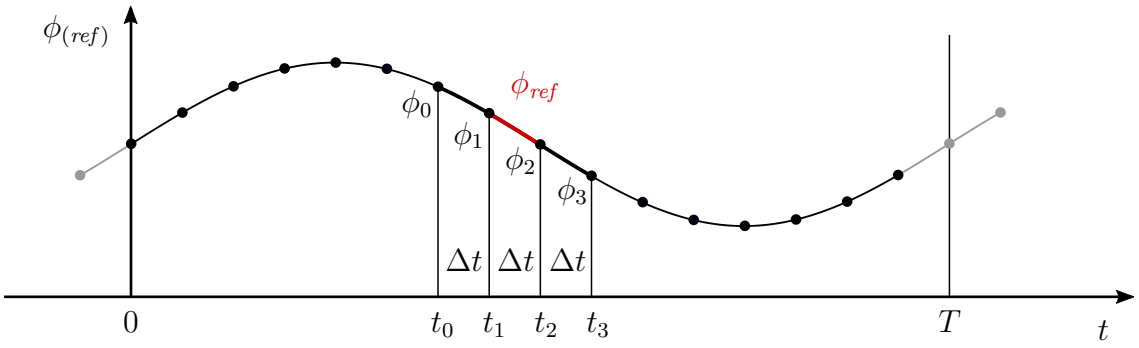

Figure 2.5: Representation of the data points of a primitive variable ϕ over one oscillation period with exemplary supporting points for a temporal interpolation with 3$^{\text{rd}}$-order Lagrange polynomials. Gray dots represent temporal "ghost points".

Consequently, a reference field for all primitive variables $\phi_{ref}(t)$ is required for the boundary conditions and sponge zones at each (sub)iteration of the Runge-Kutta time-integration. This is achieved during the DNS by temporal interpolation of the (original) transient base flow from URANS simulations, see section 2.4. The Lagrangian interpolation of the order k is given as a linear combination

$$\phi_{ref}(t) = \sum_{j=0}^{k} \phi_j L_j^k(t)\,, \tag{2.26}$$

with the discrete values ϕ_j of the original transient base flow at the time steps j and the Lagrange basis polynomial

$$L_j^k(t) = \prod_{\substack{j=0 \\ i \neq j}}^{k} \frac{t - t_i}{t_j - t_i}\,. \tag{2.27}$$

In this work, a 3$^{\text{rd}}$-order Lagrangian interpolation is applied, see illustration in figure 2.5. Therefore, ϕ_{ref} (red) in a simulation interval between two temporal data

points is always calculated with four data points over an interval of $3\Delta t$. To save computational resources, the resulting equation of (2.26) and (2.27) for $k = 3$ is rearranged such that (auxiliary) coefficients need to be computed only once per interval. For a detailed description of the implementation, see appendix B. Lower-order interpolation is not suitable for laminar flows because large discontinuities in the values or their derivatives may occur from one interval to the next, leading to unwanted artificial disturbances. Depending on the case, the original transient base flows are resolved with 150 to 350 time steps per gust period T. At the interval boundaries of T, temporal "ghost points" are used to maintain temporal periodicity, thus allowing for simulations of an arbitrary number of periods with a prescribed transient base flow, cf. figure 2.5. As described in section 2.3.2, however, in some extreme cases the URANS flows are not perfectly periodic. A small discontinuity at the periodic seam of the original flow may lead to fluctuations related to the Gibbs phenomenon, introducing an unwanted pulse at $t = T$ in the DNS. In these cases, multiple gust periods are simulated and recorded with URANS, corresponding to the entire simulation time of the subsequent DNS.

The resulting flow field with primitive variables $\phi_{ref}(t)$ is applied to the equations (2.22) and (2.23) for the unsteady characteristic boundary conditions at each (sub) iteration. These boundary conditions were also successfully used and validated for an inflow with isotropic free-stream turbulence modeled with a superposition of small-scale perturbations, see Ohno *et al.* (2020, 2023*b*). Furthermore, the forcing terms of equation (2.24) can be manipulated in time by converting the interpolated values of $\phi_{ref}(t)$ to the conservative vector $\boldsymbol{Q}_{ref}(t)$ at every (sub)iteration. With this method, the sponge acts simultaneously as an unsteady forcing region containing the gusts from URANS as well as a dampening zone for outgoing disturbances. This approach has also been applied successfully for an unsteady inflow in a non-periodic simulation of a turbulent boundary layer, see Appelbaum *et al.* (2021).

2.6.4 Disturbance strip

As in well-known fundamental studies, see Rist & Fasel (1995), amplified modes (e.g. TS-waves) are generated with time-dependent blowing and suction at the wall through a narrow strip, here referred to as "disturbance strip" (DS). This strip, which spans the entire length z and is placed just downstream of the inflow, can be used to introduce discrete perturbations into the boundary layer, allowing various transition scenarios to be simulated. The location of the disturbance strip, denoted with its central position x_{DS}, is depicted in figure 2.4 for the LTT case, see $v'_{s,DS}$ (green). As in other studies, e.g., Thumm (1991); Dörr (2018), the generated modes are labeled with (h, k), which corresponds to a notation for the double Fourier spectrum where h is the multiple of the fundamental frequency ω_0 and k is the multiple of the fundamental spanwise wavenumber β_0. Hence, the function of the

velocity disturbance in wall-normal direction for each mode reads

$$v'_{s,DS} = A_v \; g(x^*) \; \cos\left(h\omega_0 t + k\beta_0 z\right), \tag{2.28}$$

with the streamwise disturbance distribution $g(x^*)$. The disturbance amplitude A_v is normalized with the free-stream velocity u_∞. A desired property of the disturbance input is a zero-net mass flow at any time instance. For quasi-incompressible flows with $\rho \approx const.$, this can be ensured by choosing an appropriate streamwise modulation function $g(x^*)$ for the respective velocity disturbance. In case of actuation with $\beta = 0$, i.e. two-dimensional modes $(h, 0)$, a dipole function

$$g_d(x^*) = \begin{cases} \frac{81}{16}\left(2x^*\right)^3\left(3\left(2x^*\right)^2 - 7\left(2x^*\right) + 4\right) & \text{for } 0 \leq x^* \leq 0.5 \\ -\frac{81}{16}\left(2 - 2x^*\right)^3\left(3\left(2 - 2x^*\right)^2 - 7\left(2 - 2x^*\right) + 4\right) & \text{for } 0.5 < x^* \leq 1\,, \end{cases} \tag{2.29}$$

is applied. The normalized coordinate x^* is projected to the area of the slit of the disturbance strip $\Delta x_{s,DS}$. For three-dimensional (oblique) modes with $\beta \neq 0$, the monopole function

$$g_m(x^*) = \begin{cases} -3\left(2x^*\right)^4 + 4\left(2x^*\right)^3 & \text{for } 0 \leq x^* \leq 0.5 \\ -3\left(2 - 2x^*\right)^4 + 4\left(2 - 2x^*\right)^3 & \text{for } 0.5 < x^* \leq 1\,, \end{cases} \tag{2.30}$$

can be used, since zero-net flux is already provided through oscillation in spanwise direction. Here, the spanwise wavenumber β_0 also determines the domain size in z direction, which is identical to the fundamental wavelength $\lambda_{z,0} = 2\pi/\beta_0$.

In this work, fundamental resonance with the primary mode $(1, 0)$ and the secondary modes $(1, \pm 1)$, see Rist & Fasel (1995), is applied for the LTT case. In the LAINA case, oblique resonance with a pair of primary modes $(1, \pm 1)$, see Thumm (1991), is employed. More details are given in the respective sections. In the following, the frequency for all introduced modes $(1, k)$ is denoted by ω_{DS}.

Finally, it should be noted that the selected actuation frequency ω_{DS} is required to correspond to a multiple of the fundamental frequency of the simulation $\omega_{sim} = 2\pi/T_{sim}$, which in turn depends on the gust frequency and number of simulated/recorded gust periods. In other words, the fundamental frequency ω_{sim} must represent a common denominator of ω_{gust} as well as ω_{DS} in order to obtain a perfectly time-periodic simulation with respect to the introduced disturbances. This allows a fairly clean spectral analysis with FFT or CWT, see next section.

2.7 Continuous wavelet transform

To study the mechanism of natural transition (e.g. with TS-waves) of a flow, a spectral analysis is usually performed. For DNS at steady-state conditions, the fast

Fourier transform (FFT) is very well suited, which allows a double-spectral analysis in both time and spanwise direction. Therefore, the downstream development of primary, secondary and additional modes—possibly introduced via actuation at the disturbance strip, see notation in section 2.6.4—can be precisely computed. Since the Fourier analysis is completely delocalized in time, only the "averaged spectrum" over the oscillation cycle can be calculated when applied on periodic transient flows (e.g. with gusts). This is also carried out for one scenario in this work in order to obtain an overview of all relevant modes. However, to study the transient process including the time-dependent behavior of unstable modes, wavelet analysis can be employed, which works in some sense like a windowed Fourier transform in time.

Inspired by the experimental work of Studer *et al.* (2006), Reeh & Tropea (2015) and Romblad *et al.* (2020), the continuous wavelet transform (CWT) is used to calculate the time-dependent frequency spectrum. Only the most important aspects of CWT and its application to simulation results are briefly discussed here. Reviews as well as further theoretical background on wavelets can be found in detail in Farge (1992) and Mallat (1999). In this work, the MATLAB® Wavelet Toolbox is applied.

With a given mother wavelet function $\Psi(t)$, the continuous wavelet transform converts the time-dependent signal of e.g. the tangential velocity $u_s(t)$ into the complex function

$$\hat{W}(d,\theta) = \frac{1}{N(d)} \int_{-\infty}^{\infty} u_s(t)\ \Psi^{\dagger}\left(\frac{t-\theta}{d}\right)\ \mathrm{d}t\ , \tag{2.31}$$

where θ corresponds to the time shift and d to the time dilation, see Mallat (1999) and Reeh (2014). The expression $\Psi^{\dagger}$ denotes the complex conjugate of Ψ. The wavelet function—which is localized in time t and must fluctuate around the mean value of zero—can be compressed, stretched, or shifted. Thus, fluctuations in $u_s(t)$ can be approximated locally, i.e. in the frequency and time domain. The coefficient $N(d)$ depends on the choice of normalization, hence the L^1 or L^2 norm, which correspond to the amplitude or energy spectrum, respectively, see Farge (1992). Since this work focuses on the evolution of amplitudes of discrete modes and comparison with LST, the L^1 norm is used here, thus making $N(d)$ equal to d.

Depending on the investigated signal, various suitable wavelet mother functions are available for analysis. Due to the Heisenberg uncertainty bound, it is impossible to create a wavelet function that can perfectly localize both time and frequency, see Mallat (1999). However, for the investigation of modes which are exhibiting sinusoidal signals like in this study, the Morlet wavelet provides a particularly good representation, see Studer *et al.* (2006). The complex Morlet wavelet function

$$\Psi(t) = \frac{1}{\sqrt{\pi f_b}}\ e^{i2\pi f_c t}\ e^{-\frac{t^2}{f_b}}\ , \tag{2.32}$$

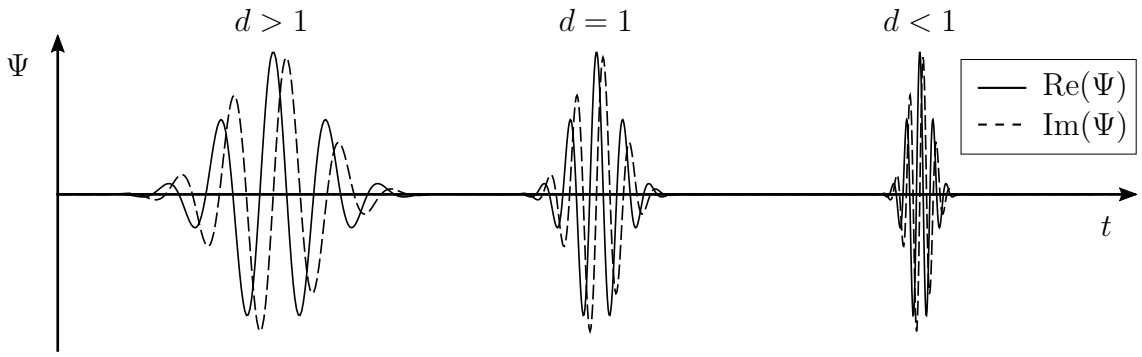

Figure 2.6: Example for the scaling of the complex Morlet wavelet function with three values for the dilatation coefficient d.

is constituted by a wave formulation with an amplitude modulation of a Gaussian envelope, wherein f_c corresponds to the central frequency and f_b to the time-decay parameter. The shape of the real and imaginary part of the complex Morlet wavelet function is exemplarily depicted in figure 2.6 for three different values of the dilatation coefficient d. The actual physical frequency can be calculated with the time dilation d and the frequency f_c by using the relation $f = f_c f_s/d$, where f_s corresponds to the sampling frequency of the input signal. Finally, the amplitude spectrum according to the L^1 norm, e.g. of the velocity fluctuations u'_s in flow direction, can be calculated with

$$u'_{s,cwt}(\omega, t) = |\hat{W}| \, . \tag{2.33}$$

Besides the tangential velocity $u_s(t)$—which is very well suited since it is directly associated with the growth of unsteady modes in the boundary layer—other primitive variables such as the pressure at the wall can be used as an input signal for analysis.

The result of $u'_{s,cwt}(\omega, t)$ at a fixed position in flow direction x and wall-normal direction y_s can already deliver deep insights into the properties of unsteady transition, see Studer *et al.* (2006) and Romblad *et al.* (2020). However, for comparison of the transient development of modal amplitudes with the prediction of the unsteady linear stability analysis—cf. depiction in figure 2.3—, further steps are necessary. First, the CWT is performed for all points in the x and y_s directions within the boundary layer, expanding the result to $u'_{s,cwt}(x, y_s, \omega, t)$. Now, to further illuminate the unsteady behavior of the flow, different frequencies of the spectrum can be chosen for analysis, such as the gust frequency ω_{gust}, the frequency of the introduced modes via disturbance strip ω_{DS}, or the respective harmonics. In this work, the most interesting aspect is the behavior of the fundamental modes of the actuation (e.g. $(1, 0)$ for fundamental resonance) which are subject to the cyclic variation imposed by the gust. Therefore, to determine the spatio-temporal development of

the convective modes, the maximum amplitude in wall-normal direction y_s within the boundary layer is calculated for the frequency ω_{DS} for all locations in x direction and all times t. In order to directly compare the transient amplitude development with the n-factors from the LST in the x/t plane, the exponent

$$n_{cwt}(x,t) = \ln(\max_{y_s}\{u'_{s,cwt}(x,y_s,\omega_{DS},t)\}/A_u)\,, \tag{2.34}$$

is introduced. Hence, the resulting maximum amplitude in wall-normal direction y_n of the CWT is normalized by a determined initial amplitude A_u and converted to the natural logarithm. The initial amplitude A_u should ideally be chosen such that $n_{cwt} = 0$ applies at the location of the disturbance strip x_{DS}. Thus A_u corresponds to the hypothetical initial perturbation A_0 of the e^n-method of van Ingen (1956). It depends to some extent on the boundary-layer receptivity to the actuation with wall-normal blowing and suction with the amplitude A_v, see section 2.6.4. However, both initial amplitudes are expected to be in the same order of magnitude $A_u = \mathcal{O}(A_v)$. Furthermore, by applying a consistant A_u in the steady-state and transient cases of the respective scenarios, a time-independent receptivity of the introduced disturbances is assumed. The validity of this assumption can be checked by looking at the temporal behavior of $n_{cwt} = 0$. In the presented results of this work, the n-factors of the linear theory and the amplitudes of the continuous wavelet transform n_{cwt} will be collectively denoted $n_{(cwt)}$ in case they show a good agreement.

In contrast to the above-mentioned experimental studies on unsteady transition, no flow data over a longer period of time (or over a high number of gust periods) is available for the wavelet analysis in this numerical study. Due to the high computational costs at high Reynolds numbers as in this case, only a single or a few gust oscillations can be simulated and recorded. The analysis of very short time signals may lead to boundary effects, especially in the regions of low frequencies, towards the beginning and end of the time domain. The cone of influence (COI) of the wavelet—often depicted in scalograms—refers to the edges of those regions, see Torrence & Compo (1998) or Nobach *et al.* (2007). The remedy for the present investigations, however, is to treat the problem as periodic. In a simple approach, the wavelet transform can therefore be fed with an input signal based on an original signal concatenated in time over multiple periods. Only one of the "inner" periods in the temporal direction of the transformation is then used for evaluation. However, this requires that the flow actually behaves approximately periodically. The periodicity of the externally introduced disturbances, i.e. the gusts at the free stream as well as the introduced modes at the disturbance strip, can be ensured in relation to the physical time of the recorded flow by selecting the frequencies accordingly. However, intrinsic disturbances and other effects in the flow are not necessarily periodic with respect to the artificially introduced frequencies. Therefore, the results in the area of the cone of influence must be regarded with caution.

3 Attached-flow scenario

In this chapter, the effect of periodic gusts on laminar-to-turbulent transition in an airfoil boundary layer is investigated. Large-scale disturbances impose a varying pressure gradient that leads to an oscillating boundary layer with potentially strong transient behavior of the transition location. As introduced in section 1.2, several experimental studies have investigated this phenomenon in detail. This work aims to understand and break down the individual physical effects influencing the natural transition in an attached flow by numerical means. These effects include the response of the base flow to the gust, the transient amplification of (convective) TS-modes described by linear theory, and non-linear effects due to the transitional part of the flow. Therefore, the numerical methods introduced in chapter 2, including URANS simulations with DVA gusts, unsteady linear stability analysis and DNS employing transient base flows, can shed light on the interlinked physical effects. Furthermore, this work aims to classify the observations of previous investigations on unsteady transition by Obremski & Fejer (1967), Studer *et al.* (2006) and Romblad *et al.* (2018) with a detailed parameter study considering gust amplitude v'_{gust} and frequency κ. The results of Romblad *et al.* (2018)—which were conducted at a comparatively low degree of flow unsteadiness—could be attributed mainly to linear effects. With a newly introduced definition of a dimensionless quantity κ^{tr} (see equation (3.7)), the transient behavior of the transition can be classified and partly predicted. The "convective-transition mode" observed by Obremski & Fejer (1967) and Studer *et al.* (2006) was found at a high degree of flow unsteadiness in terms of gust amplitude and gust frequency. In this case, the laminar-turbulent interface alternates between two phases: the "creative phase", in which the normal breakdown occurs due to amplified modes, and the "convective phase", where the turbulent flow migrates downstream similar to a turbulent spot or strip. The so-called calmed region (also "becalmed region"), which is mainly known from work on turbulent spots and wake-induced transition in turbomachinery, see e.g. Orth (1993), Gostelow *et al.* (1997) or Hughes & Walker (2001), is a consequence of the convective transition and was also observed in the present work. It is shown that the transient mean flow distortion precedes the calmed region and is responsible for the occurrence of the convective transition in the case of the natural transition with TS-waves. A tipping-point dependent on gust frequency, amplitude, and initial disturbance level—and thus κ^{tr}—is identified for the occurrence of this phenomenon.

The present studies were accompanied by experimental investigations with two measurement campaigns in the wind tunnel, see Romblad *et al.* (2020) and Romblad (2023). The experimental wind-tunnel results shown in this chapter are kindly pro-

vided by Jonas Romblad. Preliminary results on unsteady transition prediction with linear theory (without using DVA in the URANS simulations) have been published as well, see Ohno *et al.* (2022).

The chapter is structured as follows: fundamental characterization of the flow scenario including boundary-layer properties and stability analysis of the steady-state reference case in section 3.1, results and discussion of the unsteady airfoil flow from URANS simulations in section 3.2, unsteady linear stability analysis including validation with wind-tunnel measurements and a discussion based on an extensive parameter study in section 3.3, discussion of the DNS results covering the impact of transient non-linear effects on unsteady transition in section 3.4, and finally a summary of the findings in section 3.5.

3.1 Characterization of the flow scenario

The laminar-flow airfoil "MW-166-39-44-43" depicted in figure 3.1 (mirrored vertically) was used for the investigated flow scenario. The pressure (lower) side of the airfoil was of interest for the investigations were a long laminar stretch of attached boundary layer with natural transition is expected. The airfoil was designed by Weismüller (2012) based on the "DU84-158" airfoil for flight measurements using a wing glove, see also Reeh & Tropea (2015); Guissart *et al.* (2021). Furthermore, the airfoil has been extensively studied for incoming small-scale disturbances in the wind tunnel and DNS, see Romblad *et al.* (2018, 2022) and Ohno *et al.* (2020), respectively. The original coordinates used to determine the airfoil surface via NURB-splines for the numerical simulations can be found in Romblad (2023), cf. also section 2.3.1.

For the numerical and experimental wind-tunnel investigations, a Reynolds number of $Re = 3.4 \cdot 10^6$ with respect to the chord length was chosen in order to match full-scale free-flight conditions. The wind-tunnel experiments were carried out at a chord length of $\tilde{L}_c = 1.35m$ and a velocity of $\tilde{u}_\infty = 38m/s$ which corresponds to a Mach number of $Ma \approx 0.11$. For the steady-state reference case, an angle of attack of $AoA_{ref} = -1.4°$ at the lower corner of the laminar bucket is chosen. At this angle of attack, the position of the transition on the pressure (lower) side of the airfoil is particularly sensitive to changes in the inflow angle. Considering quasi-steady gusts, see definition in section 2.2, the scenario was first characterized with XFoil of Drela (1989) and later computed with RANS and LST, see section 3.3. For details on the experimental setup see Romblad *et al.* (2020); Romblad (2023).

3.1.1 Reference case

The setup of the (U)RANS simulations is explained in detail in section 2.3.1. Here, the transition locations in the (U)RANS simulations are set to $x_{tr,suction} = 0.681$ on

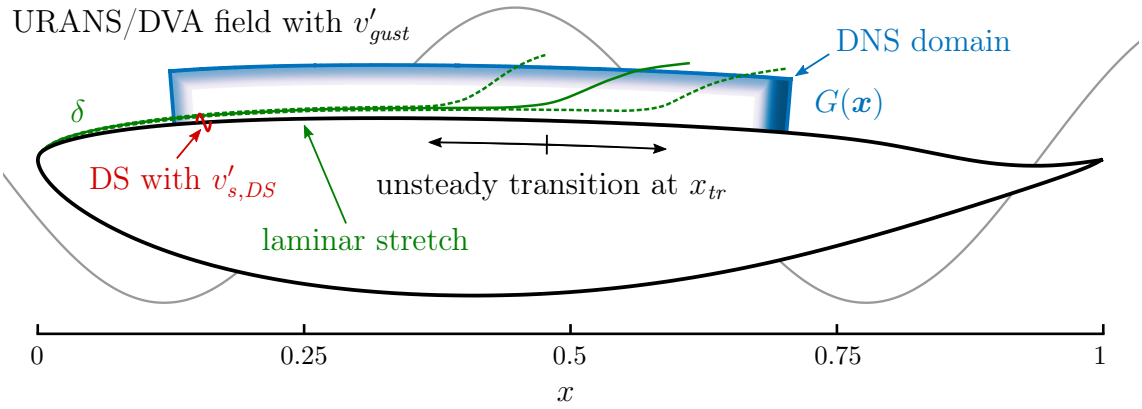

Figure 3.1: Depiction of the laminar-flow airfoil "MW-166-39-44-43" (mirrored vertically) with DNS domain and distribution of gain function $G(\boldsymbol{x})$ (blue); boundary-layer thickness δ is strongly exaggerated in wall-normal direction.

the suction (upper) side and $x_{tr,pressure} = 0.657$ at the pressure (lower) side based on a transition prediction with XFoil for $N_{crit} = 12$. This applies for the steady-state simulations as well as for unsteady simulations with DVA gusts.

Figure 3.2 features the boundary-layer properties of the steady state reference case at AoA_{ref} from RANS simulations versus streamwise direction x including the skin friction c_f, the pressure coefficient c_p, the displacement thickness δ_1, the momentum thickness δ_2, the Reynolds number Re_{δ_1} and the shape factor H_{12}. Furthermore, the Pohlhausen pressure-gradient parameter $\lambda_{\delta_2} = (\tilde{\delta}_2^2/\tilde{\nu})(\mathrm{d}\tilde{u}_s/\mathrm{d}\tilde{x}_s) = Re\,\delta_2^2\,(\mathrm{d}u_s/\mathrm{d}x_s)$ is given which is relevant for the approximation of leading- and trailing-edge velocities of convecting turbulent spots in sections 3.3.3 & 3.4.

A continuous adverse pressure gradient (APG) starting from the leading edge is clearly indicated by the course of c_p. The shape factor H_{12} slightly increases downstream from ≈ 2.7 at the front to ≈ 2.9 shortly before the transition. The prescribed transition location in the RANS simulation impacts almost all parameters at $x \approx 0.66$. In addition, H_{12} is plotted for a simulation with the transition criterion $N_{crit} = 9$ (corresponding to $x_{tr,pressure} = 0.484$ according to XFoil), see dashed line. The shape factor upstream of the transition position agrees almost perfectly with the calculation at $N_{crit} = 12$, which demonstrates that the prescribed transition point has a negligible effect on the upstream flow. Consequently, it is justified to apply a static transition location also for simulations with gusts. This has the great advantage that a (transient) laminar reference solution of the base flow is always available for the unsteady linear stability analysis as well as for the DNS, see explanation of *transient base flow* in section 2.4.

The stability diagram ("banana") for TS-modes for the steady-state reference case with AoA_{ref} is shown in figure 3.3(a). Modes with frequency ω are amplified with α_i from the point of neutral stability at branch I ($n = 0$) and are damped again

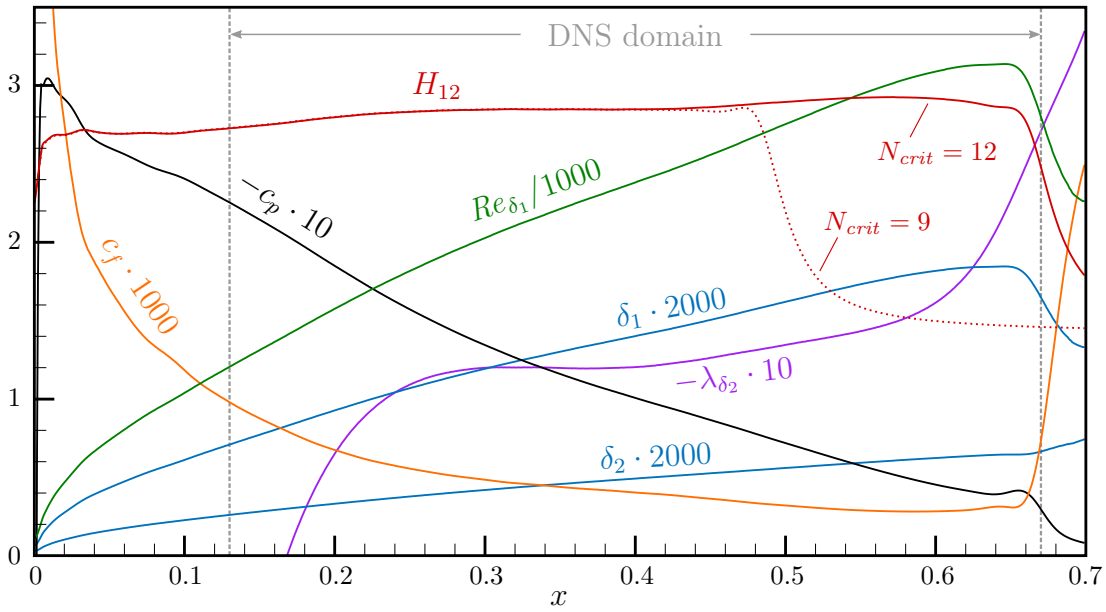

Figure 3.2: Boundary-layer properties of steady-state reference case at AoA_{ref} from RANS base flow (pressure side) with $N_{crit} = 12$; shape factor H_{12} for $N_{crit} = 9$ (dotted) for comparison.

when reaching branch II. The lines of the integrated n-factors, see equation (2.18), represent the envelope N and show that the transition location can be expected between $x \approx 0.31$ to ≈ 0.42 at realistic conditions with $N_{crit} \approx 9$ to 12. Note that the main focus of this study is on $N_{crit} \approx 10$. Furthermore, the lines indicate that the modes responsible for transition lie in the frequency range around $\omega \approx 200$. In the range of $50 < \omega < 350$, the modes exhibit streamwise wavenumbers of approximately $200 < \alpha_r < 800$ and phase velocities of $0.3 < c_{TS} < 0.4$.

At different angles of attack, the amplified zone $\alpha_i < 0$ moves its position in the x/ω plane which changes the predicted transition location was well as the frequency range critical for transition. For varying angles of attack or gusts, however, the position of the stability banana in the x/ω plane moves, which alters the predicted transition location as well as the frequency range of modes relevant for breakdown to turbulence. Therefore, the entire frequency range of amplified modes is considered in the investigations with unsteady linear stability analysis in section 3.3. Thus, a spatio-temporal development of the envelope N can be obtained, which can be directly compared with the transition location measured in the wind-tunnel experiments. In the DNS, however, only discrete modes are introduced via a disturbance strip. The position where the 2D modes (TS-waves) are introduced is indicated with "DS" in the stability diagram in figure 3.3(a) at $x_{DS} = 0.15$ with $\omega_{DS} = 201$. The amplification of oblique 3D modes with the spanwise wavenumber β at x_{DS} is shown in figure 3.3(b) along with the primary and secondary modes for *fundamental*

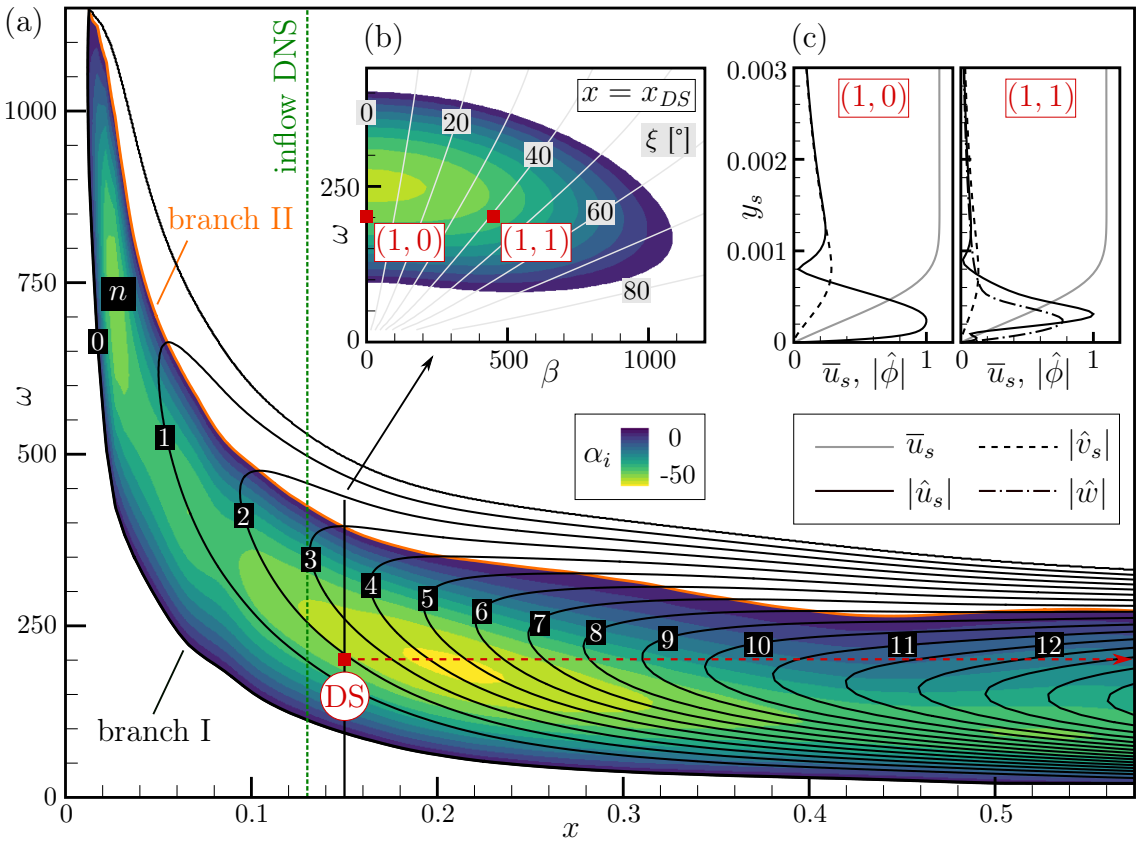

Figure 3.3: (a) Stability diagram with spatial amplification rate α_i (colors) and n-factor (lines) for steady-state reference case at AoA_{ref} for TS-modes ($\beta = 0$). (b) Spatial amplification of 3D modes over β at $x = x_{DS}$ with direction of wave propagation $\xi = \arctan(\beta/\alpha_r)$. (c) Eigenfunctions corresponding to the primary and secondary modes introduced at $x = x_{DS}$ in the DNS; normalized with $\max_{y_s}\{|\hat{u}_s|\}$.

resonance in the DNS. Note: Due to the 2D base flow, the plane can be mirrored for negative spanwise wavenumbers at $\beta = 0$. A detailed description of the disturbance input for the transition scenario in the DNS is provided in section 3.4.

In the range of $50 < \omega < 350$, the modes exhibit streamwise wavenumbers of approximately $200 < \alpha_r < 800$ and phase velocities of $0.3 < c_{TS} < 0.4$. In this chapter, however, the visualized trajectories of TS-waves in the x/t plane are simplified with the approximate average phase velocity $c_{TS} = 0.35$.

3.1.2 Investigated unsteady cases with gusts

The parameter space with respect to the reduced frequency κ and the gust amplitude v'_{gust} of the investigated cases for the present flow scenario is depicted in figure 3.4. In all cases, the reference angle of attack remains $AoA_{ref} = -1.4°$.

The cases with $\kappa \to 0$ refer to the quasi-steady (Q-S) consideration of infinitely

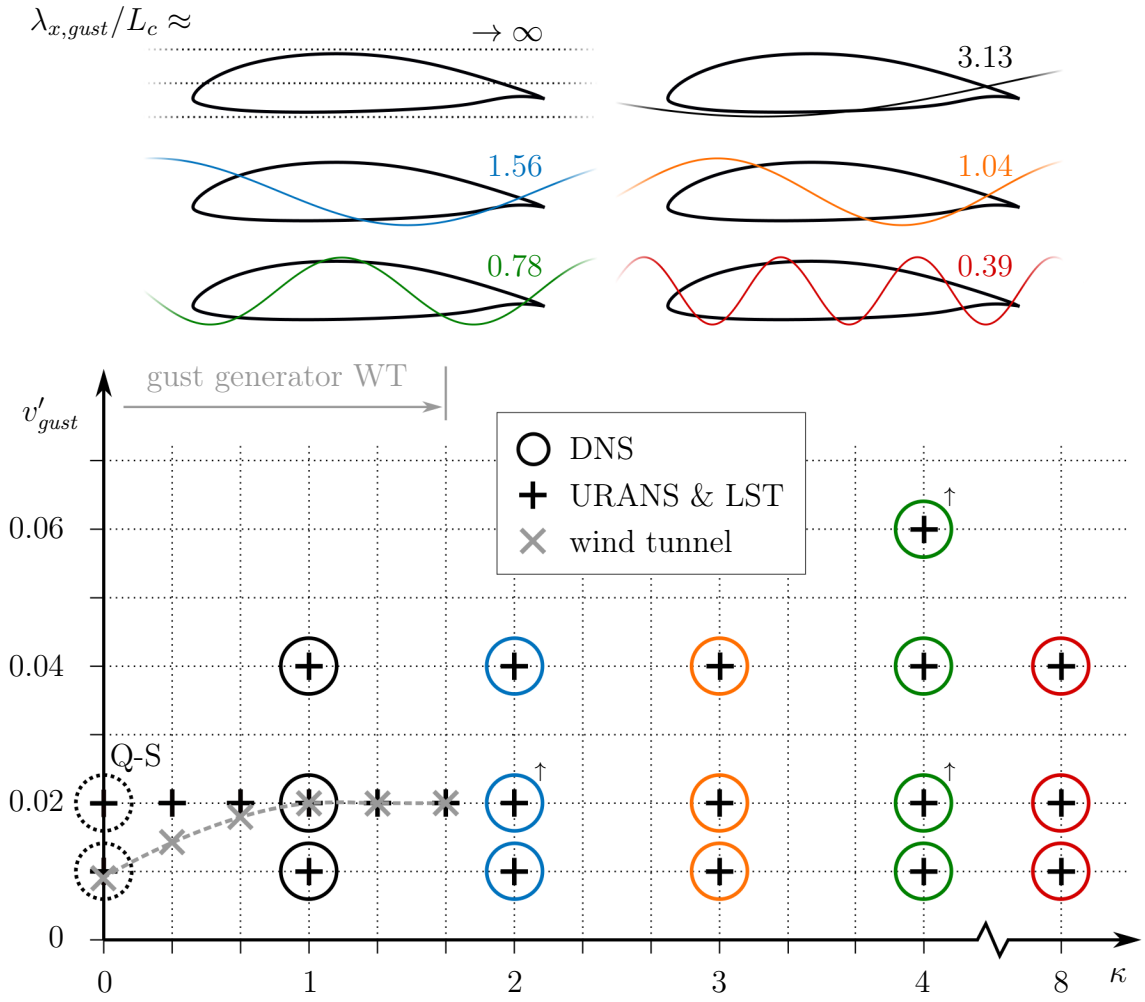

Figure 3.4: Depiction of simulated cases as well as wind-tunnel experiments within the parameter space of reduced frequency κ and gust amplitude v'_{gust}; top: illustration of ratio of gust wavelength to chord length ($\lambda_{x,gust}/L_c = \pi/\kappa$). $\bullet^{\uparrow}$ denotes additional DNS at increased disturbance amplitude of modes $A_v^{\uparrow}$.

large gusts ($\lambda_{x,gust} \to \infty$), see section 2.2. This results in a variation of the inflow angle of $AoA' = \arctan(v'_{gust}/u_\infty) \approx 0.57°$ and $\approx 1.15°$ for the two gust amplitudes $v'_{gust} = 0.01$ and 0.02, respectively. The flow fields were therefore generated with steady-state RANS simulations at different angles of attack according to equation (2.10). For cases with $\kappa > 0$, however, time-resolved gusts are simulated using URANS with the disturbance velocity approach, see section 2.3.2.

The black crosses in figure 3.4 represent the performed (U)RANS simulations with the subsequent (unsteady) linear stability analysis. The conducted DNS are represented by circles, with colors matching the gusts illustrated above with wavelengths $\lambda_{x,gust}$ in relation to the chord length L_c. DNS for the quasi-steady cases (dashed circles) are represented only by the steady-state reference case AoA_{ref}

and the two steady-state cases of the extremes $\max\{AoA\}$ and $\min\{AoA\}$. The transient cases in the DNS are conducted with the reduced frequencies of $\kappa \in \{1.005; 2.01; 3.015; 4.02; 8.04\}$. However, for simplicity, they are denoted with the rounded values of $\kappa \in \{1; 2; 3; 4; 8\}$ throughout this work. The ratio of the modal frequency of the introduced TS-wave ($\omega_{DS} = 201$) to the gust frequency is $\omega_{DS}/\omega_{gust} \in \{100; 50; 33.\bar{3}; 25; 12.5\}$, respectively. Hence, the time scales/frequencies are one to two orders of magnitude apart in this study. DNS, conducted with an elevated level of initial disturbances in the boundary layer $A_v^{\uparrow}$ are denoted with $\bullet^{\uparrow}$.

A gust generator was used in the corresponding wind-tunnel measurements to create an unsteady inflow to the airfoil with reduced frequencies up to $\kappa = 1.67$, see Romblad *et al.* (2020); Romblad (2023). Therefore, additional cases with the frequencies $\kappa \in \{0.34; 0.67; 1.34; 1.67\}$ for the aimed amplitude $v'_{gust} = 0.02$ are investigated with the means of URANS and unsteady LST. As depicted in figure 3.4 with gray crosses and a gray dashed line, the effective amplitude of the gust generator shows a considerable dependency on κ. For a discussion of possible reasons, see Romblad (2023). Due to the deviation, the experimental results at $\kappa \to 0$ are compared with the numerical case of $v'_{gust} = 0.01$, whereas the measurements at $\kappa = 1.34$ and 1.67 are compared with $v'_{gust} = 0.02$, see section 3.3.1.

3.2 Characteristics of the unsteady airfoil flow

In general, the amplification rates α_i of modes which are leading to laminar-to-turbulent transition are determined by the velocity profiles $\overline{\boldsymbol{u}}$ of the boundary layer. The global Reynolds number is assumed to be constant in the present investigations. The velocity profiles are in turn governed by the streamwise pressure gradient $\mathrm{d}p/\mathrm{d}x$. Therefore, for a fundamental understanding of the unsteady transition, it is of interest to characterize the unsteady behavior of the pressure gradient as well as the resulting unsteady velocity profiles. In this section, the results of URANS simulations are used to examine the behavior of the airfoil response to unsteady conditions with periodic gusts. Due to the complexity of the problem, the results presented focus on the qualitative behavior of the unsteady airfoil flow for the gust amplitude v'_{gust} and frequency κ. This offers a foundation of understanding the resulting unsteady laminar-to-turbulent transition. A summary of theoretical considerations concerning the airfoil response on unsteady flow fields can be found in Reeh (2014).

3.2.1 Unsteady pressure gradient

In steady and unsteady conditions for airfoils with attached flows, the pressure distribution and hence the pressure gradient $\mathrm{d}p/\mathrm{d}x$ is mostly determined by inviscid effects and can be modeled with potential flow theory, see Reeh (2014). In practice, the pressure distribution determines the circulation, which can be used to calculate

the lift coefficient c_l. In this work, the (unsteady) pressure gradients from URANS simulations are analyzed, which also takes the viscous laminar and turbulent boundary layers into account. For the investigations of unsteady transition, it is of interest how the amplitude of the pressure-gradient fluctuation behaves in the case of gusts compared to the corresponding quasi-steady case. The second interesting aspect examined here is the spatio-temporal evolution (or "convection" in some sense) of the pressure gradient over the airfoil surface.

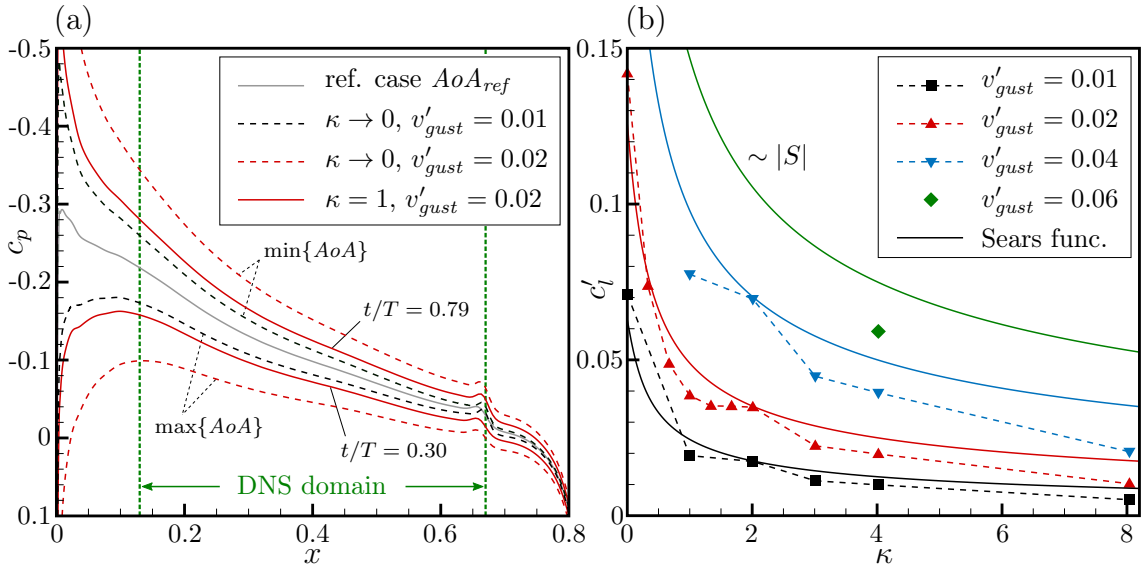

Figure 3.5: Unsteady airfoil-flow characteristics from (unsteady) RANS simulations. (a) Pressure-coefficient distribution $c_p = (p - p_\infty)/(0.5\rho_\infty u_\infty^2)$ on pressure side. (b) Amplitude of lift-coefficient oscillation c'_l with Sears (1941) function approximation.

The oscillation of the pressure-coefficient distribution c_p (pressure side) for two quasi-steady cases (dashed lines) and one unsteady case (solid lines) around the steady-state reference case are demonstrated in figure 3.5(a). All cases clearly exhibit an adverse pressure gradient at every instant for $x > 0.13$. (The small hump at $x \approx 0.67$ arises from the fixed transition in the URANS simulations.) For the quasi-stationary gusts with $\kappa \to 0$ (dashed lines), the pressure distribution for the minimum and maximum AoA corresponds to the strongest and weakest APG occurring over one period, respectively. The pressure distributions shown in figure 3.5(a) for the unsteady case with a DVA gust with $\kappa = 1$ at $v'_{gust} = 0.02$ (red solid lines) correspond to instants of maximum and minimum pressure gradients over time. Here, the gust in the inviscid outer flow convects with the free-stream velocity u_∞ (Taylor's hypothesis) over the airfoil. Therefore, the pressure distribution and the boundary layer are not (periodically) time-invariant as in the quasi-steady case. However, the fluctuation of c_p, thus here also $\mathrm{d}p/\mathrm{d}x$, is significantly attenuated compared to the quasi-steady counterpart at the same gust amplitude. This general behavior can be interpreted as a mechanical impedance, which is also observed in

the (inviscid) unsteady thin-airfoil model, see e.g. Reeh (2014) for the same airfoil. The attenuation with increasing reduced frequency can also be observed in the fluctuation of the integral value of the lift coefficient c_l' in figure 3.5(b). For all simulated gust amplitudes the same trend over κ can be seen. Furthermore, the values of c_l' coincide perfectly if the result is linearly scaled with respect to the gust amplitude.

The above described impedance of the unsteady airfoil flow can be approximated with the Sears (1941) function. The function originates from the theory of 2D thin airfoils and was derived to calculate unsteady effects on airfoil loads in the case of flight through a pattern of periodic sinusoidal vertical gusts. The complex Sears function

$$S(\kappa) = \frac{H_1^{(2)}(\kappa)(J_0(\kappa) - iJ_1(\kappa))}{H_1^{(2)}(\kappa) + iH_0^{(2)}(\kappa)} + iJ_1(\kappa)\,, \tag{3.1}$$

only depends on the reduced frequency κ and is expressed in terms of Bessel (first kind) and Hankel (second kind) functions. The amplitude $|S(\kappa)|$ of the function represents the amplitude ratio of the unsteady solution to the quasi-steady solution. Therefore, the attenuation is described with increasing κ starting from $S(\kappa \to 0) = 1$. The oscillation of the lift coefficient can therefore be calculated with

$$c_{l,sears}' = 2\pi\ v_{gust}'\ |S(\kappa)|\,. \tag{3.2}$$

Figure 3.5(b) shows the curves of $c_{l,sears}'$ for comparison with the simulation results. Taking into account that the Sears function is derived for thin airfoils, the general trend is well represented here. The Theodorsen (1935) function $C(\kappa)$ describes the related problem of a pitching airfoil, which coincides with the Sears function only for $\kappa \to 0$. For more details on both functions the reader is referred to Leishman (2006).

In general, a pressure-gradient deviation from the steady-state reference also indicates a deviation in the transition position compared to the steady-state reference. For analysis, the deviation from the steady-state reference case

$$\Delta^r\phi(x,t) = \phi(x,t) - \phi_{ref}(x)\,, \tag{3.3}$$

for different relevant boundary-layer parameters ϕ is introduced in this work. In some sense, $\Delta^r\phi(x,t)$ accounts for the contribution of the second component $\phi_{\Delta gust}'$ of the triple decomposition in equation (2.16) which represents the fluctuation induced by the gust. For the URANS base flow, $\phi_{mode}' = 0$ applies.

In order to obtain an overview of the transient behavior of the base flow, the deviation $\Delta^r\phi$ can be plotted in the x/t plane, similar to the illustration of the unsteady transition prediction in figure 2.3. Besides the spatio-temporal development of boundary layer flow properties, x/t plots can also illustrate the relevant time scales, length scales, and velocities. In the sections 3.2 & 3.3, the x/t plots are

Figure 3.6: Spatio-temporal development of pressure gradient (deviation to steady-state reference case) $\Delta^r \mathrm{d}p_w/\mathrm{d}x_s = \mathrm{d}p_w/\mathrm{d}x_s - \mathrm{d}p_w/\mathrm{d}x_s|_{ref}$ of URANS simulations, cf. matrix in figure 3.4; velocity/exemplary trajectories: - - - - - TS-waves with c_{TS}^{-1}, - - - - - free stream/gust with u_∞^{-1}; —— $\Delta^r \mathrm{d}p_w/\mathrm{d}x_s = 0$.

consistently shown for two gust periods with $0 \leq x \leq 0.55$, covering the relevant region for the unsteady transition at realistic conditions.

Figure 3.6 shows the x/t plots for the pressure-gradient deviation $\Delta^r \mathrm{d}p_w/\mathrm{d}x_s$ at the wall of all URANS simulations. For each plot, its position corresponds to the parameter space matrix in figure 3.4. The convection velocity of the gust with u_∞ is indicated with green dashed lines while the phase velocity of TS-waves $c_{TS} = 0.35$ is indicated with black dashed lines. First of all, in the quasi-steady cases $\kappa \to 0$ it can be seen that the pressure-gradient deviation is time invariant and increases from the lower to the higher gust amplitude, cf. figure 3.5. At the frequencies $\kappa = 1$ and $\kappa = 2$ a weak delay can already be seen, since the areas with stronger and weaker pressure gradients show a spatio-temporal evolution. These zones (separated with solid black lines $\Delta^r \mathrm{d}p_w/\mathrm{d}x_s = 0$) propagate roughly at the free-stream velocity u_∞ and can be understood as the "footprint" of the gust. For $\kappa \geq 3$, a more complex pattern downstream of $x \geq 0.3$ due to higher harmonics of the gust is apparent. Consequently, this pattern intensifies with increasing gust amplitude. For $\kappa = 8$, the character of a footprint is even more evident, since the gust wavelength $\lambda_{x,gust} \approx 0.39$ is smaller than the depicted airfoil surface. As for the quasi-steady cases, the amplitudes of the deviation $\Delta^r \mathrm{d}p_w/\mathrm{d}x_s$ increase for higher gust amplitudes v'_{gust}. With the exception of the higher harmonics, however, the general pattern of deviation is independent of amplitude. In accordance with the Sears function described above, the amplitudes of the pressure-gradient deviation attenuate with increasing κ. Finally, it should be noted that the TS-waves are convecting more slowly, which is why they may be exposed to different zones of stronger and weaker pressure gradients during their lifetime (especially at higher κ).

3.2.2 Viscous response of the boundary layer

The instantaneous amplification rates of the TS-waves are determined by the instantaneous boundary layer velocity profiles. Due to a viscous delay of the laminar boundary layer, the velocity profiles are not immediately adapting to the change in the pressure gradient. This delay can be exemplified by the first Stokes problem, in which a flat plate is suddenly set in motion. The resulting boundary-layer thickness $\delta \sim \sqrt{\nu\, t}$ of the self-similar solution depends only on the square root of the product of the viscosity with the time passed, see Schlichting & Gersten (2016). Consequently, the qualitative response in time only depends on the viscosity of the fluid.

For an oscillating horizontal free stream above a fixed plate (transformed second Stokes problem, see White (2006)), the so-called Stokes layer is formed. In general, this layer also occurs in oscillating boundary-layer flows in the form of shear waves, see Ackerberg & Phillips (1972). However, its thickness is significantly smaller than that of the Prandtl (velocity) boundary layer, which is why it has only a marginal

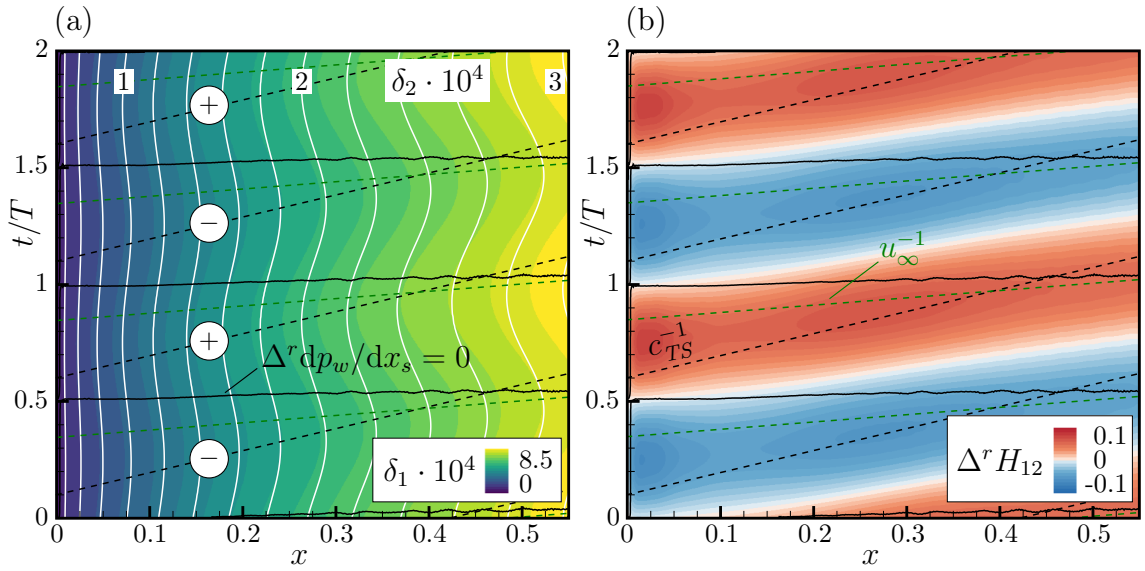

Figure 3.7: Spatio-temporal development of boundary-layer properties from URANS simulation for $\kappa = 1$, $v'_{gust} = 0.02$; velocity/exemplary trajectories: ----- TS-waves with c_{TS}^{-1}, ----- free stream/gust with u_∞^{-1}; —— $\Delta^r \mathrm{d}p_w/\mathrm{d}x_s = 0$ with ⊕/⊖ for positive or negative pressure-gradient deviation. (a) Displacement thickness δ_1 (colors) and momentum thickness δ_2 (white lines). (b) Shape factor (deviation to steady-state reference case) $\Delta^r H_{12} = H_{12} - H_{12,ref}$.

relevance for the amplification of TS-waves. The case of convective gusts is very complex as the spatially developed boundary-layer flow responds "as a whole" to the oscillations, see Reeh (2014). Unsteady laminar boundary layers have already been characterized by various experimental (see e.g. Lighthill (1954); Hancock (1984)) as well as numerical studies with analytical solutions (see e.g. Hill & Stenning (1960); Patel (1975)). However, it should be mentioned that even for simple unsteady boundary-layer flows, there are no self-similar solutions for the instantaneous velocity profiles available. The unsteady base flows can be used to validate the numerical method as well as the experimental setup by comparing its amplitude and phase profiles of the streamwise velocity in the wall-normal direction. However, unsteady hot-wire measurements of the boundary layer were not performed for the present scenario but only for the LAINA case in the next chapter. The general characteristics of the amplitude profiles known from the literature are well reflected, see figure 4.5 in section 4.2.2.

For the characterization of unsteady transition, however, the periodic spatio-temporal behavior of the boundary-layer profiles is of interest. In figure 3.7(a), the general evolution of the displacement thickness δ_1 and the momentum thickness δ_2 is plotted in the x/t plane for the case $\kappa = 1$ at $v'_{gust} = 0.02$. Furthermore, the velocity of the free stream, exemplary trajectories of TS-waves and the pressure-gradient deviation (solid lines with $\Delta^r \mathrm{d}p_w/\mathrm{d}x_s = 0$; positive ⊕ and negative ⊖

phases, cf. figure 3.6) is depicted. It can be seen that the boundary-layer thicknesses oscillate periodically and are almost in phase with each other. In addition, the viscous lag is clearly visible, since the minima and maxima of the boundary-layer thicknesses in the rear region are delayed with respect to the minima and maxima of the pressure-gradient deviation ($\ominus/\oplus$). It can also be seen that the change in the boundary-layer properties along the TS-wave trajectories is significantly stronger in the spatial direction than in the temporal direction. As explained in section 2.5.3, this further justifies the utilization of the quasi-steady approach where the parallel-flow assumption of the local LST is also extended to the temporal direction.

The shape factor $H_{12} = \delta_1/\delta_2$ is one of the boundary-layer properties which can be used to approximate the resulting amplification of TS-waves in the varying flow field. Higher values of H_{12} generally imply a stronger amplification of disturbances in an attached laminar flow, while lower values imply a weaker amplification, cf. the transition prediction method of Wazzan *et al.* (1981). Analogous to the characterization of the unsteady pressure gradient, the deviation of the shape factor $\Delta^r H_{12}$ is plotted in figure 3.7(b) for the same case. Modes traveling downstream with the phase velocity c_{TS} are expected to be more amplified in the area $\Delta^r H_{12} > 0$ (red) and less amplified in the area $\Delta^r H_{12} < 0$ (blue) compared to the steady-state case. These areas are phase-locked with the pressure-gradient deviation $\Delta^r \mathrm{d}p_w/\mathrm{d}x_s = 0$ (solid black lines) at the leading edge/stagnation point. However, the time lag of the deviation $\Delta^r H_{12}$ compared to the deviation $\Delta^r \mathrm{d}p_w/\mathrm{d}x_s$ increases significantly in downstream direction. As with the pressure-gradient deviation, a "convection velocity" of the regions with positive and negative deviation of H_{12} changes slightly over x. For the case in figure 3.7(b), however, the velocity of ≈ 0.6 for these characteristic regions can be identified, which lies between the free-stream velocity $u_\infty = 1$ and the phase speed of the modes $c_{TS} = 0.35$. The unsteadiness of the transition can be expected to be stronger for cases where the change of the base flow (convection velocity) is almost synchronized with the phase speed of the TS-waves.

In figure 3.8, the matrix with the x/t diagrams of the examined cases with the shape-factor deviation $\Delta^r H_{12}$ is shown. For reference, the isolines of $\Delta^r \mathrm{d}p_w/\mathrm{d}x_s = 0$ (see figure 3.6) are also given. As in the pressure-gradient deviation, two features can be observed: the increase of the amplitude of $\Delta^r H_{12}$ for increased v'_{gust} and the attenuation of the amplitude of $\Delta^r H_{12}$ for increased κ due to the above-described impedance described by the Sears function. However, the higher harmonics of the pressure gradient are not reflected in the change of the shape factor.

The steady-state reference case can be used to approximate the (average) region in x direction which is relevant for the TS-waves leading to transition. According to the stability diagram in figure 3.3(a) considering $N_{crit} = 10$, the most critical frequency is $\omega \approx 200$ with the first point of neutral instability at $x_{bI} \approx 0.08$ and the expected transition at $x_{tr} \approx 0.35$. This stretch, with the characteristic length $\Delta x_{TS} = x_{bI} - x_{tr} \approx 0.27$, can be considered in the x/t planes in figure 3.8 with regard

Figure 3.8: Spatio-temporal development of shape factor (deviation to steady-state reference case) $\Delta^r H_{12} = H_{12} - H_{12,ref}$ of URANS simulations, cf. matrix in figure 3.4; velocity/exemplary trajectories: ----- TS-waves with c_{TS}^{-1}, ----- free stream/gust with u_∞^{-1}; —— $\Delta^r \mathrm{d}p_w/\mathrm{d}x_s = 0$ cf. figure 3.6.

to the above-mentioned regions with more or less amplification. For $\kappa \geq 4$, most of the trajectories are either located in the purely more amplified or in the purely less amplified regions. As will be shown in the unsteady linear stability analysis in section 3.3, this intensifies the unsteadiness of the transition considerably. At $\kappa = 8$, virtually all TS-waves travel through both the more amplified and less amplified regions during their lifetime. Therefore, an attenuation of the unsteadiness of the transition behavior can be expected here.

3.3 Unsteady linear stability analysis

The unsteady linear stability analysis using the trajectory-following method introduced in section 2.5.3 can be performed on the transient base flows from URANS simulations presented in the previous section. The transient behavior of the amplification rates α_i and the integrated n-factors subjected to gusts is demonstrated for a single mode with the frequency $\omega = 201$ in figure 3.9. Here, the quasi-steady case ($\kappa \to 0$) with the amplitude of $v'_{gust} = 0.01$ in figure 3.9(a) is compared with the transient case $\kappa = 1$ with $v'_{gust} = 0.02$ in figure 3.9(b). The different gust amplitudes were chosen to roughly compensate for the attenuation of the effective amplitude for $\kappa \uparrow$ (Sears function), cf. figure 3.11. In the quasi-steady case, branch I and the spatial amplification rates α_i oscillate symmetrically over time. Consequently, the n-factors—which are calculated along the horizontal trajectories—as well as the resulting transition position x_{tr} also behave symmetrically over the oscillation period. However, for the unsteady case with $\kappa = 1$, it can be seen that the development of the amplification rates is not time-invariant over the period but "smeared" in space and time. This behavior is caused by the unsteady evolution of the base-flow velocity profiles due to viscous delay, cf. figure 3.7(b). Moreover, in this case the n-factors are calculated by integration along the trajectories with the phase velocity c_{TS} in the x/t diagram. This results in an asymmetric (or skewed) behavior of the n-factors which consequently determines the transition location over time. It is important to emphasize that this behavior is due both to the response of the airfoil boundary layer *and* the delay caused by the slow phase velocities of the TS-waves.

In the previous work of Ohno *et al.* (2022), the unsteady transition for the same flow scenario was studied in a simplified form. Here, the quasi-steady base flow with oscillating AoA (hence without DVA gusts) was used to calculate the n-factors with the trajectory-following approach by using an artificial time scale with respect to the investigated reduced frequency κ. Therefore, the influences of impedance (Sears function) and viscous delay described above were not accounted for in this numerical framework. The present section can therefore be considered to be a significantly revised and extended version of the previous publication by Ohno *et al.* (2022).

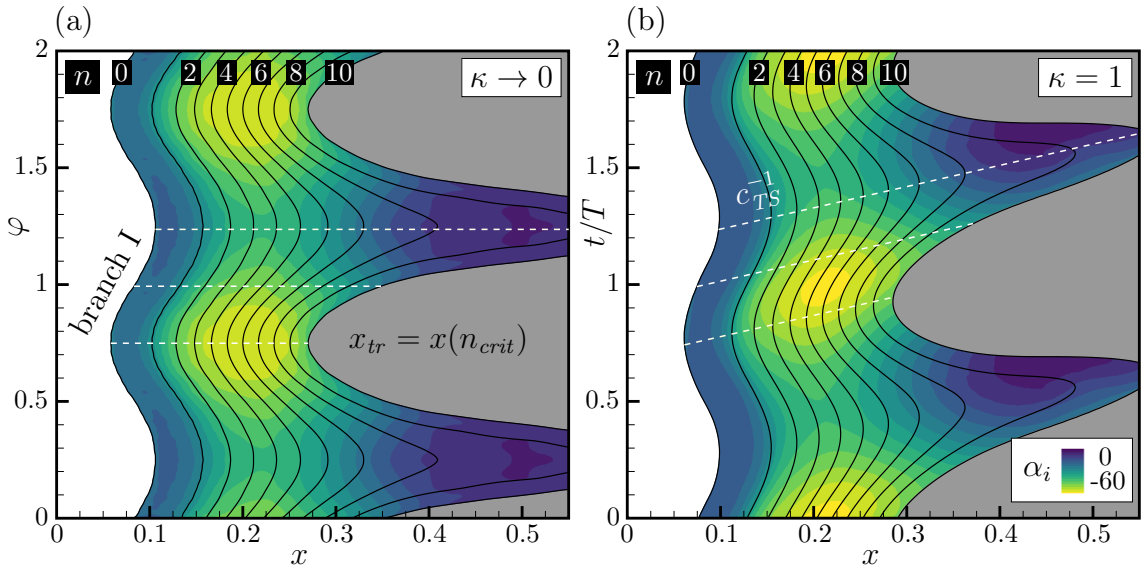

Figure 3.9: Spatio-temporal development of spatial amplification rate α_i for a mode with $\omega = 201$ and resulting n-factors from (unsteady) e^n-method; white dashed lines represent exemplary trajectories of TS-waves. (a) Quasi-steady case ($\kappa \to 0$) with $v'_{gust} = 0.01$ (b) $\kappa = 1$, $v'_{gust} = 0.02$.

3.3.1 Validation with wind-tunnel measurements

The transient envelope $N(x,t) \in \{1 \dots 12\}$ considering all relevant modal frequencies ω is shown in figure 3.10 for four cases. In order to compare the results with the experimental investigations, the gust amplitude of $v'_{gust} = 0.01$ is shown for the quasi-steady case $\kappa \to 0$ while the gust amplitude of $v'_{gust} = 0.02$ is shown for the unsteady cases $\kappa = 1$, 1.34 and 1.67. Comparing figure 3.10(a) & (b) with their counterparts at only one TS-wave frequency $\omega = 201$ in figure 3.9, it can be seen that the N-factors, and hence also the predicted transition location $x_{tr}(N_{crit})$, oscillate less drastically in upstream and downstream direction. (Note: This effect of the resulting envelope is shown schematically for two frequencies ω in figure 2.3.) For the quasi-steady case $\kappa \to 0$, a sine-like oscillation of the transition location is exhibited, e.g. for $N_{crit} = 10$ between $x = 0.25$ and 0.46. Due to this behavior, the setup/flow scenario can be considered generic (to a certain degree) for investigations on unsteady laminar-to-turbulent transition. For the cases with $\kappa > 0$, the skewed or asymmetric behavior of the N-factors over time is clearly observable. In addition, an attenuation of the up- and downstream movement of N is observed as κ increases.

The numerical results in figure 3.10 can be compared with wind-tunnel measurements from two campaigns: results from Romblad *et al.* (2020) corresponding to $N_{crit} = 10$ and from Romblad (2023) corresponding to $N_{crit} = 12$. In both studies, a slightly modified version of the M-TERA intermittency method of Zhang *et al.* (1996) with a suitable threshold for the C_3-parameter (periodic ensemble-

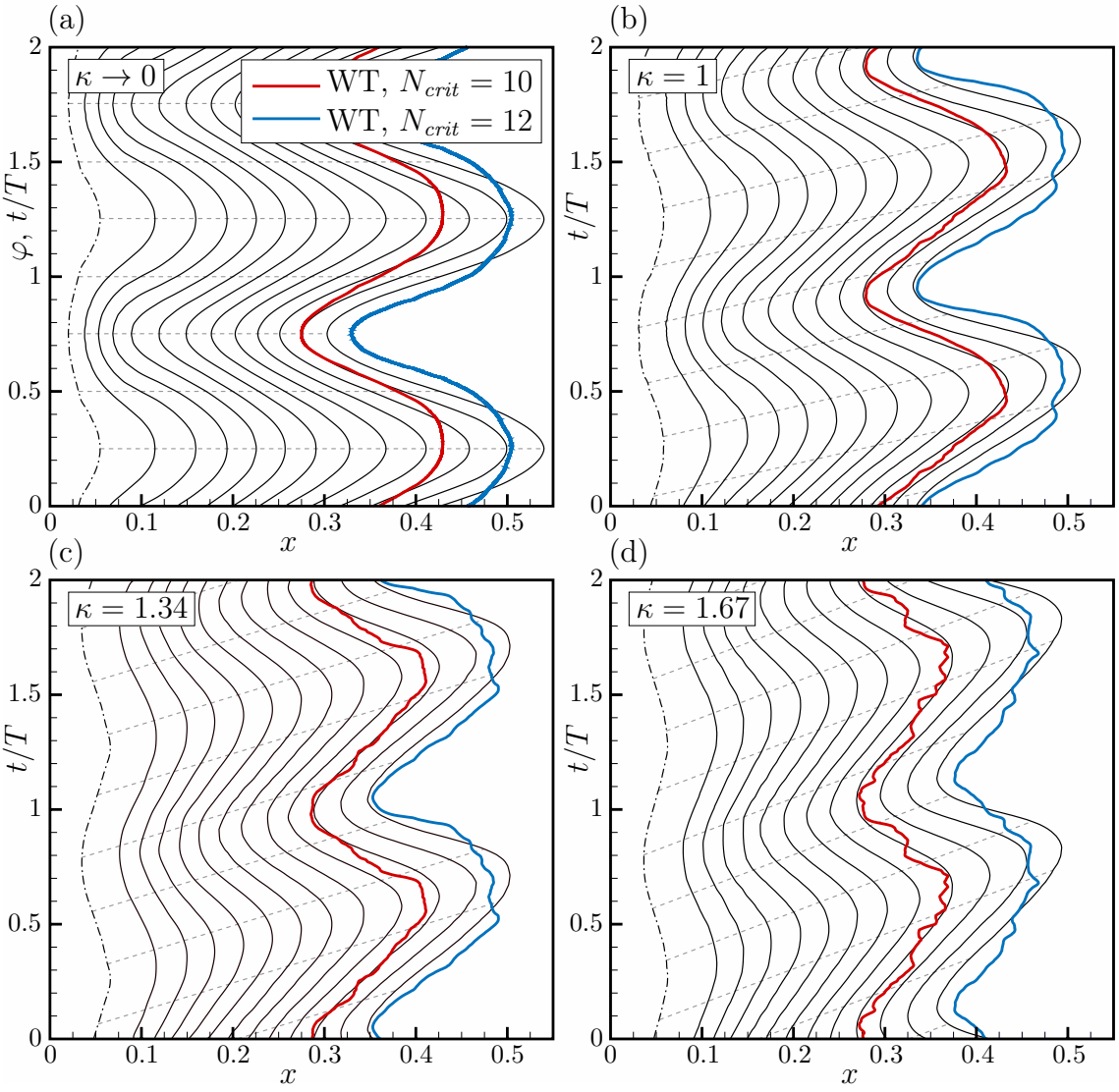

Figure 3.10: Spatio-temporal transition behavior; simulations: −·−·− $N = 0$ (branch I), —— $N \in \{1 \dots 12\}$ with $\Delta N = 1$ in downstream direction, - - - - - exemplary trajectories of TS-waves with c_{TS}^{-1}; wind-tunnel measurements: M-TERA transition criterion (a) Quasi-steady case ($\kappa \to 0$) with $v'_{gust} = 0.01$; WT: $\kappa = 0.22$ ($N_{crit} = 10$) and $\kappa = 0.06$ ($N_{crit} = 12$) (b) $\kappa = 1$, $v'_{gust} = 0.02$ (c) $\kappa = 1.34$, $v'_{gust} = 0.02$ (d) $\kappa = 1.67$, $v'_{gust} = 0.02$.

average) was used to detect the unsteady transition location. In the wind-tunnel investigations for the quasi-steady case $\kappa \to 0$, a slightly lower gust amplitude of $v'_{gust} \approx 0.0087$ ($AoA' = 0.5°$) is present compared to the numerical investigation with $v'_{gust} = 0.01$ ($AoA' \approx 0.57°$). Nevertheless, a qualitatively very similar behavior is clearly visible, where the N-factors and the transition position move upstream and downstream "symmetrically" in time. The discrepancy of the transition downstream-extreme $\max_{x,t}\{x_{tr}\}$ at $\max\{AoA\}$ (hence $t/T = 0.25$) can be explained

by the non-linear translation of the gust-generator impact in the experiments[1]. For the frequencies $\kappa > 0$, a very good agreement with the results of the measurement campaign with $N_{crit} = 10$ can be seen. It should also be pointed out that the agreement of the LST at $\kappa = 1.34$ with the case $N_{crit} = 10$ is considerably better than in the result of Ohno *et al.* (2022), where quasi-steady base flows were employed. This confirms the necessity of using URANS simulations with time-resolved DVA gusts to generate transient base flows. The results of the measurement campaign with $N_{crit} = 12$ for the cases $\kappa > 0$ also show good qualitative agreement. However, some deviation in the area around $\max_{x,t}\{x_{tr}\}$ is visible, which is most likely due to the above-mentioned gust-generator behavior. In summary, the unsteady transition in the experimental campaign with $\kappa \leq 1.67$ and $v'_{gust} \leq 0.02$ can be described by linear effects for the most part.

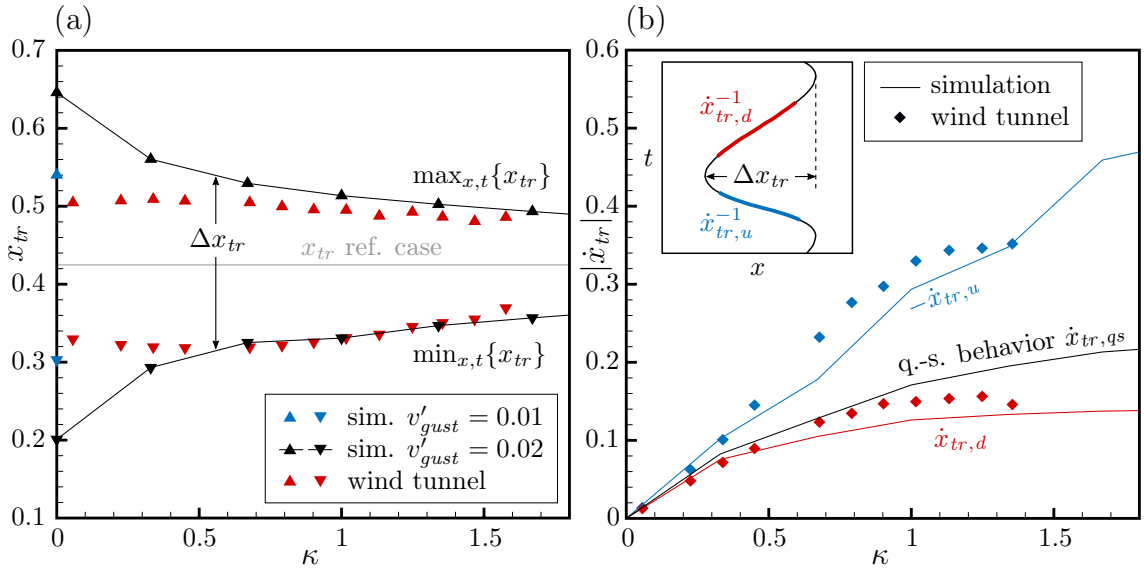

Figure 3.11: Comparison of unsteady transition from wind-tunnel measurements with transition prediction of simulations for $N_{crit} = 12$ (a) Extremes of transition location x_{tr} versus κ (b) Upstream and downstream velocities of transition front versus κ with $v'_{gust} = 0.02$ in simulations.

The results of the simulations and the experiments can also be compared quantitatively with the upstream and downstream extremes of the (predicted) transition location x_{tr}, see figure 3.11(a). For $\kappa > 0.7$, the trend of both extremes versus κ is well captured. The offset of $\max_{x,t}\{x_{tr}\}$ is explained by the above-mentioned non-linear translation of the gust generator for $N_{crit} = 12$. For $\kappa < 0.7$, a strong deviation of the experimental results from the LST for $v'_{gust} = 0.02$ is apparent. This results from the frequency dependence of the amplitude of the gust generator, see

[1]This can be explained by two separate effects: first, the transition location in the experiment is less sensitive to AoA variations close to $\max\{AoA\}$; second, the efficiency of the gust generator decreases in the same region; see Romblad (2023) for discussion.

depiction in figure 3.4 and Romblad (2023) for a detailed discussion. The maximum oscillation-length of the transition $\Delta x_{tr}(\kappa, v'_{gust}, N_{crit}) = \max_{x,t}\{x_{tr}\} - \min_{x,t}\{x_{tr}\}$ is attenuated for increasing κ and will be relevant for further characterization, see below.

The differences in the velocities of the transition front in upstream direction $\dot{x}_{tr,u}$ and downstream direction $\dot{x}_{tr,d}$ reflect the skewness or asymmetry of the transition motion over time. Both velocities from the wind-tunnel measurements and the LST ($v'_{gust} = 0.02$) are plotted in figure 3.11(b) versus κ, with their trajectories exemplified in the inset figure. In order to approximate the velocities $\dot{x}_{tr,u/d}$, a linear-fit method by Romblad (2023) was used here. In addition, for the hypothetical case of a symmetric upstream and downstream motion of the transition fronts in time (i.e. quasi-steady behavior), the theoretical non-dimensional velocity

$$\dot{x}_{tr,qs} = \Delta x_{tr} \cdot \frac{2\kappa}{\pi} \cdot 1.47 \tag{3.4}$$

can be calculated for the respective reduced frequency κ. The reciprocal of the second part $\pi/(2\kappa)$ of the equation corresponds to half the period of the oscillation $T/2$. Consequently, the product of $\Delta x_{tr} \cdot 2/T$ represents a transition-front velocity approximated as a straight line between both spatial extremes. This leads to a simplification of the transition motion to a zigzag pattern, which is therefore corrected by the factor ≈ 1.47 in equation (3.4) to account for the sine-like oscillation expected in the quasi-steady case. The factor was calculated based on the result in figure 3.10(a) using the linear-fit of Romblad (2023). Since the attenuation of the transition motion with increasing frequency is accounted for in equation (3.4) via $\Delta x_{tr}(\kappa)$, the velocity $\dot{x}_{tr,qs}$ exhibits a sublinear progression versus κ in figure 3.11(a). The velocities of the transition fronts of the numerical results deviate from the theoretical quasi-steady behavior as κ increases, with the upstream velocity $\dot{x}_{tr,u}$ becoming significantly larger and the downstream velocity $\dot{x}_{tr,d}$ becoming significantly smaller. This reflects and quantifies the degree of temporal skewness of the transition motion. Seemingly, the absolute velocity of the upstream movement increases approximately linearly with the frequency κ in the LST results. The trend of the transition front velocities measured in the wind tunnel shows a good qualitative agreement with the numerical results, despite slightly higher values. Based on the comparisons presented here, the simulation chain consisting of URANS with DVA gusts and the unsteady linear stability analysis including all assumptions can be considered validated for the investigated flow scenario at $\kappa \leq 1.67$ and $v'_{gust} \leq 0.02$.

3.3.2 Parameter study

The results of the unsteady linear stability analysis for all other investigated cases $\kappa \in \{0; 1; 2; 3; 4; 8\}$ at $v'_{gust} \in \{0.01; 0.02; 0.04; 0.06\}$ (cf. matrix in figure 3.1.2)

Figure 3.12: Spatio-temporal development of N-factors from unsteady linear stability analysis on transient base flows of URANS simulations, cf. matrix in figure 3.4; −·−·− $N = 0$ (branch I); —— $N \in \{1 \dots 12\}$ with $\Delta N = 1$ in downstream direction and —— $N = 10$; - - - - - exemplary trajectories of TS-waves with c_{TS}^{-1}.

can be found in figure 3.12. Again, all $N \in \{0 \dots 12\}$ are shown with exemplary trajectories ($c_{TS} = 0.35$) of TS-waves. Here, $N = 10$ is highlighted (red line), since this threshold is used in following analyses and corresponds to the transition with $n \approx 10$ investigated in the subsequent DNS. To gain an understanding of the resulting prediction of the unsteady transition, the effect of the transient base flows can be accounted for by a direct comparison of the figure 3.12 with the shape-factor deviation in figure 3.8.

First, the results of all cases at the lower amplitudes $v'_{gust} = 0.01$ and 0.02 are discussed. While the N-factors in the quasi-steady cases ($\kappa \to 0$) show a symmetric response in time, the motion in the transient cases ($\kappa > 0$) can again be seen to be asymmetrically or skewed over time. For e.g. $N_{crit} = 10$ at $v'_{gust} = 0.02$, the ratio of the upstream velocity $|\dot{x}_{tr,u}|$ to the downstream velocity $|\dot{x}_{tr,d}|$ of the transition front increases as the reduced frequency increases up to $\kappa \leq 4$. Moreover, it can be observed that the increase of the amplitude from $v'_{gust} = 0.01$ to $v'_{gust} = 0.02$ intensifies the asymmetry of the transition movement in time. Evidently, the distance of the oscillating transition position Δx_{tr} attenuates for both amplitudes with increasing κ, which can be attributed to the impedance (Sears function) of the airfoil flow described in section 3.2.1. At $\kappa = 8$, $N_{crit} = 10$ hardly oscillates and corresponds approximately to the transition of the steady-state reference case. The considerably higher attenuation from $\kappa = 4$ to $\kappa = 8$ can be attributed to the fact that TS-waves are traveling through more amplified and less amplified regions during their lifetime, as pointed out in section 3.2.2. Finally, it should be noted that the phase lag of the spatial extremes of the transition location (e.g. $N_{crit} = 10$) to the spatial extremes of branch I ($N = 0$) can be approximated via the phase speed, see trajectories in figure 3.12. The oscillation of branch I correlates with the signal of the gust at the leading edge. However, as in the experimental counterparts, the phase to the convecting gust is generally disregarded in this work.

The observations described above generally also apply to the results when increasing the amplitude to $v'_{gust} = 0.04$, see figure 3.12. However, for $N_{crit} = 10$ at $\kappa = 3$ and 4 for example, a very interesting phenomenon can be observed: the course of N_{crit} not only behaves asymmetrically over time but also shows an *overturned*[2] pattern over time. Hence, the overturned pattern of N_{crit} suggest that a spot[3] of transitional/turbulent flow periodically appears within the laminar flow (upstream of the "final" point of transition) for a short time during the oscillation cycle. This feature is most pronounced for $\kappa = 4$, which can be explained using the characteristic time scale t_{TS} of TS-waves with respect to their spatio-temporal behavior. As already mentioned in section 3.2.2, the characteristic length scale of the TS-wave

[2]The term "overturned" is borrowed from structural geology, where the folding of sediments is categorized as symmetrical, asymmetrical, overturned, etc.

[3]Note that the turbulent spot is strictly speaking a turbulent strip periodically/uniform in spanwise direction in this work.

trajectories $\Delta x_{TS} \approx 0.27$ can be approximated with the path where modes grow according to linear theory (from branch I to $N_{crit} = 10$) for the steady-state reference case. Consequently, the characteristic time scale $t_{TS} = \Delta x_{TS}/c_{TS} \approx 0.77$ corresponds to the approximate average "life expectancy" of the TS-waves progressing in the x/t plane. Thus, if this time scale equals approximately to the period of the gust, the TS-waves experience the maximum impact of the transient base flow. This is also due to the fact that the unsteady properties of the base flow regarding the amplification are approximately velocity-congruent with the course of the TS-waves, cf. form-factor deviation in figure 3.8. This can explain the strong asymmetry as well as the overturned N-factors for the case $\kappa = 4$, since the period $T \approx 0.78$ is indeed almost identical to the time scale t_{TS}. At an increased amplitude $v'_{gust} = 0.06$ for $\kappa = 4$, this behavior is significantly enhanced. For $\kappa = 1$ at $v'_{gust} = 0.04$, the TS-waves are passing the flow much faster in relation to the gust period ($4t_{TS} \approx T$). Accordingly, the asymmetric behavior is much less pronounced here and an overturned pattern of the N-factors is not present. For $\kappa = 8$ at $v'_{gust} = 0.04$, however, the TS-waves pass through about two gust periods during their lifetime ($t_{TS} \approx 2T$), leading to a further weakening of the oscillation as well as a disappearance of the overturned pattern for $N_{crit} = 10$. Based on the above considerations, the critical reduced frequency for the case of "maximum transient behavior" (i.e. asymmetric and potentially overturned pattern) expected at $T \approx t_{TS}$ can be estimated with

$$\kappa_{crit} \approx \pi \cdot \frac{\tilde{c}_{TS}}{\tilde{u}_\infty} \cdot \frac{\tilde{L}_c}{\Delta \tilde{x}_{TS}} = \frac{\pi\, c_{TS}}{\Delta x_{TS}}\,, \tag{3.5}$$

in a dimensional and non-dimensional formulation, respectively. The crucial parameter is obviously Δx_{TS}, which depends mainly on the threshold N_{crit} and the average/steady-state pressure gradient, i.e. AoA_{ref} in the present flow scenario.

3.3.3 Discussion

The results of the parameter study discussed above consider only effects described by linear theory based on transient laminar flow. Therefore, the question arises to what extent non-linear effects as well as turbulent sections of the flow can have an influence on the N-factors and the transition location, especially for the cases with overturned patterns. Before discussing the results of the DNS in the next section, first considerations for that regard can be made here. Therefore, the most extreme example at $\kappa = 4$ with $v'_{gust} = 0.06$ is magnified in figure 3.13(a) for a detailed discussion of multiple aspects. Here, the transition motion for $N_{crit} = 10$ shows an overturned pattern where a transitional/turbulent spot is predicted to occur for about a quarter of the period in the interval $0.3 \leq t/T \leq 0.56$. Thus, as shown in figure 3.13(a), there are instants in the oscillation cycle (see $t = const.$) where the boundary layer exhibits a pattern of laminar-turbulent-laminar-turbulent flow

(Ⓛ/Ⓣ) in downstream direction x. With the exception of very short moments at the peaks $\min_{x,t}\{x_{tr}\}$ and $\max_{x,t}\{x_{tr}\}$, the transition fronts move exclusively downstream ($\dot{x}_{tr} > 0$) in this case. Therefore, the two branches of the transition motion can no longer be referred to as the upstream ($x_{tr,u}$) and downstream-moving fronts ($x_{tr,d}$), but as the leading ($x_{tr,le}$) and trailing edges ($x_{tr,te}$) of a (temporarily isolated) transitional/turbulent section. This is illustrated in the inset figures in figure 3.14(b) where the transition fronts of the asymmetric behavior Ⓐ is contrasted with the overturned behavior Ⓞ.

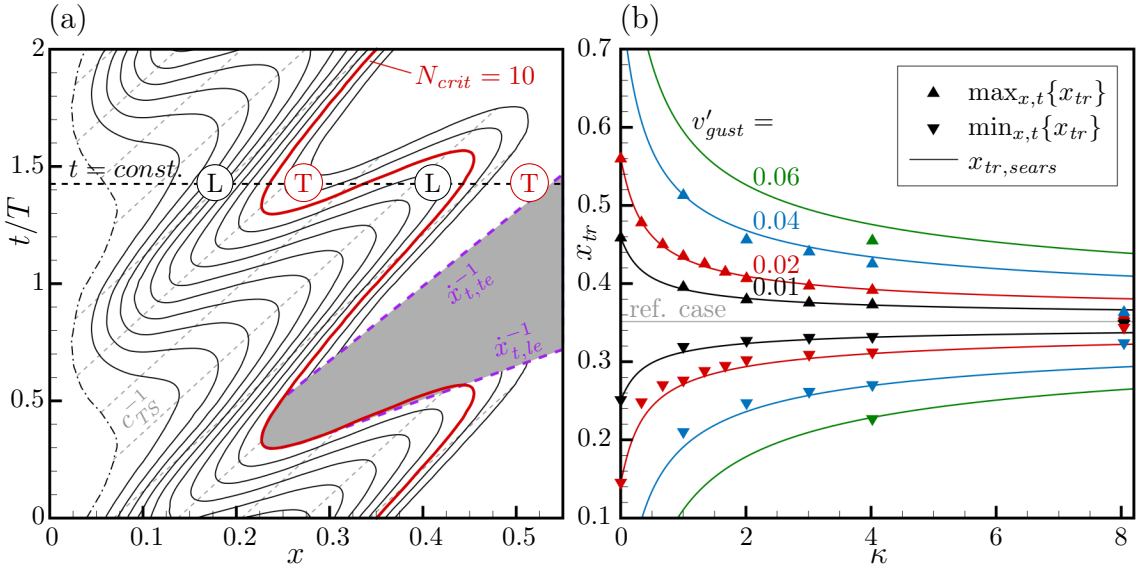

Figure 3.13: (a) Simulation for $\kappa = 4$ and $v'_{gust} = 0.06$: spatio-temporal development of −·−·− $N = 0$ (branch I); —— $N \in \{1 \dots 12\}$ with $\Delta N = 1$ in downstream direction and —— $N = 10$; - - - - - exemplary trajectories of TS-waves with $c_{TS} = 0.35$; hypothetical turbulent strip (gray) with leading-edge $\dot{x}_{t,le} = 0.9$ and leading-edge velocity $\dot{x}_{t,te} = 0.4$. (b) Extremes of transition location x_{tr} versus κ for all simulation results with the approximation $x_{tr,sears}$ based on the Sears (1941) function.

The transition pattern in figure 3.13(a) visually resembles the results of the zero-pressure gradient case *15* and adverse-pressure gradient case *D-5* of Obremski & Fejer (1967) with unsteady natural transition. For both cases, however, the behavior is explained by the identified "convective-transition mode", which is not captured by linear theory. Hence, the overturned pattern results rather from the periodic occurrence of a "creative transition" phase due to strongly amplified TS-waves and a subsequent downstream traveling turbulent spot corresponding to the phase of the so-called convective transition. In case *15* of Obremski & Fejer (1967), however, the shape of the tip of the creative transition front along with the preceding identified wave packet[4] in the x/t plane suggest an overturned N-factor behavior of the incoming TS-waves. As will be seen in the investigations with the DNS in the next

[4]Note that the term "wave packet" in Obremski & Fejer (1967) is misleading, see discussion.

section, this may reflect the contribution of linear effects to some extent. However, it should be emphasized that an overturned N-factor behavior in the theoretical laminar and linear consideration is not a necessary condition for the occurrence of the convective-transition mode in the actual flow. Studer *et al.* (2006) presented results with an asymmetric transition behavior where the upstream-moving front is identified as creative transition and the downstream-moving front as convective transition. Final conclusions and classifications of these scenarios are outlined in the summary in section 3.5.

At this point, it can be assessed whether the predicted transition pattern for $N_{crit} = 10$ in figure 3.13(a) is manipulated or even intercepted by non-linear effects and transitional/turbulent sections. A hypothetical turbulent spot convecting downstream from the apex $\min_{x,t}\{x_{tr}\}$ (creative transition) is represented by the gray zone in the x/t plane. The limits imposed by the trajectories of the leading edge $x_{t,le}$ and trailing edge $x_{t,te}$ of the spot are based on several assumptions. Obremski & Fejer (1967) observed a leading-edge velocity at free-stream velocity $\dot{x}_{t,le} = 1$ and a trailing-edge velocity of $\dot{x}_{t,te} = 0.55$ for the ZPG case *15*. However, since a different behavior is expected for an APG as present in this scenario, the results of Gostelow *et al.* (1996) on the development of triggered turbulent spots at several streamwise pressure gradients can be used here[5]. In that study, a dependency of the spot velocities on the Pohlhausen pressure-gradient parameter λ_{δ_2} is shown. Hence, with $\lambda_{\delta_2} \approx -0.1$ found for the steady-state reference case in the relevant downstream stretch of the flow, see figure 3.2, the leading edge and trailing edge velocities are estimated with $\dot{x}_{t,le} \approx 0.9$ and $\dot{x}_{t,te} \approx 0.4$, respectively. The trajectory of $\dot{x}_{t,le}$ is consequently set tangent to the trajectory of the predicted transition $\dot{x}_{tr,le}$ for $N_{crit} = 10$ in figure 3.13(a). It can be seen that from $x > 0.3$ the hypothetical turbulent spot only slightly precedes or "overtakes" the predicted transition location. Therefore—while additional influences are ignored for the time being—it can be assumed that the qualitative behavior of the overturned transition pattern according to linear theory is generally possible with respect to the transitional/turbulent leading edge.

The potential non-linear influence on the trailing edge (or the downstream-moving front for an asymmetric behavior) of the transition, on the other hand, is more difficult to ascertain. The trajectory of the trailing edge of the hypothetical spot is significantly faster than the predicted trajectory of the transition front with $\dot{x}_{tr,te} \approx 0.27$. The point at which the sketched trajectory $x_{t,te}$ departs from the predicted transition was arbitrarily chosen in figure 3.13(a) to resemble case *15* of Obremski & Fejer (1967). In general, the downstream traveling turbulent region could be expected to have no effect on the upstream flow, thus the transition front could emerge according to the linear theory. However, it is known that the so-called *calmed*

[5]It is assumed here that a 2D turbulent strip behaves almost identically to 3D turbulent spots, cf. Mayle & Dullenkopf (1991); Seifert & Hodson (1999).

region occurs immediately behind a turbulent spot, which temporarily imposes a strong attenuation of disturbances, see e.g. Orth (1993); Halstead *et al.* (1997); Hughes & Walker (2001). Since the trailing edge of a potential calmed region can be as slow as $\dot{x}_{cr,te} \approx 0.2$, see Gostelow *et al.* (1997), the incoming TS-waves with $c_{TS} \approx 0.35$ can be strongly attenuated causing the predicted natural transition not to occur here. In general, the calmed region is associated with the termination of the creative transition and thus with the initiation of the convective transition, see Walker (1993). Nevertheless, the question remains as to why a convective transition with a subsequent calmed region occurs at all, since linear theory always predicts a continuous transition location upstream under the assumption of continuous initial perturbations A_0. However, what at first glance appears to be a chicken-or-the-egg problem (calmed region vs. absent natural transition) can be settled with the subsequent DNS presented in the next section. It will be shown that the transient (viscous) delay of the *mean flow distortion* is the driving force for the occurrence of the convective-transition mode in case of natural transition with TS-waves.

3.3.4 Dimensional analysis and characterization

Nevertheless, the results of the linear stability analysis of the transient laminar flow are essential for the comprehension of the respective transitional flow with its complex non-linear effects. Furthermore, the results of the parameter study in figure 3.12 are used to venture a general description of the unsteady natural transition with the means of dimensional analysis and other considerations. An obvious start for this characterization is the assessment of the spatial extent of the oscillating transition location Δx_{tr} versus gust amplitude and reduced frequency. Figure 3.13(b) depicts the spatial extremes of the transition location at $N_{crit} = 10$ versus κ for all numerical results. As discussed above, the frequency-dependency of the gust impact due to the impedance is clearly reflected in the attenuation of the extremes and therefore Δx_{tr}. Hence, it is suggested that the Sears (1941) function from equation (3.1) can be employed to account for this effect by scaling the length of the oscillating transition from the respective quasi-steady case:

$$\Delta x_{tr,sears} = |S| \cdot \Delta x_{tr,\kappa\to 0}\,. \tag{3.6}$$

Thus, the dependency of the effective amplitude on the frequency κ (or $\lambda_{x,gust}/L_c$) is considered with $|S|$, while the gust amplitude v'_{gust} and the threshold N_{crit} is accounted for with $\Delta x_{tr,\kappa\to 0}$. The course of the extremes can therefore be approximated with $x_{tr,sears} = x_{tr,ref} \pm \Delta x_{tr,sears}/2$, see lines in figure 3.13(b). Note that linear scaling with respect to the gust amplitude is applied to calculate $\Delta x_{tr,\kappa\to 0}$ for the cases without a quasi-steady reference, cf. linear relationship of $c'_{l,sears} \sim v'_{gust}$ in equation (3.2). For $\kappa \leq 4$, a remarkably good agreement of the Sears approximation

with the extremes of the simulations can be observed. Not surprisingly, the attenuation from $\kappa = 4$ to $\kappa = 8$ is considerably stronger than the approximated effect of the impedance described by the Sears function for all amplitudes. This is in agreement with the qualitative analysis described above that the TS-waves travel several times through stronger and weaker amplified spatio-temporal regions, since their lifetime greatly exceeds the period of the oscillation at high κ. Accordingly, when estimating $\Delta x_{tr,sears}$ with equation (3.6), additional attenuation beyond the critical reduced frequency κ_{crit} (here ≈ 4) given in equation (3.5) should be considered.

To assess the degree of unsteadiness with regard to the temporal asymmetry of the transition fronts, a dimensionless number can be derived. The reduced frequency κ, cf. equation (2.6), is not a suitable characterization measure since it considers the chord $\tilde{L}_c$ as the characteristic length which has no direct relation to the local physics of the transient boundary-layer transition. Hence, a new dimensionless quantity

$$\kappa^{tr} = \frac{2\pi\ \tilde{f}_{gust}\ \Delta\tilde{x}_{tr}}{\tilde{u}_\infty} = 2\kappa\ \Delta x_{tr}\,, \tag{3.7}$$

is suggested, taking maximum length of the spatial oscillation Δx_{tr} into account in a dimensional and non-dimensional formulation, respectively.[6] This definition implicitly takes into account the effective amplitude of the gust, i.e. the absolute amplitude v'_{gust} as well as subsequent attenuation-effects described above. Therefore, by effectively multiplying the gust frequency with the amplitude effect, a suitable measure of the general unsteadiness concerning transition is derived. This contrasts with the "non-steady Reynolds number" $Re_{NS} = (\tilde{u}'_{gust}\tilde{u}_\infty)/(\tilde{\omega}_{gust}\tilde{\nu}) = Re \cdot u'_{gust}/(2\kappa)$ suggested by Obremski & Fejer (1967), where the amplitude is in the numerator and the frequency is in the denominator, see also reviews Loehrke *et al.* (1975); Walker (1993). Since the numerator of equation (3.7) is proportional to the theoretical velocity of the transition front with a quasi-steady behavior $\dot{x}_{tr,qs}$, cf. equation (3.4), and the phase speeds of the TS-waves are always coupled to u_∞, $\kappa^{tr} \sim \dot{x}_{tr,qs}/c_{TS}$ applies. Hence, this quantity can also be interpreted as a ratio of two velocities or gradients in the x/t plane. The velocities c_{TS} and $\dot{x}_{tr,qs}$ are about the same for $\kappa^{tr} \approx 1$ in case of a zigzag motion or $\kappa^{tr} \approx 1/1.47$, respectively, in case of a sine-like motion, cf. section 3.3.1.

An earlier version of this definition was already introduced by Ohno *et al.* (2022) and also taken up by Romblad (2023), in which $\Delta x_{tr,\kappa\to 0}$ of the respective quasi-steady case was used as the characteristic length. In contrast to the previous definition, the revised formulation in equation (3.7) introduces an implicit character, since κ^{tr} can also decrease for an increasing κ in case of a strong attenuation of $\Delta x_{tr}(\kappa)$. This proves to be advantageous for the following characterizations of the results from linear theory. However, a non-implicit variant κ^{tr}_{sears} of the quantity in equation

[6] Note that 2π is used in the definition of κ^{tr}, whereas only π was used for κ in this work.

(3.7) is introduced here where the amplitude $\Delta x_{tr,sears}$ of the Sears-approximation, cf. equation (3.6), is employed as the characteristic length. Consequently this definition only accounts for the effective amplitude of the gust while neglecting the above-described additional attenuation of the n-factors, especially for $\kappa > \kappa_{crit}$. In the discussion of the DNS results in section 3.4.8, it is shown that this quantity is suitable for characterizing the occurrence of non-linear effects.

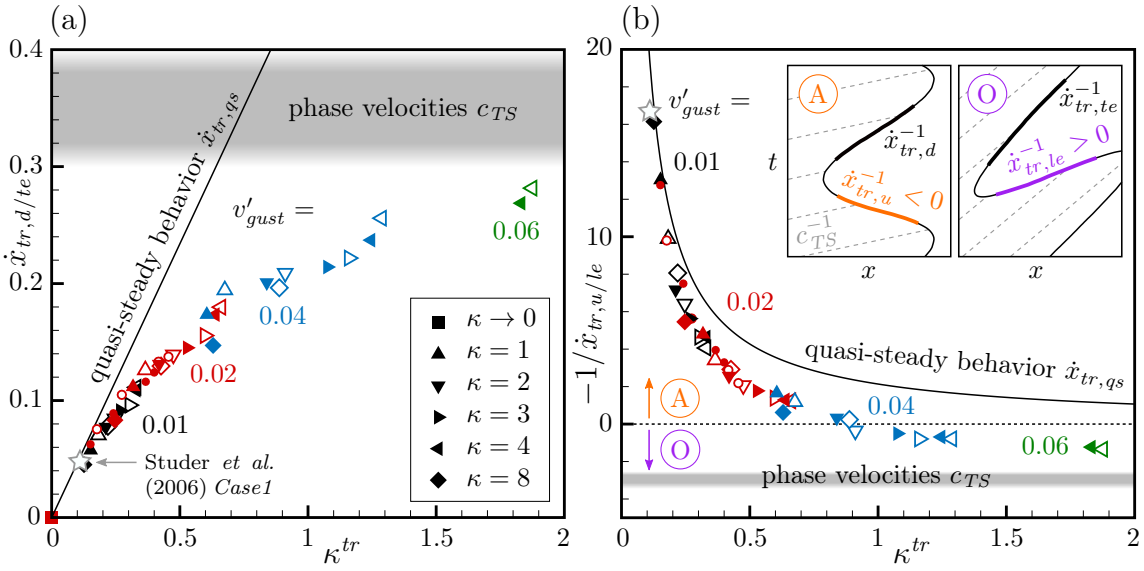

Figure 3.14: Velocities of transition front according to linear theory; full symbols: $\dot{x}_{tr}(N_{crit} = 10)$, empty symbols: $\dot{x}_{tr}(N_{crit} = 12)$; small dots: $\kappa \in \{0.34; 0.67; 1.34; 1.67\}$ (a) Downstream/trailing-edge velocity $\dot{x}_{tr,d/te}$ (b) Upstream/leading-edge velocity (negative, reciprocal) $-1/\dot{x}_{tr,u/le}$ with distinction in Ⓐ asymmetric pattern and Ⓞ overturned pattern.

In figure 3.14, the velocities of the transition fronts versus κ^{tr} are shown for all numerical results with $N_{crit} = 10$ and 12. The theoretical velocity of the transition fronts for a quasi-steady behavior from equation (3.4)—which can now be simplified to $\dot{x}_{tr,qs} = \kappa^{tr}/\pi \cdot 1.47$—is employed again. In contrast to the course of $\dot{x}_{tr,qs}(\kappa)$ in figure 3.11(b), $\dot{x}_{tr,qs}(\kappa^{tr})$ represents all gust amplitudes v'_{gust} and shows a linear trend in figure 3.14(a) since the attenuation for increasing frequencies is eliminated when using κ^{tr}. Likewise, the downstream/trailing edge velocities $\dot{x}_{tr,d/te}$ for all cases coincide to a clear trend for increasing κ^{tr}, see figure 3.11(a). In this course it can be seen that the velocities initially correspond to the quasi-steady behavior for very small $\kappa^{tr} \lessapprox 0.2$. However, for increasing unsteadiness κ^{tr}, they continuously deviate from the quasi-steady behavior reflecting the asymmetry of the transition with respect to $\dot{x}_{tr,d/te}$. Apart from the apparent constraint $\dot{x}_{tr,d/te} < \dot{x}_{tr,qs}$, the velocities can obviously never exceed the phase velocities of the TS-waves c_{TS}, at least in the purely linear consideration presented here. Looking closely at, e.g., the amplitude $v'_{gust} = 0.04$, it can be seen that the velocity increases steadily along with

κ^{tr} from $\kappa = 1$ to $\kappa = 4$. The case with the highest frequency $\kappa = 8$ exhibits a slower velocity but still agrees with the general course due to its characterization with κ^{tr} which decreases as well.

A very clear trend can be also found for the upstream/leading edge velocities $\dot{x}_{tr,u/le}$ of all cases in figure 3.14(b). The reciprocal formulation is used here to overcome the "jump" from $\dot{x}_{tr,u} \to -\infty$ to $\dot{x}_{tr,le} \to +\infty$ in the change from the asymmetric transition pattern (A) to the overturned transition pattern (O), cf. inset figures. Consequently, $1/\dot{x}_{tr,u/le} = 0$ also determines the boundary of the asymmetric and overturned behavior, with which a critical value for the unsteadiness parameter based on the trend of the results with $\kappa^{tr} \approx 0.9$ is found. Note: The red line in figure 3.29 qualitatively corresponds to this value and therefore represents the limit for the occurrence of the overturned pattern. The upstream velocity is always faster than the theoretical quasi-steady velocity $|\dot{x}_{tr,u}| > \dot{x}_{tr,qs}$. In this concept with the linear theory, the leading-edge velocity for the case of the overturned pattern cannot be slower than the phase velocity of the TS-waves ($\dot{x}_{tr,le} > c_{TS}$), see trajectories in inset figure.

The experimental results of Romblad *et al.* (2020); Romblad (2023) used for validation in section 3.3.1 were attributed to purely linear effects and consequently show a good agreement with the numerical results using the dimensionless characterization (not depicted in figure) with $\kappa^{tr} \leq 0.39$. Another example from the literature with apparent linear behavior is *Case1* by Studer *et al.* (2006) with $\kappa \approx 0.44$ ($St = 0.14$). Here, the level of unsteadiness is $\kappa^{tr} \approx 0.11$ with the transition front velocities $\dot{x}_{tr,d} \approx 0.048$ and $\dot{x}_{tr,u} \approx -0.06$, see gray stars in figure 3.14. For *Case2* of the same work with $\kappa \approx 1.35$ ($St = 0.43$) and a higher amplitude, however, $\kappa^{tr} \approx 1.49$ with $\dot{x}_{tr,d} \approx 0.348$ and $\dot{x}_{tr,u} \approx -1.51$ can be determined which does not agree with the trend in figure 3.14. This is not surprising since a convective transition was identified for the downstream-moving transition front which is not covered by the purely linear considerations here. The same applies to the cases *15*, *D-5* and *D-6* of Obremski & Fejer (1967) where $\kappa^{tr} \approx 5.53$, 3.77 and 2.06 with $\dot{x}_{tr,d/te} \approx 0.55$, 0.53 and 0.5 is found, respectively. Hence, also in agreement with the DNS results of the next section, non-linear effects are to be expected for $\kappa^{tr} \gtrapprox 0.5$.

Based on the analyses described above, a general scheme for predicting the oscillating transition location can be outlined as follows:

(a) Linear stability analysis of quasi-steady case $\kappa \to 0$ for base flows $AoA'(v'_{gust})$ (acquired e.g. with XFoil or RANS) to determine $\Delta x_{tr,\kappa\to 0}$ and the characteristic length scale of the trajectories Δx_{TS} for a given N_{crit}.

(b) Approximation of the effective transition amplitude $\Delta x_{tr}(\kappa)$ with the Sears function, cf. equation (3.1), while modeling additional attenuation for $\kappa > \kappa_{crit}(\Delta x_{TS})$, see equation (3.5).

(c) Estimation of transition front velocities $\dot{x}_{tr}$ according to the trend in figure

3.14 by employing the unsteadiness quantity κ^{tr}, cf. equation (3.7).

(d) Consideration of additional non-linear effects for $\kappa^{tr} \gtrapprox 0.5$ based on DNS/WT results, potentially with a semi-empirical approach.

Furthermore, the unsteady stability analysis could be employed as a transition model for URANS simulations of flows with natural transition at unsteady conditions, requiring only point (d) to be additionally considered.

3.4 Direct numerical simulations

In the DNS of the present flow scenario, transient base flows from (U)RANS simulations are prescribed as unsteady boundary conditions. The numerical setup of the underlying (U)RANS simulations is consistent with the investigations discussed above. At the comparatively high Reynolds number of $Re = 3.4 \cdot 10^6$, compressible DNS at lower Mach numbers are almost impossible due to limited computational resources. Consequently, the DNS are performed with $Ma = 0.3$ to allow calculations with a non-prohibitive time step. Even though this Mach number is considerably larger than in the wind-tunnel investigations ($Ma \approx 0.11$), the flow can still be considered as quasi-incompressible.

3.4.1 Numerical setup and processing

Figure 3.1 depicts the location and extent of the curvilinear DNS domain. The position of the wall-normal inflow boundary $x_{in} = 0.13$ is selected with regard to the modal disturbance input just downstream at $x_{DS} = 0.15$. In contrast to the investigations with unsteady linear stability analysis, it is not possible to spawn TS-waves at the upstream and downstream oscillating branch I. Actuation upstream of branch I would lead to a rapid vanishing of the modes. Accordingly, the TS-waves have to be introduced downstream of branch I where amplification $\alpha_i < 0$ is present over the whole gust period, see location in the stability diagram in figure 3.3(a) for the steady-state reference case at AoA_{ref}. The outflow boundary is located at $x_{out} \approx 0.704$, whereby the flow is only analyzed up to $x = 0.67$ due to the adjacent sponge zones and grid stretching (see section 2.6.2) at the outflow. As can be seen in figure 3.5(a), the flow in the selected streamwise domain extent is exposed to an APG at every instant. The constant wall-normal height of the DNS domain is set to $y_{s,top} = 0.05$, whereby the grid stretching is defined according to the description in section 2.4. The spanwise extent of the domain $\Delta z_0 = 0.0134$ is determined on the selection of the disturbance input, see below. A grid resolution of $5120 \times 200 \times 256 \approx 262.2M$ points is chosen along the airfoil contour, the wall-normal direction and the spanwise direction, respectively.

With this grid, the modes introduced at the disturbance strip (see below) are resolved with ≈ 105 points in x_s direction and 256 points in z direction. The boundary layer is resolved with > 40 points in y_s direction. Given the utilization of a high-order code, this is a very high resolution for the laminar flow region containing linear modes. However, this ensures that potential non-linear transient effects (such as the motion of the transition location) are also resolved when gusts are applied. Furthermore, this high resolution allows the generation of a sufficient number of higher harmonics to simulate the (weakly) non-linear transitional part of the flow. In general, the resolution of the transition process is validated with results from LST, see below. The flow downstream of the transition is sufficiently resolved with the inner units of $\Delta x_s^+ < 16$, $\Delta y_{s,w}^+ < 1.4$ and $\Delta z^+ < 8$ (see Poggie *et al.* (2015)) to describe the qualitative behavior of the turbulent boundary layer. The simulations are performed with a time step of $\Delta t_{sim} = 1.56 \cdot 10^{-6}$.

The boundaries at the inflow, free stream, and outflow are treated with characteristic unsteady boundary conditions including forcing terms, see section 2.6.2 & 2.6.3 for fundamentals. The corresponding sponge zones are applied at the inflow, outflow and the free stream, cf. distribution of $G(\boldsymbol{x})$ in figure 3.1. In streamwise direction, the sponge at the inflow ends at $x_{sp,in} = 0.148$ while the sponge at the outflow starts at $x_{sp,out} = 0.671$ with the maximum values of the gain distribution for equation (2.24) set to $G_{max,in} = 250$ and $G_{max,out} = 500$, respectively. In wall-normal direction, the sponge for the free-stream boundary starts at $y_{s,sp,top} = 0.031$ with $G_{max,top} = 250$. The wall boundary condition is chosen to be adiabatic, while periodic boundary conditions are used for the spanwise direction.

In this flow scenario, the so-called *fundamental resonance* is employed to simulate a controlled transition to turbulence. This secondary instability with its consequent breakdown scenario with aligned Λ-vortices was first observed by Klebanoff *et al.* (1962) and later applied in several investigations with DNS, see e.g. Rist & Fasel (1995). Thereby, three modes with the same frequency are introduced: a 2D TS-wave as the primary mode and a pair of oblique waves as secondary modes running in opposite spanwise direction z with lower initial amplitudes. These modes are denoted here as $(1, 0)$ and $(1, \pm 1)$, respectively, according to the definition in the double Fourier spectrum (h, k) described in section 2.6.4. Here, the disturbance strip is located at $x_{DS} = 0.15$ with a slit size of $\Delta x_{s,DS} = 2.5 \cdot 10^{-3}$. A summary of disturbance-input parameters for the definition of the disturbance function $v'_{s,DS}$ in equation (2.28) is given in table 3.1.

As can be seen in the stability diagram in figure 3.3(a), the primary mode (see "DS") with $\omega_{DS} = 201$ is chosen to be in the center of the range of amplified TS-waves. Selecting lower frequencies might be problematic, since branch I can potentially be temporarily further downstream than the disturbance strip during the oscillation. At higher frequencies, however, there is a risk of "dropping" behind branch II in case of strong gusts. For a clean spectral analysis of the laminar stretch of the flow

	$(1,0)$			$(1,\pm1)$			
Case	ω_{DS}	β_{DS}	A_v	$\omega_{DS,sec}$	$\beta_{DS,sec}$	$A_{v,sec}$	n_{crit}
$\bullet$	201	0	$5 \cdot 10^{-6}$	201	±450	$2.5 \cdot 10^{-7}$	≈ 10
$\bullet^{\uparrow}$	201	0	$1 \cdot 10^{-4}$	201	±450	$5 \cdot 10^{-6}$	≈ 7

Table 3.1: Overview of disturbance-input parameters for fundamental resonance for the default case as well the case with increased initial amplitudes $\bullet^{\uparrow}$.

field with FFT and CWT, the precise value of $\omega_{DS} = 201$ was chosen because it always corresponds to a multiple of the fundamental frequency of the simulation ω_{sim}, which depends on the gust frequency and number of simulated gusts. Figure 3.3(b) shows the amplification rate at x_{DS} versus the spanwise wavenumber $\beta_{DS,sec}$ with the position of the secondary mode $(1,1)$ with $\beta = 450$. Despite the wave-propagation angle of $\xi = \arctan(\beta_{DS,sec}/\alpha_r) \approx 41°$ typical for oblique modes for fundamental resonance, the amplification is still high. Due to the 2D base flow, the mode traveling in negative z direction for $\beta = -450$ exhibits the same stability properties. The spanwise wavenumber also determines the size of the domain in the z direction, which is identical to the fundamental wavelength $\lambda_{z,0} = 2\pi/\beta_{DS,sec} = 0.0134$. The characteristic eigenfunctions of a 2D TS-wave as well as an oblique 3D mode with the corresponding base-flow velocity profile are shown in figure 3.3(c). In the default case of this flow scenario, the initial amplitude of the primary mode is set to $A_v = 5 \cdot 10^{-6}$, with the amplitude of the superimposed secondary modes being one-tenth of this. As demonstrated in the following results, this actuation scenario leads to a transition point at $n_{crit} \approx 10$. Simulations with gusts at a higher n_{crit} are not possible due to the spatial limitation of the transient base flow in streamwise direction. However, three additional simulations are performed with an initial perturbation amplitude of $A_v^{\uparrow} = 1 \cdot 10^{-4}$ (20 times higher than the default case), corresponding to a transition location at $n_{crit} \approx 7$. These cases are indicated with $\bullet^{\uparrow}$ in the parameter space in figure 3.4.

At least one gust period and at least three characteristic time units (number of runs through domain with u_∞) are simulated for all cases before recording the time-dependent flow fields for analysis. One gust period is recorded for the cases with $\kappa = 1$, two periods for $\kappa = 2$ and 4, three periods for $\kappa = 3$ and four periods for $\kappa = 8$. The sampling rate for the recorded flow fields is chosen to continuously capture the period of the TS-waves at ω_{DS} with 8 time steps.

The results of the URANS simulations and the LST in the previous sections are discussed for $0 \leq x \leq 0.55$ while considering the oscillating natural branch I. In the DNS, however, the analyzed region $0.13 \leq x \leq 0.67$ is located further downstream. With the exception of the double-spectral analysis and flow visualizations,

only spanwise averaged flow fields are used for analysis. This leads to the neglect of the secondary (oblique) modes which have significantly lower amplitudes compared to the analyzed 2D TS-wave. For post-processing, the discrete TS-wave in the instantaneous flow field can be canceled out by applying a temporal running-average with respect to the period of the harmonic mode. This results to a flow field which contains the transient DNS solution of the gust impact without the TS-wave in the laminar stretch. The running-average of primitive variables and boundary-layer parameters based on the respective flow fields are denoted here with $\langle\phi\rangle_\omega$. Consequently, $\langle\phi\rangle_\omega$ should be equal to the transient base flow ϕ_{tbf} of equation (2.16) in the pristine laminar flow were linear theory applies. Furthermore, when subtracting the running-averaged flow field from the instantaneous flow field,

$$\phi'_\omega(t) = \phi(t) - \langle\phi\rangle_\omega(t)\,, \tag{3.8}$$

the transient modal disturbance—representing ϕ'_{mode} in equation (2.16)—can be calculated[7]. This method is used for visualization of the modes in this section. However, the continuous wavelet transform, see section 2.7, is employed for the transient spectral analysis of the primary mode $(1,0)$ with the amplitude n_{cwt}.

The deviation of the DNS solution from the laminar base flow acquired with (U)RANS simulations generally indicates non-linear effects including sections of turbulent boundary-layer flow. In unsteady flows, the transient base flow ϕ_{tbf} can therefore be subtracted from the instantaneous running-averaged DNS flow field $\langle\phi\rangle_\omega$, allowing a spatio-temporal characterization of these effects. Here, the deviation from the time-dependent laminar solution is denoted with

$$\Delta^l\langle\phi\rangle_\omega(x,t) = \langle\phi\rangle_\omega(x,t) - \phi_{tbf}(x,t)\,, \tag{3.9}$$

where ϕ represents a primitive variable or a boundary-layer parameter. Furthermore, a definition of the transient mean flow distortion (MFD) can be introduced based on the deviation of the tangential velocity profile $\Delta^l\langle u_s\rangle_\omega$. The MFD can be viewed as the action of the Reynolds stresses and represents $(0,0)$ in the double-spectral notation. For consistency, the transient MFD is formulated in this work with

$$\ln(MFD(x,t)) = \ln(\max_{y_s}\{\Delta^l\langle u_s\rangle_\omega(x,y_s,t)\}/A_u)\,, \tag{3.10}$$

which corresponds to the definition of the modal amplitude n_{cwt} of the primary mode $(1,0)$, see equation (2.34).

[7]Note that the URANS field ϕ_{tbf} is not suitable for subtraction here, since the actual mean flow in the DNS shows a slight drift which needs to be considered for filtering low-amplitude modes.

3.4.2 Steady-state baseline case

Before discussing the results of the transient cases with gusts, the setup for the steady-state reference case at AoA_{ref} is evaluated here. A snapshot of the three-dimensional instantaneous flow using the Q-criterion for vortex visualization (colored with streamwise velocity u) is shown in figure 3.15. As expected, a clear Λ-vortex including an emerging Ω-vortex at its tip can be seen at $x \approx 0.45$ where the breakdown to turbulence occurs. By employing the filtering method of equation (3.8), the characteristic eigenfunction of the 2D TS-wave can be clearly seen in $u'_{s,\omega}$. Downstream of the transition, however, $u'_{s,\omega}$ reflects spanwise 2D structures in the turbulent boundary layer at the frequency ω_{DS}. The isolines represent the pressure distribution of the steady-state 2D base flow from RANS.

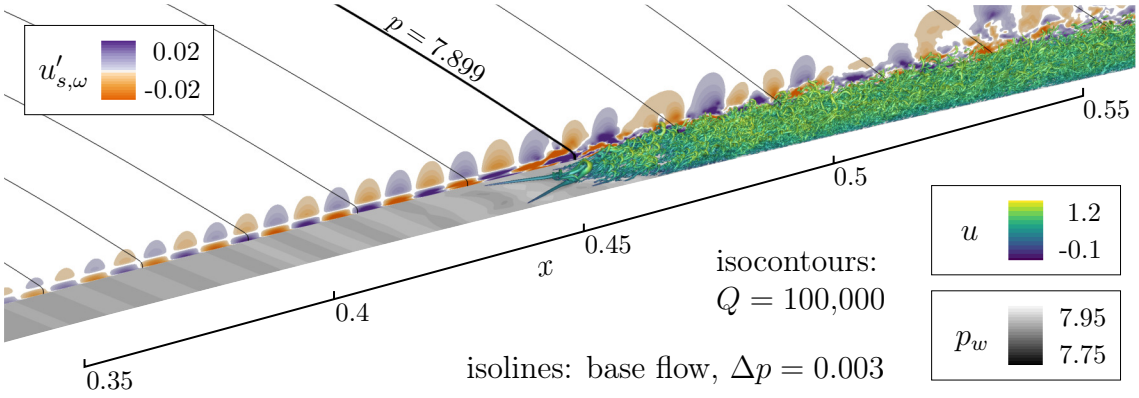

Figure 3.15: Visualization of DNS for steady-state reference case at AoA_{ref}.

Figure 3.16 depicts the downstream development of the introduced modes from double-spectral analysis. The FFT of the amplitudes of the primary mode $(1, 0)$ and the secondary modes $(1, \pm 1)$ show a generally good agreement with the LST. The occurrence of the secondary instability can be clearly recognized by the strong increase (hence deviation from the LST) of the modes $(1, \pm 1)$ starting at $x \approx 0.34$. At this location, the amplitude of the 2D mode with $\max_{y_s}\{u'_{s,(1,0)}\} > 0.01$ is reached, which is consistent with the threshold value for the onset of fundamental resonance, see Kachanov (1994). Accordingly, the (weakly) non-linear stage can be found between this point and the final breakdown to turbulence further downstream. The transition location can be identified by the peak at $x_{tr} \approx 0.46$ before the final non-linear saturation. The DNS of the steady-state case is validated with hot-wire measurements by Romblad (2023), see symbols in figure 3.16 representing the primary mode. Furthermore, the applicability of the continuous wavelet transform (see section 2.7) for this flow scenario can be verified here. The time-averaged result of the CWT shows an excellent agreement with the FFT for mode $(1, 0)$ in the laminar and non-linear transitional part of the flow. The slight discrepancy in the turbulent boundary layer is irrelevant for the investigations here. The introduced normaliza-

tion for the transient amplitude n_{cwt} is plotted on the right ordinate in figure 3.16. For its definition in equation (2.34), the initial amplitude of the modal disturbance must be determined, which is found here to be $A_u = 2.3 \cdot 10^{-6}$ and $A_u^{\uparrow} = 4.5 \cdot 10^{-5}$ for the default case and the case with an increased disturbance level, respectively. Accordingly, the effective initial amplitude has a ratio of $A_u/A_v \approx 0.5$ to the amplitude of the wall-normal blowing and suction. These values are also consistently used for the transient cases. Consequently, the mode $(1,0)$ starts with $n_{cwt} = 0$ at the location of the disturbance strip x_{DS}. Furthermore, a threshold value of $n_{crit} \approx 10$ can be determined for the above-mentioned transition location, see dashed black line. This value is found slightly downstream compared to the prediction by linear theory due to the attenuation in the (weakly) non-linear transitional region.

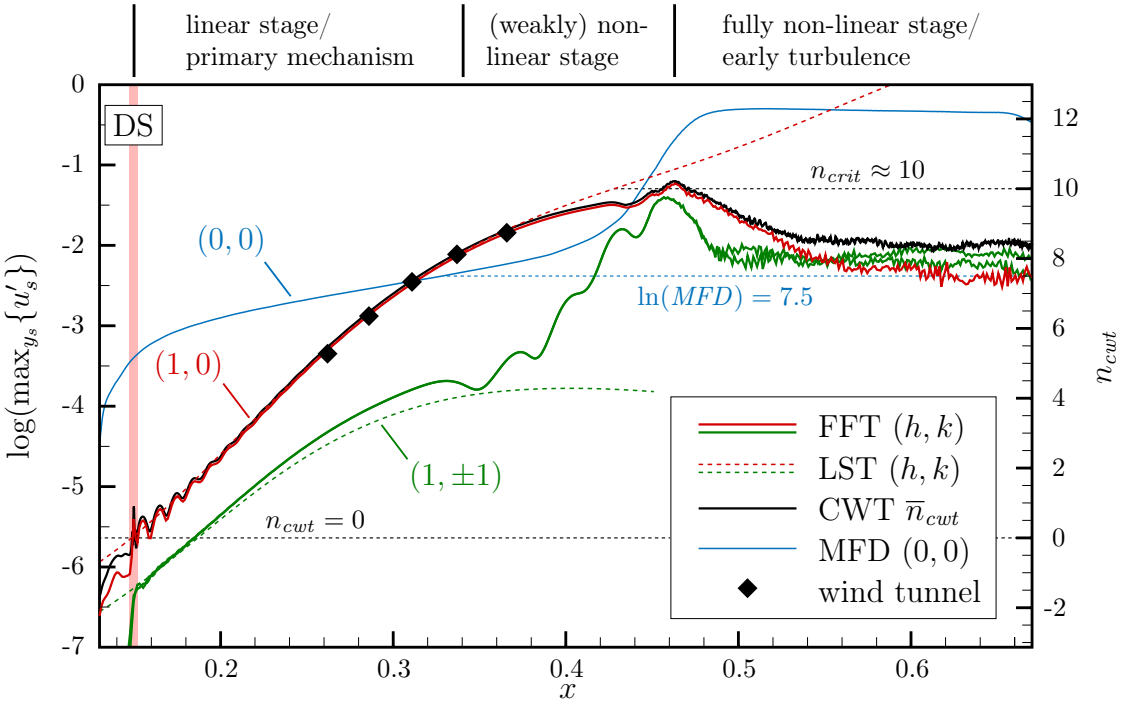

Figure 3.16: Downstream development of modal disturbance amplitude $u'_{s,(h,k)}$ (maximum over y_s) from FFT, CWT ($\omega_{DS} = 201$) and wind tunnel ($\omega \approx 203$) of steady-state reference case at AoA_{ref}.

The mean flow distortion $(0,0)$ in figure 3.16 is comparatively high over the entire flow, since the RANS solution is used as a reference here, see equation (3.10), and not a converged steady-state DNS base flow. This is consistent with the following transient solutions of the MFD for cases with gusts. The MFD shows a strong increase starting at $x \approx 0.4$ before reaching the plateau with $\ln(MFD) \approx 12$ in the turbulent flow. However, the value relating to the onset of the (weakly) non-linear stage is roughly $\ln(MFD) = 7.5$, see dashed blue line. This value is represented by the second contour line in the following x/t diagrams for the characterization of the transient MFD for cases with gusts.

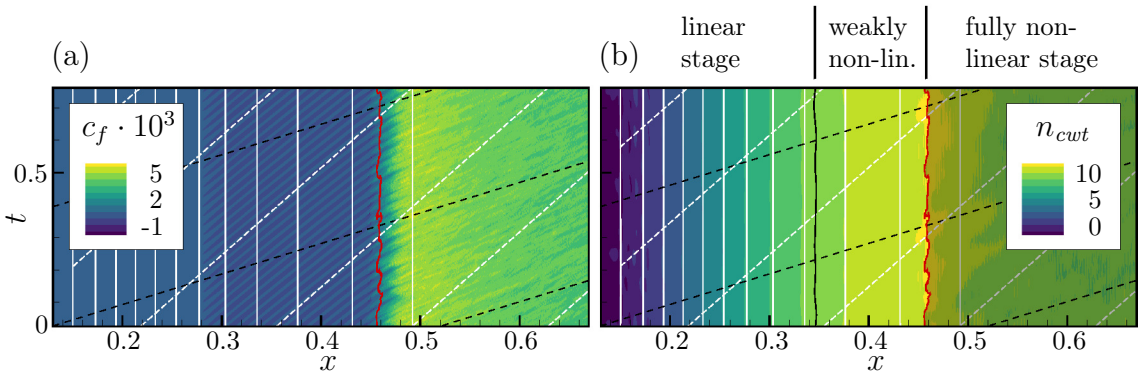

Figure 3.17: Spatio-temporal development of steady-state reference case at AoA_{ref} (a) Skin friction c_f (b) Amplitudes of continuous wavelet transform n_{cwt}; solid white lines: LST with $n \in \{0 \dots 11\}$ with $\Delta n = 1$ in downstream direction, —— $\Delta^l \langle c_f \rangle_\omega = 0.001$, —— $\max_{y_s}\{u'_{s,cwt}\} = 0.01$, dashed white lines: exemplary trajectories of TS-waves c_{TS}^{-1}, - - - - - free-stream velocity u_∞^{-1}.

The quality of the simulation in terms of the temporal steadiness/regularity of the transition as well as the methods for transient analysis can be evaluated for the steady-state case in x/t diagrams. Figure 3.17(a) shows the spatio-temporal evolution of the skin friction c_f with a continuous, non-intermittent transition front, indicated by a sudden jump at $x \approx 0.46$. In addition, clear traces of the TS-waves are imprinted in the laminar part of the flow, which are congruent with the theoretical average phase velocity of $c_{TS} = 0.35$ of the linear theory represented by dashed white lines. Traces in the turbulent flow are found to be close to u_∞, which is represented by the dashed black lines. As a tentative criterion for the instantaneous unsteady transition location, the threshold value $\Delta^l \langle c_f \rangle_\omega = 0.001$ (hence a value for the deviation of c_f of the running-averaged flow from the instantaneous laminar reference) is used in this work[8]. The skin friction c_f is a local quantity at the wall which—in contrast to e.g. H_{12}—is not an integral boundary-layer parameter. Furthermore, the quantity is directly related to the turbulent fluctuations in the flow, which is why it is assumed to be a suitable criterion for the unsteady transition here. In the steady-state case, this threshold exhibits a relatively constant position in the x/t diagram, see red line in figure 3.17.

Figure 3.17(b) shows the spatio-temporal behavior of the modal amplitudes n_{cwt} (colors) captured by the continuous wavelet transform. A remarkable good agreement with the linear theory (white lines) up to $n_{(cwt)} = 9$ can be observed. In addition, it is also clearly visible here that the amplification in the linear stage as well as the transition front behave approximately stationary with no significant fluctuations to be seen. Since no temporal boundary effects are visible here, the time-periodic

[8]Note that a phase/periodic-ensemble average is not applicable here due to the limited number of simulated gust periods.

treatment of the DNS results as introduced in section 2.7 can be considered to be valid in this scenario with attached flow. The above-mentioned threshold value for the onset of non-linear effects $\max_{y_s}\{u'_{s,cwt}\} = 0.01$ equals $n_{cwt} \approx 8.35$ and is represented by the black line. The criterion for the final transition $\Delta^l\langle c_f\rangle_\omega = 0.001$ is in perfect agreement with the peak around $n_{cwt} \approx 10$ at $x_{tr} \approx 0.46$. Consequently, these two thresholds can be used to separate the linear, the (weakly) non-linear, and the fully non-linear stage in space and time. The latter region is shaded in the CWT results and represents the turbulent region of the flow.

3.4.3 Low degrees of unsteadiness

In this section, the results of two cases with relatively low degrees of unsteadiness are selected for discussion. The unsteady behavior of the transition can be mostly attributed to linear effects here.

Case: $\kappa = 1$, $v'_{gust} = 0.01$

Figure 3.18 gives the main aspects of the results for the case with $\kappa = 1$ and $v'_{gust} = 0.01$, which corresponds to the DNS at the lowest degree of unsteadiness with $\kappa^{tr} = 0.15$. The instantaneous skin friction in figure 3.18(a) shows that the transition location oscillates with the gust frequency in upstream and downstream direction. The transition front shows a very orderly and continuous behavior over the whole period, which generally resembles the transition in the steady-state case.

The modal amplitude n_{cwt} from the CWT in figure 3.18(b) shows a remarkably good agreement with the time-dependent prediction of the LST for $n \leq 8$ in terms of levels and phase[9]. First of all, it can be observed that the "receptivity" of the disturbance strip is completely steady over the oscillation period, since the value $n_{cwt} = 0$ is practically steady and the following levels do not show any deviation from the LST. The level $n_{cwt} = 9$ behind the threshold for the (weakly) non-linear stage shows a minor deviation at the downstream extreme. The phase of the upstream extreme exhibits a good agreement with the LST, while the peak with $n_{cwt} > 10$ is more pronounced compared to the steady-state case. Moreover, it can be seen that the spatial extent of the (weakly) non-linear stage remains almost constant during the gust period while moving upstream and downstream. As a consequence, the range Δx_{tr} of the oscillation of the transition (red line) is smaller compared to $n = 10$ of the unsteady linear stability analysis. This is not surprising even in a purely quasi-steady consideration, since the secondary mechanism of fundamental resonance is not accounted for by the (primary) LST. In general, the transition prediction downstream the threshold $\max_{y_s}\{u'_{s,cwt}\} = 0.01$ must be viewed with cau-

[9]Note that the phase between URANS simulations, DNS and LST is always consistent and is not retroactively adjusted.

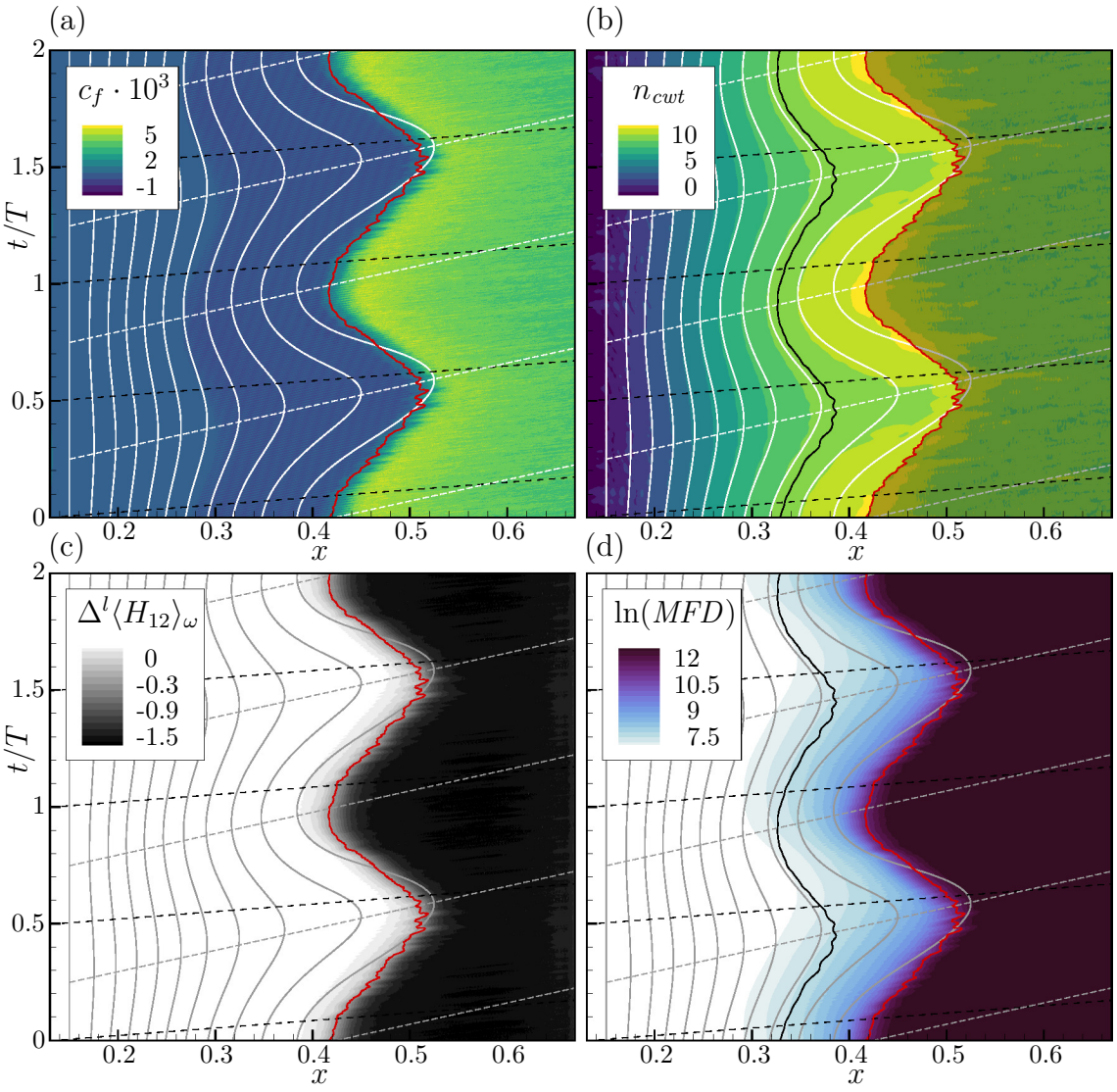

Figure 3.18: Spatio-temporal development for $\kappa = 1$ at $v'_{gust} = 0.01$ (a) Skin friction c_f (b) Amplitudes of continuous wavelet transform n_{cwt} (c) Shape-factor deviation $\Delta^l\langle H_{12}\rangle_\omega$ (d) Mean flow distortion ln(*MFD*); solid white/gray lines: LST with $n \in \{0 \dots 10\}$ with $\Delta n = 1$ in downstream direction, —— $\Delta^l\langle c_f\rangle_\omega = 0.001$, —— $\max_{y_s}\{u'_{s,cwt}\} = 0.01$, dashed white/gray lines: exemplary trajectories of TS-waves c_{TS}^{-1}, - - - - - free-stream velocity u_∞^{-1}.

tion, since transient, non-linear effects may occur here, see below. The transition location shows only a slight asymmetric behavior in time, with the upstream and downstream velocities being $\dot{x}_{tr,u} = -0.098$ and $\dot{x}_{tr,d} = 0.075$, respectively. Therefore, this case is qualitatively comparable with *Case1* of Studer *et al.* (2006) or the measurements of Romblad (2023) for $\kappa < 0.5$.

The time-dependent shape-factor deviation $\Delta^l\langle H_{12}\rangle_\omega$ given in figure 3.18(c) can be regarded as the imprint of the turbulent flow into the theoretical unsteady laminar

flow. The location of the relatively acute jump from ≈ 0 to ≈ -1.5 of this integral value is in perfect agreement with the location of the threshold value $\Delta^l\langle c_f\rangle_\omega = 0.001$ for the transition in the x/t diagram. This behavior contrasts the strongly unsteady cases shown later and implies a continuous creative-transition mode.

Finally, the transient behavior of the mean flow distortion can be seen in figure 3.18(d) with values for $\ln(MFD) < 7.25$ blanked out. In contrast to $\Delta^l\langle H_{12}\rangle_\omega$, a clear increase of $\ln(MFD)$ can be seen well ahead of the transition front continuously over the oscillation. Since the MFD is defined analogously to the exponentially growing modes (h, k) and is plotted in a logarithmic scale, the sensitivity for detecting a change in the base flow is significantly higher here. The growth of the MFD is mainly related to the primary 2D mode in the (weakly) non-linear region. First of all, a phase lag of the MFD with respect to the onset of that region (black line) can be observed. The MFD shows a hysteresis or asymmetric behavior over time with the contour levels moving slower in downstream direction compared to the upstream direction. Physically, this can be interpreted as a temporal "recovery" of the base flow back to the fully linear state. Comparable to the viscous response of the base flow (see section 3.2.2), this delay has its own time scale which is independent from the gust period. Literature on the transient behavior of the MFD is not known. In Wassermann & Kloker (2002), however, a delay of the MFD can be observed.

A closer look at the instantaneous skin friction in figure 3.18(a) reveals that the downstream-moving transition front shows a somewhat "trembling" behavior, while the upstream-moving front seems to be even more determinate than the transition in the steady-state case in figure 3.17(a). In general, the MFD-delay can be suspected to be responsible for this behavior, as it is also identified as the driving force for the occurrence of the convective-transition mode at the downstream-moving front, see below. However, a more self-evident explanation in which the Doppler effect is used as an analogy is suggested here: The frequency of arriving crests of TS-modes is generally higher at the upstream-moving front ($\omega_{front} > \omega_{DS}$) and lower at the downstream-moving front ($\omega_{front} < \omega_{DS}$). In other words, more discrete crests of TS-waves arrive at the upstream transition front than at the downstream transition front for the same time span, leading to a more or less determinate breakdown to turbulence, respectively. With the formulation of the Doppler effect with a stationary source (disturbance strip) and an unsteady receiver (transition front), a new dimensionless quantity for the temporal density of transitional modes

$$D_{tr} = \frac{\omega_{front}}{\omega_{DS}} = 1 - \frac{\dot{x}_{tr}}{c_{TS}}\,, \tag{3.11}$$

can be introduced[10]. Therefore, this number always gives the "transitional density"

[10]For natural initial disturbances, the relative motion of branch I needs to be included in $\dot{x}_{tr}$. For the consideration of a broad spectrum of disturbances, D_{tr} is independent of ω_{DS} in case a constant phase speed c_{TS} for all frequencies is assumed.

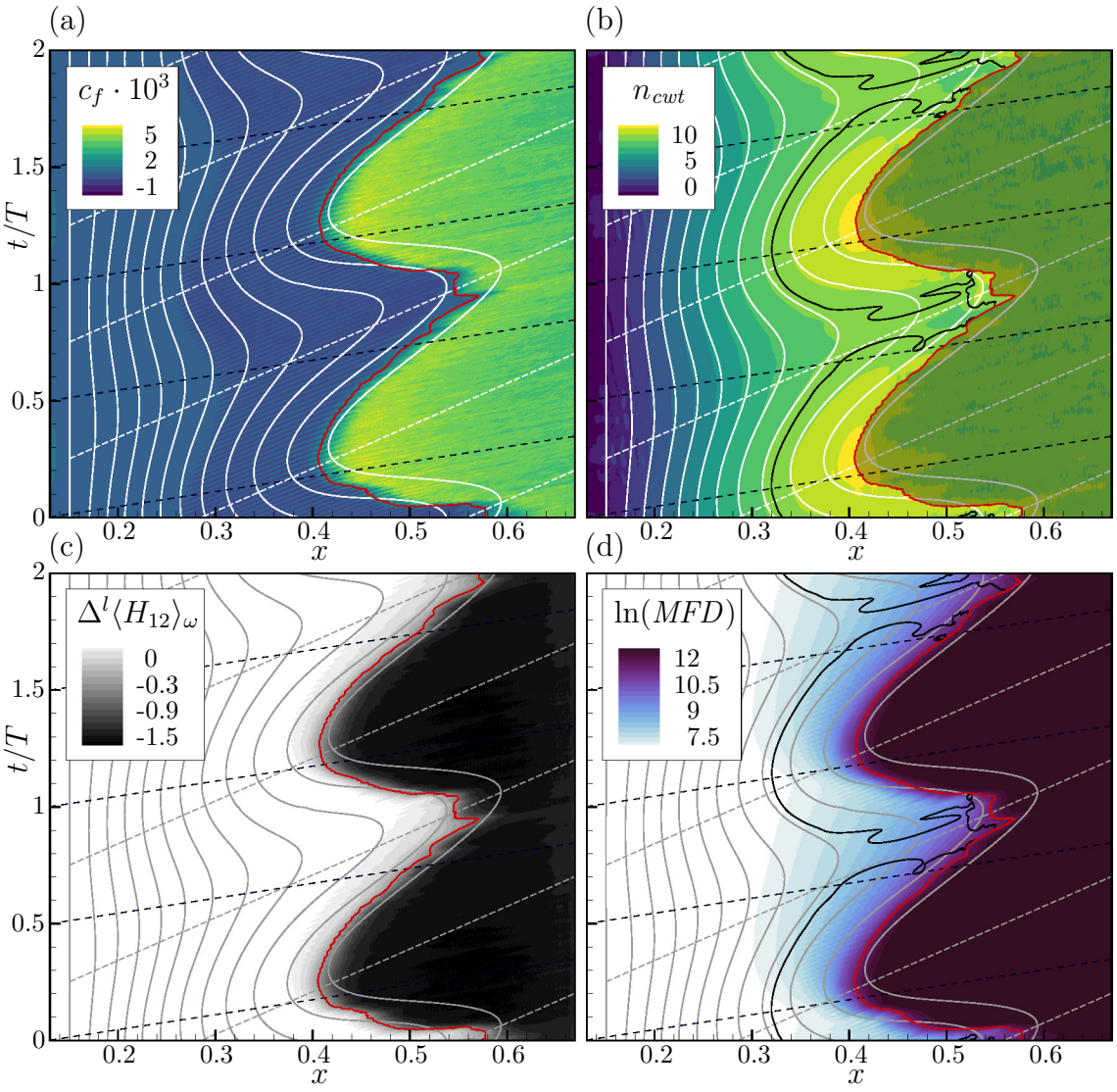

Figure 3.19: Spatio-temporal development for $\kappa = 2$ at $v'_{gust} = 0.02$ (a) Skin friction c_f (b) Amplitudes of continuous wavelet transform n_{cwt} (c) Shape-factor deviation $\Delta^l\langle H_{12}\rangle_\omega$ (d) Mean flow distortion ln(*MFD*); solid white/gray lines: LST with $n \in \{0\,...\,11\}$ with $\Delta n = 1$ in downstream direction, —— $\Delta^l\langle c_f\rangle_\omega = 0.001$, —— $\max_{y_s}\{u'_{s,cwt}\} = 0.01$, dashed white/gray lines: exemplary trajectories of TS-waves c_{TS}^{-1}, ----- free-stream velocity u_∞^{-1}.

in relation to the steady-state reference with $D_{tr,s} = 1$. It is important to emphasize that the frequency ω_{front} is only experienced at the traveling transition front—the modal frequency ω_{DS} remains the same throughout the flow. In general, this inherent effect can also occur for a quasi-steady/symmetric temporal behavior of n_{crit} for the transition in case $c_{TS} \not\gg |\dot{x}_{tr,qs}|$ applies. However, with the asymmetric temporal behavior of the transition location observed in this work, this effect is intensified for the upstream-moving front and attenuated for the downstream-moving front.

With the mentioned transition-front velocities of the case above, the values $D_{tr,u} = 1.28$ and $D_{tr,d} = 0.79$ are obtained for the upstream and downstream direction, respectively. Consequently, the upstream-moving front has a higher transitional density by a factor of ≈ 1.62 compared to the downstream-moving front, which is already a considerable strong deviation given the generally low degree of unsteadiness of this case. In addition, it can be argued that more kinetic energy per time can be expected when integrating along the upstream-moving transition compared to integrating along the downstream-moving transition. Therefore—besides the observations for the instantaneous c_f—the slightly more pronounced peak of n_{cwt} at the upstream-moving front may also be attributed to the Doppler-like effect.

Case: $\kappa = 2$**,** $v'_{gust} = 0.02$

The results for the case with $\kappa = 2$ at $v'_{gust} = 0.02$ which corresponds to an unsteadiness parameter of $\kappa^{tr} = 0.42$ are depicted in figure 3.19. The transition location exhibits a very strong asymmetric behavior in time and approximately coincides with $n = 10$ of the LST. The velocities of the transition front are $\dot{x}_{tr,u} = -0.598$ and $\dot{x}_{tr,d} = 0.147$ with the transitional densities of $D_{tr,u} = 2.7$ and $D_{tr,d} = 0.58$, respectively. As in the first case, a full-scale convective-transition mode at the oscillation frequency is not visible. The case qualitatively resembles the measurements of Romblad (2023) for $\kappa > 1$.

Again, the CWT in figure 3.19(b) shows a remarkably good agreement with the unsteady transition prediction for $n_{(cwt)} \leq 8$ representing the fully-linear stage of the pristine laminar flow. In addition, the phase at the spatial minimum agrees well for $n_{(cwt)} = 9$. However, in the proximity of the spatial maximum extreme, a sudden drop in amplitude n_{cwt} is evident at $x = 0.5$ and $t/T = 0.85$, which is followed by a short interruption of the transition front downstream. A preceding "plunge" of the amplitude can be already seen upstream/earlier at $x = 0.4$ and $t/T = 0.8$ indicated by the black line which represents $n_{cwt} \approx 8.35$. This divergence from the transition prediction based on the pristine laminar (but unsteady) flow can be explained with the impact of the MFD-delay, which is depicted in figure 3.19(d). In comparison to the first case above, the higher gust amplitude v'_{gust} increases the spatial extent of the lagging MFD. In addition, the doubled gust frequency κ shortens the time (relative to the gust period T) in which the base flow can recover to the original, undistorted laminar flow. Since the MFD generally represents a change in the mean velocity profiles, it also implies an alteration of the stability properties and hence the amplification rates α_i. For example, a study by Dörr & Kloker (2018) with a scenario at steady-state conditions showed that the amplification of TS-waves can be suppressed by manipulating the mean flow using plasma actuators. In the case discussed here, the transient MFD appears to momentarily attenuate the amplification rates of the incoming modes in the "wake" of the downstream-moving

transition front/non-linear stage. Therefore, the modal amplitude n_{cwt} can decrease along the wave trajectories c_{TS} which may have consequences for the subsequent transition front. However, in this case, this weakening is not yet sufficient for the occurrence of a full, self-perpetuating convective-transition mode.

3.4.4 Comparison to wind-tunnel measurements

In this section, one simulated case is directly compared to the corresponding wind-tunnel measurements of Romblad (2023). Furthermore, additional experimental results of this study will be briefly discussed in order to support the reasoning of the Doppler analogy suggested above.

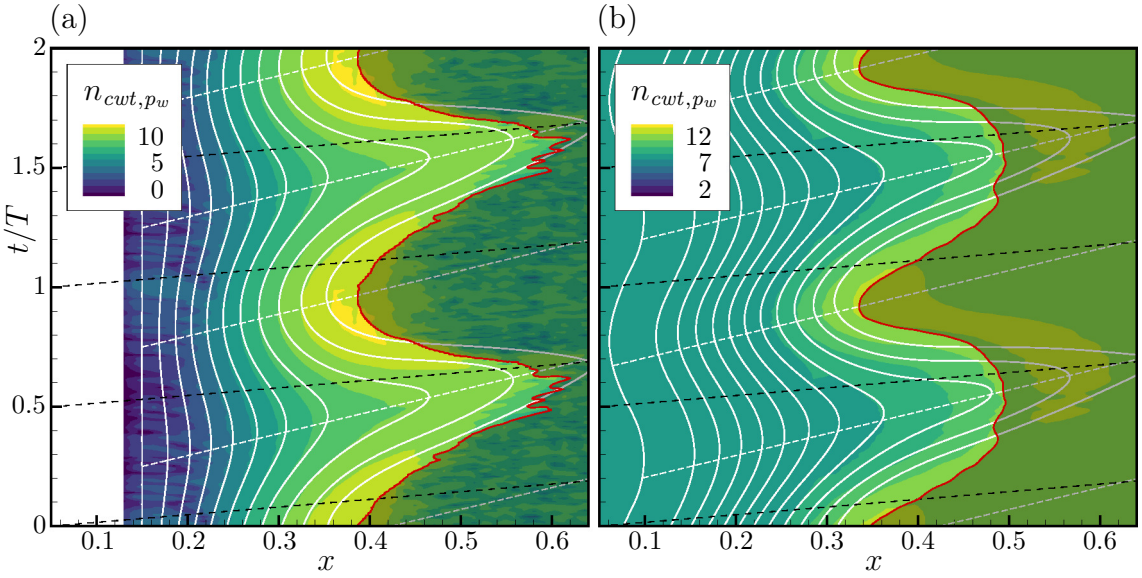

Figure 3.20: Spatio-temporal development of wall-pressure amplitudes n_{cwt,p_w} for $\kappa = 1$ at $v'_{gust} = 0.02$ (a) DNS, solid white lines: LST with $n \in \{0 \dots 10\}$ with $\Delta n = 1$ in downstream direction, —— $\Delta^l \langle c_f \rangle_\omega = 0.001$ (b) Wind tunnel, solid white lines: LST with $n \in \{0 \dots 11\}$ with $\Delta n = 1$ in downstream direction, —— M-TERA transition criterion; dashed white lines: exemplary trajectories of TS-waves c_{TS}^{-1}, - - - - - free-stream velocity u_∞^{-1}.

Case: $\kappa = 1$, $v'_{gust} = 0.02$

A comparison of DNS results with wind-tunnel measurements for the case $\kappa = 1$ at $v'_{gust} = 0.02$ with the unsteadiness quantity $\kappa^{tr} = 0.32$ can be found in figure 3.20. Since the physical effects resemble qualitatively the last case discussed, only aspects regarding the validation with the experiments are reviewed here. For detailed plots of the numerical results, see figure C.1 in appendix C. The experimental results correspond to the campaign in Romblad (2023) with $N_{crit} = 12$ and have already been compared with the transient envelope N from the unsteady linear stability

analysis in figure 3.10(b). Since the measurements are conducted with pressure taps, the formulation of the modal amplitude n_{cwt,p_w} of equation (2.34) is based on the wall pressure with the initial amplitudes $A_p = 7 \cdot 10^{-7}$ and $8 \cdot 10^{-8}$ for the DNS and the wind tunnel, respectively.

The DNS results in figure 3.20(a) show a good agreement with the linear theory, especially around the spatial minimum of the transition. At lower levels, however, the modal growth is not detected in the pressure-fluctuation p'_w in contrast to the velocity disturbance u'_s in figure C.1(b). Figure 3.20(b) shows the spatio-temporal amplitude development from CWT of the wind-tunnel measurements for $\omega = 201$. This frequency corresponds to the discrete mode introduced in the DNS which allows a direct comparison of the linear stage. Four levels $n_{cwt,p_w} \in \{8, 9, 10, 11\}$ are available which relate to the unsteady transition prediction. The smoothness of the experimental results compared to the DNS results is due to the periodic ensemble mean. Two conceptual differences need to be considered when comparing both results. First, the LST shows that the spatial oscillation of n_{crit} is slightly increased in the wind-tunnel studies due to the naturally oscillating branch I compared to the DNS with a fixed primary instability point. This explains the difference in shapes of the spatial minimum of n_{crit}, which is pointy in the measurements and rather blunt in the simulations. Nevertheless, the LST can serve as a bridge for validation between the numerical and experimental results here. Second, a broadband spectrum of TS-waves is present in the wind tunnel, which is why the transition can also be triggered by other frequencies. Therefore, in order to narrow down the valid area of exponential amplification according to the linear theory for $\omega = 201$, the turbulent flow (downstream of the M-TERA transition criterion) is grayed out in the result of the CWT. The spatio-temporal evolution of the first contour line with $n_{cwt,p_w} = 8$ shows a remarkable good agreement with the linear theory. This explicitly validates the assumption of a "mobile" branch I at unsteady conditions as well as a quasi-steady receptivity behavior. The spatial minimum of the oscillating transition exhibits a good qualitative agreement. However, the spatial maximum of the transition location is caused by TS-waves at different modal frequencies reaching critical amplitudes earlier, cf. envelope N in figure 3.10(b).

In addition, it can be seen in figure 3.20(b) that the amplitude maximum in the non-linear region is considerably higher for the upstream-moving transition front than for the downstream-moving transition front. This behavior is even more pronounced in the transient RMS-values of the wall pressure (running window) presented in Romblad (2023). An intuitive explanation for this observation is the transitional density from the Doppler analogy discussed in section 3.4.3. This effect could be even more dramatic here, since the wide spectral range of disturbances as present in the wind tunnel might lead to increased non-linear interactions. With the transition-front velocities $\dot{x}_{tr,u} = -0.340$, $\dot{x}_{tr,d} = 0.152$ and the consideration of the motion of branch I, the transitional densities are $D_{tr,u} = 1.9$ and $D_{tr,d} = 0.66$. Con-

sequently, a ratio of ≈ 2.9 for the arrival of TS-wave crests between the upstream and downstream-moving transition is present in the experimental setup.

Further cases of experimental study

To support the argumentation for the origin of this phenomenon, the measurement results of Romblad (2023) are briefly assessed here with theoretical considerations. In this work, the more pronounced RMS-peaks at the upstream-moving transition front compared to the downstream-moving transition front can be even observed at extremely low gust frequencies. This is surprising at first, since the transition location is explained for all cases with the (unsteady) primary mechanism of linear theory without the occurrence of a (non-linear) convective-transition mode. One explanation would be an unknown effect of the secondary mechanism at unsteady conditions. However, since the (weakly) non-linear stage approximately keeps the same length for the case $\kappa = 1$ at $v'_{gust} = 0.01$ (cf. figure 3.18), a quasi-steady behavior is assumed here for low degrees of unsteady conditions. The probability of the Doppler analogy to be responsible for the pronounced upstream RMS-peak is demonstrated with the two cases of Romblad (2023) corresponding to the lowest frequencies κ. For $\kappa = 0.06$, a perfectly symmetric temporal movement of the transition with $|\dot{x}_{tr,u/d}| = 0.01$ can be observed. The transitional densities $D_{tr,u} = 1.03$ and $D_{tr,d} = 0.97$ results in a deviation of only ≈ 1.06, which corresponds to the negligible difference in upstream and downstream RMS-peaks. For $\kappa = 0.3$, the very light asymmetric motion over time with $\dot{x}_{tr,u} = -0.1$ and $\dot{x}_{tr,d} = 0.07$ is still barely visible. Due to the higher *absolute* velocity of the transition fronts, however, the transitional densities $D_{tr,u} = 1.29$ and $D_{tr,d} = 0.8$ result in a considerably high deviation of ≈ 1.61 for arriving TS-wave crests. At the upstream traveling transition front, more non-linear interactions in a very dense spatial and temporal domain are expected. Therefore, this concept serves a plausible explanation for the clearly pronounced RMS-peak which is observable in this case. Moreover, it can be assumed that the fully non-linear stage also features a transient behavior—e.g., temporarily increased entrainment—which may also have a (reinforcing) impact.

3.4.5 High degrees of unsteadiness with convective transition

In this section, the results of two cases with a high degree of unsteadiness, in which the convective-transition mode appears, have been selected for discussion.

Case: $\kappa = 4$, $v'_{gust} = 0.02$

For case $\kappa = 4$ at $v'_{gust} = 0.02$ ($\kappa^{tr} = 0.64$) depicted in figure 3.21, a clear convective-transition mode is evident. The instantaneous skin friction c_f in figure 3.21(a) indicates a phase of natural transition that periodically coincides with the upstream

extreme value of $n_{crit} \approx 10$ from linear theory. During downstream motion, however, the creative transition appears to "stall" and the laminar-turbulent interface no longer matches with the LST. The subsequent downstream movement of the turbulent flow is referred to as the convective-transition phase. The trailing-edge velocity with $\dot{x}_{t,te} = 0.4$ is faster than the average phase speed $c_{TS} = 0.35$ of the TS-modes. In addition, the spatio-temporal evolution of the turbulent part of the flow exhibits an overturned pattern with a spatially enclosed spot for $0.7 \leq t/T \leq 0.9$. However, this observation is explained with non-linear effects and is therefore different from the overturned n-factor scenario discussed in sections 3.3.2 to 3.3.4. Responsible for this behavior is the so-called calmed region, which arises as a consequence of the convective transition in the wake of the downstream-traveling turbulent flow ($\dot{x}_{t,te}$). It is known that this area has velocity profiles with extremely stable properties (hence high positive α_i) regarding disturbances, see e.g. Gostelow *et al.* (1997). This can already be observed in the instantaneous skin friction where the traces of the incoming TS-waves disappear when they arrive in the wake of the turbulent spot. The calmed region persists for a considerable amount of time and is only interrupted by the turbulent flow which is spawned by the next creative-transition phase. Consequently, the resulting turbulent-laminar interface with a leading-edge velocity of $\dot{x}_{t,le} = 0.95$ can be also attributed to the convective-transition phase. The threshold value $\Delta^l\langle c_f\rangle_\omega = 0.001$ neatly separates the (fully non-linear) turbulent flow with increased c_f from the laminar flow and therefore proofs to be also suitable as a tentative "transition" criterion involving alternating creative/convective phases.

The calmed region as a result of the convective transition is also reflected in the unsteady shape-factor deviation $\Delta^l\langle H_{12}\rangle_\omega$ in figure 3.21(c). While an uninterrupted sudden drop of $\Delta^l\langle H_{12}\rangle_\omega$ coincides with the criterion for the oscillating transition (red line) in the cases under low degrees of unsteadiness presented in section 3.4.3, a smooth progression can be seen here in the wake behind the downstream convecting turbulent flow. The physics behind this lagging behavior of the integral quantity H_{12} can be explained in short by the following: Turbulent fluctuations migrate downstream (at about $\dot{x} \approx 0.5$) without new disturbances being supplied upstream due to the absent creative transition. This leads to the collapse of the characteristic velocity profile of the turbulent boundary layer, which is immediately reflected in the decrease of the skin friction c_f. However, the entire velocity distribution in wall-normal direction still needs to undergo a relaxation back to the (unsteady) laminar solution. Like the viscous base-flow response to the gust or the MFD-delay described above, this happens at its own pace, which is evident in the gradual recovery of the shape factor in the x/t diagram. The short-time non-turbulent flow of the calmed region is generally characterized by a relatively full profile at low boundary-layer thickness, see also Wygnanski *et al.* (1976); Gostelow *et al.* (1997).

The CWT in figure 3.21(b) shows the transient modal behavior including its non-linear implications and provides a profound analysis with respect to cause-and-effect

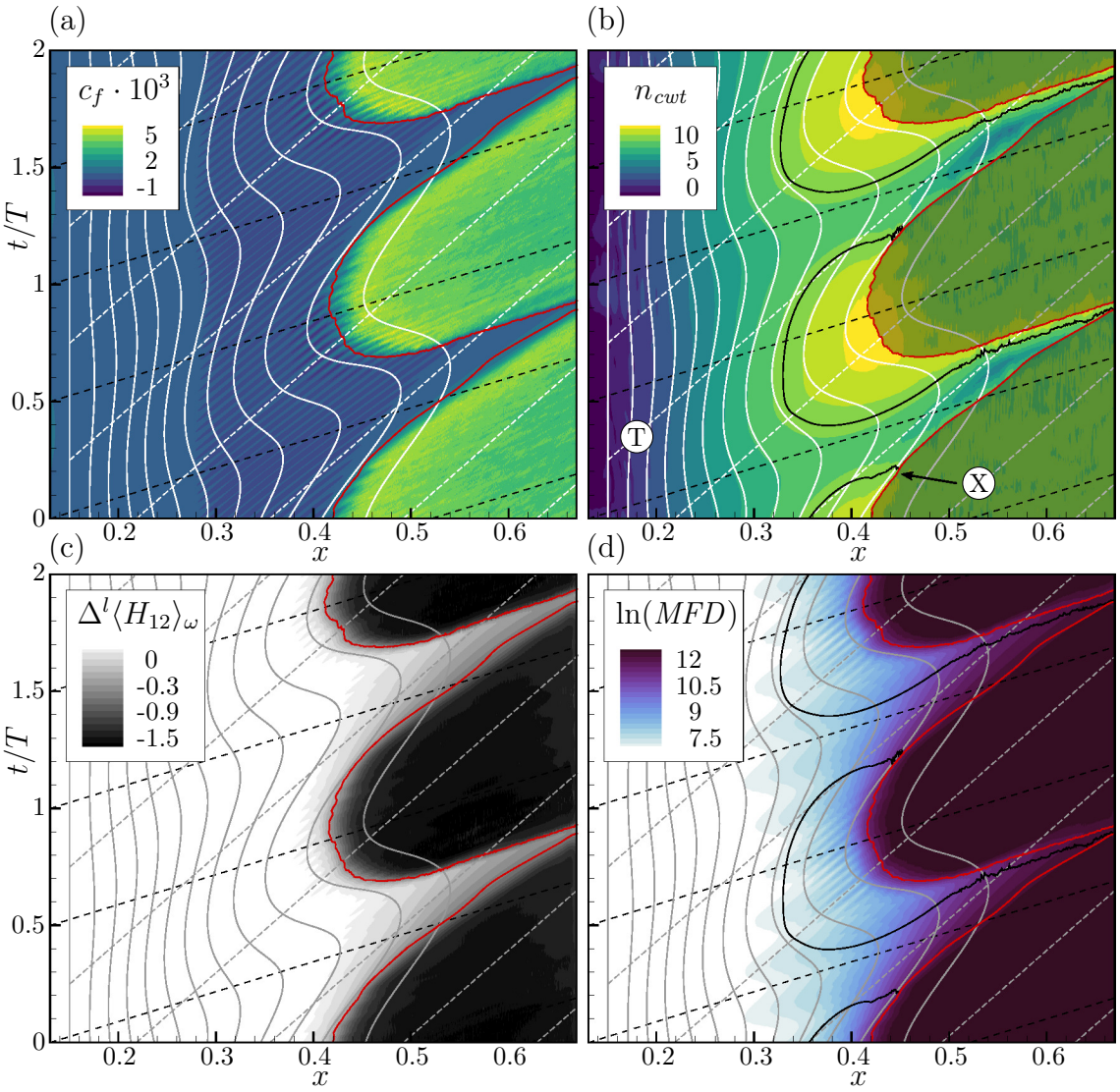

Figure 3.21: Spatio-temporal development for $\kappa = 4$ at $v'_{gust} = 0.02$ (a) Skin friction c_f (b) Amplitudes of continuous wavelet transform n_{cwt} (c) Shape-factor deviation $\Delta^l\langle H_{12}\rangle_\omega$ (d) Mean flow distortion ln(*MFD*); solid white/gray lines: LST with $n \in \{0 \dots 11\}$ with $\Delta n = 1$ in downstream direction, —— $\Delta^l\langle c_f\rangle_\omega = 0.001$, —— $\max_{y_s}\{u'_{s,cwt}\} = 0.01$, dashed white/gray lines: exemplary trajectories of TS-waves c_{TS}^{-1}, - - - - - free-stream velocity u_∞^{-1}.

of the convective-transition mode. The perfect spatio-temporal agreement between DNS and LST for $n_{(cwt)} \leq 7$ indicates the pristine (unsteady) laminar flow which is unaffected by non-linear effects. It should be noted here that the performance of the quasi-steady stability analysis with the trajectory-following method is very impressive given the already high frequency with $\omega_{DS}/\omega_{gust} = 25$. For $n_{(cwt)} = 8$, 9 and 10, a good agreement is only visible for the spatial minimum of the oscillating prediction by linear theory. This area refers only to the (weakly) non-linear stage which

evidently precedes the final creative transition. In contrast to the cases discussed above, this stage is clearly confined in the x/t diagram with $\max_{y_s}\{u'_{s,cwt}\} = 0.01$ (black line) and is periodically interrupted by the phase of the convective transition. This spatio-temporal domain with high-amplitude TS-waves resembles the identified "wave packet" by Obremski & Fejer (1967) before the creative-transition mode.

The calmed region in the wake of the turbulent flow is clearly reflected by the amplitudes from CWT with values as low as $n_{cwt} \approx 3.5$. The "origin" of this region can be approximately identified at the point Ⓧ where the (weakly) non-linear stage vanishes and the non-transitional convection begins. Based on this point, the trailing-edge velocity $\dot{x}_{cr,te} = 0.2$ of the calmed region can be approximated, which corresponds to $\Delta^l\langle H_{12}\rangle_\omega = -0.2$ (third contour line). The leading edge of the turbulent flow features a peak which might be a spectral remnant of the creative transition at ω_{DS}. This suggestion is supported by the fact that the limit of the (weakly) non-linear region $\max_{y_s}\{u'_{s,cwt}\} = 0.01$ is pushed forward at a constant distance $\Delta x \approx 0.028$ from the turbulent region.

The most striking observation in figure 3.21(b) is the attenuation of the amplitudes $n_{cwt} \geq 8$ during $0.1 \leq t/T \leq 0.4$ compared to the steadily increasing n-factors of the original laminar flow. Again, the increased stability ($\alpha_i \uparrow$) indicates a change of the transient base flow due to non-linear effects. However, unlike the calmed region and the observed slight amplitude-dips in the cases discussed above, this behavior is found further upstream and not just in the wake of the turbulent flow. Here, the (weakly) non-linear stage of the creative-transition phase is held responsible for this behavior since it spatially coincides ($0.33 \leq x \leq 0.45$) and periodically precedes the affected region. This can be confirmed with the MFD in figure 3.21(d), where the levels remain almost constant spatially at $x \approx 0.38$. The MFD does not appear to be stronger than in the cases at low degrees of unsteadiness. However, due to the higher frequency $\kappa = 4$, the mean flow has "less time" to recover with respect to the period T which causes an early attenuation of incoming modes.

The spatio-temporal evolution of the MFD in the non-turbulent flow is very continuous and does not display any evidence of a "trailing edge" of the calmed region. Both, the MFD (caused by the (weakly) non-linear stage with high-amplitude TS-waves) as well as the calmed region (caused by the fully non-linear turbulent flow) can be regarded as phases where the flow recovers from the preceding action of the Reynolds stresses. Consequently, the early MFD and the calmed region can be considered as related transient non-linear effects of the unsteady transitional flow.

The observations regarding the MFD are consistent with results of Gostelow *et al.* (1997). In this study, an "early calmed region" was found behind a wave packet in absence of a turbulent flow using wall-normal vorticity profiles for detection. The authors therefore suggested that the nature of the calmed region is connected more to the stability properties of the velocity profile than to the turbulent flow. In this study, a periodic wake-induced transition was investigated at a low Reynolds

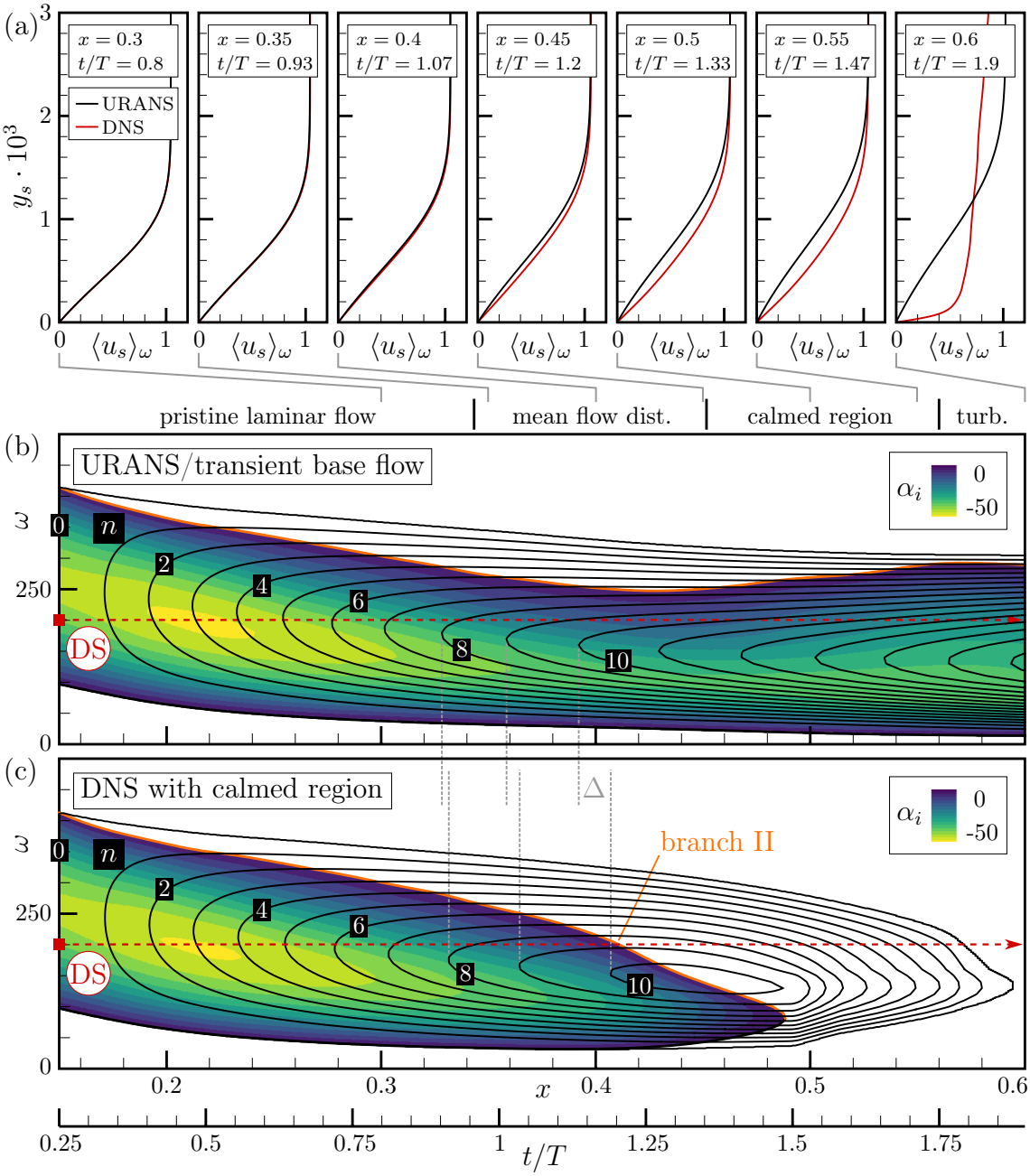

Figure 3.22: Analysis for $\kappa = 4$ at $v'_{gust} = 0.02$ along trajectory Ⓣ in figure 3.21(b); DNS flow: running and spanwise average (a) Velocity profiles (b) Stability diagram of transient base flow (c) Stability diagram of DNS flow field.

number where TS-waves are not relevant. The attenuation of modes due to the MFD-delay/early calmed region has therefore a minor impact on the qualitative behavior of the unsteady flow.

However, in the present flow scenario, TS-waves are continuously introduced with

the disturbance strip which corresponds to the unsteady natural transition investigated by Obremski & Fejer (1967), Studer *et al.* (2006) and Romblad (2023). Here, the delay of the MFD can be identified as the actual cause of the stalling of the creative-transition mode and the occurrence of the convective-transition mode. The crucial point for this transient mechanism can be located at the temporal end of the (weakly) non-linear stage, where the downstream movement of the transition begins. TS-waves (e.g. with the trajectory Ⓣ in figure 3.21(b)) already exhibit a decreasing amplitude before reaching the calmed region. Accordingly, this can be referred to as a *transient branch II*, which is momentarily generated by the lagging MFD. In addition, the decreasing density of TS-wave crests is expected to promote the final stalling of the creative-transition at point Ⓧ. The transitional densities at the creative phase can be approximated with $D_{tr,u} = 3.41$ and $D_{tr,d} = 0.69$. Since the calmed region (with a leading-edge velocity of $\dot{x}_{cr,le} = 0.4$) is initiated at this point, all following modes are strongly damped, which results to a self-perpetuating convective-transition phase. This phase is interrupted once new modes are strong enough (due to base-flow oscillation or weakening MFD) with the calmed region weak enough for a new creative-transition.

Figure 3.22 contrasts the laminar/linear transient base flow (URANS) with the actual non-linear flow solution (DNS) for the trajectory Ⓣ in picture 3.21(b). With the flow properties along this trajectory—which corresponds to a TS-wave passing through different stages of the convective-transition phase—the effect of the transient branch II can be illustrated and further analyzed. The increasing deviation of the (running and spanwise averaged) velocity profiles is given in 3.22(a). The DNS shows practically no difference to the URANS at $x = 0.3$, $t/T = 0.8$, which is why the label "pristine laminar flow" is appropriate here. However, in the stage attributed to a significant mean flow distortion, a discrepancy of one to four line-thicknesses are evident. The profiles from DNS are fuller compared to the slightly inflectional profiles of the theoretical laminar flow. This is consistent with the observation of increased stability ($\alpha_i \uparrow$) of the transient flow indicated by the attenuation of modal amplitudes in the DNS. The calmed region in the wake of the turbulent spot is characterized by even fuller velocity profiles. The instantaneous velocity distributions reflect the relaxation from the turbulent to a laminar boundary layer and qualitatively agrees with findings of Seifert & Wygnanski (1995); Gostelow *et al.* (1997). A gradual progression from the early MFD to the calmed region is evident in the velocity profiles, again indicating the common nature of both effects. The final velocity profile at $x = 0.6$, $t/T = 1.9$ represents the turbulent flow originating from the most recent creative-transition phase.

The impact of the transient non-linear effect of the MFD/calmed region on the linear modes can be further analyzed with the stability diagrams based on the URANS and DNS solutions, see figure 3.22(b) & (c), respectively. While the stability banana of the URANS flow qualitatively compares to the steady-state reference case in figure

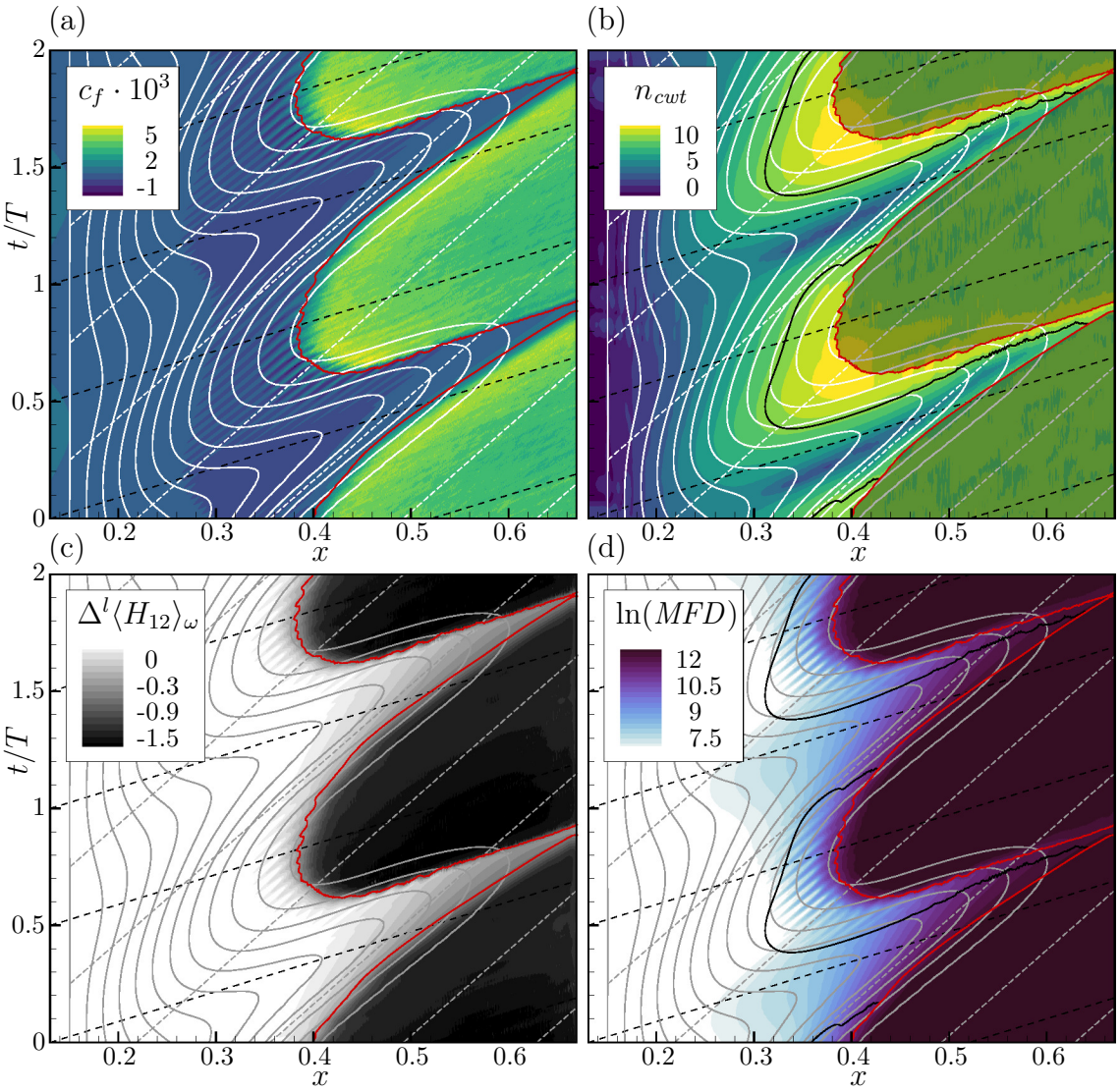

Figure 3.23: Spatio-temporal development for $\kappa = 4$ at $v'_{gust} = 0.06$ (a) Skin friction c_f (b) Amplitudes of continuous wavelet transform n_{cwt} (c) Shape-factor deviation $\Delta^l\langle H_{12}\rangle_\omega$ (d) Mean flow distortion ln(*MFD*); solid white/gray lines: LST with $n \in \{0 \dots 11\}$ with $\Delta n = 1$ in downstream direction, —— $\Delta^l\langle c_f\rangle_\omega = 0.001$, —— $\max_{y_s}\{u'_{s,cwt}\} = 0.01$, dashed white/gray lines: exemplary trajectories of TS-waves c_{TS}^{-1}, - - - - - free-stream velocity u_∞^{-1}.

3.3(a), the amplified region ($\alpha_i < 0$) of the spanwise-averaged DNS flow along the trajectory is truncated and ends at $x \approx 0.49$. The progression of the n-factors downstream of the unstable zone shows the rapid attenuation of linear modes within the calmed region. However, the damping effect of the MFD can already be identified upstream through the spatial lag of the n-factors which is illustrated with the gray Δ in figure 3.22(c). The transient branch II for the introduced disturbance ω_{DS} can be found at $x \approx 0.41$ and coincides with the beginning of the descent of n_{cwt} in the

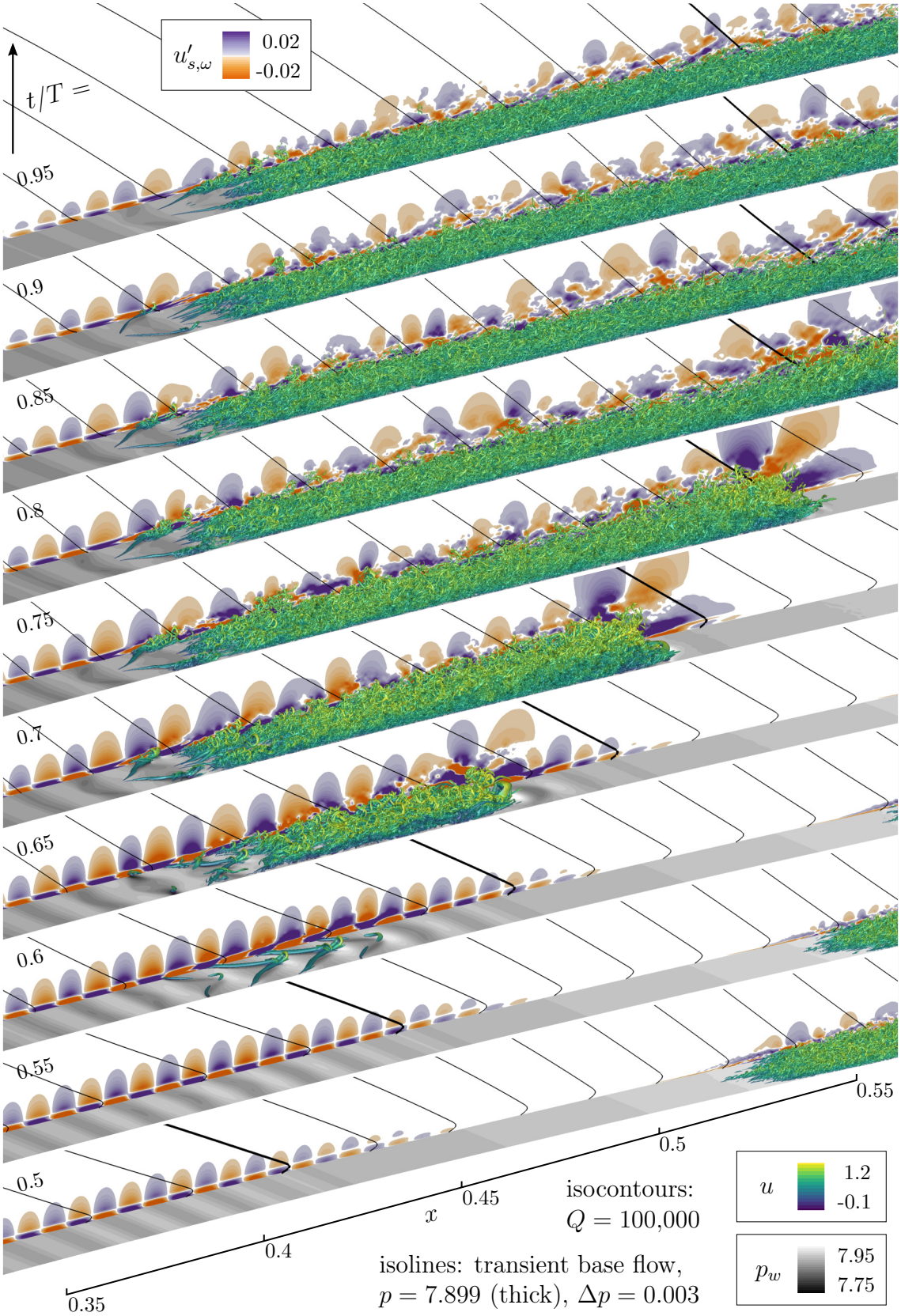

Figure 3.24: Visualization of DNS with $\kappa = 4$ at $v'_{gust} = 0.06$ for $t/T \in [0.5, 1)$.

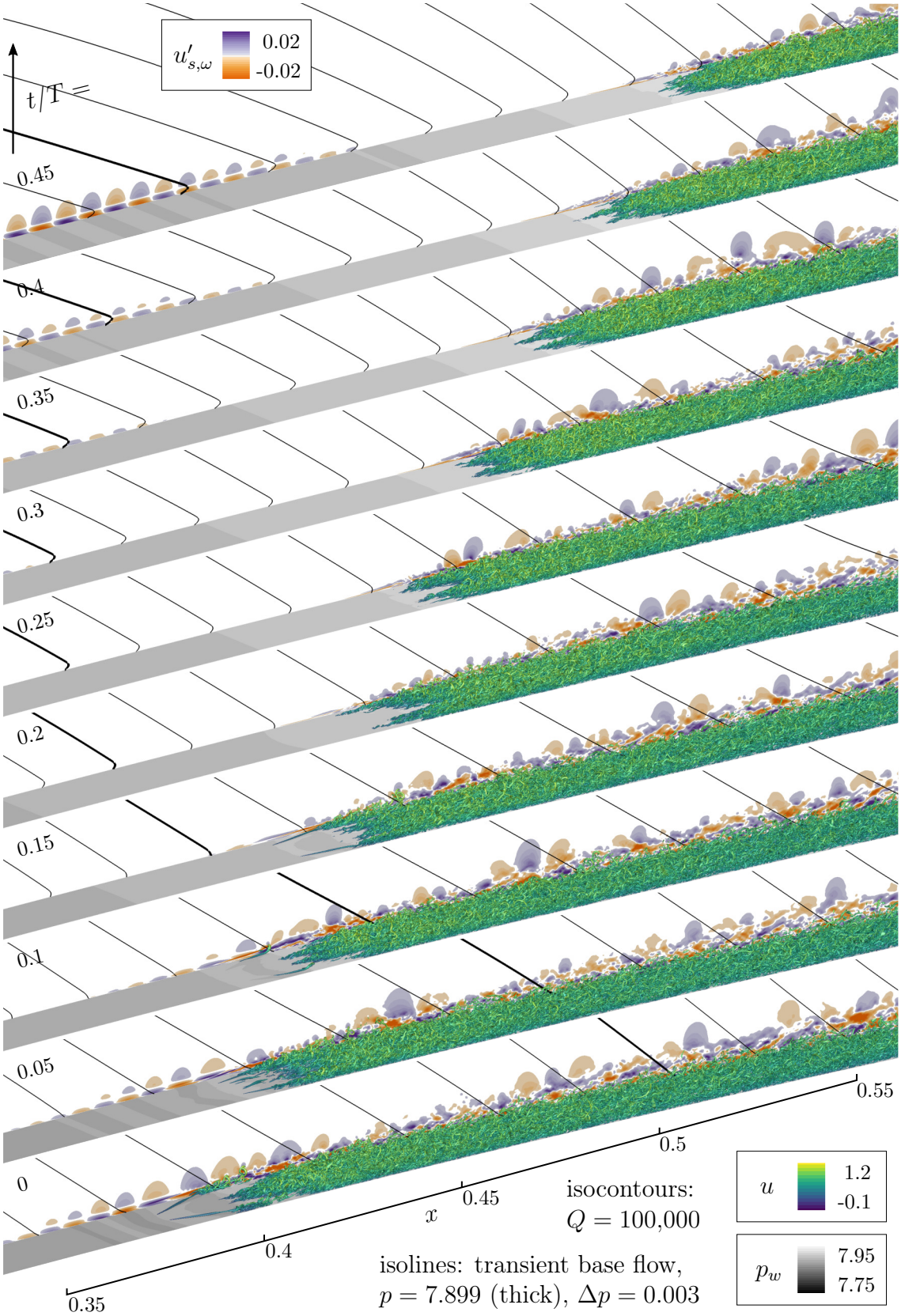

Figure 3.25: Visualization of DNS with $\kappa = 4$ at $v'_{gust} = 0.06$ for $t/T \in [0, 0.5)$.

DNS. At this point, the mode still has a value of $n \approx 8.8$, which, however, is below the threshold required to trigger the transition. Since transient branch II spans over the entire frequency range ω for amplified modes, the described mechanism for the occurrence of the convective-transition mode is also expected to apply in case of a broad spectrum of disturbances. In this case, however, the stalling and resuming of the creative-transition phase must be expected to be different due to the change of the underlying linear problem, then described with the transient envelope N.

Case: $\kappa = 4$**,** $v'_{gust} = 0.06$

The case with $\kappa = 4$ at $v'_{gust} = 0.06$, shown in figure 3.23, corresponds to the highest degree of unsteadiness $\kappa^{tr} = 1.83$ which is investigated in this work. Increasing the amplitude by a factor of three compared to the previous case results in an overturned pattern of the n-factors in the purely laminar/linear consideration. The unsteady transitional flow is again characterized by a creative-transition phase and a subsequent convective-transition phase. A spatially enclosed turbulent zone periodically appears for $0.6 \leq t/T \leq 0.9$. In the present case, the overturned pattern is the product of both the corresponding amplification of the modes by linear effects and the following non-linear convective transition. Nevertheless, the transition indicated by c_f in figure 3.23(a) appears to have a good agreement with the linear theory. The overturned spatio-temporal behavior of the creative-transition phase due to linear theory is evident due to the traces of TS-waves in c_f and in the spectral analysis in figure 3.23(b). Here, the peak of $n_{cwt} > 10$ exhibits a sharp shape and is aligned to the TS-wave trajectory. Moreover, several peaks of $n_{cwt} > 10$ further downstream and slightly later indicate a continuous creative transition before the turbulent flow eventually reaches its leading-edge velocity of $\dot{x}_{t,le} = 0.95$ at $x \approx 0.53$.

Noteworthy in this case is the behavior of the amplitudes n_{cwt} temporally between the creative-transition phases. The discrepancy of the amplitudes from the linear theory already starts for $n_{cwt} = 5$ with a saddle point emerging at $x = 0.28$. This continues downstream through a narrow zone of very small amplitudes with values as low as $n_{cwt} \approx 1.5$ and extends to the laminar-turbulent interface of the convective transition. It is noticeable that lower values are found far upstream after the passing of the (weakly) non-linear stage than in the wake of the turbulent flow. This indicates an early calmed region caused only by high-amplitude waves, which relates to the observations of Gostelow *et al.* (1997). However, the question must be asked why TS-waves seem to cross the calmed region but then rapidly recover their amplitude n_{cwt} just before transition. This is also indicated by the traces of the TS-waves in c_f, which seem to be barely affected by the calmed region. Consequently, effects are most likely present here that cannot be described by linear theory with the quasi-steady assumption. The transient MFD in figure 3.23(d) generally agrees with the location of the calmed region in the x/t diagram. Interestingly, the MFD appears

to extend in upstream direction during the convective-transition phase, which is not reflected in the transient shape-factor deviation in figure 3.23(c). An additional (modal) response of the boundary layer, not covered by the URANS equations but simulated in DNS, is conceivable here. The behavior of the MFD/calmed region as well as the TS-waves is therefore not yet fully understood for this case.

As an example, the case $\kappa = 4$ at $v'_{gust} = 0.06$ is selected for an instantaneous, three-dimensional visualization over one gust period, see figures 3.24 & 3.25. The oscillating transient base flow is indicated by the upstream and downstream-moving isolines of the pressure. The times with creative-transition $t/T \in [0.6, 0.05]$ can be identified with high-amplitude 2D TS-waves in $u'_{s,\omega}$ and subsequent Λ-vortices. Note that the spanwise position of the Λ-vortex alternates with π, since the phase synchronization of the secondary mechanism is constantly disturbed over the oscillation. In contrast, the flow upstream of the laminar-turbulent interface of the convective-transition phase (starting at $t/T = 0.1$) is characterized by an absence of disturbances in $u'_{s,\omega}$ and wall pressure p_w, which indicates the calmed region. For $t/T \in [0.4, 0.55]$, a train of approaching TS-waves with steadily increasing amplitudes can be observed. This behavior reflects the overturned pattern of n-factors predicted by linear theory and therefore corresponds to the spatial and temporal modulation of the waves imposed by the oscillating boundary-layer flow. At $t/T = 0.6$, four clearly isolated Λ-vortices can be seen which represents the onset of the creative-transition phase. The inner two Λ-vortices already depict an advanced stage with ejecting Ω-vortices, which again is consistent with the overturned transitional behavior. This leads to an isolated turbulent spot which can be observed starting at $t/T = 0.65$. The leading edge of the patch moves rapidly with $\dot{x}_{t,le} = 0.95$ and outruns the remaining downstream TS-waves. Nevertheless, two Λ-vortices can be still found at $t/T = 0.65$ and $t/T = 0.7$ behind the turbulent flow, which can be attributed to the overturned n-factor behavior. The large fluctuations in $u'_{s,\omega}$ at the leading edge of the turbulent flow relate to 2D structures at the frequency ω_{DS}. This is consistent with the CWT in figure 3.23(b) and suggest that spectral remnants or 2D structures from the creative-transition are pushed downstream by the turbulent spot. Finally, the turbulent flow penetrates the calmed region before merging with the previous turbulent spot (not shown) at its much slower trailing edge with the velocity $\dot{x}_{t,te} = 0.4$.

3.4.6 Parameter study

The results of the CWT for all other simulations with $\kappa \in \{1; 2; 3; 4; 8\}$ at $v'_{gust} \in \{0.01; 0.02; 0.04; 0.06\}$ (cf. matrix in figure 3.1.2) are given in figure 3.26. They demonstrate that the transition prediction with the trajectory-following method shows a (qualitatively) good agreement for the pristine laminar flow and the phase of creative transition in all cases. However, for $\kappa = 8$, the n-factors deviate slightly

Figure 3.26: Spatio-temporal development of amplitudes n_{cwt} from DNS, cf. matrix in figure 3.4; solid white lines: n-factors from LST with $\Delta n = 1$, —— $\Delta^l \langle c_f \rangle_\omega = 0.001$, —— $\max_{y_s}\{u'_{s,cwt}\} = 0.01$, dashed white lines: exemplary trajectories of TS-waves c_{TS}^{-1}, ----- free-stream velocity u_∞^{-1}.

from the modal amplitudes in the DNS. Since the temporal scales of the TS-waves and the gusts are only about one order apart with $\omega_{DS}/\omega_{gust} = 12.5$, the quasi-steady approach for the stability analysis may reach its limits here. In addition, a mildly increasing deviation from LST is observed with increasing gust amplitude.

Generally, a clear trend of the unsteady transition behavior is evident versus gust frequency κ and gust amplitude v'_{gust}. The individual effects and types of transition have already been discussed in detail in sections 3.4.3 to 3.4.5. Apparently, the occurrence of the convective-transition mode depends on the gust frequency *and* the gust amplitude. All cases with $v'_{gust} = 0.01$ show a continuous creative-transition mode with an uninterrupted (weakly) non-linear stage. For $v'_{gust} = 0.02$, however, a convective-transition mode for the cases $\kappa \geq 3$ is apparent. At $\kappa = 8$, the convective transition/calmed region can hardly develop spatially, as it is directly overrun by a new turbulent spot emerging from the next creative-transition phase. For $v'_{gust} \geq 0.04$, all cases exhibit a convective-transition mode. For $\kappa = 1$ at $v'_{gust} = 0.04$, it should be noted that a transient branch II is already reached in the theoretical consideration of the undisturbed but unsteady laminar flow. This is indicated by the white lines of the linear theory extending only to $n \leq 6$. For a broad spectrum of modal disturbances, a convective-transition mode might not be present here. A slight fluctuation of $\Delta^l\langle c_f\rangle_\omega = 0.001$ can be seen at the trailing edge of the turbulent flow in case $\kappa = 4$ at $v'_{gust} = 0.04$. This is attributed to an acoustic perturbation emanating from the upstream creative transition via a trajectory with the velocity $\approx u_\infty(1 + 1/Ma)$.

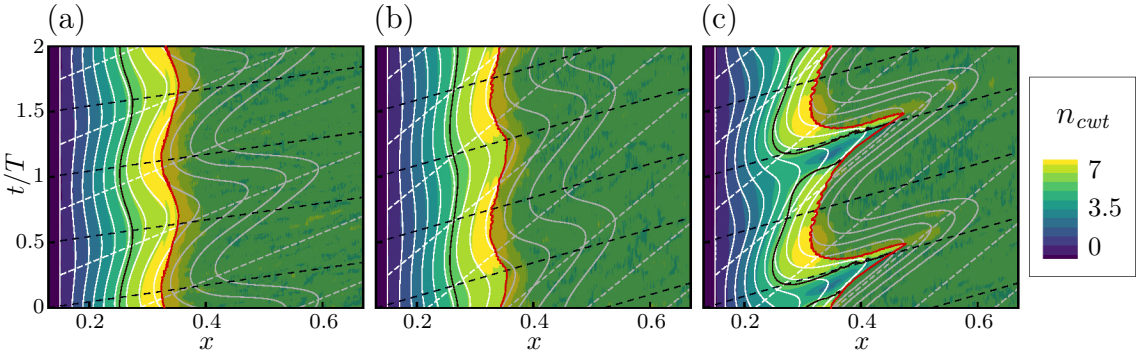

Figure 3.27: Spatio-temporal development of amplitudes n_{cwt} from DNS at increased disturbance amplitude of modes $A_v^\uparrow$ (a) $\kappa = 2$ at $v'_{gust} = 0.02$ (b) $\kappa = 4$ at $v'_{gust} = 0.02$ (c) $\kappa = 4$ at $v'_{gust} = 0.06$; solid white lines: n-factors from LST with $n \in \{0 \dots 11\}$ with $\Delta n = 1$ in downstream direction, —— $\Delta^l\langle c_f\rangle_\omega = 0.001$, —— $\max_{y_s}\{u'_{s,cwt}\} = 0.01$, dashed white lines: exemplary trajectories of TS-waves c_{TS}^{-1}, ----- free-stream velocity u_∞^{-1}.

The results of the CWT for the simulations with increased initial modal amplitudes $A_v^\uparrow$ and the resulting threshold value $n_{crit} = 7$ are depicted in figure 3.27. In agreement with linear theory, the case $\kappa = 2$ at $v'_{gust} = 0.02$ in figure 3.27(a) shows

an earlier transition location which oscillates only weakly in contrast to the case with $n_{crit} = 10$ discussed above. The same observations apply to the case $\kappa = 4$ at $v'_{gust} = 0.02$ in figure 3.27(b). However, it is interesting to note that the convective-transition mode does not occur here due to the increased initial perturbation (smaller n_{crit}), cf. default case in figure 3.19(b). For the case with $\kappa = 4$ at $v'_{gust} = 0.06$ in figure 3.27(c), the convective-transition mode is sill present but greatly reduced in space and time. Accordingly, the occurrence of the convective-transition mode also depends on the threshold value n_{crit}/initial amplitude A_v. Moreover, another interesting observation here is that the length of the (weakly) non-linear stage in figures 3.27(a) & (b) oscillates harmonically and without interruptions at about the same length in the x direction. Given the comparatively high frequencies $\kappa = 2$ and 4, this supports the assumption made above that the transient behavior of the secondary mechanism (fundamental resonance) can also be considered as quasi-steady here.

3.4.7 Discussion and comparison with literature

The general phenomenon for the occurrence of the convective-transition mode as found in this work is depicted in figure 3.28(a) and is revisited here. This qualitative description of the physical process therefore refers to the case of natural transition with TS-waves in an oscillating flow with an (average) APG. The white region represents the pristine laminar flow which relates to the transient base flow. In this range, deformations of the velocity profiles are still negligible. Therefore, TS-waves show linear but unsteady behaviour along their trajectories, corresponding to the quasi-steady LST (black lines). The fully non-linear turbulent flow (gray) is periodically triggered by the creative transition (thick red line) were TS-waves reach critical amplitudes. This phase is preceded by the weakly non-linear stage (thin red lines) in which the secondary mechanism (resonance) leads to the final three-dimensional breakdown.

The cycle can be divided into three intervals along the trajectories, referred to here as TS-wave "cohorts" (i) to (iii). Cohort (i) corresponds to the second half of the creative-transition phase where the amplitudes agree with the linear theory based on the theoretical unsteady laminar flow. As for steady-state conditions, the MFD (light blue) increases due to the high-amplitude waves with $u' > 0.01$ in the (weakly) non-linear stage. For the transient flow, however, the MFD is lagging and does not decrease at the same velocity as the theoretical downstream movement of critical n-factors for transition. The MFD-delay therefore causes fuller velocity profiles with increased stability properties $\alpha_i \uparrow$ for the TS-wave cohort (ii). Consequently, these modes experience a transient branch II ($\alpha_i > 0$) which is indicated by the divergence of the actual amplitudes (thin red lines) from the theoretical pristine laminar/linear behavior (gray lines). This is identified to be the key mechanism for

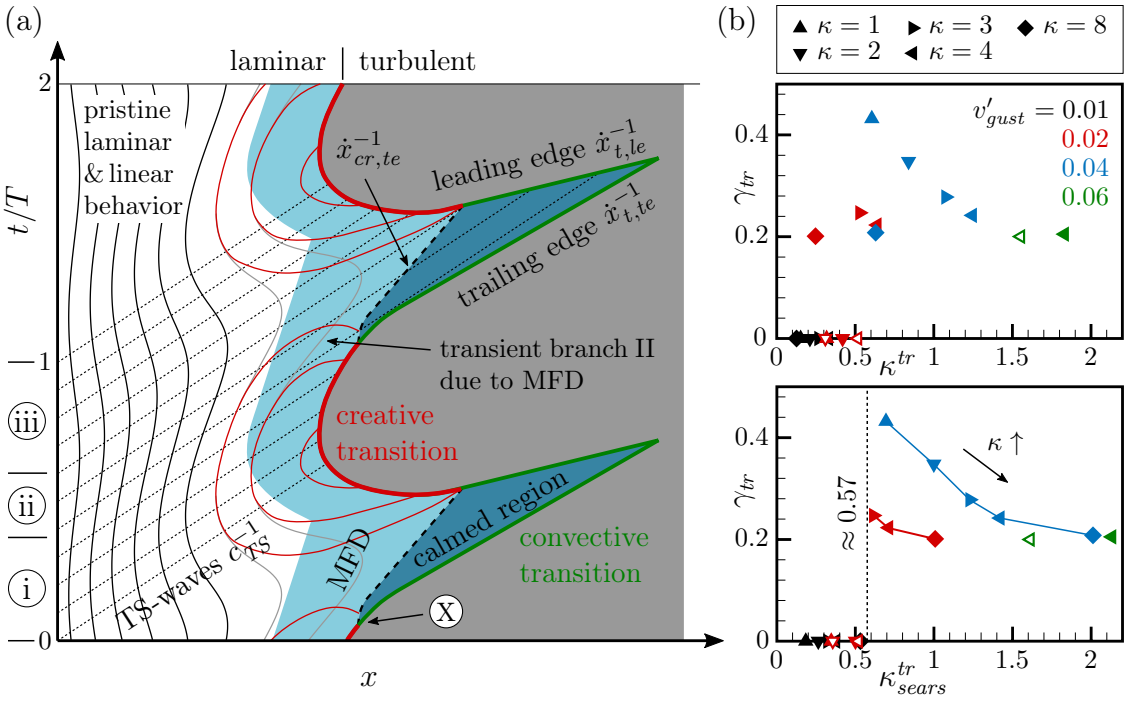

Figure 3.28: (a) Spatio-temporal depiction of the emergence of the convective-transition mode for natural transition with $c_{TS} = 0.35$, $\dot{x}_{t,le} = 0.95$, $\dot{x}_{t,te} = \dot{x}_{cr,le} = 0.4$, $\dot{x}_{cr,te} = 0.2$; MFD = mean flow distortion. (b) Fraction of the convective transition over one period γ_{tr} versus unsteadiness quantities κ^{tr} and κ^{tr}_{sears}; full symbols: $n_{crit} = 10$, empty symbols: $n_{crit} = 7$ (increased disturbance amplitude $A_v^{\uparrow}$).

the emergence of the convective-transition mode, as the TS-waves fail to reach the threshold required for the natural transition to turbulence. The stalling point of the creative transition is found at (X), which coincides with the disappearance of the secondary mechanism indicated by $u' < 0.01$ for the 2D modes (outer thin red line). It is assumed that the decreased frequency of arriving TS-wave crests (and thus also of Λ-vortices) at the downstream-moving transition front (Doppler effect analogy) has an additional reinforcing effect on the emergence of the transition stalling. In other words, the turbulent flow is expected to be more prone to convect downstream if the transition front is fed at a less frequent rate with incoming disturbances. The onset of the convective transition initiates the calmed region (dark blue) in the wake of the turbulent spot, which also briefly forms a spatial "hole" in the turbulent flow. At this point, the convective-transition phase can be considered to be self-perpetuating, since the subsequent modes of the cohort (ii) will be damped as they enter the calmed region. This phase can only be overcome once the TS-waves are strong enough and/or the calmed region is weak enough to trigger natural transition. Hence, the beginning of cohort (iii) is defined with the associated trajectory. This interval refers to the first half of the creative-transition phase, in which the modes are still attenuated (cf. gray lines) due to the not fully recovered mean flow. Therefore,

compared to the theoretical laminar/linear prediction, the transition location in the streamwise direction is slightly delayed.

The velocities of relevant characteristics of the convective-transition mode, cf. figure 3.28(a), remain approximately constant for the investigated cases. This is not surprising since all cases relate to the same average flow with the same APG and the transition oscillates only in a limited range of Re_x. The velocities of the leading and trailing edges of the turbulent flow detected with the criterion $\Delta^l\langle c_f\rangle_\omega = 0.001$ are found at $\dot{x}_{t,le} = 0.95$ and $\dot{x}_{t,te} = 0.4$, respectively. The values are consistent with the extremes of the measured velocities for the convection of a turbulent spot under an APG by Seifert & Wygnanski (1995). In the work of Gostelow *et al.* (1996, 1997) with an APG, the velocities $\dot{x}_{t,le} = 0.872$ and $\dot{x}_{t,te} = 0.413$ were determined. For the convective phase at natural transition, Obremski & Fejer (1967) found trailing-edge velocities of $\dot{x}_{t,te} = 0.53$ and $= 0.5$ for the APG cases *D-5* and *D-6*, respectively. For the related *Case2* of Studer *et al.* (2006), $\dot{x}_{t,te} = 0.348$ was observed. A summary of spot velocities for ZPG cases is given in Pfeil *et al.* (1983).

The leading edge of the calmed region $\dot{x}_{cr,le} = 0.4$ is equal to the trailing edge of the turbulent flow and is inaccessible for the TS-waves with $c_{TS} = 0.35$. The approximation of the trailing-edge velocity of the calmed region $\dot{x}_{cr,te} = 0.2$ is based on the transient behavior of modal amplitudes n_{cwt}, which coincides with the constant level of $\Delta^l\langle H_{12}\rangle_\omega = -0.2$. This is in agreement with Gostelow *et al.* (1997) where a threshold for the velocity fluctuations was selected to identify the calmed region with $\dot{x}_{cr,te} = 0.194$. However, due to the observed transient behavior of the MFD, it is questionable whether the calmed region can be confined precisely in space and time. Levels of $\ln(MFD)$ which relate to the onset of the convective-transition phase are found to move downstream at velocities as slow as $\dot{x}_{mfd} = 0.05$. For ZPG flows, the calmed region exhibits higher velocities with $\dot{x}_{cr,te} \approx 0.3$ due to the increased velocity of the spot trailing edge, see e.g. Orth (1993); Halstead *et al.* (1997). Consequently, the calmed region cannot be accessed by TS-waves in this case, since their phase velocities are usually found at $c_{TS} < 0.3$.

Most comparable to the observed transient mechanism presented in figure 3.28(a) is *Case2* of Studer *et al.* (2006), where a convective phase was found for natural TS-wave transition at an APG. In this case, however, the (creative) transition front is continuously moving upstream without being interrupted by a calmed region. Accordingly, no overturned pattern with spatially enclosed turbulent and laminar regions can be found. With the new findings, the cause of this difference could be either explained with a weaker calmed region or stronger disturbances. The latter is likely due to the broad frequency range of TS-waves which indicates "more" chances to reach critical n-factors, cf. envelope in figure 2.3. The APG case *D-5* of Obremski & Fejer (1967) shows periodic turbulent spots and agrees qualitatively very well with the convective-transition found in the investigated scenario of this thesis. The case *15* of the same study shows different characteristics due to the

ZPG. In comparison to the APG case, the TS-waves at a decreased phase speed are too slow to reach the calmed region which has an increased trailing-edge velocity. However, this does not explain the origin of the convective-transition phase. Since natural transition is investigated here (confirmed by Obremski & Morkovin (1969)), a theoretical transition location based on the pristine laminar flow can be also imagined. This location would be continuous over time with the limit for the downstream velocity $\dot{x}_{tr,d}(n_{crit}) \leq c_{TS} = 0.29$, see section 3.3.3. However, the succeeding "wave packets" indicate a periodic modification of the laminar mean flow, see discussion above. Consequently, a dampening effect of the MFD is identified to be responsible for the stalling of the creative-transition phase and the resulting convection with $\dot{x}_{t,te} = 0.55$. Furthermore, the observed "wave packets" are rather continuous TS-waves with spatiotemporally modulated amplitudes due to the oscillating flow, cf. (weakly) non-linear stage in the present work. According to the theoretical considerations, this effect may also occur in FPG flows. However, this becomes increasingly unlikely due to the slower phase velocities of the modes (see Wazzan *et al.* (1981)) and the faster calmed region/turbulent spot (see Gostelow *et al.* (1996)).

3.4.8 Dimensional analysis and characterization

The simulation results of the parameter study show that the occurrence of a fully-developed, self-perpetuating convective-transition mode depends on the gust frequency κ, the gust amplitude v'_{gust}, and the threshold value n_{crit}/initial modal amplitude A_v. A qualitative physical explanation for this *tipping-point* can be established when considering the transient effects discussed above. Theoretically, if the mean flow distortion had no delay and the base flow recovered instantaneously, a continuous creative transition in accordance with the predicted n_{crit} from linear theory would always be present. However, since the transient behavior of the MFD is independent from the gust frequency, there is always the danger of the emergence of a convective transition at the downstream-moving transition front. With an increasing frequency κ, the critical n-factors of the linear theory migrate faster downstream in contrast to the MFD which decreases at its own speed. Hence, at a certain gust frequency, the amplification of TS-waves is not sufficient to overcome the stabilizing properties of the lagging MFD, leading to the convective-transition mode with a subsequent calmed region. Another important factor for this tipping-point versus frequency is probably the increasing reduction of the incoming TS-wave crests (Doppler analogy) at the beginning of the downstream-moving transition. The same conclusions can be drawn for the dependence on the gust amplitude: With larger v'_{gust}, the velocity of the downstream-moving n-factors also increases, which favors the emergence of a convective-transition mode. Likewise, the dependence of the tipping-point on the modal initial perturbation A_v can be explained. With an in-

creased A_v, lower velocities $\dot{x}(n_{crit})$ are present at the downstream-moving transition front, making the convective-transition mode less likely. Accordingly, it can be assumed that the convective-transition mode appears in nature primarily at high N_{crit}, which is only found at low turbulence intensities of the free stream.

An obvious choice for the characterization of this tipping-point is the unsteadiness quantity κ^{tr} introduced with equation (3.7). This non-dimensional number accounts for the gust frequency as well as (indirectly) the gust amplitude via the maximum length of the oscillation of n_{crit} in x direction. Furthermore, it is shown in section 3.3.4 that this quantity is very well suited to characterize the velocities of the oscillating n-factors. Since the transient MFD-delay is generally independent of the gusts properties, a threshold value may be identified for the occurrence of the convective-transition mode using the parameter κ^{tr}. In figure 3.28(b), the fraction of the convective-transition mode over one period (with respect to the TS-wave trajectories) γ_{tr} is plotted versus two definitions of κ^{tr} for all cases. Consequently, γ_{tr} equals $\Delta t/T$ of the modes corresponding to cohort (ii) in figure 3.28(a). For the standard definition κ^{tr} (upper), all cases without the convective transition ($\gamma_{tr} = 0$) are found in $\kappa^{tr} < 0.55$. However, a clear threshold is only evident for the related second definition (lower) for $\kappa^{tr}_{sears} \approx 0.57$. The quantity κ^{tr}_{sears} only considers the effective gust amplitude with the Sears function in contrast to κ^{tr} which also accounts for additional attenuation of the oscillation of n_{crit} due to linear effects, see section 3.3.4. As can be seen from the DNS results in figure 3.26, the LST overestimates the attenuation of the oscillation of $n_{(cwt)}$-factors for the cases at $\kappa = 8$. Therefore, κ^{tr} based on LST fails for threshold characterization due to the already (weakly) non-quasi-steady stability behavior. The decline of the fraction γ_{tr} versus κ for the cases with a convective-transition phase can be partially related to the Sears function. Note that this threshold value also "sorts" the cases with different n_{crit}, see $\kappa = 4$ at $v'_{gust} = 0.02$ in figure 3.28(b). However, for other transition scenarios featuring e.g. a different secondary mechanism, a broad range of primary TS-modes or a naturally oscillating branch I, the threshold value for κ^{tr}_{sears} is expected to vary. The blue line in the matrix in figure 3.29 corresponds qualitatively to the tipping-point for the emergence of the convective-transition mode based on κ^{tr}_{sears}.

The non-steady Reynolds number of Obremski & Fejer (1967) mentioned in section 3.3.4 does not prove to be a suitable quantity for characterization here. In that study, unstable wave packets were found for all cases. However, a bursting to turbulence of the packets was only observed for $Re_{NS} > 27{,}000$, see also White (2006). The results of the present work correspond to $2{,}000 < Re_{NS} < 53{,}000$ with high values for low frequencies at high amplitudes and low values for high frequencies at low amplitudes. Since no corresponding observations could be made here regarding the threshold value, doubts arise as to the general applicability of Re_{NS}.

As outlined at the end of section 3.3.4, data from DNS could be employed to enhance the unsteady transition-prediction method with regard to non-linear effects

(point ⓓ). For instance, the emergence of the convective-transition mode could be incorporated in a URANS transition model with a a semi-empirical approach. The quantity κ^{tr} is of limited use here, since it refers only to the global properties of the unsteady flow and not to the local/instantaneous flow. A method for predicting the "local" tipping-point for the convective transition (point Ⓧ in the x/t diagram in figure 3.28(a)) could be derived with physical properties (e.g. predicted amplitude n, modeled MFD, D_{tr}) found at the beginning of the downstream motion of n_{crit}. Conceivable are non-dimensional quantities involving a ratio of the downstream velocities $\dot{x}(\ln(MFD) = const.)$ and $\dot{x}(n = const.)$ or the differences $\Delta\ln(MFD)$ and Δn with respect to the fully non-linear stage.

3.5 Summary

This section summarizes the most important aspects of the research presented in this chapter. First, a brief review of the numerical setup is given, followed by an enumeration of the identified physical effects and a classification into identified unsteady flow scenarios. A comprehensive summary with further conclusions can be found in chapter 5.

The unsteady behavior of natural transition in an attached boundary-layer flow of an NLF airfoil due to periodic vertical gusts was numerically investigated. First, transient base flows were generated using URANS simulations in conjunction with the disturbance velocity approach for different frequencies κ and amplitudes v'_{gust}. The periodic unsteady laminar flows were investigated with linear stability analysis by using an extension of the e^n-method. By following the TS-waves along their trajectories, the theoretical motion of the transition location according to linear theory can be characterized. As a hybrid approach, the URANS flow fields were also used for DNS, with a domain covering the relevant part of the flow for the unsteady transition. Thereby, the transient base flows containing the airfoils gust response were prescribed with modified unsteady boundary conditions. The continuous wavelet transform was used to determine the spatio-temporal evolution of TS-wave amplitudes in the oscillating flow. Having a theoretical laminar and linear reference along with the non-linear results of the DNS proved to be very helpful in deducing cause and effect physics. The numerical methods were validated with experimental results of Romblad *et al.* (2020); Romblad (2023). Even though a specific airfoil geometry is being used, a claim to generality can be made for this study due to the following properties: a generic definition for periodic gusts; relevant Reynolds number and N_{crit}; a comparably constant streamwise pressure gradient; and most important a sinusoidal response of the transition location for the quasi-steady case $\kappa \to 0$.

With the findings of this chapter, the physical effects responsible for the behavior of natural transition with (convective) TS-modes at unsteady conditions can be

dissected. In direct comparison to the classical transition under steady-state conditions, four major consecutive effects are identified for the airfoil boundary-layer flow with gusts:

(1) **Response to gust and unsteady pressure gradient:** The oscillating pressure gradient is determined by the gust amplitude and frequency. Due to the response of the airfoil flow to the gust, however, there is a strong attenuation of the effective amplitude with increasing frequency κ, which can be described with the Sears (1941) function. The absolute amplitude v'_{gust} has a quasi-linear influence in this respect. In addition, the sinusoidal gust signal leaves a spatio-temporal footprint in the pressure gradient whose characteristics migrate downstream with approximately u_∞. See discussion in section 3.2.1.

(2) **Viscous delay of the boundary layer:** The viscous laminar boundary layer directly responds to the unsteady pressure gradient imposed by the gust. However, the velocity profiles are lagging behind due to an inherent viscous delay. This also results in a spatio-temporal delay of the change of the amplification rates α_i for the linear modes. See URANS results in section 3.2.2.

(3) **Spatio-temporal development of TS-waves:** The phase speed of the TS-waves with $c_{TS} \approx 0.35$ is considerably slower than the gust with u_∞ and is approximately velocity congruent with the characteristics of the lagging velocity profiles and consequently α_i. The amplification of the TS-waves along their spatio-temporal trajectories in the lagging transient base flow results in an asymmetric (or overturned) motion of the transition front over time. At κ_{crit}, which refers to the frequency where the mean lifetime of the TS-waves is equal to the period of the gust, the most skewed or asymmetric temporal behavior of the transition is found. The amplitude of the streamwise oscillation of the transition motion can be directly related to the Sears (1941) function. Furthermore, the velocities of the transition fronts in both upstream and downstream directions follow a clear trend over the newly introduced unsteadiness quantity κ^{tr}. This behavior can be entirely described with linear theory, see results in section 3.3.

(4) **Transient non-linear effects:** At high levels of unsteadiness, the (weakly) non-linear stage and the fully non-linear turbulent flow can cause a mean flow distortion that temporarily alters the stability properties for the flow. This can create a transient branch II for the forthcoming TS-waves, resulting in a drop below the thresholds required for the transition. The so-called convective-transition mode, in which the natural transition front is interrupted, is explained with this effect. The fewer incoming TS-wave crests at the downstream-moving front (Doppler analogy) is expected to contribute to the "stalling" of the creative transition. The self-perpetuating convective-transition phase creates a calmed region in the wake of the turbulent flow,

which further alters the stability properties of the flow. A tipping-point for the occurrence of the convective-transition mode was identified with a variant of the unsteadiness quantity κ^{tr}_{sears}. See DNS results in section 3.4 with sections 3.4.7 & 3.4.8 for a detailed discussion. In the case of an overturned linear behavior, the potentially faster leading edge of a convective turbulent spot must be considered. In the non-linear stage of the transition, the amplitudes of the velocity fluctuations at the upstream-moving front are considerably higher compared to the downstream-moving front. This is also explained by the Doppler analogy for the incoming TS-wave crests which leads to more non-linear interactions.

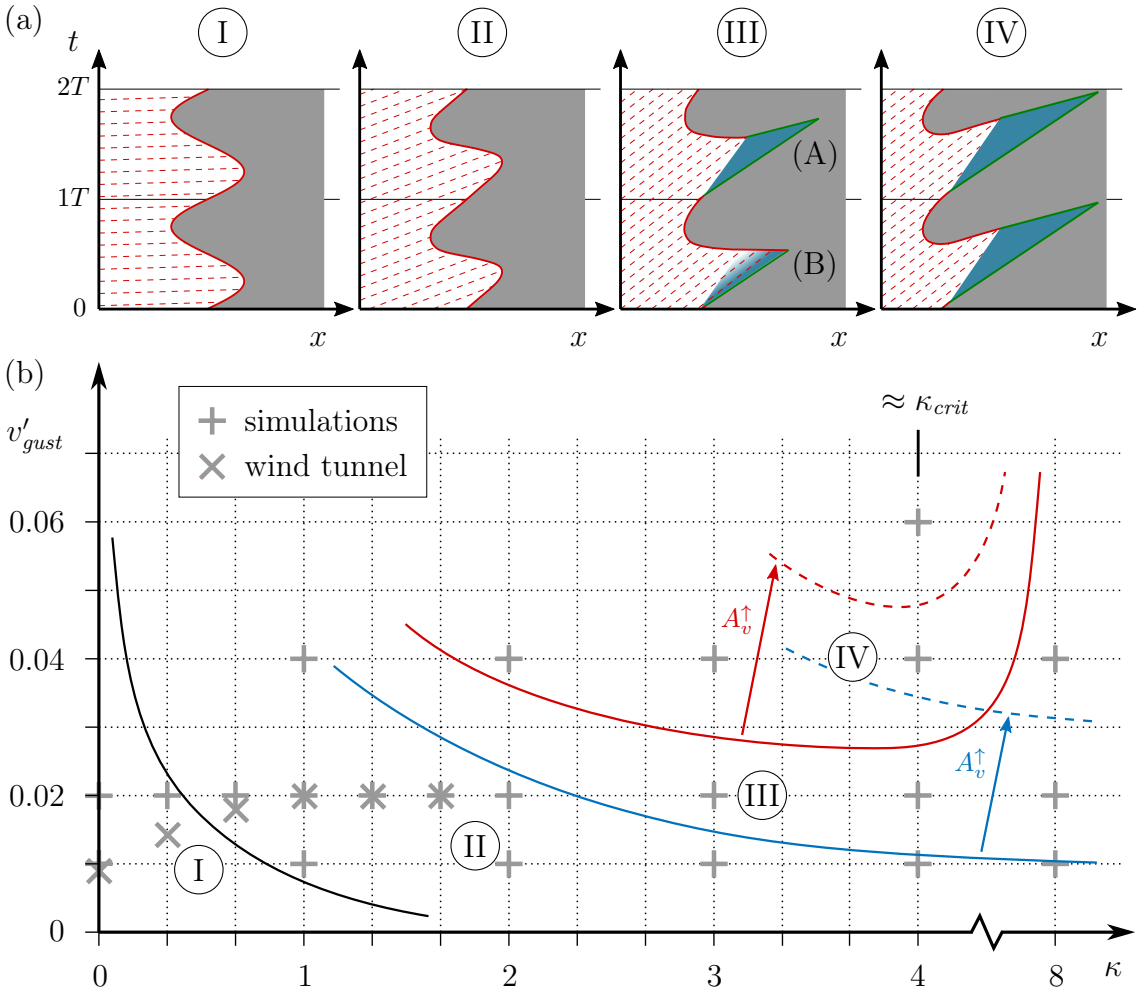

Figure 3.29: Classification of the identified scenarios of unsteady natural transition. (a) Schematic spatio-temporal development. (b) Parameter space of the investigations. Dashed lines correspond to the separation at higher initial disturbance-amplitudes $A_v^{\uparrow}$ or lower n_{crit}.

Figure 3.29 shows a classification of the unsteady transition scenarios based on

the findings of this work. The schematic spatio-temporal development for all cases is depicted in figure 3.29(a) with TS-wave trajectories (dashed red), the creative transition (red) as well as the convective-transition (green) including the calmed region (blue). Figure 3.29(b) shows the parameter space of reduced frequency κ and gust amplitude v'_{gust} with the investigated numerical and experimental cases (gray), cf. figure 3.4. The separation of the scenarios in the matrix is based on the two variations of the unsteadiness quantity introduced in section 3.3.4. Here, the black line corresponds to $\kappa^{tr} \approx \kappa^{tr}_{sears} \approx const.$, the blue lines to $\kappa^{tr}_{sears} \approx const.$, and the red lines to $\kappa^{tr} \approx const$. The same thresholds apply to the third parameter of the dimensional analysis, which corresponds to the variation of the initial amplitudes of the modes. Accordingly, the isolines for $A_v^{\uparrow}$ are shifted in the κ/v'_{gust} plane, see dashed lines. The four scenarios can be distinguished as follows:

(I) **Quasi-steady behavior** for $\kappa^{tr} \lessapprox 0.1$: The trajectories of the TS-waves are (almost) horizontal in the x/t diagram due to the low gust frequency. The resulting transition behaves "symmetrically" over time, moving sinusoidally at nearly equal speeds in the upstream and downstream directions. Consequently, the transition motion can be considered as quasi-steady and may be approximated with the classical e^n-method. However, increased amplitudes in the non-linear stage of the transition can already occur at the upstream-moving front due to more incoming crests of TS-waves (Doppler analogy). Experimental results that can be attributed to this category are *Case1* of Studer *et al.* (2006) and Romblad *et al.* (2020); Romblad (2023) for $\kappa < 0.5$.

(II) **Unsteady behavior due to linear effects** for $\kappa^{tr} \gtrapprox 0.1$ with $\kappa^{tr}_{sears} \lessapprox 0.57$: The laminar boundary layer exhibits a viscous delay and the phase speed of the TS-waves (see inclined trajectories) causes additional hysteresis. The resulting transition, here referred to as "asymmetric" in time, has a fast upstream- and a slow downstream-moving front. This behavior can be entirely attributed to linear effects. For transition prediction, the LST can be extended with a trajectory-following method which is applied on the spatio-temporal velocity profiles of the transient base flow. However, due to the increased effect of the Doppler analogy, much higher amplitudes at the upstream transition front are to be expected. The experimental results of Romblad *et al.* (2020); Romblad (2023) for $0.5 < \kappa < 1.7$ can be attributed to this category.

(III) **Unsteady behavior with convective transition** for $\kappa^{tr}_{sears} \gtrapprox 0.57$: The effects of the previous case are also found here. However, the "convective transition" is present here, which appears at a certain threshold of unsteadiness (blue line in figure 3.29(b)). Due to a delay of the mean flow distortion which alters the stability properties, the "creative transition" is stalled at the downstream-moving front. In the simulations, variation (A) in figure 3.29(a) was observed where a calmed region spatially interrupts the turbulent flow.

Experimental results which can be attributed to variation (A) of this category are e.g. the cases *15* and *D-5* of Obremski & Fejer (1967). However, the variation (B) in figure 3.29(a) where a continuous creative transition is present at the upstream-moving front is identified in *Case2* of Studer *et al.* (2006) or *D-6* of Obremski & Fejer (1967). In the latter cases, the TS-waves are apparently strong enough to overcome the calmed region.

(IV) **Unsteady behavior with overturned n-factors** for $\kappa^{tr} \gtrapprox 0.9$: The effects of the previous case are also found here. However, an additional "overturned" pattern of the spatio-temporal motion of the creative transition is present. This can be described by the linear theory and is independent of the non-linear convective transition which occurs in parallel. As seen in figure 3.29(b), this behavior is most pronounced for $\approx \kappa_{crit}$, where the TS-wave life span roughly matches the oscillation period. The results of the wind-tunnel measurements *15* and *D-5* of Obremski & Fejer (1967) indicate some contribution of an overturned behavior of the linear modes. For periodic unsteady transition, an overturned pattern of n-factors purely based on linear theory *without* the presence of a convective transition is rather unlikely. For isolated or pulsed "1-cos" gusts, however, the overturned linear effect might be more relevant due of the absence of an earlier non-linear impact on the transient base flow.

4 Separated-flow scenario

The aim of this chapter is to extend the findings of the previous chapter to the case of boundary-layer flow with a laminar separation bubble under unsteady conditions due to periodic gusts. An introduction to previous studies on this topic is given in section 1.2. The structure of this chapter differs from the previous because the unsteady stability analysis is only performed based on the DNS results and fundamental characteristics of unsteady laminar boundary layers due to gusts have already been discussed in section 3.2.2. Hot-wire measurements are available for the associated experimental campaign—which are not available for the LTT case—allowing the numerical approach to be further validated. The content of this chapter is largely based on Ohno *et al.* (2023*a*). The experimental wind-tunnel results shown in this chapter are kindly provided by Michael Greiner.

The chapter is structured as follows: fundamental characterization of the scenario including steady-state stability analysis in section 4.1, validation of the URANS base flows in section 4.2, discussion of the DNS results for the steady-state reference case in section 4.3, the DNS results with gusts in section 4.4 including the characterization of the unsteady separation, transition and reattachment as well as the influence of effects such as the absolute instability and lock-in, and finally a summary of the results in section 4.5.

4.1 Characterization of the flow scenario

The laminar flow airfoil "LNA-19121" depicted in figure 4.1 was designed for experimental investigations as well as the numerical investigations on unsteady laminar separation. While considering the flow conditions in the wind tunnel, the geometry was designed in such a way that a laminar separation bubble (LSB) is formed in the rear section on the suction (upper) side. The original coordinates used to determine the airfoil surface via NURB-splines (see explanation in section 2.3.1) for the numerical simulations can be found in Greiner (2024). In accordance with the corresponding wind-tunnel experiments, a Reynolds number of $Re = 880{,}000$ with respect to the chord length and a Mach number of $Ma = 0.056$ are chosen here. The wind-tunnel experiments were carried out at a chord length of $\tilde{L}_c = 0.7m$ and a velocity of $\tilde{u}_\infty = 19m/s$. An angle of attack of $AoA_{ref} = 1.5°$ as the steady-state reference case is selected. For further results and details of the experimental setup, see Greiner & Würz (2021); Greiner (2024).

4.1.1 Properties of numerical setups

As for the scenario in the previous chapter, the setup of the URANS simulations is explained in detail in section 2.3.1. In the present scenario, the transition locations are held at $x_{tr,suction} = 0.644$ on the suction (upper) side and $x_{tr,pressure} = 0.15$ on the pressure (lower) side in all simulations. The transition location on the pressure side refers to a trip wire installed on the airfoil in the wind-tunnel experiments in order to prevent additional laminar separation.

As shown in figure 4.1, the curvilinear DNS domain starts at $x_{in} = 0.5$ and ends just before the trailing edge at $x_{out} \approx 0.991$. However, the analyzed region of the DNS extends from the inflow only up to $x = 0.82$ since grid stretching followed by sponge zones is applied at this point towards the outflow. A grid stretching in wall-normal direction according to the description in section 2.4 is applied with a constant height of the DNS domain of $y_{s,top} = 0.06$. The spanwise extent of the domain, $\Delta z_0 = 0.0314$, is determined with the selection of the disturbance input, see section 4.1.3. In this flow scenario, a grid resolution of $1500 \times 300 \times 256 = 115.2M$ points is chosen along the airfoil contour, the wall-normal direction and the spanwise direction, respectively.

Analogously to the LTT case in the previous chapter, the sufficiency of the grid resolution for the simulation of the flow characteristics is given by multiple aspects. The modes introduced at the disturbance strip are resolved with ≈ 120 points in x_s direction and 256 points in z direction. This considerably high resolution with a high-order DNS code allows the generation of a sufficient number of higher harmonics to simulate the non-linear transitional part of the flow. Again, the resolution of the transition process can be validated with results from LST, see sections 4.3 & 4.4. Furthermore, the flow downstream of the transition is sufficiently resolved with the inner units of $\Delta x_s^+ < 9$, $\Delta y_{s,w}^+ < 1.2$ and $\Delta z^+ < 5$ (see Poggie *et al.* (2015)) to describe the qualitative behavior of turbulent parts of the boundary layer. The simulations were performed with a time step of $\Delta t_{sim} = 2.5 \cdot 10^{-7}$.

As in the LTT case, the boundaries at the inflow, free stream, and outflow are treated with characteristic (unsteady) boundary conditions including forcing terms, see section 2.6.2 & 2.6.3 for fundamentals. The sponge zones which are applied at the outflow and the free stream, cf. figure 4.1, start at $x_{sp} \approx 0.871$ and $y_{s,sp} \approx 0.0388$ in streamwise and wall-normal direction, respectively. Here, the maximum value of the gain distribution for equation (2.24) is set to $G_{max} = 100$ at both boundaries. In contrast to the LTT case, it was not necessary to use a sponge zone at the inflow to prevent reflections. Again, the wall boundary condition is chosen to be adiabatic, while periodic boundary conditions are used for the spanwise direction.

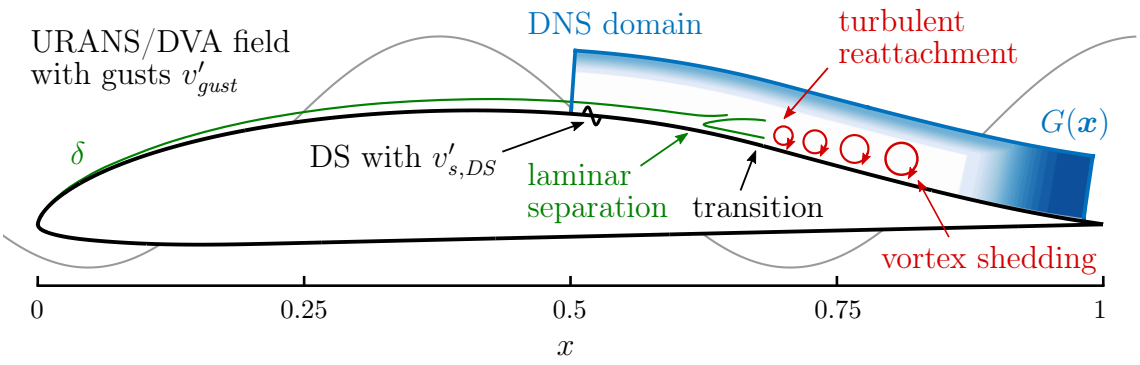

Figure 4.1: Depiction of the "LNA19121" laminar flow airfoil with DNS domain and distribution of gain function $G(\boldsymbol{x})$ (blue); boundary-layer thickness δ and separation bubble is strongly exaggerated in wall-normal direction.

4.1.2 Investigated steady-state and unsteady cases

In addition to the simulation of the reference case with $AoA_{ref} = 1.5°$, two additional steady-state simulations with $AoA_{\pm}$ are conducted to provide insights into the theoretical case with $\kappa \to 0$. With this quasi-steady consideration of an "infinitely large" gust $\lambda_{x,gust} \to \infty$ introduced in section 2.2 one can speak of a variation of the angle of attack around $AoA' = \arctan\left(v'_{gust}/u_\infty\right) \approx 2.3°$. Therefore, the simulations with $AoA_{\pm} = AoA_{ref} \pm AoA'$ correspond to the maximum ($AoA_{+} = 3.79°$) and minimum ($AoA_{-} = -0.79°$) angles of attack (or quasi-steady gusts impact). In the matrix or parameter space in figure 4.2, this theoretical case is marked "Q-S".

Four cases with frequencies, $\kappa = 1.04$, $\kappa = 2.08$, $\kappa = 4.16$ and $\kappa = 8.32$ at an amplitude $v'_{gust} = 0.04$ (i.e. 4% of free-stream velocity u_∞) are selected for the DNS with oscillating boundary conditions, see parameter space in figure 4.2. At the higher two frequencies, the wavelength $\lambda_{x,gust}$ is shorter than the chord length L_c. For all cases, at least one gust period and at least five characteristic time units (number of runs through domain with u_∞) were simulated before recording the time-dependent flow fields for analysis. One gust period was recorded for $\kappa = 1.04$ and $\kappa = 2.08$, while two and four gust periods were recorded for $\kappa = 4.16$ and $\kappa = 8.32$, respectively. Therefore, T_{sim}—which corresponds to the total physical time of the simulation data written out—differs depending on the case. In the corresponding experimental campaign, a gust generator was used to create an unsteady inflow to the airfoil with frequencies up to $\kappa = 2.08$, see Greiner & Würz (2021); Greiner (2024). In this work, however, only the measurement results of the two frequencies $\kappa = 1.1$ and $\kappa = 1.7$ with an effective gust amplitude of $v'_{gust} \approx 0.01$ are used for validation, see matrix in figure 4.2.

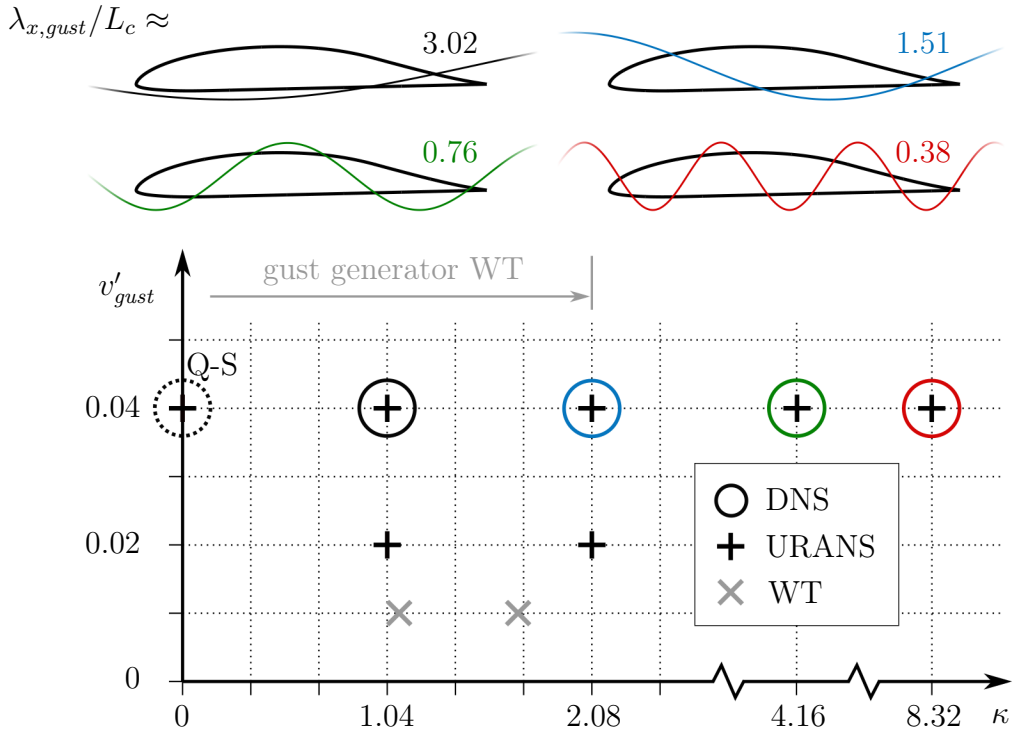

Figure 4.2: Depiction of simulated cases as well as wind-tunnel (WT) experiments within the parameter space of reduced frequency κ and gust amplitude v'_{gust}; top: illustration of ratio of gust wavelength to chord length ($\lambda_{x,gust}/L_c = \pi/\kappa$).

4.1.3 Linear stability properties and actuation

The stability diagram of 2D modes (i.e. with spanwise wavenumber $\beta = 0$) for the reference case is shown in figure 4.3(a). As a base flow for the steady-state stability analysis, the URANS mean flow is used up to $x = 0.5$. For $x > 0.5$, the spanwise averaged DNS mean flow is utilized, due to a better agreement with the experimental results. The evolution of the eigenfunction amplitudes of the amplified 2D modes in downstream direction is depicted in figure 4.3(b) for the corresponding positions marked in figure 4.3(a). At the positions $x = 0.4$ and $x = 0.515$, the eigenfunctions of the modes exhibit the shape of TS-waves under the influence of an adverse pressure gradient. Downstream of $x \approx 0.55$ towards the separation point, however, eigenfunctions display the shape of a shear-layer instability with three peaks in y_s direction, see mode at position $x = 0.6$. Furthermore, the spectrum of amplified modes broadens while shifting up to higher frequencies. Nevertheless, the highest n-factors are reached at the lower frequencies $\omega \approx 120$ due to the head start of the TS-waves in the attached flow upstream.

As in the flow scenario of chapter 3, disturbances may also be introduced into the boundary layer via blowing and suction at the wall, see section 2.6.4 for details.

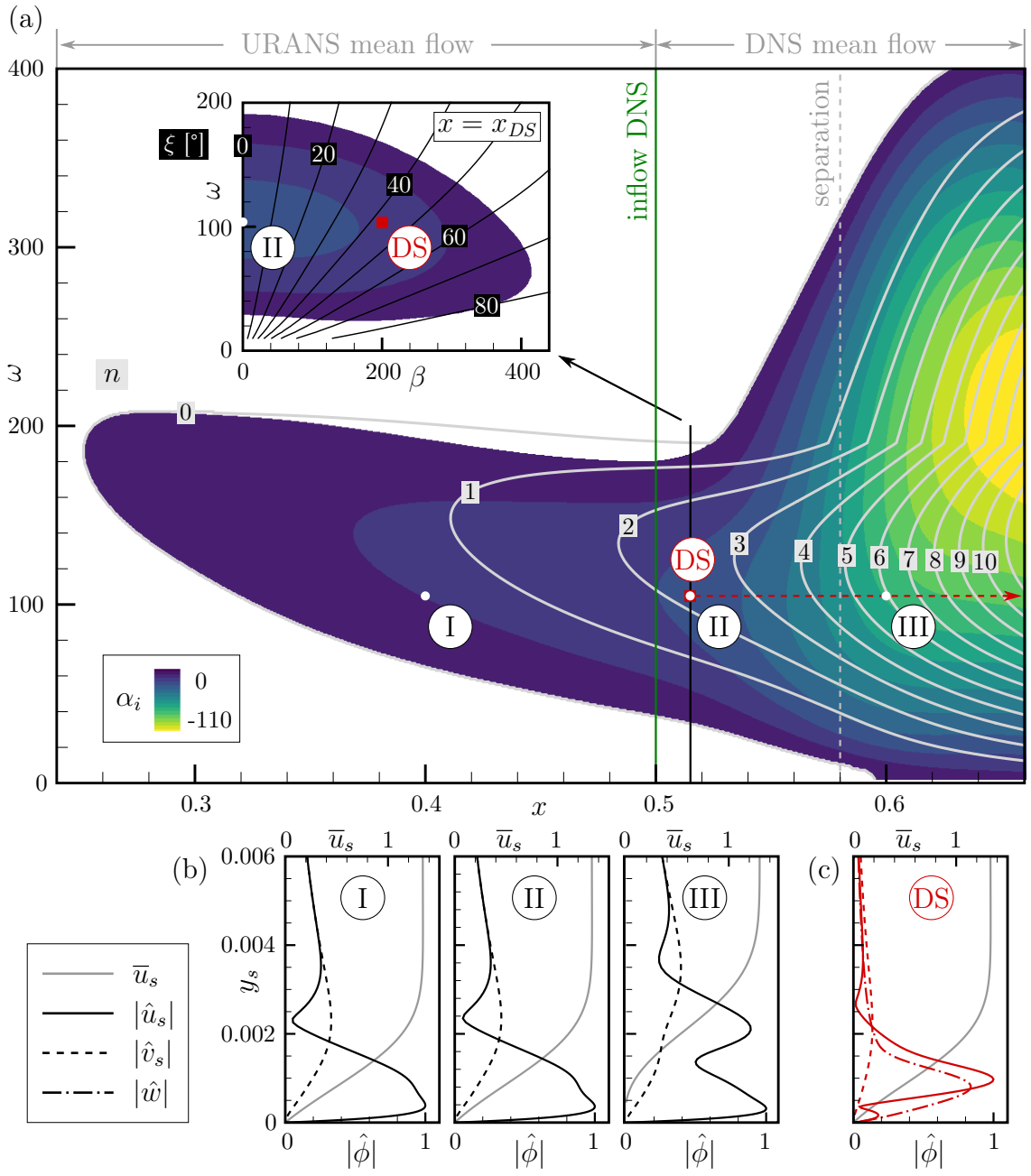

Figure 4.3: (a) Stability diagram with spatial amplification rate α_i and n-factor for steady-state reference case with $AoA_{ref} = 1.5°$ for $\beta = 0$; Inset figure: spatial amplification of 3D modes over β at $x = x_{DS}$ with direction of wave propagation $\xi = \arctan(\beta/\alpha_r)$ (b) Eigenfunctions with $\beta = 0$ (c) Eigenfunctions of oblique modes with $\beta = \pm 200$ at the disturbance strip; all normalized with $\max_{y_s}\{|\hat{u}_s|\}$.

Here, a disturbance strip is placed downstream from the inflow of the DNS domain at $x_{DS} = 0.515$, see $v'_{s,DS}$ in figure 4.1. The amplitudes of realistic disturbances in the laminar boundary layer missing in the simulation can be "recovered" this way, since the domain only starts in the amplified region behind branch I, see position

of disturbance strip "DS" (red) in figure 4.3(a). In addition, this adds the character of *convective instability* to the already existing *absolute instability* of the separation bubble.

In this flow scenario, the so-called *oblique resonance* or *oblique breakdown* with two modes running in opposite spanwise direction z is used. First simulations with this scenario were carried out by Thumm (1991) and Schmid & Henningson (1992). Rist *et al.* (1996) conducted simulations of laminar separation bubbles with the oblique mechanism and compared it to the subharmonic transition scenario. This scenario was chosen for this work, since the 2D structures in the rear region of the separation bubble (favored by the narrow domain in the spanwise direction) are broken up three-dimensionally. Here, the frequency $\omega_{DS} = 104$ and spanwise wavenumbers $\beta_{DS} = \pm 200$ is selected for the pair of oblique modes. Therefore, the modes are labeled $(1, \pm 1)$, based on the definition (h, k) in the double Fourier spectrum, introduced in section 2.6.4. Despite the oblique angle, the modes with ω_{DS} are still highly amplified. The inset figure in figure 4.3(a) shows the amplification in the wavenumber-frequency space at x_{DS} with the position of the mode "DS" (red) with $\beta = 200$ introduced via actuation at the wall traveling in positive z direction. Therefore, as is common for oblique resonance, the direction of wave propagation features an angle of $\xi = \arctan(\beta_{DS}/\alpha_r) \approx 42°$. The respective eigenfunction amplitude of this mode at the disturbance strip is depicted in figure 4.3(c). Again, to allow a clean spectral analysis of the laminar stretch of the flow field with FFT and CWT, the frequency $\omega_{DS} = 104$ was chosen because it always corresponds to a multiple of the fundamental frequency of the simulation ω_{sim}, which depends on the gust frequency and number of simulated gusts. Here, the spanwise wavenumber also determines the size of the domain in the z direction, which is identical to the fundamental wavelength $\lambda_{z,0} = 2\pi/\beta_{DS} = 0.0314$. Based on LST and wind-tunnel measurements ($N_{crit} \approx 12$) of the transition location including turbulent reattachment, a total amplitude of $A_v = 2 \cdot 10^{-5}$ is chosen for the superposed disturbances $v'_{s,(h,k)}$, see equation (2.28). In streamwise direction, the wall-normal blowing/suction is defined with a monopole function (see equation (2.29)) whereas the slit size is $\Delta x_{s,DS} = 5 \cdot 10^{-3}$. The sampling rate for the recorded flow fields is chosen to continuously capture the period of the introduced modes at ω_{DS} with 20 time steps.

4.2 Validation of URANS base flows

In this section, the steady and transient base flows acquired with URANS simulations are validated with experimental results. Furthermore, the feasibility of using these base flows as (unsteady) boundary conditions in the DNS is discussed. In contrast to the LTT case in chapter 3, unsteady velocity profiles were also measured during the

wind-tunnel tests, which are compared with the simulation results in this section.

4.2.1 Mean-flow properties

For validation and fundamental characterization, the steady-state case with AoA_{ref} without gusts is analyzed in terms of the time- and spanwise-averaged pressure distribution c_p as well as skin friction c_f, see figure 4.4. In these distributions, the laminar separation bubble is indicated by a small region of almost constant pressure in c_p and negative values of skin friction $c_f < 0$. The laminar separation bubble in the flow solution of the (2D) URANS turned out to be significantly shorter compared to the results from experiments and subsequent DNS. However, this deviation, which results from the simplified flow physics of the turbulence model used, is not necessarily problematic for the process chain including the following investigations with DNS and LST. The unsteady field solution of the URANS simulations are only imposed on the boundaries of the DNS domain. Again, the velocity profile at the inflow boundary and the pressure gradient at the free stream are most important for the correct representation of the unsteady flow with regard to this application. The results of the following two DNS cases, where the full three-dimensional Navier–Stokes equations are solved, show a flow with an prolonged separated region ($\Delta x_{LSB} \approx 0.12$ which equals ≈ 3.8 domain widths) and an adequate matching of the pressure distribution of the wind-tunnel experiments, see figure 4.4. Furthermore, it is evident from the curve of c_f that the separation point (S) of the DNS results almost perfectly matches the URANS result. This implies that the effect of the pressure gradient in the DNS is consistent with the URANS simulations. Therefore, the URANS flow field can nevertheless be considered as a suitable base flow for the DNS, in case the above specified domain is used. For the (unsteady) linear stability analysis, the flow field of the DNS can be applied as a base flow instead of the URANS solution.

Using hot-wire measurements, the two-dimensional steady-state URANS results can also be validated using the time-averaged profiles of the absolute velocity $|\overline{\boldsymbol{u}}| = \sqrt{\overline{u}^2 + \overline{v}^2}$, see figure 4.5. A typical dimensionless similarity variable

$$\eta = \tilde{y}_s \sqrt{\frac{\tilde{u}_\infty}{\tilde{\nu}\tilde{x}_s}} = y_s \sqrt{Re/x_s}\,, \tag{4.1}$$

is used here for the wall-normal direction. The two locations shown, $x = 0.564$ and $x = 0.594$, are located just before and just after the separation point (S), respectively. As expected, the boundary layer rapidly increases in downstream direction in this area. The boundary-layer thickness seems to be somewhat smaller in the experimental investigations compared to the simulations, which can be explained by a minimal offset of the separation point x_{sep} in the flow direction. However, considering the complexity of the numerical and experimental setups and taking into account this particularly critical position, the agreement is very satisfactory.

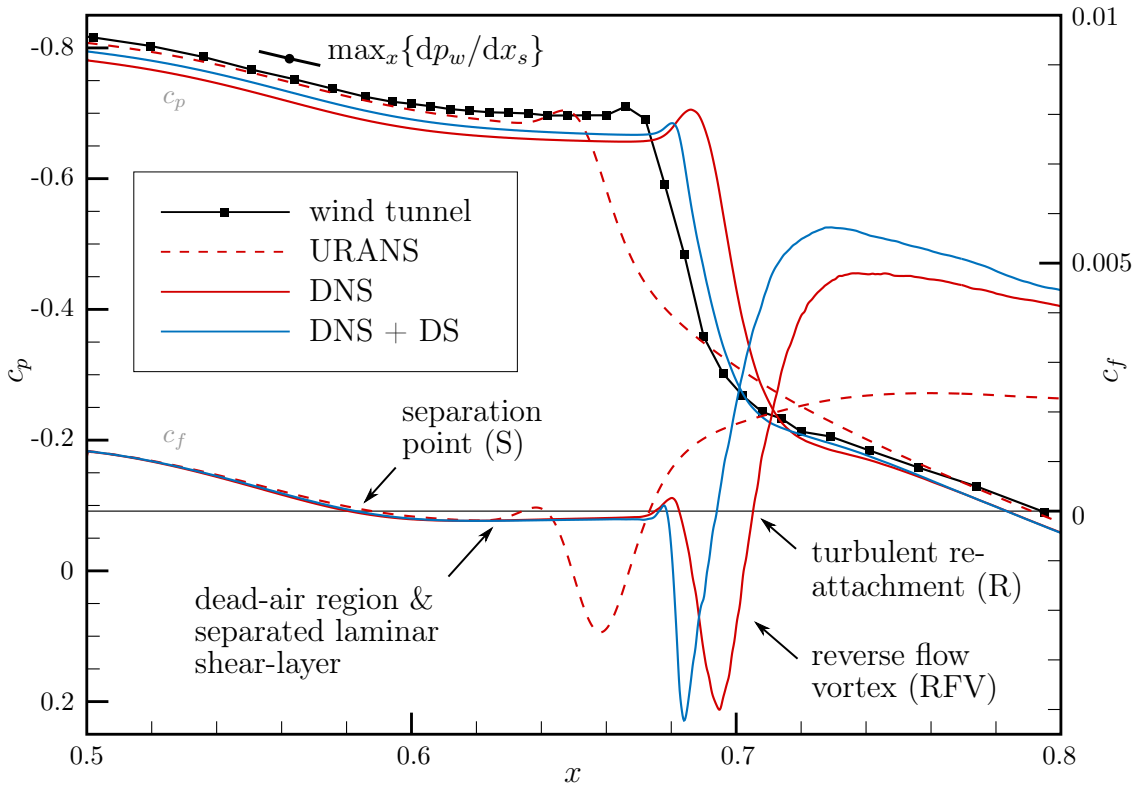

Figure 4.4: Temporal and spanwise averaged pressure distribution c_p and skin friction c_f for steady-state reference case AoA_{ref}.

4.2.2 Unsteady amplitude profiles

In the next step, the transient base flows with DVA gusts can also be characterized and validated with the wind-tunnel measurements. In general, the amplitude profile of the velocity—defined here as the maximum oscillation of the absolute velocity over a full period $\Delta u_{tbf}(\eta) = \max_t\{|\boldsymbol{u}_{tbf}|\} - \min_t\{|\boldsymbol{u}_{tbf}|\}$—provides a deeper insight into the transient boundary-layer development. Oscillating boundary-layer flows are typically characterized by such amplitude profiles in the wall-normal direction, see Hill & Stenning (1960), Reeh (2014) or Agarwal *et al.* (2022). Figure 4.5 shows the amplitude profiles of the simulations and the wind-tunnel measurements for different frequencies κ at the corresponding x positions mentioned above. A special feature of the plot is that the profiles are linearly scaled to the case with a gust amplitude of $v'_{gust} = 0.01$ with $\Delta u^*_{tbf} = \Delta u_{tbf} \cdot 0.01/v'_{gust}$ for better comparability. Moreover, this scaling is also used because the numerical simulations were performed at $v'_{gust} = 0.02$ and 0.04, while an amplitude of $v'_{gust} \approx 0.01$ was yielded in the wind-tunnel experiments. First of all, it can be observed that the scaled profiles for both amplitudes v'_{gust} of the URANS simulations in figure 4.5 (thin solid and dashed lines) match almost perfectly. This is true for the two frequencies κ as well as positions of x depicted here and confirms the validity of the above described

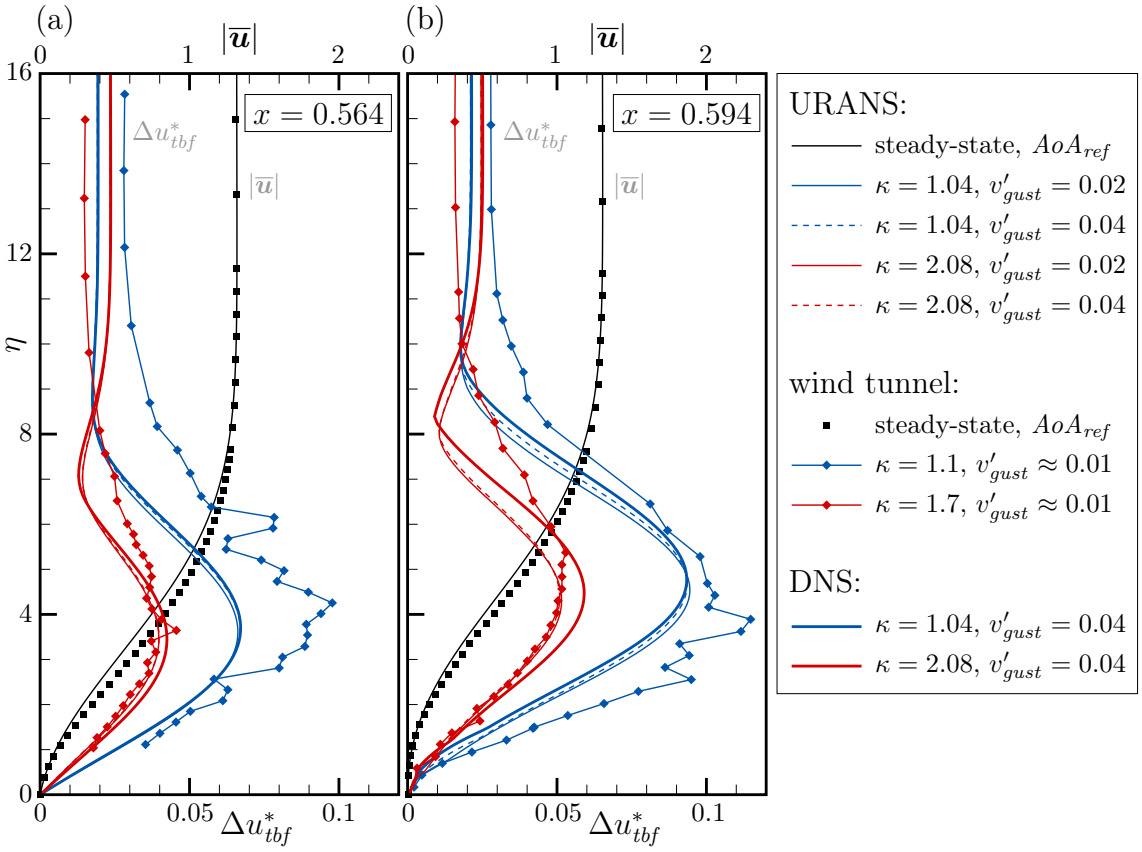

Figure 4.5: Averaged profiles of the absolute velocity $|\overline{\boldsymbol{u}}| = \sqrt{\overline{u}^2 + \overline{v}^2}$ for AoA_{ref} (black) and amplitude profiles of the boundary-layer oscillations Δu^*_{tbf} (scaled to $v'_{gust} = 0.01$) for transient cases (red/blue) in the wall-normal direction η at (a) $x = 0.564$ and (b) $x = 0.594$.

linear amplitude scaling of the profiles for general characterization of the transient base flow. Moreover, it can be concluded that the shape of the amplitude profile essentially depends only on the frequency κ, while the gust amplitude v'_{gust} influences only its scaling. A peak or overshoot can be seen in the profiles within the boundary layer, which is significantly larger than the fluctuation above the boundary-layer edge. The wall-normal distance of the peak increases in proportion to the growth of the boundary-layer thickness from $\eta \approx 2$ at $x = 0.564$ to $\eta \approx 2.8$ at $x = 0.594$. Furthermore, the amplitude profile for $\kappa = 2.08$ exhibits a dip towards the boundary-layer edge. This qualitative behavior is in agreement with the results of previous work on generic, unsteady, flat plate boundary-layer flows, see Hill & Stenning (1960); Obremski & Fejer (1967); Reeh (2014); Agarwal *et al.* (2022).

The most remarkable aspect of the amplitude profiles in figure 4.5, however, is the dependence of the peaks on the gust frequency κ. When doubling the frequency from $\kappa = 1.04$ to $\kappa = 2.08$, the maximum decreases by the factor ≈ 0.64 and ≈ 0.54, respectively for $x = 0.564$ and $x = 0.594$. In general, it is known that the

characteristics of the amplitude-profile overshoot can change with frequency κ, see Reeh (2014). However, the "viscous response" of the airfoil boundary layer cannot be held solely responsible for this behavior. The fluctuation of the velocity profiles—from which the amplitude profiles result—is mainly determined by the pressure gradient $\mathrm{d}p/\mathrm{d}x$, which in turn is imposed by the gusts. However, the "effective amplitude" of the pressure-gradient variation decreases with larger κ. This is due to the fact that the wavelength of the gust $\lambda_{x,gust}$ becomes smaller in relation to the chord length L_c, which increasingly "integrally smears" the influence of the gust amplitude over the finite body of the airfoil. The Sears (1941) function, introduced in section 3.2.1, can again quantify the impact of this effect to some degree. The ratio of the absolute values of the Sears function of the two frequencies is $|S(\kappa = 2.08)|/|S(\kappa = 1.04)| = 0.73$. As expected, this value is close to the above-mentioned factors of the amplitude reduction of the peaks.

The amplitude profiles can likewise be validated with hot-wire measurements carried out in the wind tunnel at different frequencies κ. However, in the experimental investigations, such measurements were performed only at the frequencies $\kappa = 1.1$ and $\kappa = 1.7$ at the gust amplitude of $v'_{gust} \approx 0.01$, see matrix in figure 4.2. First of all, it can clearly be seen in figure 4.5 that the wall-normal distances η of the maxima of the amplitude profiles agree very well with those of the simulations. Furthermore, the above-described trend of the amplitude decrease of the peaks with increasing frequency κ is clearly present in the measurements at a similar rate. It should also be noted that the dip seen in the amplitude profile at $\kappa = 2.08$ in the simulation is not present in the experiment at the higher frequency $\kappa = 1.7$. Possibly the frequency in the experiment is not high enough for this characteristic shape. Again, taking into account the complexity of the numerical and experimental setups, it can be concluded that the unsteady flow physics observed in the wind-tunnel measurements and in the simulations are in satisfactory qualitative agreement.

At this point, it can also be checked whether the unsteady laminar boundary layer is correctly simulated by the subsequent DNS with its unsteady boundary conditions. The amplitude profiles of the DNS (thick lines) show only a slight deviation from the original URANS solution before the separation point (with respect to steady-state reference case) at $x = 0.564$ in figure 4.5(a). At $x = 0.594$ in figure 4.5(b), however, there is a significantly stronger deviation, especially at the frequency $\kappa = 2.08$. This stems from the different equations used in the simulation methods, with the DNS employing the full three-dimensional Navier–Stokes equations to calculate the actual flow physics under the given (transient) boundary conditions. Since the point $x = 0.594$ lies already in the continuously separated flow for both frequencies κ, the deviation of the amplitude profiles is not surprising, because the turbulence model lacked the correct representation of the separation bubble in the steady-state case.

In both DNS and wind-tunnel experiments, the influence of unstable modes such as TS-waves on Δu_{tbf} can be neglected since their amplitudes in the laminar flow

(where linear theory applies) are extremely small compared to the induced boundary-layer fluctuations of the gusts. Rather, the periodic fluctuation of the boundary-layer profiles characterized here is one of the aspects of the resulting unsteady base flow, which determines the transient evolution of amplified modes. The general spatio-temporal impact of these large-scale perturbations including the viscous delay of the boundary layer on the development of modes has already been presented and discussed in detail for the LTT case (attached flow) in sections 3.2 & 3.3. Here, the same qualitative behavior is observed, which is why only the resulting n-factors are discussed in the 4.4.4 section.

4.3 DNS of steady-state reference case

In the previous section, the URANS flow fields were validated for the steady-state case as well as for the case with gusts, and their applicability as transient base flows for DNS was confirmed. In this section, the resulting flow field of the DNS is validated with spectral means and characterized in detail.

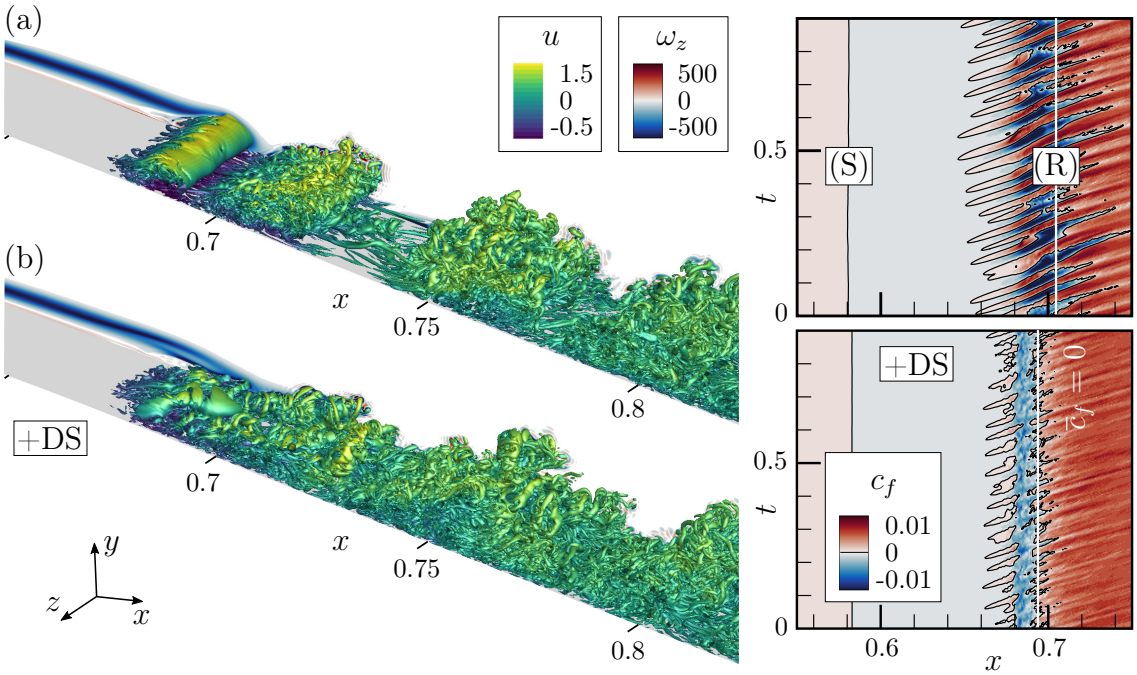

Figure 4.6: Instantaneous vortex visualizations with isocontours for $Q = 10,000$ (left) with spanwise averaged skin friction c_f in the x/t plane (right) for the steady-state case with AoA_{ref}. (a) DNS without actuation (b) DNS with disturbance strip.

As displayed in figure 4.4, the laminar separation bubble in the DNS with a disturbance strip "+DS"—see explanation in section 4.1.3—is slightly smaller and closes earlier than in the DNS without disturbance input. Due to a shorter reverse flow

vortex, the point of turbulent reattachment (R) moves upstream. As for the pressure distribution c_p, this result matches better to the wind-tunnel measurements, which suggests that the disturbance input "recovers" the missing disturbance level (free-stream turbulence and upstream TS-waves) at the inflow. However, this also changes the nature of the flow with respect to laminar-to-turbulent transition of the separated shear-layer and the following turbulent reattachment, see the instantaneous flow visualizations in figure 4.6 (left).

The simulation without disturbance input in figure 4.6(a) shows coherent 2D structures traveling in streamwise direction which are arising in the rear region of the laminar separation bubble. The roll-up of these structures can be attributed to the shear-layer or *Kelvin–Helmholtz* instability. Several authors concluded that for incompressible flows (hence for low Mach numbers as in this case) a 2D absolute instability is only expected if the mean flow exhibits at least 15% of reverse-flow intensity in the separation bubble, see Rist & Maucher (2002). Since the reference case with AoA_{ref} shows a reverse-flow intensity of 20%, the presence of a self-sustaining absolute instability can be assumed with confidence. The transition from laminar-to-turbulent flow is thus caused by an intrinsic absolute instability involving natural frequencies and does not necessarily depend on upstream disturbances, but rather on local flow properties. However, it must be mentioned that a two-dimensional character is favored here, since the relatively narrow simulation domain in the spanwise direction with the size $\lambda_{z,0}$ doesn't allow "slightly oblique" waves which could break up the structures. The spanwise averaged spectral analysis of the wall pressure p'_w of the simulation without disturbance input shows a reasonable agreement with the wind-tunnel measurements with respect to frequency content, cf. figure 4.7(a) with (b). In both results, the dominant natural frequency lies at $\omega \approx 110$. Shortly downstream of the occurrence of those peaks, the frequency spectrum fills up rapidly due to non-linear interactions indicating breakdown to turbulence. As expected and in agreement with the pressure distribution c_p described above, this occurs slightly further upstream in the measurements, since initial disturbances are present in contrast to this simulation.

In addition to the absolute instability, a convective instability is added when introducing unsteady modes via the disturbance strip. The impact of the application of an oblique resonance scenario (see description in section 4.1.3) can be observed in the instantaneous vortex visualization in figure 4.6(b). Compared to the simulation without disturbance input, the dominant 2D structures break up three-dimensionally due to the oblique modes. These observations are consistent with the results of Rist *et al.* (1996), where large 2D disturbance waves were found in the case of subharmonic resonance, but a rapid breakdown to 3D structures in the case of oblique resonance. As expected, the most prominent frequency in the Fourier analysis of the wall pressure—see figure 4.7(c)—is that of the disturbance input $\omega_{DS} = 104$, while its higher harmonics are likewise visible. In a sense, the separation bubble

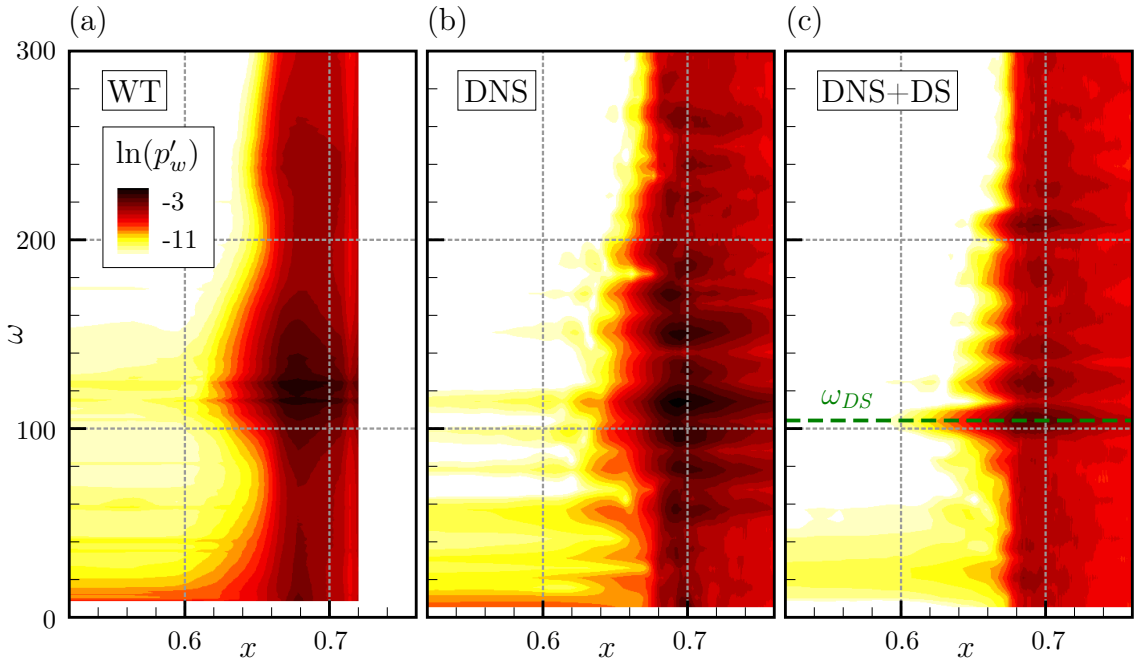

Figure 4.7: FFT of wall pressure p'_w for steady-state case with AoA_{ref}. (a) Wind tunnel (b) DNS (c) DNS with disturbance strip.

now acts as a resonator to the actuation signal.

Another possibility to compare both simulation scenarios is the visualization of the (spanwise averaged) skin friction in the x/t plane, see figure 4.6 (right). Without disturbance input, the coherent 2D structures are clearly visible in the form of inclined footprints or traces with $c_f < 0$ and $c_f > 0$ starting from $x \approx 0.65$. Evidently, these 2D structures have an impact on the wall ranging from the center of the separation bubble to far behind the turbulent reattachment point, where vortex-shedding is observed. Even though a clear natural frequency can be seen here, it is fair to speak of a relatively high temporal intermittency of the flow. This is not the case in the simulation with the disturbance input—see figure 4.6(b)—in which no footprints of 2D structures are found and the flow is hardly intermittent in time. Here, the transition in the shear-layer occurs in a regular manner, resulting in a relatively ordered reattachment in which the reverse-flow vortex can be seen continuously over time.

For a detailed examination of the transition process, the double-spectral analysis is utilized. Figure 4.8 shows the modal amplitudes of the disturbance velocity component $u'_{s,(h,k)}$ in the wall-normal system with $h \in \{0.5;\ 1 \dots 6\}$ and $k \in \{1 \dots 5\}$ with respect to ω_{DS} and β_{DS}, respectively. In both scenarios, the point of non-linear saturation occurs at about $x \approx 0.68$. However, the cases differ significantly with respect to the transition mechanism. Well before the separated region, two-dimensional perturbations can be observed for several frequencies $(h, 0)$ for the case without dis-

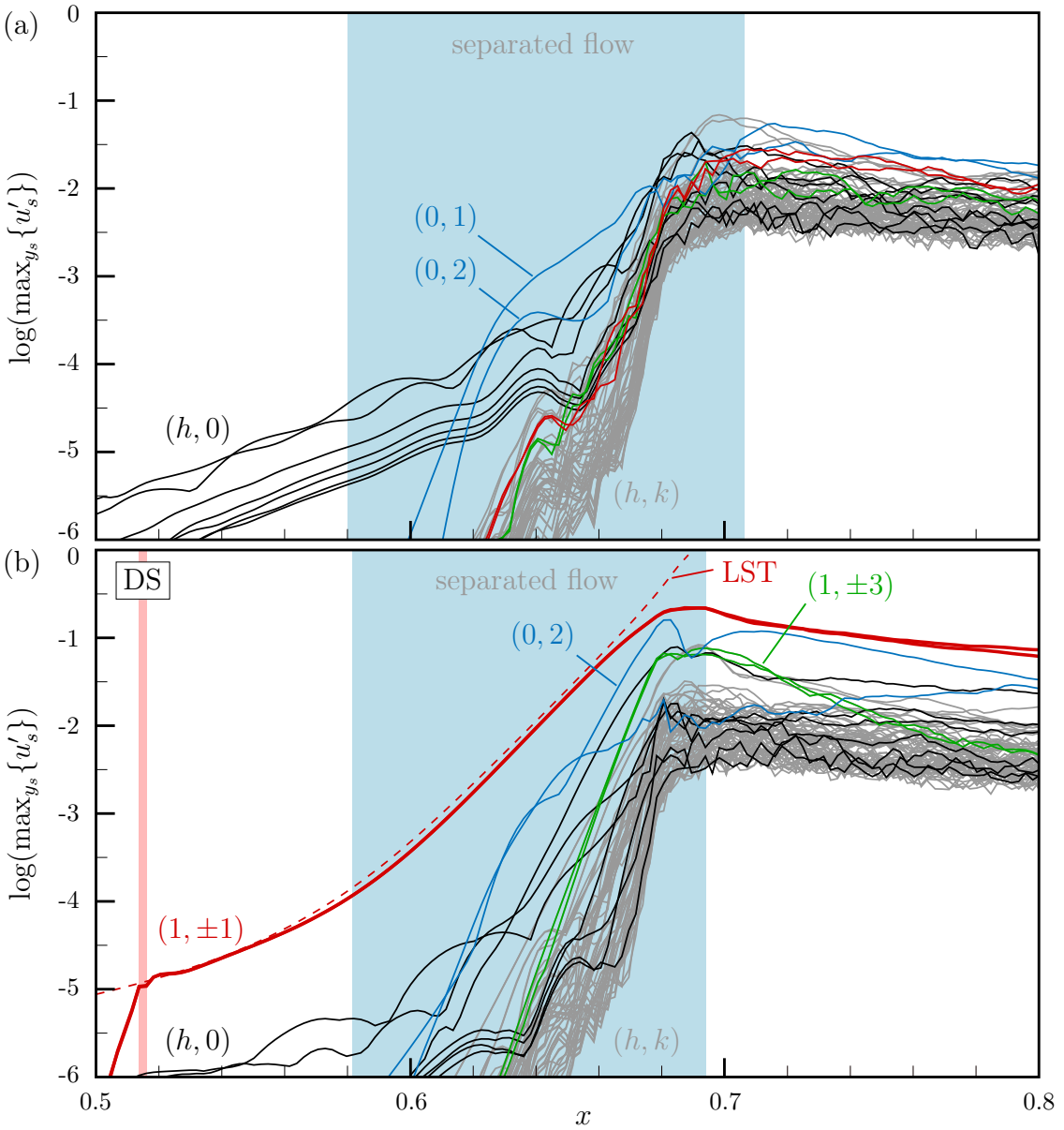

Figure 4.8: Downstream development of modal disturbance amplitude $u'_{s,(h,k)}$ (maximum over y_s) for steady-state with AoA_{ref}. (a) DNS without actuation (b) DNS with disturbance strip.

turbance input, see figure 4.8(a). These stem from upstream traveling waves from the strongly fluctuating rear part of the separation bubble, which in turn excite the boundary layer upstream of the separation. Therefore, this can be considered as a kind of feedback-loop, i.e. an absolute (or global) instability. The steady modes $(0, 1)$ and $(0, 2)$—which can be regarded as a mean flow distortion in spanwise direction or streaks—grow quickly before the wavenumber-frequency spectrum fills up due to non-linear interactions. In contrast, the modal development of the case with

disturbance input behaves according to the oblique resonance transition scenario, see figure 4.8(b). With the introduced modes $(1, \pm 1)$ at the disturbance strip, mode $(0, 2)$ is generated which in turn generates the modes $(1, \pm 3)$. A resonance of the latter modes with the introduced (primary) modes ultimately leads to transition. The modal development of the pair of oblique waves follows linear theory. Here, the location $x_{tr} = 0.665$ can be considered as the point of shear-layer transition, since the amplitudes deviate from linear theory just before reaching the non-linear saturation. An important finding is that the 2D waves $(h, 0)$ do not play an active role before the onset of the non-linear interactions in this simulation. Therefore, it can be concluded that the absolute instability plays a minor role—at least in the steady-state case with AoA_{ref}—if the disturbance strip is switched on. This is an important observation which will be relevant for the interpretation of the respective analyses of transition in separation bubbles under the influence of gusts in section 4.4.5.

4.4 DNS of unsteady cases with gusts

Results of the simulations with gusts including interpretations and conclusions are presented in this section, which is divided into five sections: the results of the quasi-steady consideration with $\kappa \to 0$, the results of transient flows with actual gusts at different frequencies $\kappa > 0$, the characterization of the separation point, the characterization of the reattachment including the transition behavior and finally the contribution of the absolute instability as well as lock-in effects.

4.4.1 Quasi-steady consideration ($\kappa \to 0$)

The impact of a quasi-steady gust ($\kappa \to 0$) can be characterized with steady-state simulations at different angles of attack AoA according to the gust amplitude. In this section, only results of simulations where the disturbance strip was activated are presented.

The spatial separation intermittency γ_{z,c_f}, representing the fraction of separated flow over the spanwise direction z (therefore $c_f < 0$), is shown in the x/t plane for AoA_+, AoA_{ref} and AoA_- in figure 4.9. As expected, the separation bubble shifts upstream or downstream depending on the adverse pressure gradient for each AoA, indicated by the black/dark area. (The two contour colors for $\gamma_{z,c_f} > 0.5$ represent the areas in which the spanwise average of skin friction c_f is negative.) By using γ_{z,c_f}, it is easy to identify whether coherent 2D structures are formed during reattachment of the transient separation bubble at a given time t and location x. The point of separation (S) as well as the time averages of the locations of shear-layer transition (T) and turbulent reattachment (R) are also marked in figure 4.9. The transition point (T) is defined according to the amplitude development of the

introduced modes, see spectral analysis in section 4.3. Moreover, the reverse-flow vortex can be seen in this plot represented by a darker (hence mostly separated) zone, which is marked "RFV". This area serves to locate the end of the separation bubble, since the reattachment point (R) naturally lies directly behind it. The length of the laminar separation bubble from point (S) to point (R) is denoted here as Δx_{LSB}, see figure 4.9(a).

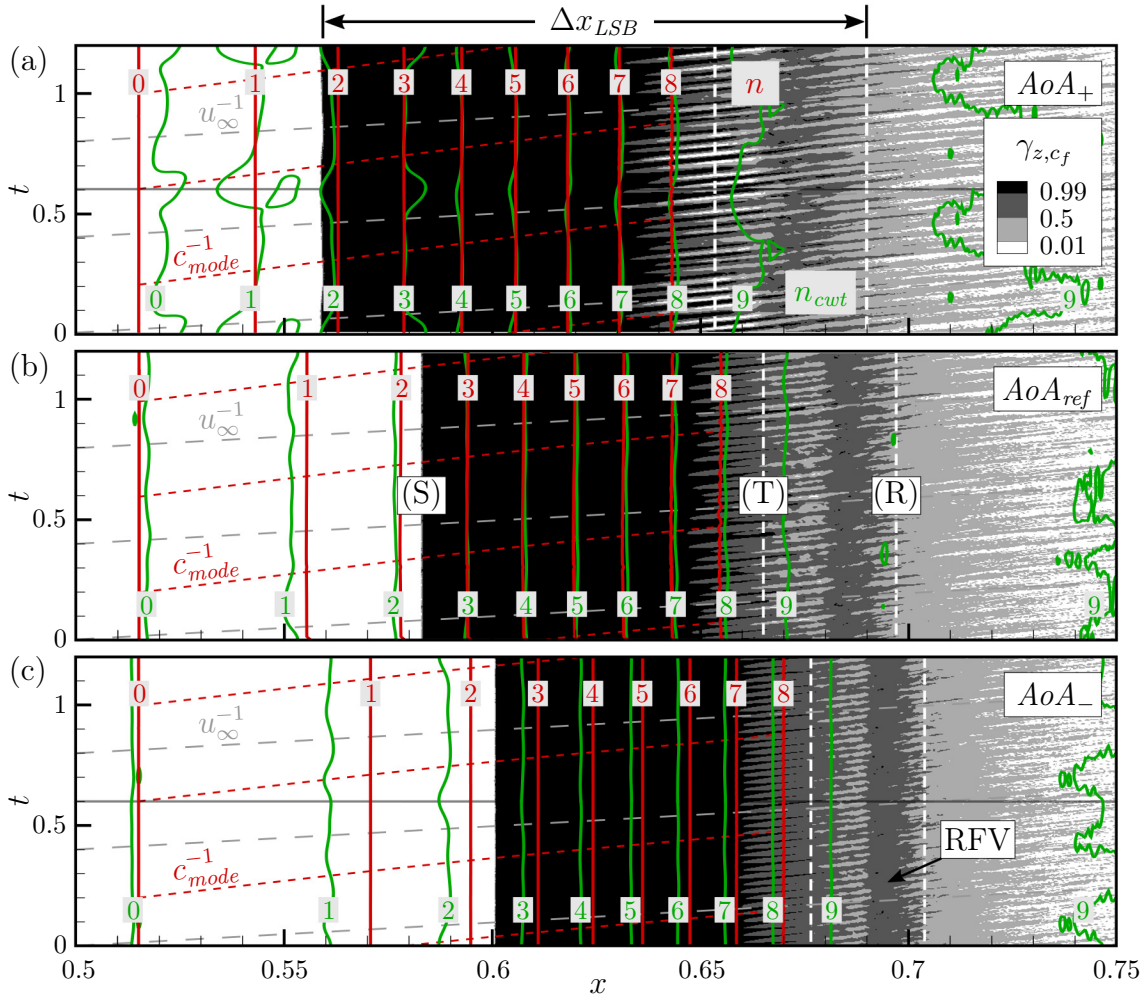

Figure 4.9: Separation intermittency γ_{z,c_f} in spanwise direction z with n-factors from LST and amplitudes of the continuous wavelet transform n_{cwt} in the x/t plane for steady-state cases: (a) AoA_+ (b) AoA_{ref} (c) AoA_-.

Furthermore, the n-factors of the modes $(1, \pm 1)$ calculated with equation (2.20) along the trajectories with the phase velocity c_{mode} is given in figure 4.9. Due to the steady-state conditions, the result is equivalent to that of the classical e^n-method. Nevertheless, the instantaneous (spanwise averaged) flow fields of the DNS served as base flows here. This further demonstrates the robustness of the method, since it is possible to properly calculate the amplification rates even if intrinsic oscillations

are present towards the end of the analyzed flow field. In all cases, the phase velocity c_{mode} of the shear-layer instability increases with downstream convection, as indicated by the decreasing inclination of the trajectories (red dashed lines) in the x/t plane. This is particularly pronounced in the separated region, since the velocity at the inflection point of the base-flow velocity profile grows due to the increasing distance from the wall. The mean phase speeds c_{mode} (integrated from the disturbance strip up to $n = 8$) for the three cases AoA_+, AoA_{ref} and AoA_- are $0.46u_\infty$, $0.51u_\infty$ and $0.55u_\infty$, respectively. Although the shortest separated region is found for AoA_-, the modes here exhibit a higher phase speed on average due to the extended length up to $x \approx 0.67$. Performing the (unsteady) LST based on flow fields from the DNS with the disturbance strip turned off did not result in a significant difference in the n-factors.

Due to transient, non-linear or non-parallel effects, the amplitudes of the actual amplified modes may deviate from the calculated n-factors of the local linear stability analysis based on the instantaneous base flow. As in the DNS of LTT case in section 3.4, the unsteady flow field is analyzed with the means of CWT in order to acquire the corresponding downstream development of the streamwise velocity perturbation u'_s. Therefore, n_{cwt} relates to the introduced amplified modes $(1, \pm 1)$ with ω_{DS} which are subject to the cyclic variation imposed by the gust. In this section, the application of this method for a *separated* flow is first validated and evaluated for the quasi-steady cases before being applied to the transient cases with gusts in the next section. It should be noted that, in contrast to the fundamental resonance scenario in section 3.4, the spanwise averaged flow field is unsuitable for analysis here, since the u'_s perturbations cancel each other out when employing the oblique resonance scenario. Hence, the CWT is performed at a given spanwise position $z = const.$ Based on the average amplitude found at the disturbance strip in the steady-state case AoA_{ref}, $A_u = 3 \cdot 10^{-5}$ was determined and used to calculate n_{cwt} with equation (2.34) for all other flow cases. Due to boundary-layer receptivity, the induced amplitude in flow direction A_u is slightly higher than the forced vertical amplitude $A_v = 2 \cdot 10^{-5}$ (see section 4.1.3) of the wall-normal blowing and suction.

In figure 4.9, the spatio-temporal development of n_{cwt} is indicated by the green contour lines. A very good agreement with the n-factors of the linear theory can be found for AoA_{ref}. Furthermore, the levels barely fluctuate in time as expected for a steady-state case. For AoA_+, the upper values $n_{cwt} > 3$ are also in perfect agreement with linear theory. However, a slight deviation due to a quicker increase of the values n_{cwt} can be seen for AoA_-. In contrast to the LST with the maximum value of $n = 8$, the CWT reaches a value up to $n_{cwt} = 9$ and reflects the peak of non-linear saturation. The temporal boundary effects—also known as cone of influence (COI), see explanation in section 2.7,—can be evaluated here. The results presented for AoA_{ref} in figure 4.9(b) are based on simulation data obtained over time $T_{sim} = 1.2$. For AoA_+ and AoA_- in figure 4.9(a) & (c), however, only half of

the time is available, which is why the data is "doubled" in time, see in horizontal line at $t = 0.6$ indicating the separation of the "periodic" time series. For AoA_{ref} as well as AoA_{-} no significant boundary effects are visible at the beginning and end of the time series. At AoA_{+}, however, fluctuations of n_{cwt} can indeed be found, which are outside the temporal limit of the COI at this frequency. This is especially true for the attached flow, where the amplitudes of $u'_{s,cwt}$ are still small. Responsible for this are intermittent disturbances which travel upstream from the inherently unstable separation bubble. These perturbations affect the result at the temporal edges because, unlike the actuation with ω_{DS}, they do not behave periodically with respect to the gust frequency ω_{gust}.

As described in section 4.2.1, the time average of the shear-layer transition location can be pinned at $x_{tr} = 0.665$ for the stationary case AoA_{ref}, which corresponds to $n_{cwt} \approx 8.6$, see white dashed lines (T) in figure 4.9. In all three cases, the earliest temporary occurring local reattachments ($\gamma_{z,c_f} < 0.99$) start at $n_{(cwt)} \approx 7.5$. First of all, it is interesting that the introduced convective modes do not seem to be affected by those reattachment fluctuations near the wall, since linear stability theory and wavelet analysis agree very well. Given that those fluctuating structures always occur at the same level of $n_{(cwt)}$, they can be assumed to be associated with the transition point (T) and the final reattachment (R) of the flow further downstream. Therefore, the early local reattachments implicitly depend on the amplification of the introduced oblique modes, at least at steady-state conditions. However, at AoA_{+}, distinct 2D structures ($\gamma_{z,c_f} > 0.99$ and $\gamma_{z,c_f} < 0.01$) can again be found in the trailing region of the bubble including some intermittency in time, resembling figure 4.6(a). Furthermore, the instantaneous transition location is mildly fluctuating over time (indicated by the line of $n_{cwt} = 9$), most likely due to an impact of the 2D structures on the transient base flow. In the case of AoA_{-}, on the other hand, the transition and area of reattachment seems to be even more determined and locked onto the disturbance input compared to AoA_{ref}. Therefore, it can be assumed that at AoA_{+}—which corresponds to the quasi-steady gust phase at maximum adverse pressure gradient—the absolute instability again plays a partial role.

4.4.2 Simulations with gusts ($\kappa > 0$)

The DNS with periodic gusts employing transient base flows are presented analogously to the analysis for the steady-state cases described in the previous section. Unless explicitly stated otherwise, all results presented here are from simulations with the disturbance strip turned on. In figures 4.10 & 4.11, the spanwise separation intermittency γ_{z,c_f} for the four simulations with different reduced frequencies κ is plotted in the x/t plane. The time in this graph is normalized by the respective oscillation period T. However, the y axis is scaled to physically match the non-dimensional time t in figure 4.9 of the steady-state cases for better compari-

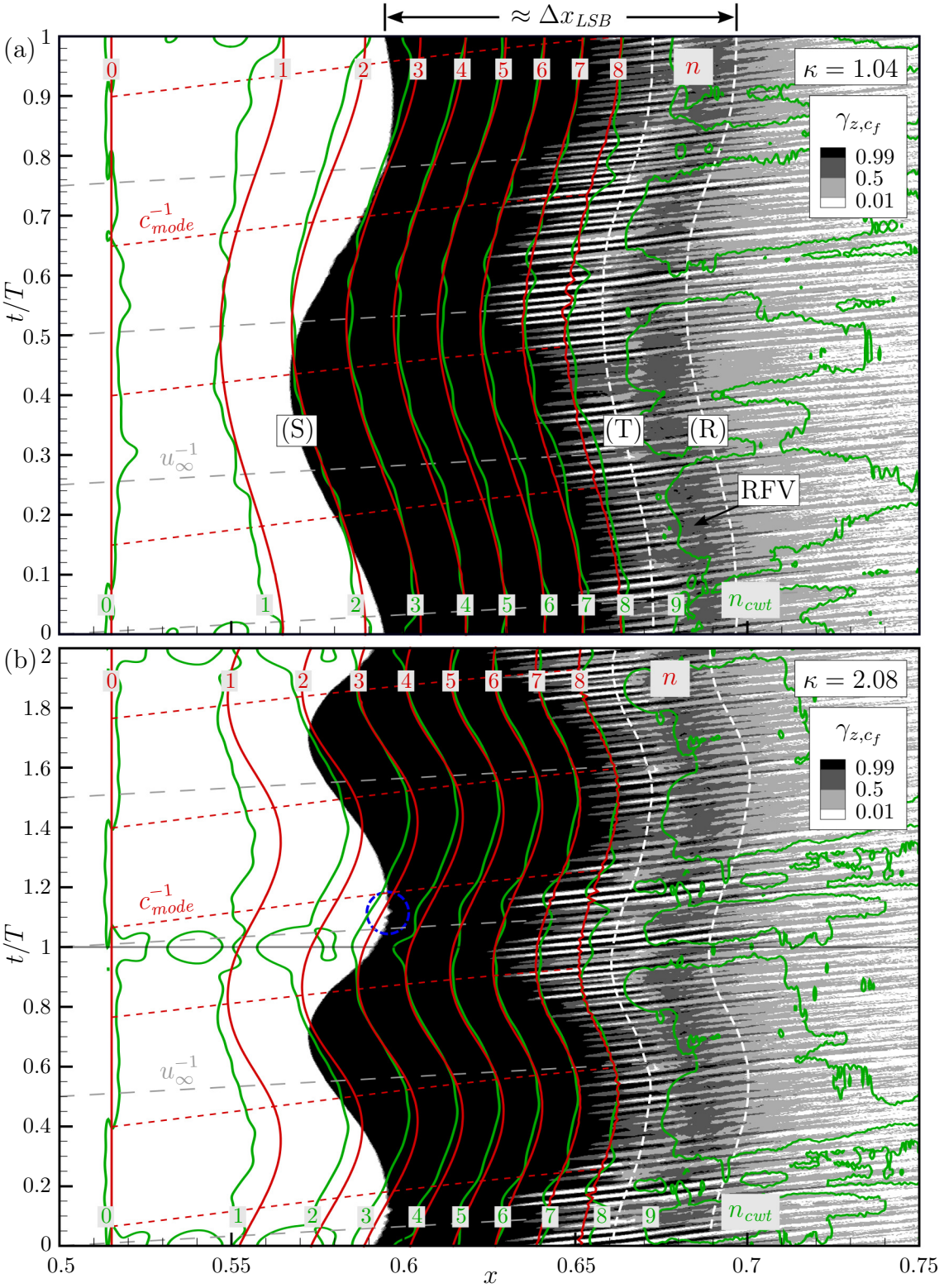

Figure 4.10: Separation intermittency γ_{z,c_f} in spanwise direction z with unsteady n-factors from LST and amplitudes of the continuous wavelet transform n_{cwt} in the x/t plane for simulations with gust frequencies: (a) $\kappa = 1.04$ (b) $\kappa = 2.08$.

son. Here, the separation bubble (indicated by the black/dark area) actually travels upstream and downstream within the period T of the oscillating adverse pressure gradient induced by a physical gust with $\kappa > 0$.

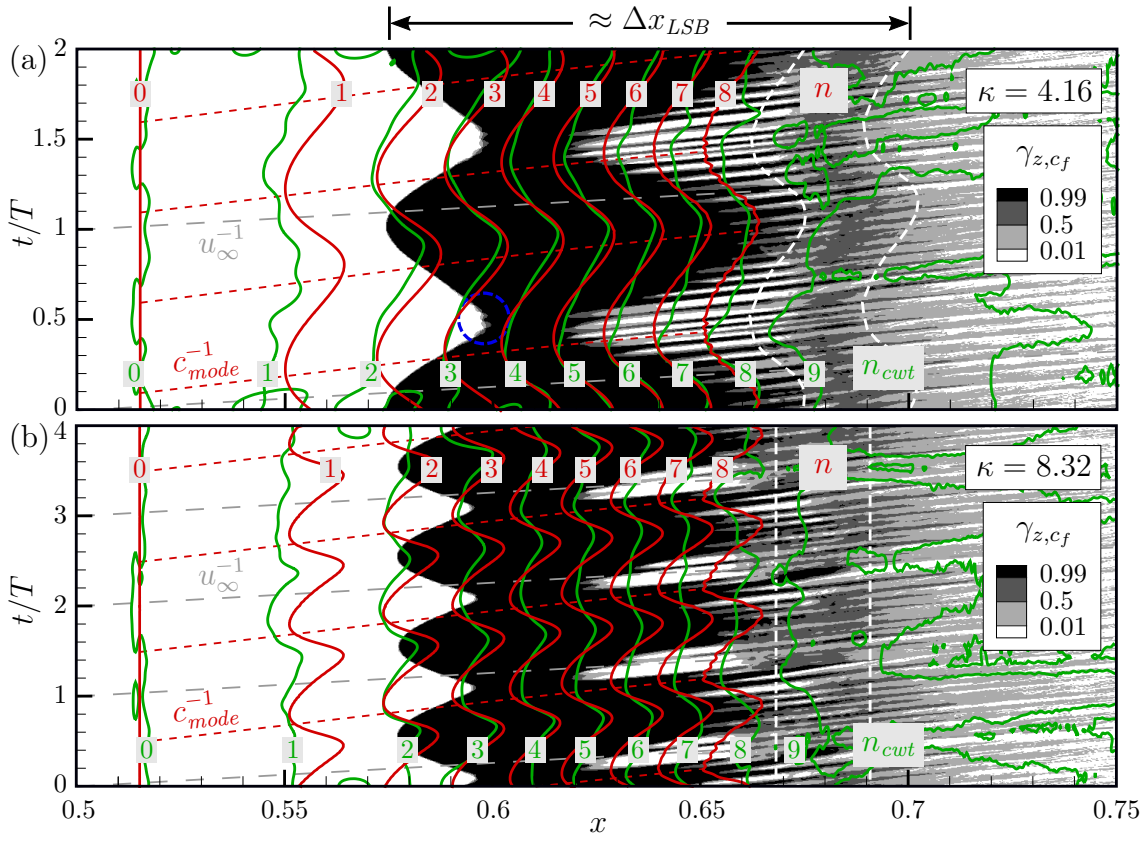

Figure 4.11: Separation intermittency γ_{z,c_f} in spanwise direction z with unsteady n-factors from LST and amplitudes of the continuous wavelet transform n_{cwt} in the x/t plane for simulations with gust frequencies: (a) $\kappa = 4.16$ (b) $\kappa = 8.32$.

In figures 4.10 & 4.11, the unsteady n-factors from linear theory oscillate periodically due to the DNS flow solution used as a transient base flow. In contrast to the quasi-steady cases, the values for the amplification rate α_i of the modes are time-dependent and lead to a harmonic oscillation of the n-factor contour lines in the x/t plane. Moreover, in these transient cases, the spatio-temporal dependence of the phase velocity c_{mode} (see inclination of mode trajectories) has an influence on the position of the resulting n-factor curves. This factor is more significant here in comparison to the attached flow scenario of chapter 3, since the phase speed changes even more in downstream direction.

The n_{cwt}-factors of the continuous wavelet transform show in general a very good agreement with the n-factors of the linear stability analysis. As in the LTT case presented in chapter 3, not only is the periodic behavior of the amplified modes qualitatively very well reflected, but also the levels of the highest $n_{(cwt)}$-factors match

remarkably well. Since the values for $n_{cwt} = 0$ fluctuate only very little around the position of the disturbance strip ($n = 0$), the assumption of quasi-steady behavior of the receptivity can be confirmed, at least for transient cases investigated here. (On close inspection, a slight oscillation of $n_{cwt} = 0$ to the period T of the gusts can be observed for the cases $\kappa = 2.08$ and $\kappa = 4.16$, but this is nevertheless neglected here.) The low values of n_{cwt} in the region of attached flow are somewhat wiggly in all cases. Since the amplitudes of $u'_{s,cwt}$, which are still very small in this region, are superimposed by noise from other inherent disturbances as well as interference, these slight deviations are not surprising. The results of $\kappa = 1.04$, $\kappa = 4.16$, and $\kappa = 8.32$ shown in figures 4.10 & 4.11 represent the complete time T_{sim} of the recorded simulation data. At $\kappa = 2.08$ in figure 4.10(b), however, the simulation result is shown in sequence twice for better illustration which is indicated by a thin horizontal line at $t/T = 1$ for separation. Accordingly, the already mentioned boundary effects on n_{cwt} can be found at the temporal beginning and end of the data, as well as for $\kappa = 2.08$ at $t/T = 1$. As in the steady-state case of AoA_+, see figure 4.9, the temporal influence of the effects—which are mainly seen at low levels of n_{cwt}—correspond to the COI.

4.4.3 Characterization of separation point

First of all, the motion of the separation point can be characterized for the quasi-steady consideration ($\kappa \to 0$). The distinct interface between the attached flow and the fully separated flow at (S) in figure 4.9 shows that the separation point does not vary with time in either flow direction x or spanwise direction z. As commonly known, the separation location of laminar separation bubbles is mainly determined by the pressure gradient $\mathrm{d}p/\mathrm{d}x$. Figure 4.12(a) shows the spanwise mean of the separation point x_{sep} with the streamwise pressure gradient in the x/t plane for the three steady-state cases. It can be seen that the separation always occurs downstream of the maximum of the pressure gradient $x(t)|_{\max_x\{\mathrm{d}p_w/\mathrm{d}x_s\}}$ (black dashed line) at a similar distance.

In the simulations with actual gusts ($\kappa > 0$), the separation point of the bubble also seems to remain almost continuously uniform in the spanwise direction z over the entire period in all cases, see figures 4.10 & 4.11. However, slight variations in the downstream movement are apparent, which will be discussed later in the characterization of the unsteady reattachment. As for the steady-state flows, figure 4.12(b) & (c) depict the spanwise mean of the separation point x_{sep} with the instantaneous streamwise pressure gradient in the x/t plane for $\kappa = 1.04$ and $\kappa = 2.08$, respectively. Here, in contrast to figures 4.10 & 4.11, the time scale is not normalized to the period T. Based on the behavior of the quasi-steady consideration in figure 4.12(a), it can be assumed that the separation point for an "infinitely large" gust with $\kappa \to 0$ is always in phase with the maximum of the pressure gradient $x(t)|_{\max_x\{\mathrm{d}p_w/\mathrm{d}x_s\}}$. For

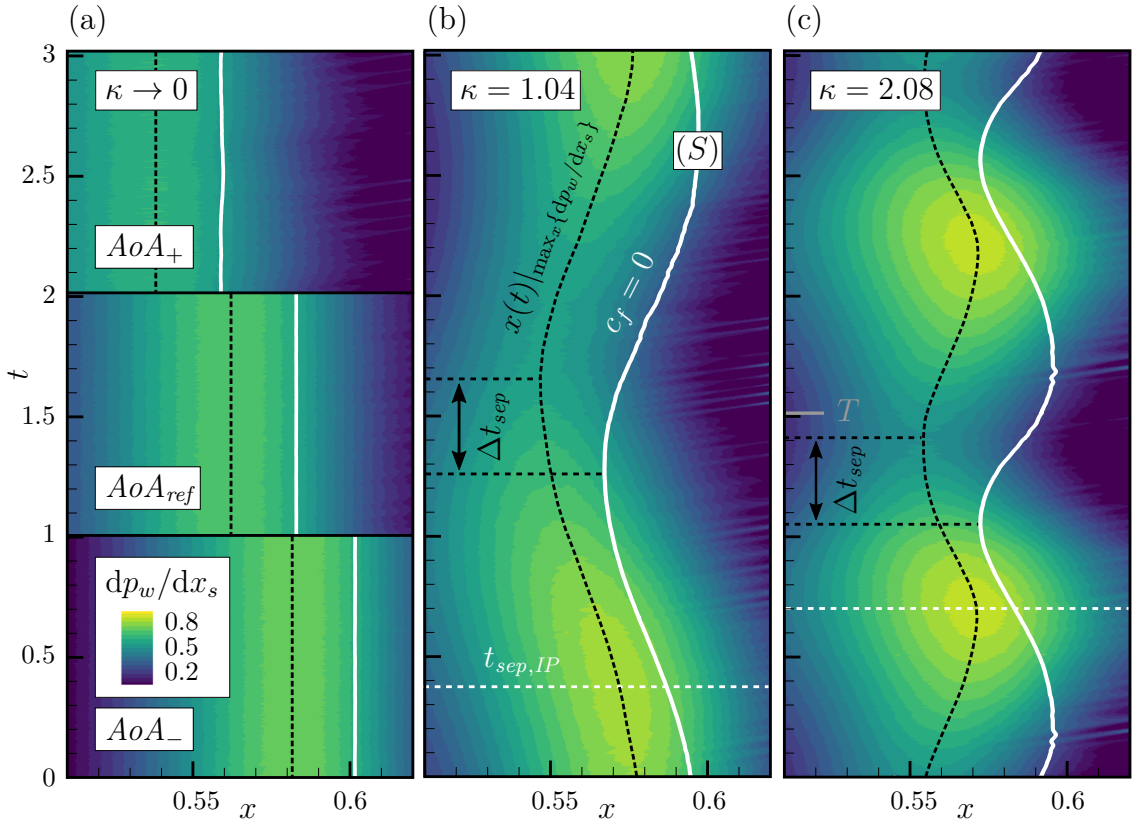

Figure 4.12: Unsteady streamwise pressure gradient $\mathrm{d}p_w/\mathrm{d}x_s$ (black dashed line: maximum in x direction) with point of separation (S) with $c_f = 0$ in the x/t plane. (a) $\kappa \to 0$ (steady-state cases) (b) $\kappa = 1.04$ (c) $\kappa = 2.08$.

$\kappa = 1.04$, however, a phase lag Δt_{sep} of the oscillation of the separation line to the oscillation of the pressure gradient maximum can already be observed. Similar to the behavior of the shape factor observed in the attached-flow scenario in section 3.2.2, this transient effect arises from the viscous time scale of the boundary layer. Furthermore, it can be assumed that additional delaying effects are induced by the separated region. The relative phase lag with respect to a period $\Delta t_{sep}/T$ becomes significantly larger for the higher frequency $\kappa = 2.08$ in figure 4.12(c). Interestingly, the physical time delay Δt_{sep} with respect to the spatial minima of these oscillations remains almost the same from $\kappa = 1.04$ to $\kappa = 2.08$, which furthermore suggests a viscous time delay which is not tied to the gust period T. Among other characteristics of the motion of the separation point, the phase offset $\Delta t_{sep}/T$ is plotted over the investigated frequencies κ in figure 4.13. This trend behaves sublinearly up to $\kappa = 4.16$, since the physical unnormalized Δt_{sep} changes only slightly. As for the other characteristics, $\kappa = 8.32$ has to be considered as a special case here, since lock-in effects are present which will be discussed in section 4.4.5.

Moreover, it can be observed in figure 4.12(b) & (c) that the inflection point of

the motion of the separation point x_{sep} is in phase with the temporal maximum of the pressure gradient $x(t)|_{\max_x\{\mathrm{d}p_w/\mathrm{d}x_s\}}$ for both transient cases, see dashed line with $t_{sep,IP}$. In other words, the separation point has the highest velocity in the upstream direction at the time of the maximum pressure gradient. This observation also holds for $\kappa = 4.16$, but not for $\kappa = 8.32$. Furthermore, the upstream and downstream velocities of the separation point $\dot{x}_{sep}$ start to differ towards higher frequencies κ. While for $\kappa = 1.04$ the upstream and downstream velocities are about the same, for $\kappa = 2.08$ the separation point is found to move slightly slower upstream than downstream. This is interesting since this is exactly the opposite for the periodic motion of the laminar-to-turbulent transition in oscillating boundary layers, see discussion regarding unsteady n-factors below or chapter 3. Such behavior can be explained by the fact that the pressure gradient during the downstream movement is significantly weaker at $\kappa = 2.08$ compared to $\kappa = 1.04$, which causes the separation point to be pushed downstream more rapidly. The same characteristics can also be found for $\kappa = 4.16$, but not for $\kappa = 8.32$, cf. figure 4.13.

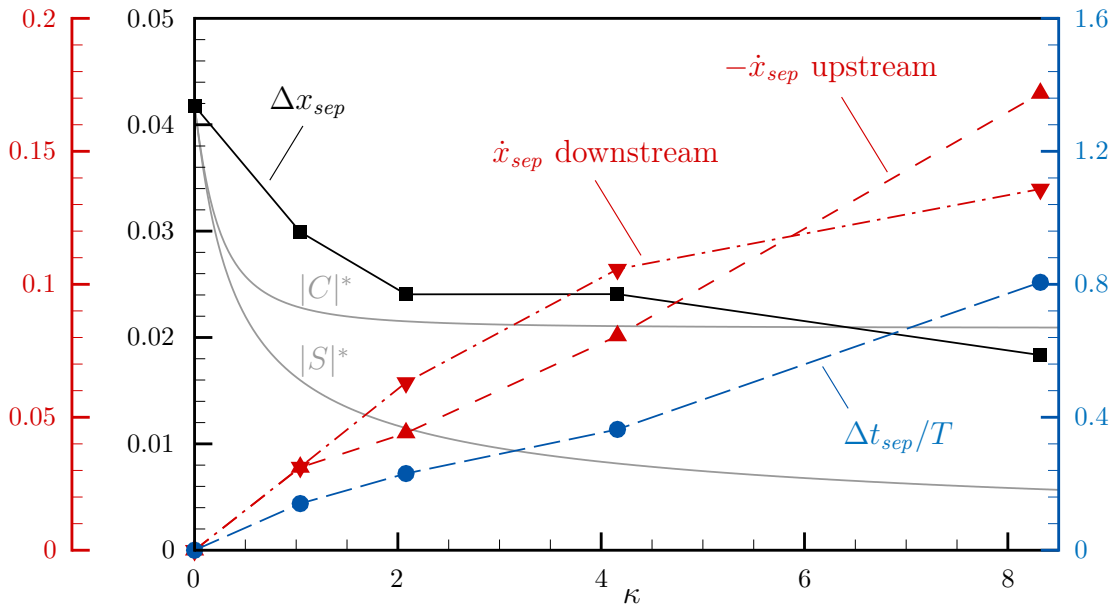

Figure 4.13: Characterization of unsteady separation point (S) or x_{sep} versus gust frequency κ. $|C|^*$ and $|S|^*$ represent the scaled Theodorsen and Sears function, respectively. The colors of the curves match the colors of the corresponding ordinate axis.

The amplitude of the separation-point motion in the flow direction Δx_{sep} also depends strongly on the gust frequency. In figure 4.13, it can be clearly seen that this amplitude decreases with higher κ. An obvious approach to explain this trend would be—analogous to the approximation of the transition motion Δx_{tr} in section 3.3.2 (LTT case)—to apply the Sears (1941) function here. However, despite a

qualitative similarity, the scaled Sears function $|S|^*$ in figure 4.13 does not reflect the unsteady behavior over κ. This is not surprising, as multiple factors are responsible for this particular separation movement. The scaled Theodorsen (1935) function $|C|^*$, exhibits a much better agreement with $\Delta x_{sep}(\kappa)$. This function is related to the Sears function and is derived to approximate the oscillation of the lift of an unsteady *pitching airfoil*, see Leishman (2006) for details. An explanation for the agreement can be given by the fact that the dead-air region (see figure 4.4) might experience the gust more like a standing wave instead of a traveling wave due to the inertia effects of the lower flow velocities. The Theodorsen function, where fluid is moved up and down due to the pitching motion, can be related to a problem with a standing wave, see Turhan *et al.* (2022).

4.4.4 Characterization of transition and reattachment

In contrast to the separation point x_{sep} or (S), neither the transition position (T) nor the location of reattachment (R) can be determined unambiguously or smoothly over time due to the fluctuations in the rear region of the separation bubble. The application of a running mean would merely blur the results, since the time scales of vortex-shedding are already too close to the periods of the applied gusts. Therefore, an exact characterization of the unsteady transition and reattachment versus the gust frequency κ—analogous to the plot of the separation point in figure 4.13—cannot be created. A possible solution would be to evaluate the data over numerous gust periods in experimental investigations or simulations which require fewer resources. With a phase (or periodic ensemble) average, the positions can then be determined. Nevertheless, by observing γ_{z,c_f} as well as the instantaneous results of LST and CWT, the transient behavior of the transition location as well as the reattachment can be qualitatively evaluated. The two lines (T) and (R) drawn manually in figures 4.10 & 4.11 for the three lower κ represent the approximate periodic behavior. The first line is based on the knowledge about the critical value $n_{(cwt)} \approx 8.6$ of the transition in the quasi-steady case, while the second represents the approximate end of the intermittent reverse-flow vortex (RFV) with $\gamma_{z,c_f} < 0.5$. At $\kappa = 8.32$, however, the unsteady transition location and the reattachment point is difficult to localize, which is why the periodic mean is shown here instead. With these lines drawn in figures 4.10 & 4.11, the time evolution of the approximated length of the laminar separation bubble Δx_{LSB} can be visualized.

The modes with phase velocity of $c_{mode} \approx 0.5 u_\infty$ on average travel significantly slower downstream than the gust which convects with $c_{gust} = u_\infty$ (see gray dashed lines in figures 4.10 & 4.11) through the airfoil flow. Naturally, this results in a time delay of the oscillation of the n-factors with respect to the gust as well as other flow characteristics. The phase shift of the oscillation of the separation point x_{sep}—which also has its own viscous delay, see above—to the oscillation of the highest factor from

stability analysis $n = 8$ (closely linked to transition (T) and reattachment (R)) is of special interest here. Therefore, this shift characterizes the qualitative development of the streamwise separation bubble length Δx_{LSB} over time. For the low-frequency case $\kappa = 1.04$, only a slight phase lag of the n-factor curves to the separation point can be seen. Therefore, the length of the separation bubble Δx_{LSB} varies little over the period T and behaves similarly to the quasi-steady case with $\kappa \to 0$, see figure 4.9. However, at $\kappa = 2.08$, the phase offset is so large that the motion of x_{sep} is beginning to oppose the motion of the higher $n_{(cwt)}$-factors and therefore the approximate transition point (T). This is even more pronounced at $\kappa = 4.16$ with a phase shift of $\approx \pi$, where the lines (T) and (R) always move in the opposite direction to the separation line (S) over the gust period. While the separation point responds directly to the pressure gradient induced by the gust (with some degree of viscous delay), the resulting transition motion is still bound to the phase velocity of the modes c_{mode}. Due to this effect, the length of the separated region Δx_{LSB} varies much more dramatically for $\kappa = 2.08$ and $\kappa = 4.16$ compared to the low-frequency case with $\kappa = 1.04$. In other words, at high frequencies the separation bubble "breathes" or changes its size in both directions, while at lower frequencies it instead moves upstream and downstream as in the quasi-steady case. Therefore, at these two frequencies κ we can speak of an "amphora-shaped" footprint of the separation bubble Δx_{LSB} in the x/t plane, see figures 4.10(b) & 4.11(a).

As known for oscillating transitional boundary-layer flows without separation, see results of LTT case in chapter 3 or Ohno *et al.* (2022); Romblad *et al.* (2020); Studer *et al.* (2006), it can be observed that the $n_{(cwt)}$-factors move faster upstream than downstream. This deviation of $\dot{x}(n_{(cwt)} = 8)$ is especially visible for $\kappa = 4.16$ in figure 4.11(a). Since the velocity of the motion of the separation point $\dot{x}_{sep}$ behaves inversely for $\kappa = 2.08$ and $\kappa = 4.16$, the "amphora shape" of the separation bubble is even further enhanced here. For $\kappa = 8.32$, however, the higher values of $n_{cwt} > 7$ no longer oscillate over the gust period and therefore deviate from the n-factors of the linear theory. Here, the quasi-steady approach of the stability analysis with steady-state equations probably reaches its limits, since the actuation frequency is already very close to the (fundamental) gust frequency $\omega_{DS}/\omega_{gust} = 6.25$. However, more plausible for the deviation is the lock-in effect of the gust with the separation bubble, leading to non-linear interaction, see end of this section.

A particularly interesting transient behavior is also observed for the early intermittent reattachment with $\gamma_{z,c_f} < 0.99$ further upstream. For all three angles of attack AoA of the steady-state cases, these near-wall structures were found at $n_{(cwt)} \approx 7.5$, see figure 4.9. For $\kappa \to 0$, it can be assumed that these structures are always present at this $n_{(cwt)}$-factor and are implicitly bound to the transition location (T) as well as bubble length Δx_{LSB}. However, in all simulations with actual gusts, see figures 4.10 & 4.11, there is a spatial undershoot of these structures with respect to the quasi-steady reference of $n_{(cwt)} \approx 7.5$. Since this undershoot

occurs periodically and the momentary reattachments are in contrast to the steady-state cases almost exclusively two-dimensional ($\gamma_{z,c_f} < 0.01$), the observation can definitely be considered an unsteady effect. This is already apparent in the lowest frequency case $\kappa = 1.04$. For most of the period, though, the structures here also appear mainly at $n_{(cwt)} \approx 7.5$ and are barely two-dimensional similar to the steady-state cases. However, for the interval of $0.45 < t/T < 0.8$ structures which are consistently two-dimensional are already apparent at $n_{(cwt)} \approx 6.5$. This behavior is even more pronounced at higher frequencies. For $\kappa = 4.16$, for example, the momentary reattachments appear as early as $n_{(cwt)} \approx 5$. Due to those structures, the above-mentioned graphical impression of an "amphora shape" in the x/t plane can also be found for the purely separated region with $\gamma_{z,c_f} > 0.99$ for $\kappa = 2.08$ as well as $\kappa = 4.16$. However, the periodically occurring spatio-temporal "streaks" with $\gamma_{z,c_f} < 0.01$ in the x/t plane, indicating near-wall 2D structures, strongly resemble the simulation results of the steady-state reference case without the disturbance strip turned on, see figure 4.6(a). It can therefore be assumed that absolute instability has an impact here. It should be mentioned that the $n_{(cwt)}$-factors do not take into account the potential influence of the absolute instability. Unlike a global analysis, the local (unsteady) LST can only calculate the amplification of convective modes and therefore cannot predict self-sustaining instabilities. Furthermore, the spectral result of the CWT refers only to the actuation frequency ω_{DS}, which is why other disturbances with different frequencies are disregarded here.

4.4.5 Absolute instability and lock-in with gust

However, the influence of absolute stability over one gust period can be investigated with a double-spectral analysis. The modal development for the simulation with $\kappa = 2.08$ without additional disturbance input is shown in figure 4.14(a), where the fundamental gust frequency—denoted with $(1,0)_{gust}$—can be seen with its higher harmonics. In direct comparison with the steady-state simulation, see figure 4.8(a), the 2D disturbances $(h,0)$ obtain larger amplitudes due to the influence of the gust. This influence becomes more obvious when comparing the simulations with the disturbance strip turned on: While in the steady-state simulation in figure 4.8(b) the 2D perturbations $(h,0)$ are not relevant for the transition process, they appear with higher levels in the simulation with gust in figure 4.14(b). This confirms the occurrence or influence of absolute instability, which increases as soon as gusts affect the flow. In contrast to the stationary counterpart in figure 4.8(b), the amplification of the modes $(1,\pm1)$ in figure 4.14(b) is clearly reduced downstream. Furthermore, it can be observed that the peak of non-linear saturation is attenuated over the oscillation period, which also indicates the increased influence of absolute instability.

Besides the higher influence of an absolute instability, other effects may be involved. At $\kappa = 2.08$ and $\kappa = 4.16$, small fluctuations of the separation point are seen

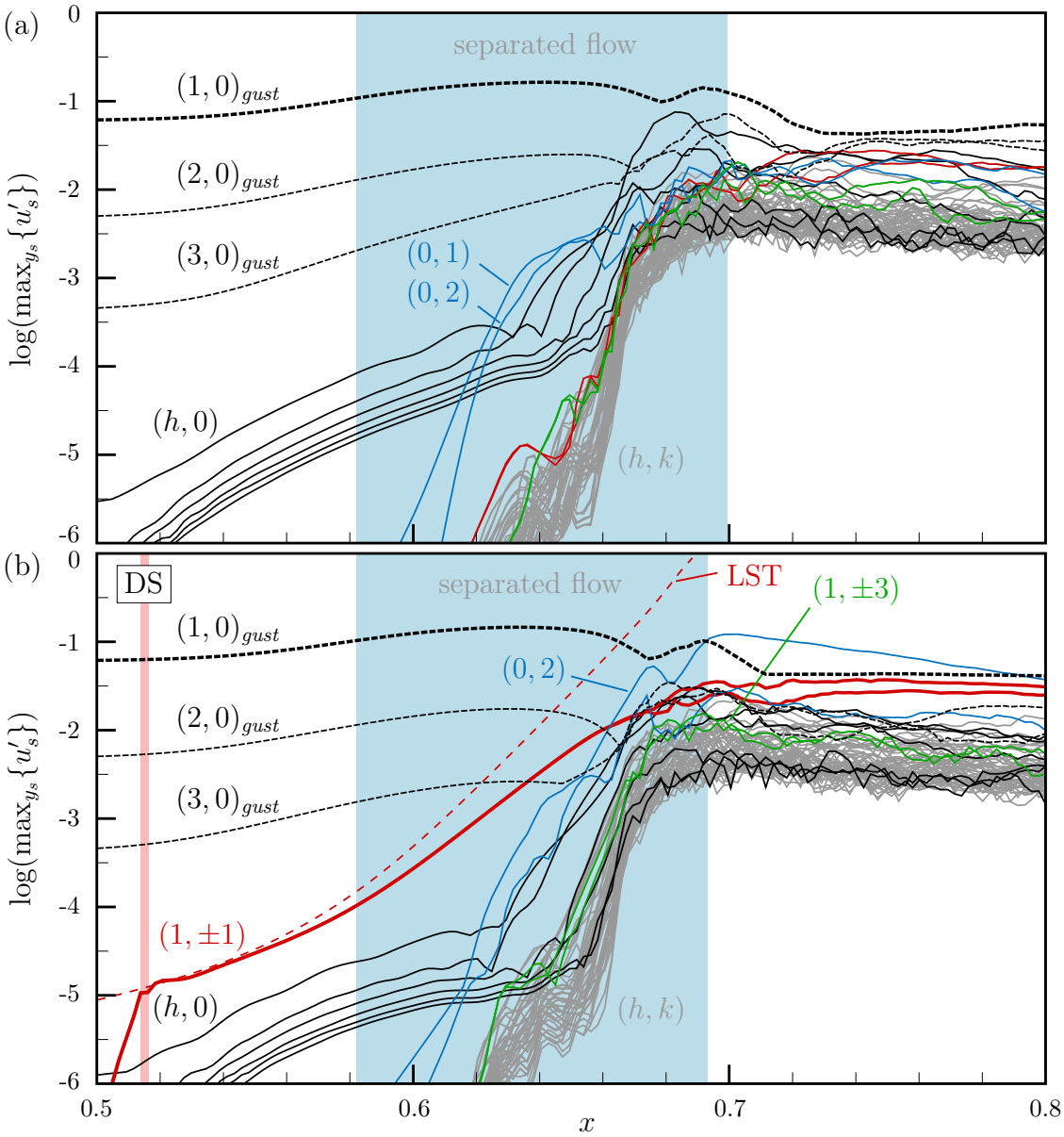

Figure 4.14: Downstream development of modal disturbance amplitude $u'_{s,(h,k)}$ (maximum over y_s) for gust frequency $\kappa = 2.08$. (a) DNS without actuation (b) DNS with disturbance strip. "Separated flow" refers to the periodic mean.

at the maximum point (or apex) of x_{sep}, see blue dashed circle in figure 4.10(b) & 4.11(a). When considering the trajectory of c_{mode} for case $\kappa = 2.08$, it seems apparent that the strong 2D structures which appear during reattachment (at $x \approx 0.63$ and $t/T \approx 1.15$) are caused upstream by the fluctuations of the separation point. These waves reoccur at each period and therefore might be seen as a kind of instability of the laminar separation point. Upon closer examination, it can be seen that the separation line is generally somewhat more "shaky" when moving downstream

compared to the upstream movement. This is counterintuitive in a sense, since the most downstream separation position (see figure 4.9(c)) turned out to be the most stable in the quasi-steady consideration. These fluctuations can be seen as an effect of the transient flow and may also be responsible for the increased occurrence of 2D structures in the reattachment zone during this particular time period. However, this behavior indicates a short-term increase of the absolute instability (hence a feedback-loop of the flow), which makes it difficult to argue with cause-and-effect at this point. Another and rather intuitive explanation is that 2D structures may also be generated due to the "stretching" and "squeezing" of the separation bubble through the oscillating pressure gradient $\mathrm{d}p/\mathrm{d}x$ in the flow direction. These observations and tentative conclusions require further investigation, possibly under more generic conditions.

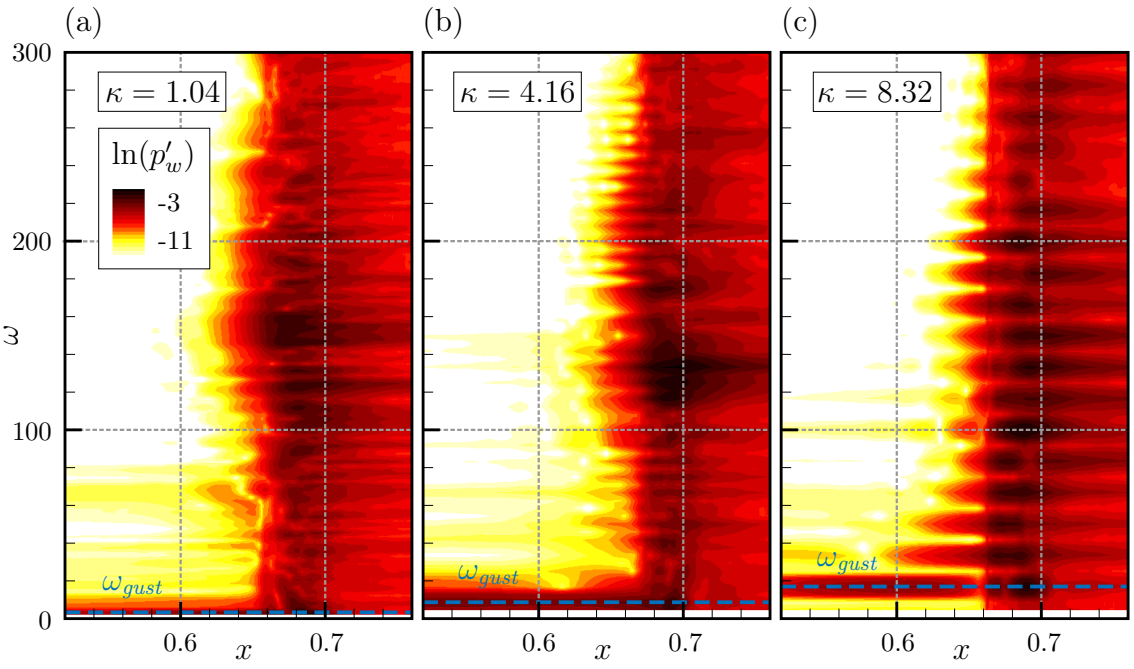

Figure 4.15: FFT of wall pressure p'_w for simulations with gusts. (a) $\kappa = 1.04$ (b) $\kappa = 4.16$ (c) $\kappa = 8.32$.

In addition, the question arises as to what point a so-called lock-in effect between the gust and the laminar separation bubble occurs. This effect can also be observed in separation control, where the vortex-shedding frequency may be locked onto the actuation frequency, see Dianics *et al.* (2015) or Kang *et al.* (2020). For the case with $\kappa = 4.16$ in figure 4.11(a), a clear regularity of the structures over one period can already be observed. This is even more evident in figure 4.11(b), where the frequency of the natural oscillation is only about six times of the gust frequency $\kappa = 8.32$. The lock-in effect can also be confirmed in the spectral analysis of the wall pressure, see figure 4.15.

The spectrum for $\kappa = 1.04$ in 4.15(a) shows a broader hump centered at $\omega \approx 150$ in comparison to the narrower one of the steady-state case in figure 4.7(b). This can be explained by the fact that the natural frequencies vary depending on the position and size of the laminar separation bubble during one gust period. For $\kappa = 4.16$ in figure 4.15(b) the higher harmonics of the gust can already be seen. Nevertheless, the spectrum is still relatively broad with a peak at $\omega \approx 115$, which is why there is not yet a complete lock-in to the gust. A complete lock-in of the flow, however, is evident at $\kappa = 8.32$ in figure 4.15(c), since the whole spectrum follows the multiples of the gust frequency. Here, the separated flow resonates primarily with the periodic gust. The characteristics of c_f for $\kappa = 8.32$, as depicted in figure 4.11(b), are practically identical to the case with no actuation via disturbance strip. This is another indication of lock-in to the gust, since the reattachment process is no longer influenced by the actuation signal. Nevertheless, for the case with actuation, the lock-in effect does not seem to have a strong impact on the amplification rates of the modes, since n_{cwt} evolves similarly to n. However, for higher values of n_{cwt} the periodic pattern is "smeared" over time, leading to an almost quasi-steady behavior.

4.5 Summary

This section aims to summarize the most important aspects of the research presented in this chapter. The conclusions drawn here directly follow the deductions of the attached-flow scenario of the previous chapter, see summary in section 3.5. First, the numerical setup is briefly reviewed, followed by an enumeration of the identified physical effects and a classification into identified scenarios for unsteady flows with separation. A comprehensive summary with more conclusions is given in chapter 5.

The behavior of laminar separation bubbles on an NLF airfoil under the influence of periodic vertical gusts was investigated with direct numerical simulations. The hybrid approach, in which flow fields of URANS simulations with gusts are used for unsteady boundary conditions in the DNS, has been shown to perform robustly for a flow with laminar separation. The numerical method was validated through results from corresponding wind-tunnel experiments (see Greiner (2024)) with respect to the mean-flow properties, oscillating boundary-layer profiles as well as in spectral content. The linear behavior of the convective shear layer instability is characterized by comparing the amplitudes from the continuous wavelet transform with the predicted n-factors from the (unsteady) linear stability analysis. Furthermore, the presence of the absolute instability was investigated in steady-state simulations of the reference case, in particular by comparing the results with and without the excitation of oblique resonance via a disturbance strip.

In the case of the attached-flow scenario presented in the previous chapter, four consecutive physical effects were identified as most important to explain the char-

acteristics of unsteady transition: (1) The "footprint" of the gust in form of an unsteady pressure gradient which depends on the amplitude v'_{gust} and the relation of $\lambda_{x,gust}(\kappa)/L_c$ (Sears function), (2) a viscous delay of the laminar boundary layer responding to the change of pressure gradient leading to a spatio-temporal lag of amplification rates α_i for convective modes, (3) the spatio-temporal trajectories due to the gust-independent phase speed c_{mode} of the modes causing skewed or even overturned transition behavior and finally (4) a non-linear distortion of the mean flow leading to altered stability properties. (See section 3.5 for details.) With the exception of the last point—which might occur at at higher amplitudes—, these effects were also found in this flow scenario involving laminar separation. However, for the present scenario, two further transient effects are identified, hence the list can be extended by:

(5) **Absolute instability increased:** With increasing gust frequency, the impact of the absolute instability in the transition process of the laminar separation bubble increases. The structures in the turbulent reattachment of the flow are also increasingly coherent and two-dimensional.

(6) **Lock-in effect:** At very high gust frequencies, a lock-in or resonance of the separation bubble with the gust occurs, whereby convective modes play a minor role. The reattachment is entirely governed by the gust frequency and its higher harmonics.

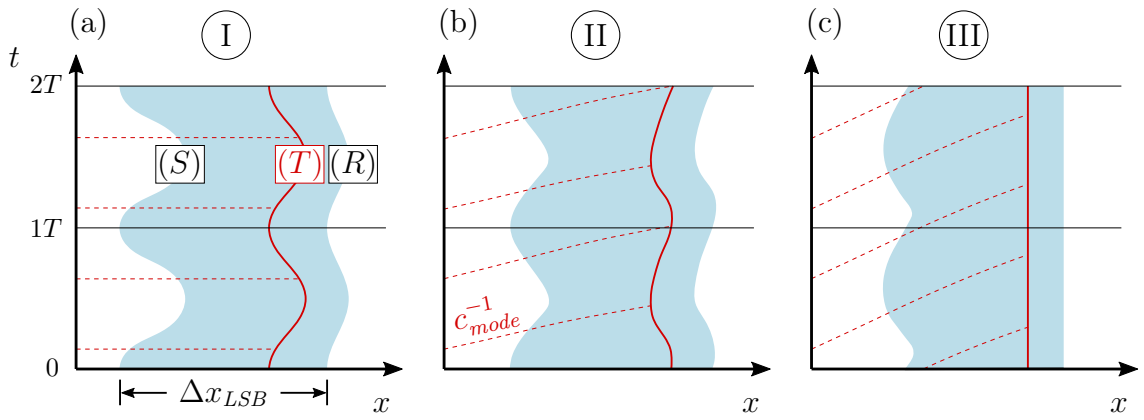

Figure 4.16: Schematic spatio-temporal development of separated area (blue) with transition movement (red). (a) Quasi-steady behavior $\kappa \lessapprox 0.5$ (b) Unsteady behavior ("amphora shape") $0.5 \lessapprox \kappa \lessapprox 5$ (c) Lock-in with gust $\kappa \gtrapprox 5$.

A tentative breakdown of transient cases of this scenario for an increasing frequency κ at $v'_{gust} = 0.04$ is shown in figure 4.16, where the spatio-temporal development of the laminar separation bubble (blue area) is schematically depicted. The trajectories of the convective instability with the phase velocity c_{mode}^{-1} (dashed red)

with the resulting unsteady shear layer transition (solid red) are also shown. The three simplified cases can be distinguished as follows:

(I) **Quasi-steady behavior** for $\kappa \lessapprox 0.5$: The trajectories of the amplified modes are (almost) horizontal in the x/t diagram due to the low-frequency gust. The separation bubble moves upstream and downstream while changing its size over one oscillation period. A quasi-steady consideration is therefore sufficient here.

(II) **Unsteady behavior** for $0.5 \lessapprox \kappa \lessapprox 5$: The point of separation responds quickly (with some degree of viscous delay) to the time-dependent pressure gradient and oscillates over a shorter stretch compared to the quasi-steady case. The transition and the subsequent turbulent reattachment exhibits a phase lag with regard to the upstream separation line, due to the gust-independent phase speeds c_{mode} of the modes. This results to a "breathing" separation bubble with an "amphora-shaped" spatio-temporal development of the separated region in the x/t plane. Furthermore, the impact of an absolute instability is increased. However, the behavior can be mostly attributed to unsteady laminar effects and the behavior of time-dependent convective disturbances which can be described by local linear theory.

(III) **Lock-in with gust** for $\kappa \gtrapprox 5$: The distance of the oscillation of the separation location further decreases. The rear region of the bubble including the resulting vortex-shedding is fully determined by the gust frequency and its superharmonics, hence a lock-in with the gust is present. Due to the short period of the pressure-gradient oscillation T in relation to the lifespan of the convective modes, the transition and the subsequent reattachment exhibit a quasi-steady behavior, cf. unsteady transition-behavior at high frequencies in section 3.3.2.

5 Conclusions

The unsteady behavior of the boundary-layer flow on two NLF airfoils subjected to periodic vertical gusts has been numerically investigated. In the first scenario, the unsteady natural transition with TS-waves in an attached flow was investigated. Building on this, the transient behavior of a laminar separation bubble was studied in the second scenario.

Transient base flows for different gust frequencies κ and amplitudes v'_{gust} were generated using URANS simulations in conjunction with the disturbance velocity approach. As a new hybrid approach, these unsteady flow fields were used for direct numerical simulations, with domains covering the relevant part of the boundary-layer flows. Thereby, the transient base flows containing the gust response of the airfoils were prescribed with modified unsteady boundary conditions. The spatio-temporal evolution of the modal amplitudes in the oscillating flows was determined using the continuous wavelet transform. Those amplitudes could be compared with the linear theory by using an unsteady extension of the e^n-method where modes are followed along their trajectories. Having theoretical laminar and linear references from URANS along with the non-linear results of the DNS proved to be very helpful in deducing cause-and-effect physics.

Attached-flow scenario

First, the spatio-temporal behavior of unsteady laminar flows from URANS simulations was qualitatively characterized. A "footprint" of the gust could be identified in the unsteady pressure gradient, which convects with the free-stream velocity u_∞ and becomes more distinctive with increasing frequency κ. The subsequent response of the velocity profiles shows a lagging behavior, which is inherent to the viscous boundary layer and leads to a hysteresis of the amplification rates α_i. Furthermore, the phase speed of the TS-waves c_{TS} is considerably slower than the gust. Both transient effects are accounted for by the unsteady linear stability analysis used for time-dependent transition prediction. The numerical method was validated with the measurements of Romblad *et al.* (2020); Romblad (2023). In those cases, the unsteady transition location exhibits an "asymmetric" behavior over time, with a faster upstream-moving front and a slower downstream-moving front.

A general characterization of the linear effects was carried out with a parameter study for $0 \leq \kappa \leq 8$ and $0.01 \leq v'_{gust} \leq 0.06$. It was found that the amplitude of the streamwise oscillation of the transition can be approximated by the Sears (1941) function. The most skewed or asymmetric temporal behavior of the transition was

found at κ_{crit}, which refers to the frequency where the average lifetime of the TS-waves is equal to the period of the gust. For high amplitudes at this frequency, a so-called overturned pattern of the transition location is found. In this case, an isolated turbulent stretch within the laminar flow is predicted according to the linear theory. A dimensionless number κ^{tr} based on frequency and effective amplitude has been suggested to quantify the degree of unsteadiness of the cases. This parameter proved to be well suited for characterizing the unsteady transition, since the velocities of the fronts in both upstream and downstream directions (or leading and trailing edges for the overturned pattern) follow a clear trend over κ^{tr}. A general transition prediction method is suggested based on the laminar/linear considerations.

The physics of unsteady flow including non-linear effects were investigated with DNS. For all simulations, fundamental resonance was applied as a breakdown scenario with initial amplitudes corresponding to $n_{crit} \approx 10$ and ≈ 7. The steady-state reference case was characterized and validated with wind-tunnel measurements. In the simulations with gusts, the n-factors of the linear theory (based on the transient base flow) were directly compared with the amplitudes of the introduced modes, which were obtained using the continuous wavelet transform. A perfect agreement of the transient modal development with the linear theory was found for the cases at low degrees of unsteadiness with low frequencies and low amplitudes. The (weakly) non-linear stage and the fully non-linear turbulent flow oscillate continuously in upstream and downstream direction. In addition, a transient delay of the mean flow distortion was observed. A consistent qualitative behavior of the unsteady transition was found in the comparison with the wind-tunnel measurements from Romblad (2023). The observed pronounced amplitudes of the upstream-moving transition front were interpreted in analogy to the Doppler effect with an increased number of incoming TS-wave crests.

The convective-transition mode—which was described by Obremski & Fejer (1967) and Studer *et al.* (2006)—was found for cases at higher levels of unsteadiness. In this work, it was shown that the transient delay of the mean flow distortion is primarily responsible for the occurrence of this phenomenon for natural transition. The MFD-delay generally appears to attenuate the amplification rates of the TS-modes at the onset of the downstream-moving transition phase. Accordingly, a transient branch II is present, which ensures that TS-waves no longer reach the necessary thresholds for transition for a short time. Furthermore, the effect of fewer incoming TS-wave crests at the downstream-moving front (Doppler analogy) is assumed to contribute to the "stalling" of the creative transition. A calmed region—well known from studies of turbulent spots and wake-induced transition in turbomachinery—is eventually formed in the wake of the convecting turbulent flow. In all cases, the spatio-temporal evolution of the modes leading to creative transition shows good agreement with the unsteady n-factors from quasi-steady LST. Therefore, an extended transient approach as proposed by Citro & Luchini (2015) is not necessary

in this scenario. Based on physical considerations, a tipping-point for the occurrence of the convective-transition mode was identified. This corresponds to a threshold value of a variation of the unsteadiness quantity with $\kappa_{sears}^{tr} \approx 0.57$.

A claim to generality can be made for this study due to the following properties: a generic definition for periodic gusts; relevant Reynolds number and realistic N_{crit}; a comparatively constant streamwise pressure gradient; and most importantly, a sinusoidal response of the transition location for the quasi-steady case $\kappa \to 0$.

Separated-flow scenario

The laminar separation bubble was first characterized through three different steady-state simulations at different angles of attack, which relates to the theoretical quasi-steady case of an "infinitely large" gust with frequency $\kappa \to 0$. In the investigations with actual gusts with $1 \leq \kappa \leq 8$ at the amplitude $v'_{gust} = 0.04$, several transient effects of the LSB were identified. In particular, the motion of the separation point as well as the transient behavior of the rear region of the LSB with regard to the transition location was investigated.

The unsteady modal amplitudes and the resulting unsteady transition position exhibit an inherent delay due to the time-dependent amplification rates α_i and the slower phase velocity of the convective modes c_{mode} compared to the gust with the free-stream velocity u_∞. As already known from attached boundary-layer flows, these (linear) influences also cause the transition front to move faster upstream than downstream, which is especially noticeable at the higher gust frequencies. Clear trends were found regarding the movement of the separation point, which for the most part can be regarded as effects of viscous delay of the boundary layer. The separation point reacts faster to the oscillating pressure gradient than the transition location and the subsequent turbulent reattachment of the separation bubble. Interestingly, at some frequencies κ the separation point moves faster downstream than upstream—exactly the reverse of the behavior of the transition position.

In the simulation with the lowest frequency, it was observed that the separated area essentially moves upstream and downstream according to the oscillation, while the length of the LSB varies only mildly. However, at the higher frequencies, a "breathing" LSB, which grows or shrinks simultaneously in both the upstream and downstream directions was observed. The LSB leaves an impression of an "amphora-shaped" footprint in the x/t plane, which is mainly due to the delay of the higher n-factors of the modes due to their gust-independent phase velocity c_{mode}. Furthermore, it was found that in the unsteady flow with gusts, the absolute instability inherent to the LSB becomes more influential. Apparently, this leads to coherent near-wall 2D structures in the rear region of the LSB, which occur periodically at certain times of the cycle. At the highest frequency investigated, a clear lock-in effect or resonance of the LSB onto the disturbance of the gust was identified.

Outlook

In this work, a general formulation for an unsteady transition prediction method based on quasi-steady LST was presented and validated by experimental investigations and DNS. Consequently, the method can be implemented as a transition model for URANS simulations, enabling transient studies of full-scale aircraft configurations. This would also allow the unsteady characterization of the transition in novel configurations e.g. with (hybrid) laminar flow control ((H)LFC). In this case, the base flows are manipulated (e.g. with boundary-layer suction), which potentially results in a significantly different behavior of the transient flow with respect to stability properties.

In addition, prospects for further research on the fundamentals of unsteady transition can be outlined. An extended formulation of the unsteady LST—possibly using Floquet theory—could be derived for cases with very high degrees of unsteadiness. DNS corresponding to this work with a variation of the mean (steady-state) pressure gradient as well as the Reynolds number are desirable for further characterization. In addition, the transient behavior of the secondary mechanism and the subsequent late stages of breakdown can be studied in depth. More insights are expected for transient DNS with a disturbance formulation where the mean flow distortion is suppressed. This study also demonstrated the importance of transient mean flow distortion behavior, which is not yet investigated. An appropriate general characterization and modeling is therefore of great interest for transient flow problems. This can also be of use for new transition prediction methods for unsteady conditions.

A Flux vectors of Navier–Stokes equations

For numerical solution with *NS3D*, the set of equations presented in section 2.1 is rewritten to flux vectors, i.e.

$$\frac{\partial \boldsymbol{Q}}{\partial t} + \underbrace{\frac{\partial \boldsymbol{F}}{\partial x} + \frac{\partial \boldsymbol{G}}{\partial y} + \frac{\partial \boldsymbol{H}}{\partial z}}_{-\mathcal{N}(\boldsymbol{Q})} = 0\,, \tag{A.1}$$

with the state vector of conservative variables $\boldsymbol{Q} = (\rho, \rho u, \rho v, \rho w, E)^T$. Here, $\mathcal{N}$ denotes the general compressible Navier–Stokes operator. The flux vectors $\boldsymbol{F}$, $\boldsymbol{G}$, $\boldsymbol{H}$ read

$$\boldsymbol{F} = \begin{pmatrix} \rho u \\ \rho u^2 + p - \tau_{xx} \\ \rho uv - \tau_{xy} \\ \rho uw - \tau_{xz} \\ u(E+p) + q_x - u\tau_{xx} - v\tau_{xy} - w\tau_{xz} \end{pmatrix}, \tag{A.2a}$$

$$\boldsymbol{G} = \begin{pmatrix} \rho v \\ \rho uv - \tau_{xy} \\ \rho v^2 + p - \tau_{yy} \\ \rho vw - \tau_{yz} \\ v(E+p) + q_y - u\tau_{xy} - v\tau_{yy} - w\tau_{yz} \end{pmatrix}, \tag{A.2b}$$

$$\boldsymbol{H} = \begin{pmatrix} \rho w \\ \rho uw - \tau_{xz} \\ \rho vw - \tau_{yz} \\ \rho w^2 + p - \tau_{zz} \\ w(E+p) + q_z - u\tau_{xz} - v\tau_{yz} - w\tau_{zz} \end{pmatrix}, \tag{A.2c}$$

where c_v denotes the specific heat capacity, the normal stresses

$$\tau_{xx} = \frac{\mu}{Re}\left(\frac{4}{3}\frac{\partial u}{\partial x} - \frac{2}{3}\frac{\partial v}{\partial y} - \frac{2}{3}\frac{\partial w}{\partial z}\right), \tag{A.3a}$$

$$\tau_{yy} = \frac{\mu}{Re}\left(\frac{4}{3}\frac{\partial v}{\partial y} - \frac{2}{3}\frac{\partial u}{\partial x} - \frac{2}{3}\frac{\partial w}{\partial z}\right), \tag{A.3b}$$

$$\tau_{zz} = \frac{\mu}{Re}\left(\frac{4}{3}\frac{\partial w}{\partial z} - \frac{2}{3}\frac{\partial u}{\partial x} - \frac{2}{3}\frac{\partial v}{\partial y}\right), \tag{A.3c}$$

the shear stresses

$$\tau_{xy} = \frac{\mu}{Re}\left(\frac{\partial u}{\partial y} + \frac{\partial v}{\partial x}\right), \tag{A.4a}$$

$$\tau_{xz} = \frac{\mu}{Re}\left(\frac{\partial u}{\partial z} + \frac{\partial w}{\partial x}\right), \tag{A.4b}$$

$$\tau_{yz} = \frac{\mu}{Re}\left(\frac{\partial v}{\partial z} + \frac{\partial w}{\partial y}\right), \tag{A.4c}$$

the heat fluxes

$$q_x = -\frac{\vartheta}{(\gamma-1)RePrMa^2}\frac{\partial T}{\partial x}, \tag{A.5a}$$

$$q_y = -\frac{\vartheta}{(\gamma-1)RePrMa^2}\frac{\partial T}{\partial y}, \tag{A.5b}$$

$$q_z = -\frac{\vartheta}{(\gamma-1)RePrMa^2}\frac{\partial T}{\partial z}, \tag{A.5c}$$

and the total energy

$$E = \rho \int c_v dT + \frac{\rho}{2}(u^2 + v^2 + w^2). \tag{A.6}$$

B Lagrange polynomials for DNS

In this section, the formulation of the 3rd-order Lagrange polynomials implemented in *NS3D* for temporal interpolation is given. In order to save computational resources, it is important to use an efficient interpolation scheme since it is performed during the DNS. With an equidistant time step Δt of the original URANS flow data, the numerical formulation of the Lagrange polynomials can be simplified. The general concept is illustrated in figure 2.5.

The Lagrange interpolation from equation (2.26) for an arbitrary primitive variable ϕ with the Lagrange basis polynomials of equation (2.27) can be rearranged for the order of $k = 3$ to

$$\phi_{ref}(t) = a_3 t^3 + a_2 t^2 + a_1 t + a_0 \,, \tag{B.1}$$

for $t \in [0, T)$. This calculation is performed at all relevant grid points at every (sub)iteration of the DNS. However, the coefficients a_0 to a_3 are updated in case the simulation time reached a new interval between two temporal data points t_1 and t_2. This is done by the following calculation of coefficients in the given order, while first calculating the auxiliary coefficients

$$b_1 = \frac{\phi_2 - 2\phi_1 + \phi_0}{2\Delta t^2} \,, \quad b_2 = \frac{\phi_3 - 6\phi_2 + 3\phi_1 + 2\phi_0}{6\Delta t} \,. \tag{B.2}$$

The final coefficients for equation (B.1)

$$\begin{aligned} a_3 &= \frac{\phi_3 - 3(\phi_2 - \phi_1) - \phi_0}{6\Delta t^3} \,, \quad a_2 = b_1 - 3a_3 t_1 \,, \\ a_1 &= 3a_3 t_1^2 - 2b_1 t_1 - b_2 \,, \quad a_0 = -a_3 t_1^3 + b_1 t_1^2 + b_2 t_1 + \phi_1 \,, \end{aligned} \tag{B.3}$$

can be calculated in sequence. Numerically, current time t in equation (B.1) is always determined by a modulo operation on the physical time in the simulation with the period T as a divisor. Therefore, the interpolation is repeated cyclically over several periods.

C Supplementary plots

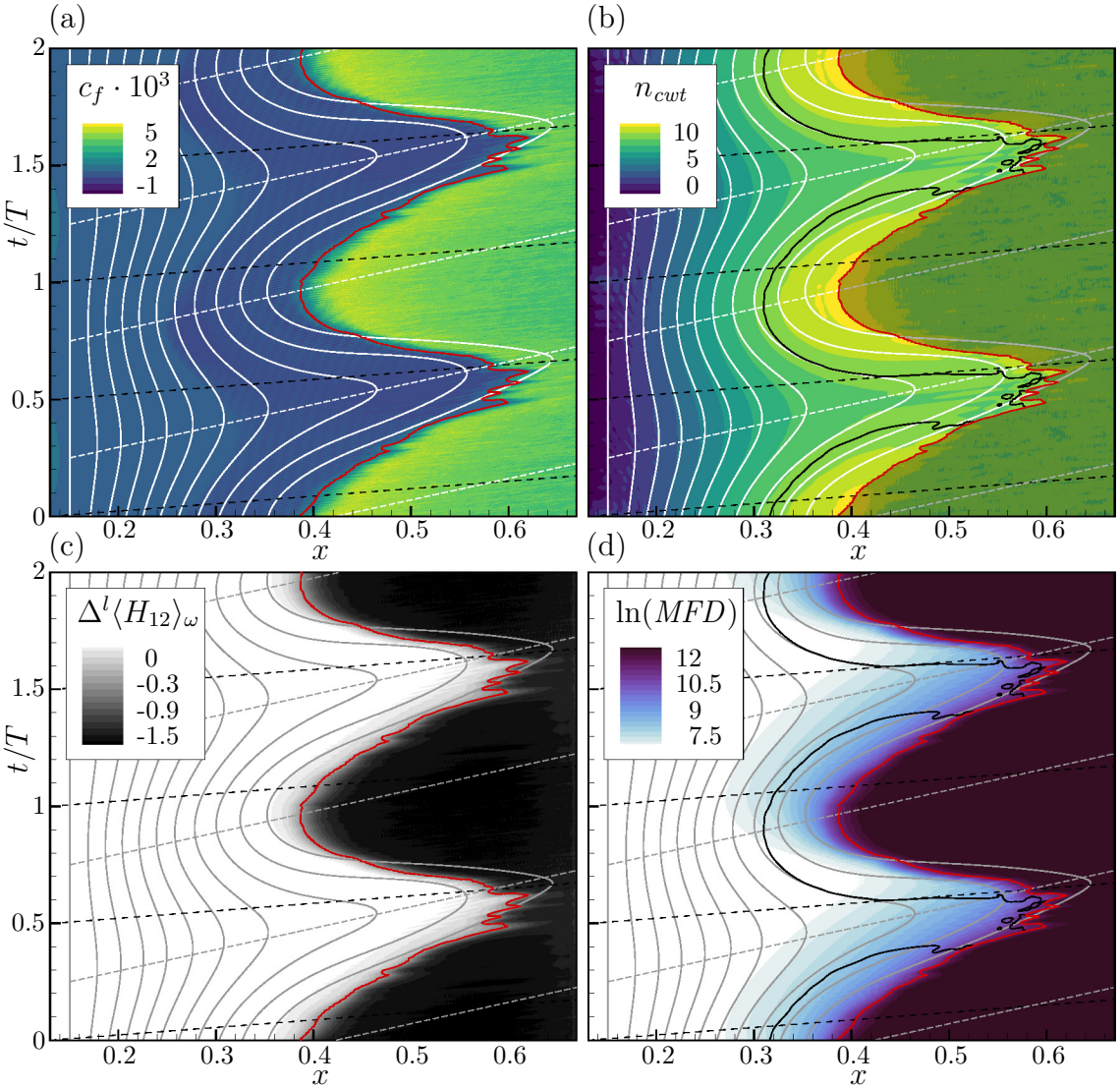

Figure C.1: Spatio-temporal development for $\kappa = 1$ at $v'_{gust} = 0.02$ (a) Skin-friction c_f (b) Amplitudes of continuous wavelet transform n_{cwt} (c) Shape-factor deviation $\Delta^l\langle H_{12}\rangle_\omega$ (d) Mean flow distortion ln(*MFD*); solid white/gray lines: LST with $n \in \{0 \dots 10\}$ with $\Delta n = 1$ in downstream direction, —— $\Delta^l\langle c_f\rangle_\omega = 0.001$, —— $\max_{y_s}\{u'_{s,cwt}\} = 0.01$, dashed white/gray lines: exemplary trajectories of TS-waves c_{TS}^{-1}, - - - - - free-stream velocity u_∞^{-1}.

References

Ackerberg, R. C. & Phillips, J. H. 1972 The unsteady laminar boundary layer on a semi-infinite flat plate due to small fluctuations in the magnitude of the free-stream velocity. *Journal of Fluid Mechanics* 51, 137–157.

Agarwal, T., Cukurel, B. & Jacobi, I. 2022 Localized drag modification in a laminar boundary layer subject to free-stream travelling waves via critical and stokes layer interactions. *Journal of Fluid Mechanics* 937, A10.

Alam, M. & Sandham, N. D. 2000 Direct numerical simulation of 'short' laminar separation bubbles with turbulent reattachment. *Journal of Fluid Mechanics* 410, 1–28.

Appelbaum, J., Ohno, D., Rist, U. & Wenzel, C. 2021 DNS of a turbulent boundary layer using inflow conditions derived from 4D-PTV data. *Experiments in Fluids* 62 (9), 1–21.

Babucke, A. 2009 Direct numerical simulation of noise-generation mechanisms in the mixing layer of a jet. PhD thesis, IAG, University of Stuttgart.

Brown, S. & Smith, F. 2005 Modelling the calmed region behind a spot. *Philosophical Transactions of the Royal Society A: Mathematical, Physical and Engineering Sciences* 363 (1830), 1069–1078.

Citro, V. & Luchini, P. 2013 Unsteady boundary-layer transition prediction. In *Memorie del XXI Congresso AIMETA 2013, Torino, 17-20 Sep.*, pp. 1–9.

Citro, V. & Luchini, P. 2015 Multiple-scale approximation of instabilities in unsteady boundary layers. *European Journal of Mechanics - B/Fluids* 50, 1–8.

Colonius, T., Lele, S. K. & Moin, P. 1993 Boundary conditions for direct computation of aerodynamic sound generation. *AIAA Journal* 31 (9), 1574–1582.

Crouch, J. & Ng, L. 2000 Variable N-factor method for transition prediction in three-dimensional boundary layers. *AIAA Journal* 38 (2), 211–216.

de'Pompeis, R., Cinquetti, P. & Martini, P. S. 1991 Development and certification flight test on the Piaggio P.180 Avanti aircraft: A general overview. In *General, Corporate & Regional Aviation Meeting & Exposition*. SAE International.

Dianics, J., Ohno, D., Fuggmann, S., Lay, J., Heim, D. & Fasel, H. 2015 Numerical and experimental wind tunnel and flight testing of active flow control for modified NACA 64_3-618 airfoil. In *53rd AIAA Aerospace Sciences Meeting*.

Dörr, P. C. 2018 Numerical investigation of crossflow transition control using plasma actuators. PhD thesis, IAG, University of Stuttgart.

Dörr, P. C. & Kloker, M. J. 2018 Numerical investigations on Tollmien–Schlichting wave attenuation using plasma-actuator vortex generators. *AIAA Journal* 56 (4), 1305–1309.

Drela, M. 1989 XFOIL: An analysis and design system for low Reynolds number airfoils. In *Low Reynolds Number Aerodynamics*, pp. 1–12. Springer.

Farge, M. 1992 Wavelet transforms and their applications to turbulence. *Annual Review of Fluid Mechanics* 24 (1), 395–458.

Fasel, H. 1976 Investigation of the stability of boundary layers by a finite-difference model of the Navier-Stokes equations. *Journal of Fluid Mechanics* 78 (2), 355–383.

Gaster, M. 1965 On the generation of spatially growing waves in a boundary layer. *Journal of Fluid Mechanics* 22 (3), 433–441.

Gaster, M. 1967 The structure and behaviour of laminar separation bubbles. *Tech. Rep.* 3595. Aeronautical Research Council.

Giles, M. 1990 Nonreflecting boundary conditions for Euler equation calculations. *AIAA Journal* 28 (12), 2050–2058.

Gostelow, J., Melwani, N. & Walker, G. 1996 Effects of streamwise pressure gradient on turbulent spot development. *Journal of Turbomachinery* 118 (4), 737–743.

Gostelow, J., Walker, G., Solomon, W., Hong, G. & Melwani, N. 1997 Investigation of the calmed region behind a turbulent spot. *Journal of Turbomachinery* 119 (4), 802–809.

Greiner, M. 2024 Experiments on laminar separation bubbles under inflow conditions of atmospheric turbulence. PhD thesis, IAG, University of Stuttgart, manuscript submitted.

Greiner, M. & Würz, W. 2021 Laminar separation bubbles at unsteady inflow conditions – a status report. In *XXXIV OSTIV CONGRESS*.

Guerra, A., Hosseinverdi, S., Singh, A., Little, J. & Fasel, H. 2021 Unsteady evolution of a laminar separation bubble subjected to structural motion. In *AIAA Aviation 2021 Forum*.

Guissart, A., Romblad, J., Nemitz, T. & Tropea, C. 2021 Small-scale atmospheric turbulence and its impact on laminar-to-turbulent transition. *AIAA Journal* 59 (9), 3611–3621.

Halstead, D., Wisler, D., Okiishi, T., Walker, G., Hodson, H. & Shin, H.-W. 1997 Boundary layer development in axial compressors and turbines: Part 1 of 4—Composite picture. *Journal of Turbomachinery* 119 (1), 114–127.

Hancock, G. 1984 Unsteady boundary layers. *IMA Journal of Applied Mathematics* 32 (1-3), 175–185.

Heinrich, R. & Reimer, L. 2013 Comparison of different approaches for gust modeling in the CFD code TAU. In *International Forum on Aeroelasticity & Structural Dynamics 2013*.

Heisenberg, W. 1924 Über Stabilität und Turbulenz von Flüssigkeitsströmen. *Annalen der Physik* 74 (4), 577–627.

Helm, S., Fehrs, M., Kaiser, C., Krimmelbein, N. & Krumbein, A. 2023 Numerical simulation of the Common Research Model with natural laminar flow. *Journal of Aircraft* 60 (2), 449–460.

Herbert, T. 1983 Secondary instability of plane channel flow to subharmonic three-dimensional disturbances. *Physics of Fluids* 26 (4), 871–874.

Herbert, T. 1988 Secondary instability of boundary layers. *Annual Review of Fluid Mechanics* 20 (1), 487–526.

Hill, P. G. & Stenning, A. H. 1960 Laminar boundary layers in oscillatory flow. *Journal of Basic Engineering* 82 (3), 593–607.

Huerre, P. & Monkewitz, P. 1985 Absolute and convective instabilities in free shear layers. *Journal of Fluid Mechanics* 159, 151–168.

Huerre, P. & Monkewitz, P. 1990 Local and global instabilities in spatially developing flows. *Annual Review of Fluid Mechanics* 22 (1), 473–537.

Hughes, J. & Walker, G. 2001 Natural transition phenomena on an axial compressor blade. *Journal of Turbomachinery* 123 (2), 392–401.

van Ingen, J. 1956 A suggested semi-empirical method for the calculation of the boundary layer transition region. *Tech. Rep.* V.T.H.-74. Delft University of Technology.

van Ingen, J. 2008 The e^n method for transition prediction. Historical review of work at TU Delft. In *38th Fluid Dynamics Conference and Exhibit*. American Institute of Aeronautics and Astronautics.

Jocksch, A. & Kleiser, L. 2008 Growth of turbulent spots in high-speed boundary layers on a flat plate. *International Journal of Heat and Fluid Flow* 29 (6), 1543–1557.

Kachanov, Y. 1994 Physical mechanisms of laminar-boundary-layer transition. *Annual Review of Fluid Mechanics* 26 (1), 411–482.

Kang, W., Xu, M., Yao, W. & Zhang, J. 2020 Lock-in mechanism of flow over a low-Reynolds-number airfoil with morphing surface. *Aerospace Science and Technology* 97, 105647.

Katz, Y., Seifert, A. & Wygnanski, I. 1990 On the evolution of the turbulent spot in a laminar boundary layer with a favourable pressure gradient. *Journal of Fluid Mechanics* 221, 1–22.

Keller, M. 2016 Numerical investigation of gaseous film and effusion cooling in supersonic boundary-layer flows. PhD thesis, IAG, University of Stuttgart.

Khaled, M. 2019 Beitrag zur Transitionsvorhersage an einem Laminarprofil unter oszillierender Anströmung mittels einer quasistationären linearen Stabilitätsanalyse. Bachelor's thesis, IAG, University of Stuttgart; Supervisors: Ohno, D. & Rist, U.

Klebanoff, P., Tidstrom, K. & Sargent, L. 1962 The three-dimensional nature of boundary-layer instability. *Journal of Fluid Mechanics* 12 (1), 1–34.

Kloker, M. J. 1997 A robust high-resolution split-type compact FD scheme for spatial direct numerical simulation of boundary-layer transition. *Applied Scientific Research* 59 (4), 353–377.

Kolmogorov, A. 1941 The local structure of turbulence in incompressible viscous fluid for very large Reynolds numbers. *Doklady Akademii Nauk SSSR* 30, 9–13.

Kurz, H. 2016 Towards laminar flow on a swept wing: Direct numerical simulation of discrete-roughness receptivity and turbulence tripping. PhD thesis, IAG, University of Stuttgart.

Kurz, H. B. & Kloker, M. J. 2014 Receptivity of a swept-wing boundary layer to micron-sized discrete roughness elements. *Journal of Fluid Mechanics* 755, 62–82.

Lee, T. & Gerontakos, P. 2004 Investigation of flow over an oscillating airfoil. *Journal of Fluid Mechanics* 512, 313–341.

Leishman, G. 2006 *Principles of Helicopter Aerodynamics*. Cambridge University Press, Cambridge.

Lighthill, M. 1954 The response of laminar skin friction and heat transfer to fluctuations in the stream velocity. *Proceedings of the Royal Society of London. Series A. Mathematical and Physical Sciences* 224 (1156), 1–23.

Loehrke, R., Morkovin, M. & Fejer, A. 1975 Review—Transition in nonreversing oscillating boundary layers. *Journal of Fluids Engineering* 97 (4), 534–549.

Luo, J. & Wu, X. 2010 On the linear instability of a finite Stokes layer: Instantaneous versus Floquet modes. *Physics of Fluids* 22 (5), 054106.

Mack, L. 1984 Boundary-layer linear stability theory. *Tech. Rep.* No.709 (Special Course on Stability and transition of Laminar Flow). AGARD.

Mack, L. M. 1977 Transition and laminar instability. *Tech. Rep.* CP-153203. NASA.

Mallat, S. 1999 *A Wavelet Tour of Signal Processing*. Elsevier, Amsterdam.

Mayle, R. E. & Dullenkopf, K. 1991 More on the turbulent-strip theory for wake-induced transition. *Journal of Turbomachinery* 113 (3), 428–432.

McKenzie, J. 2022 Green-sky thinking. *Physics World* 35 (7), 21.

Miller, J. & Fejer, A. 1964 Transition phenomena in oscillating boundary-layer flows. *Journal of Fluid Mechanics* 18 (3), 438–448.

Müller, J., Hillebrand, M., Ehrle, M., Schollenberger, M., Lutz, T. & Krämer, E. 2021*a* Studies on the applicability of a simplified gust simulation approach in the CFD code TAU. In *High Performance Computing in Science and Engineering '20*, pp. 401–418. Springer.

Müller, J., Hillebrand, M. & Lutz, T. 2021*b* Assessment of the disturbance velocity approach to determine the gust impact on airfoils in transonic flow. In *New Results in Numerical and Experimental Fluid Mechanics XIII.*, pp. 14–23. Springer.

Müller, J., Lutz, T. & Krämer, E. 2020 Numerical simulation of the swept FNG wing in atmospheric turbulence. In *AIAA Aviation 2020 Forum*.

Nati, A., De Kat, R., Scarano, F. & van Oudheusden, B. 2015 Dynamic pitching effect on a laminar separation bubble. *Experiments in Fluids* 56 (9), 1–17.

Nobach, H., Tropea, C., Cordier, L., Bonnet, J., Delville, J., Lewalle, J., Farge, M., Schneider, K. & Adrian, R. 2007 Review of some fundamentals of data processing. In *Springer Handbook of Experimental Fluid Mechanics*, pp. 1337–1398. Springer.

Obremski, H. & Fejer, A. 1967 Transition in oscillating boundary layer flows. *Journal of Fluid Mechanics* 29 (1), 93–111.

Obremski, H. & Morkovin, M. 1969 Application of a quasi-steady stability model to periodic boundary-layer flows. *AIAA Journal* 7 (7), 1298–1301.

Ohno, D., Greiner, M., Müller, J. & Rist, U. 2023*a* Numerical investigations of laminar separation bubbles under the influence of periodic gusts. *AIAA Journal* 61 (6), 2486–2499.

Ohno, D., Romblad, J., Khaled, M. & Rist, U. 2022 Investigations of laminar to turbulent transition in an oscillating airfoil boundary layer. In *IUTAM Laminar-Turbulent Transition*, pp. 469–478. Springer.

Ohno, D., Romblad, J. & Rist, U. 2020 Laminar to turbulent transition at unsteady inflow conditions: Direct numerical simulations with small scale free-stream turbulence. In *New Results in Numerical and Experimental Fluid Mechanics XII*, pp. 214–224. Springer.

Ohno, D., Selent, B., Kloker, M. & Rist, U. 2023*b* Direct numerical simulation of bypass transition under free-stream turbulence for compressible flows. In *High Performance Computing in Science and Engineering '21*, pp. 223–238. Springer.

Orr, W. M. 1907 The stability or instability of the steady motions of a perfect liquid and of a viscous liquid. Part I–II. *Proceedings of the Royal Irish Academy. Section A: Mathematical and Physical Sciences* 27, 9–138.

Orth, U. 1993 Unsteady boundary-layer transition in flow periodically disturbed by wakes. *Journal of Turbomachinery* 115 (4), 707–713.

Patel, M. 1975 On laminar boundary layers in oscillatory flow. *Proceedings of the Royal Society of London. A. Mathematical and Physical Sciences* 347 (1648), 99–123.

Pfeil, H., Herbst, R. & Schröder, T. 1983 Investigation of the laminar-turbulent transition of boundary layers disturbed by wakes. *Journal of Engineering for Power* 105 (1), 130–137.

Poggie, J., Bisek, N. J. & Gosse, R. 2015 Resolution effects in compressible, turbulent boundary layer simulations. *Computers & Fluids* 120, 57–69.

Poinsot, T. & Lele, S. 1992 Boundary conditions for direct simulations of compressible viscous flows. *Journal of Computational Physics* 101 (1), 104–129.

Pope, S. 2000 *Turbulent Flows*. Cambridge University Press, Cambridge.

Prandtl, L. 1904 Über Flüssigkeitsbewegung bei sehr kleiner Reibung. In *Third International Congress of Mathematicians, Heidelberg*.

Radespiel, R., Windte, J. & Scholz, U. 2007 Numerical and experimental flow analysis of moving airfoils with laminar separation bubbles. *AIAA Journal* 45 (6), 1346–1356.

Reeh, A. 2014 Natural laminar flow airfoil behavior in cruise flight through atmospheric turbulence. PhD thesis, Technical University of Darmstadt.

Reeh, A. & Tropea, C. 2015 Behaviour of a natural laminar flow aerofoil in flight through atmospheric turbulence. *Journal of Fluid Mechanics* 767, 394–429.

Reynolds, O. 1883 An experimental investigation of the circumstances which determine whether the motion of water shall be direct or sinuous, and of the law of resistance in parallel channels. *Philosophical Transactions of the Royal Society of London* (174), 935–982.

Rist, U. & Fasel, H. 1995 Direct numerical simulation of controlled transition in a flat-plate boundary layer. *Journal of Fluid Mechanics* 298, 211–248.

Rist, U. & Maucher, U. 2002 Investigations of time-growing instabilities in laminar separation bubbles. *European Journal of Mechanics-B/Fluids* 21 (5), 495–509.

Rist, U., Maucher, U. & Wagner, S. 1996 Direct numerical simulation of some fundamental problems related to transition in laminar separation bubbles. *Computational Fluid Dynamics* 96, 319–325.

Romblad, J. 2023 Experiments on the laminar to turbulent transition under unsteady inflow conditions. PhD thesis, IAG, University of Stuttgart.

Romblad, J., Ohno, D., Guissart, A., Würz, W. & Krämer, E. 2022 Response of NLF airfoils to small scale turbulence. In *IUTAM Laminar-Turbulent Transition*, pp. 243–253. Springer.

Romblad, J., Ohno, D., Nemitz, T., Würz, W. & Krämer, E. 2018 Laminar to turbulent transition under unsteady inflow conditions: Wind tunnel experiments at increased turbulence levels. In *Deutscher Luft- und Raumfahrtkongress (DLRK)*. Deutsche Gesellschaft für Luft-und Raumfahrt - Lilienthal-Oberth e.V.

Romblad, J., Ohno, D., Würz, W. & Krämer, E. 2020 Laminar to turbulent transition at unsteady inflow conditions: wind tunnel measurements at oscillating inflow angle. In *New Results in Numerical and Experimental Fluid Mechanics XII*, pp. 254–264. Springer.

Sayadi, T., Hamman, C. W. & Moin, P. 2013 Direct numerical simulation of complete H-type and K-type transitions with implications for the dynamics of turbulent boundary layers. *Journal of Fluid Mechanics* 724, 480–509.

Schlichting, H. 1933 Zur Enstehung der Turbulenz bei der Plattenströmung. *Nachrichten von der Gesellschaft der Wissenschaften zu Göttingen, Mathematisch-Physikalische Klasse* pp. 181–208.

Schlichting, H. & Gersten, K. 2016 *Boundary-Layer Theory*. Springer, Heidelberg.

Schmid, P. & Henningson, D. 1992 A new mechanism for rapid transition involving a pair of oblique waves. *Physics of Fluids A: Fluid Dynamics* 4 (9), 1986–1989.

Schmidt, O. T. & Rist, U. 2014 Viscid-inviscid pseudo-resonance in streamwise corner flow. *Journal of Fluid Mechanics* 743, 327–357.

Schubauer, G. & Klebanoff, P. 1955 Contributions on the mechanics of boundary-layer transition. *Tech. Rep.* NACA-TN-3489.

Schubauer, G. B. & Skramstad, H. K. 1947 Laminar boundary-layer oscillations and transition on a flat plate. *Journal of Research of the National Bureau of Standards* 38, 251–292.

Schwamborn, D., Gerhold, T. & Heinrich, R. 2006 The DLR TAU-code: Recent applications in research and industry. In *European Conference on Computational Fluid Dynamics ECCOMAS CFD*.

Sears, W. 1941 Some aspects of non-stationary airfoil theory and its practical application. *Journal of the Aeronautical Sciences* 8 (3), 104–108.

Seifert, A. & Hodson, H. P. 1999 Periodic turbulent strips and calmed regions in a transitional boundary layer. *AIAA Journal* 37 (9), 1127–1129.

Seifert, A. & Wygnanski, I. 1995 On turbulent spots in a laminar boundary layer subjected to a self-similar adverse pressure gradient. *Journal of Fluid Mechanics* 296, 185–209.

Selent, B. & Rist, U. 2010 Direct numerical simulation of jet in crossflow actuators. In *High Performance Computing in Science and Engineering '09*, pp. 241–253. Springer.

Sherer, S. E. & Scott, J. N. 2005 High-order compact finite-difference methods on general overset grids. *Journal of Computational Physics* 210 (2), 459–496.

Smith, A. M. O. & Gamberoni, N. 1956 Transition, pressure gradient and stability theory. *Tech. Rep.* ES-26388. Douglas Aircraft Co.

Solomon, W. J., Walker, G. J. & Hughes, J. D. 1999 Periodic transition on an axial compressor stator: Incidence and clocking effects: Part II—Transition onset predictions. *Journal of Turbomachinery* 121 (3), 408–415.

Sommerfeld, A. 1908 Ein Beitrag zur hydrodynamischen Erklärung der turbulenten Flüssigkeisbewegung. *Proceedings of the 4th International Congress of Mathematicians* III, 116–124.

Spalart, P. & Allmaras, S. 1991 A one-equation turbulence model for aerodynamic flows. In *30th Aerospace Sciences Meeting and Exhibit*.

Studer, G., Arnal, D., Houdeville, R. & Seraudie, A. 2006 Laminar–turbulent transition in oscillating boundary layer: experimental and numerical analysis using continuous wavelet transform. *Experiments in Fluids* 41 (5), 685–698.

Tani, I. 1964 Low-speed flows involving bubble separations. *Progress in Aerospace Sciences* 5, 70–103.

Theodorsen, T. 1935 General theory of aerodynamic instability and the mechanism of flutter. *Tech. Rep.* NACA-TR-496.

Thumm, A. 1991 Numerische Untersuchungen zum laminar-turbulenten Strömungsumschlag in transsonischen Grenzschichtströmungen. PhD thesis, IAG, University of Stuttgart.

Tollmien, W. 1929 Über die Entstehung der Turbulenz. 1. Mitteilung. *Nachrichten von der Gesellschaft der Wissenschaften zu Göttingen, Mathematisch-Physikalische Klasse* pp. 21–44.

Torrence, C. & Compo, G. 1998 A practical guide to wavelet analysis. *Bulletin of the American Meteorological Society* 79 (1), 61–78.

Turhan, B., Wang, Z. & Gursul, I. 2022 Coherence of unsteady wake of periodically plunging airfoil. *Journal of Fluid Mechanics* 938, A14.

Visbal, M. R. & Gaitonde, D. V. 2002 On the use of higher-order finite-difference schemes on curvilinear and deforming meshes. *Journal of Computational Physics* 181 (1), 155–185.

Walker, G. 1989 Transitional flow on axial turbomachine blading. *AIAA Journal* 27 (5), 595–602.

Walker, G. 1993 The role of laminar-turbulent transition in gas turbine engines: A discussion. *Journal of Turbomachinery* 115 (2), 207–216.

Walker, G., Hughes, J. & Solomon, W. 1999 Periodic transition on an axial compressor stator: Incidence and clocking effects: Part I—Experimental data. *Journal of Turbomachinery* 121 (3), 398–407.

Wassermann, P. & Kloker, M. J. 2002 Mechanisms and passive control of crossflow-vortex-induced transition in a three-dimensional boundary layer. *Journal of Fluid Mechanics* 456, 49–84.

Wazzan, A., Gazley, C., J. & Smith, A. 1981 H-R_x method for predicting transition. *AIAA Journal* 19, 810–812.

Weismüller, M. 2012 A new approach to aerodynamic performance of aircraft under turbulent atmospheric conditions. PhD thesis, Technical University of Darmstadt.

Wenzel, C. 2019 DNS of compressible turbulent boundary layers: pressure-gradient influence and self-similarity. PhD thesis, IAG, University of Stuttgart.

White, F. 2006 *Viscous Fluid Flow*. McGraw-Hill, New York.

Williams, G. 2017 Aerospace technology demonstration: BLADE, the flagship laminar flow project within the Clean Sky Programme. In *AeroTech Congress & Exhibition*. SAE International.

Wissink, J. & Rodi, W. 2003 DNS of a laminar separation bubble in the presence of oscillating external flow. *Flow, Turbulence and Combustion* 71 (1), 311–331.

Wygnanski, I., Sokolov, M. & Friedman, D. 1976 On a turbulent 'spot' in a laminar boundary layer. *Journal of Fluid Mechanics* 78 (4), 785–819.

Yarusevych, S. & Kotsonis, M. 2017 Steady and transient response of a laminar separation bubble to controlled disturbances. *Journal of Fluid Mechanics* 813, 955–990.

Zhang, D., Chew, Y. & Winoto, S. 1996 Investigation of intermittency measurement methods for transitional boundary layer flows. *Experimental Thermal and Fluid Science* 12 (4), 433–443.

Zilberman, M., Wygnanski, I. & Kaplan, R. 1977 Transitional boundary layer spot in a fully turbulent environment. *Physics of Fluids* 20 (10), S258–S271.